# PROJECT 13-5000

**FINAL REPORT**

# Model validation using CFD-grade experimental database for NGNP Reactor Cavity Cooling Systems with water and air


**Prepared by:**

**Dr. Annalisa Manera[1] (PI) (manera@umich.edu)**
**Dr. Michael Corradini[2] (Co-PI) (corradini@engr.wisc.edu)**
**Dr. Victor Petrov[1] (Co-PI) (petrov@umich.edu)**
**Dr. Mark Anderson[2] (Co-PI) (manderson@engr.wisc.edu)**
**Casey Tompkins (catompkins@wisc.edu)**
**Daniel Nunez (danielnu@umich.edu)**

**[1]Department of Nuclear Engineering and Radiological Sciences**
**University of Michigan**
**2355 Bonisteel Blv, Ann Arbor, MI 48109-2104**

**[2]Engineering Physics**
**University of Wisconsin-Madison**
**1500 Engineering Drive, Madison, WI 53706**



**Performed under:**
**NEUP 13-5000**
**TPOC: Mitch Farmer**
**Rev. 0**

(This page intentionally left blank)

# EXECUTIVE SUMMARY

This project has been focused on the experimental and numerical investigations of the water-cooled and air-cooled Reactor Cavity Cooling System (RCCS) designs. At this aim, we have leveraged an existing experimental facility at the University of Wisconsin-Madison (UW), and we have designed and built a separate effect test facility at the University of Michigan.

The experimental facility at UW has underwent several upgrades, including the installation of advanced instrumentation (i.e. wire-mesh sensors) built at the University of Michigan. These provides high-resolution time-resolved measurements of the void-fraction distribution in the risers of the water-cooled RCCS facility.

A phenomenological model has been developed to assess the water cooled RCCS system stability and determine the root cause behind the oscillatory behavior that occurs under normal two-phase operation. Testing under various perturbations to the water-cooled RCCS facility have resulted in changes in the stability of the integral system. In particular, the effects on stability of inlet orifices, water tank volume have and system pressure been investigated.

MELCOR was used as a predictive tool when performing inlet orificing tests and was able to capture the Density Wave Oscillations (DWOs) that occurred upon reaching saturation in the risers.

The experimental and numerical results have then been used to provide RCCS design recommendations.

The experimental facility built at the University of Michigan was aimed at the investigation of mixing in the upper plenum of the air-cooled RCCS design. The facility has been equipped with state-of-the-art high-resolution instrumentation to achieve so-called CFD grade experiments, that can be used for the validation of Computational Fluid Dynanmics (CFD) models, both RANS (Reynold-Averaged) and LES (Large Eddy Simulations). The effect of risers penetration in the upper plenum has been investigated as well.

# CONTENTS

# INTRODUCTION

This project has been focused on the experimental and numerical investigations of the water-cooled and air-cooled Reactor Cavity Cooling System (RCCS) designs. At this aim, we have leveraged an existing experimental facility at the University of Wisconsin-Madison (UW), and we have designed and built a separate effect test facility at the University of Michigan.

The experimental facility at UW has underwent several upgrades, including the installation of advanced instrumentation (i.e. wire-mesh sensors) built at the University of Michigan. These provides high-resolution time-resolved measurements of the void-fraction distribution in the risers of the water-cooled RCCS facility.

A phenomenological model has been developed to assess the water cooled RCCS system stability and determine the root cause behind the oscillatory behavior that occurs under normal two-phase operation. Testing under various perturbations to the water-cooled RCCS facility have resulted in changes in the stability of the integral system. In particular, the effects on stability of inlet orifices, water tank volume have and system pressure been investigated.

MELCOR was used as a predictive tool when performing inlet orificing tests and was able to capture the Density Wave Oscillations (DWOs) that occurred upon reaching saturation in the risers.

The experimental and numerical results have then been used to provide RCCS design recommendations.

The experimental facility built at the University of Michigan was aimed at the investigation of mixing in the upper plenum of the air-cooled RCCS design. The facility has been equipped with state-of-the-art high-resolution instrumentation to achieve so-called CFD grade experiments, that can be used for the validation of Computational Fluid Dynanmics (CFD) models, both RANS (Reynold-Averaged) and LES (Large Eddy Simulations). The effect of risers penetration in the upper plenum has been investigated as well.

The report is organized in two parts, the first one focused on the water-cooled RCCS system and the second one focused on the air-cooled RCCS system.

# PART I – EXPERIMENTAL INVESTIGATIONS IN A WATER-COOLED RCCS USING ADVANCED INSTRUMENTATION FOR THE STUDY OF INSTABILITIES AND THEIR IMPACT ON THE SYSTEM PERFORMANCE

## 1 REACTOR CAVITY COOLING SYSTEM

Passive safety systems are being considered as the primary method for decay heat removal in accident and off-normal operation scenarios in many of the Generation IV reactor designs (Wu et al. (2002)). Generation IV reactors are intended to operate at higher temperatures than are typical of current BWRs and PWRs. The higher temperatures can cause enhanced degradation of the biological shield, but also allow for new methods of decay heat removal due to the radiative heat load of the reactor pressure vessel.

Certain advanced reactor designs employ a reactor cavity cooling system (RCCS), which passively removes decay heat from the reactor pressure vessel (RPV) primarily by radiative and convective heat transfer. These systems were initially designed for Very High Temperature Reactors (VHTR), but can be extended to many of the Gen IV concept designs that operate with core vessel temperatures greater than 300 ◦C. The RCCS concept has two main variations being investigated: water-based cooling and air-based cooling. The air based system's key advantage is its ability to operate indefinitely without any loss of coolant, but air has a comparatively lower heat capacity and heat transfer ability than water. The air-system is also highly dependent on external weather conditions, which can induce flow reversal and hamper heat removal capabilities (Muci (2014)). The water-based system on the other hand has much better heat transfer capabilities due to a higher fluid density and heat capacity, which allows for a more compact design. However, the use of water suffers from a low boiling point at atmospheric pressures. During off-normal reactor conditions, the water-based system will reach two-phase natural circulation flow and oscillations can arise that have the potential to diminish heat removal efficiency and/or generate fatigue in the system. The water-based system also has a finite fluid inventory that is boiled-off over the course of a few days, after which operator action is required to refill the storage tank.

Successful deployment of the water-based system is highly dependent on analysis of the instabilities and oscillations that are formed in the system and the design's ability to mitigate their appearance and/or magnitude. Lisowski et al. (2014) performed initial characterization of the water-based system and showed the appearance of geysering and hydrostatic head fluctuations. Testing showed that the oscillations produced from the hydrostatic head fluctuations deviate 20 - 30% from the mean and are pseudo-stable, but geysering that later develops in the system leads to large flow excursions and potential vibrational fatigue on the network piping. Understanding what mechanisms cause the system to change operating mode can lead to mitigation of the development of these oscillations and ensure stability when a full scale RCCS design is implemented.

Various researchers have studied the RCCS using system level modeling efforts. Lisowski et al. (2011) showed that the prediction capabilities in MELCOR and RELAP 5 are not consistent upon reaching saturation in the RCCS, where MELCOR predicts large instabilities and RELAP predicts stable flashing. Oh (2015) attempted to study the water-based RCCS using a MELCOR model and showed that it was possible to accurately model single-phase natural circulation, but upon reaching saturation the model failed to accurately capture the oscillatory phenomena. The model was very sensitive to meshing, especially in the tank, and overestimated the oscillatory frequency and

magnitude compared to experimental data. Haskin (2016) created a new system code to deal with the inability of MELCOR and RELAP to accurately linear stability of the RCCS.

This new code attempts to better deal with geometry where there are multiple possible flow paths, such as those present at the inlet and outlet of the risers as well as updated numerical schemes. The common consensus among the researchers is that the RCCS system requires experimental validation, which can be used to improve and/or validate the predictive capabilities of the models.

Table 1.1: Overview of current RCCS concepts for VHTR (Oh et al. (2006), Wu et al. (2002), IAEA (2001a), and HTGR-86-024 (1986))

| Reactor | RCCS Coolant Type | Thermal Power |
|---|---|---|
| HTTR | Water Forced Flow | 30 MW |
| HTR-10 | Water Natural Circulation | 10 MW |
| PBMR | Water Natural Circulation | 400 MW |
| GT-MHR | Air Natural Circulation | 500 MW |
| MHTGR | Air Natural Circulation | 350 MW |

The RCCS concept was formulated in the 1950's for very high temperature reactors (VHTR). Many variations on the design are planned for use in Gen IV reactors (Tbl. 1.1). All of the designs whether air or water based involve reactor vessel temperatures greater than 300 $^{\circ}$C in order to provide sufficient radiative transfer to the cooling system (Simoneau et al. (2007) and IAEA (2001a)). RCCS designs have three primary implementation goals as designated by IAEA (2001a):

- Heat removal from the reactor cavity during normal plant operation with the capability to ensure the required temperature conditions for the reactor cavity concrete.
- Removal of decay heat and heat accumulated in the core and structural elements, as well as maintaining the reactor vessel, fuel, reactor internals and reactor cavity concrete temperatures within allowable limits during emergency cool-down.
- Confining of radioactivity released into the reactor cavity during normal operation and in emergencies.

The Generation IV reactors utilizing RCCS technology have very similar methods for implementation of the RCCS (Fig. 1.1). Each design has a system of ducts or tubes that surround the outside of reactor pressure vessel (RPV) to remove the excess heat load. These ducts are then joined in a plenum to allow the working fluid to either leave the system or recirculate. Many of the water-based designs include a steel plate that connects the heated ducts in order to enhance thermal conduction between the risers and help to limit the radiative load on other support structures and the biological shield. The ducts in all concepts are radiatively and convectively heated by the reactor pressure vessel. The working fluid, either air or water, is then heated within the risers and a density differential is created between the hot and cold legs. Buoyancy induced flow is then able to extract heat from the reactor cavity. In the air system, hot air is exhausted directly to the atmosphere. In the case of the water-based system, a secondary forced flow loop is implemented in the water storage tank in order to remove heat during steady-state operation. Upon reaching off-normal conditions in the reactor such as loss of power, the water-based system is allowed to reach saturation and heat is removed through evaporation and subsequent release of steam to the environment.

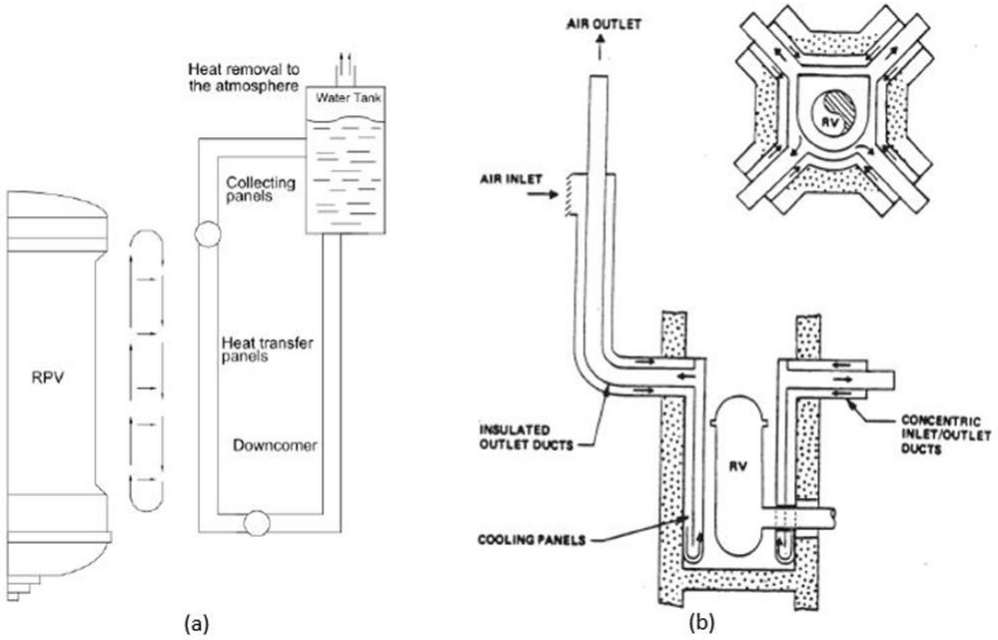


Figure 1.1: Reactor cavity cooling system concepts for water (a) and air (b) (Lisowski et al. (2011) and C.P. Tzanos (2006))

## 1.1 PROJECT GOALS – PART I

The work presented here is focused on the study of two-phase flow phenomena that includes the mechanisms behind the development and decay of oscillations and instabilities in the water-based RCCS, as well as methods for mitigating their effect on the system's performance. The oscillatory flow present in the RCCS results in thermal oscillations of the wall temperature, which need to be accommodated for in the full scale design and can hamper the heat transfer capabilities of the RCCS. This particular study is an extension of previous work on RCCS systems and is intended to garner greater insight into the mechanisms behind the oscillatory flow through increasing the instrumentation (specifically Wire Mesh Sensors) for study of voiding behavior. The geometry of the RCCS concept is also unique from previous natural circulation experiments due to the asymmetry created in the piping network, which results in variation of the flashing phenomenon.

Studying the stability in the RCCS is achieved through perturbing the operating point in order to find and expand the envelope of operational stability. The system has undergone multiple perturbations in tank volume, inlet throttling, and pressure in order to discover the stability envelope. These perturbations help to reveal the underlying phenomena responsible for the oscillatory behavior and instabilities in order to expand the stable operational envelope.

# 2 OVERVIEW ON FLOW INSTABILITIES

## 2.1 Two-Phase Instabilities and Oscillations

Natural Circulation and two-phase flow in general are prone to exhibit certain unstable or pseudo-unstable phenomena when specific conditions are met due to the extremely low driving force behind their operation. These instabilities and oscillations can become detrimental to the system's mechanical structure and ability to perform their intended functions, thereby causing premature

failure. Classifying the behavior and eventually determining the conditions for their appearance can help to remove or limit the instabilities' effect on system performance.

Two-phase instabilities are generally classified into two types: Static or Dynamic (Tbl. 2.1). Static instabilities are those that can be predicted by steady-state analysis and result from a small shift in the system flow to an unstable operating point. They can result in flow excursions or other dynamic instabilities. Dynamic instabilities are produced by feedback effects in the system between different primary state variables. These result in periodic or chaotic changes in the system performance (Boure et al. (1973)).

### 2.1.1 Static Instabilities

Static instabilities are instabilities that can be predicted from steady-state analysis when a system has multiple steady-state operating points for a given set of boundary condition. Shifts in the flow that lead to operation in these unstable regions can cause the system to transition to a new steady-state or undergo a dynamic instability to regain stability. These types of instabilities can be either fundamental or compound, which means that either single or multiple mechanisms control the instability.

***Pure Static Instabilities***

Flow excursions (Ledinegg Instability) occur when a small change in the system flow rate causes the system to reach an unstable operating zone in which the driving pressure is greater than the pressure drop through the system. This was first seen by Ledinegg (1938) and occurs because the pressure drop during all steam flow is larger than that of a fully liquid flow, so a change in the channel pressure drop with respect to mass flow rate can become negative for certain flow rates. When operating according to the Ledinegg Criterion a flow excursion can occur if the mass flow rate is perturbed (Eq. 2.1). If the mass flow rises slightly the driving force in the system will be higher than the frictional drop causing the flow to accelerate to a stable operating point or vise versa. This instability can be experimentally observed by a sudden drop or rise in the flow rate.

Table 2.1: Overview of two-phase instabilities as characterized by Boure et al. (1973)

| Class | Type | Mechanism | Characteristics |
|---|---|---|---|
| | | **Static Instabilities** | |
| *1.1 Fundamental Static Instabilities* | 1. Flow excursion or Ledinegg instability | $\frac{d\Delta P}{dG}\Big\|_{int} < \frac{d\Delta P}{dG}\Big\|_{ext}$ | Flow undergoes sudden, large amplitude excursion to a new, stable operating condition |
| | 2. Boiling Crisis | Ineffective removal of heat from heated surface | Wall temperature excursion and flow oscillation |
| *1.2 Fundamental Relaxation Instability* | 1. Flow Pattern transition instability | Bubbly flow has less void but higher $\Delta P$ than that of annular flow | Cyclic flow pattern transitions and flow rate variation |
| *1.3 Compound Relaxation Instability* | 1. Bumping, geysering or chugging | Periodic adjustment of metastable condition, usually due to lack of nucleation sites | Period process of super-heat and violent evaporation with possible expulsion and refilling |
| | | **Dynamic Instabilities** | |
| *2.1 Fundamental Dynamic Instabilities* | 1. Acoustic Oscillations | Resonance of pressure waves | high frequencies (10-100 Hz) related to time required for pressure wave propagation in system |
| | 2. Density Wave Oscillations | Delay and feedback effects in relationship between flow rate, density, and pressure drop | Low frequencies (1 Hz) related to transit time of a continuity wave |
| *2.2 Compound Dynamic Instabilities* | 1. Thermal Oscillations | Interaction of variable heat transfer coefficient with flow dynamics | Occurs in film boiling |
| | 2. BWR Instability | Interaction of void re- activity coupling with flow dynamics and heat transfer | Strong only for a small fuel time constant and under low pressures |
| | 3. Parallel channel instability | Interaction among small number of parallel channels | Various modes of flow redistribution |
| *2.3 Compound Dynamic Instabilities as a secondary phenomena* | 1. Pressure Drop Oscillation | Flow excursion initiates dynamic interaction between channel and compressible volume | Very low frequency periodic process (0.1 Hz) |

$$\left(\frac{d\Delta P}{dG}\right)_{channel} \leq \left(\frac{d\Delta P}{dG}\right)_{driver} \quad 2.1$$

***Fundamental Relaxation***

Fundamental relaxation or flow transition instabilities occur when the flow transitions between flow patterns. Generally, this instability refers to a transition between annular and bubbly flow, because annular flow has a noticeably lower frictional pressure drop than bubbly flow which causes an increase in the flow rate. The increased flow can reduce the amount of void formed due to a lower enthalpy riser in a thermo-fluid system. If the lowered void fraction cannot sustain annular flow, the flow reverts back to bubbly-slug flow. This process can be repeated periodically as long as the system remains at the same operating conditions (Jiang et al. (1995)).

Oscillations produced by the flow transition instability are suspected to be the primary instability mech-anism in natural circulation systems compared to other dynamic instabilities such as the density wave oscillation (Nayak and Vijayan (2008)). Like the Ledinegg instability the effect can be predicted using steady-state analysis, but at each operating point where the instability is present there are multiple modes of operation available to the system. A small change in the mass flow causes a jump to a different flow pattern (operational mode) that may or may not be sustainable. Nayak et al. (2003) has also shown through modeling that the modes of operation for the flow transition instability are greater than the Ledinegg instability and that the region of instability is greater than that of the Ledinegg-type, further making it a prime suspect for natural circulation instabilities. Models for this type of instability require further experimental verification in order to fully classify them.

***Compound Relaxation***

Compound relaxation instabilities including geysering, bumping and chugging are flow transitions, but require different operating conditions from the fundamental relaxation and occur sporadically. This phe-nomenon occurs when fluid cycles through stages including a reheat, sudden propagating vaporization, and then a return of subcooled fluid re-wetting the walls. Each burst of vapor can be considered as its own hydraulic cycle and is not necessarily coupled to other excursions. The geysering effect has been documented by Griffith (1962) to be on periods of 10-1000 seconds and is dependent on geometry, power, and pressure. Geysering and chugging instabilities have been seen in various natural circulation systems (Chexal and Bergles (1972), and Lisowski et al. (2014)). In the case of the WRCCS, Lisowski documented the geysering occurrence only after the flow loop was broken due to significant evaporation of the water inventory exposing the chimney exit.

### 2.1.2 Dynamic Instabilities

Dynamic instabilities are formed from propagation of time lag between states and feedback effects throughout the system. Unlike static instabilities, dynamic ones require more complex theoretical analysis because they are entirely due to transient effects. In a dynamic instability, the system starts in or enters an unstable operating mode and attempts to return to a stable operating state. The dynamic instabilities are also classified into fundamental and compound instabilities similar to their static counterparts.

***Fundamental Instabilities***

Similar to the fundamental static instabilities the dynamic counterpart propagates an instability by a single mechanism, either Acoustic pressure waves or density(void) waves. The nature of wave propagation makes these instabilities highly dependent on geometry.

### *Acoustic Oscillations*

Acoustic oscillations are high frequency flow oscillations on the order of the travel time for pressure waves propagating though a system. Acoustic waves form by compressing and decompressing the voids in the system, the density shift causes the collapse or generation of additional vapor. Generally, the acoustic waves have negligible effects on the system due to high frequency (10 - 1000Hz) and low magnitude, but a few cases have been reported where the waves can have a substantial effect on the base line pressure drop (Bergles et al. (1967) and Boure et al. (1973)). In addition to geometric effects on propagation, the acoustic waves are also dependent on the bubble size and density in the fluid (Ardron and Duffey (1978)).

### *Density Wave Oscillations*

Density wave oscillations (DWO) are instabilities that form from feedback effects between pressure, density (void formation), and flow rate. When pressure is perturbed downstream due to a change in voiding behavior, a change is produced in the driving forces causing a flow excursion. The flow excursion causes further changes to the downstream density; lowering it due to a higher flow rate that causes a lower temperature rise and therefore less void production. Lower voiding causes the driving pressure to drop and the process then repeats yielding an oscillatory behavior in the flow rate. The density waves generally oscillate on a period 1 to 2 times the fluid particle resonance time as it travels through the channel or loop.

Density waves have been classified into two different types by Fukuda and Kobori (1979). Type I are present under low power low mass quality conditions and are dominated by gravitational forces. At low vapor qualities a small change in the quality will cause a larger change in void and therefore a large change in the driving force. Type II requires higher powers and is driven by the frictional forces between the two phases. Void fraction is much larger under these conditions so the frictional losses are also large. When void changes by a small amount the frictional losses change by a comparably larger amount than the driving head resulting in a reduction in flow speed and therefore an accumulation of excess void and variations in density.

### *Compound Instabilities*

Parallel channel interaction involves flashing or boiling between multiple parallel channels, which results in flow rate variation between the channels. This instability can be formed from combinations of other instabilities occurring in some or all of the channels. Marcel et al. (2010) observed three different modes of operation including in-phase periodic oscillations where the channel oscillations are in-phase with the feed line, a-periodic where the system exhibits chaotic oscillations, and out-of-phase oscillations where the channel oscillation period is a multiple that of the feed line period and oscillations alternate between channels.

### *Compound Instabilities as a secondary phenomenon*

The pressure drop instability is considered a secondary phenomenon because it is always initiated by a static instability and therefore operates in the same negative d P/dG regime as them. This particular instability requires the presence of a downstream compressible volume such as the gas space in the RCCS water tank. When flow excursions occur, the system ejects large amounts of steam pressurizing the compressible volume and effectively modifying the saturation temperature in the system. The fluid then becomes either superheated or subcooled, limiting or enhancing void production in the system.

## 2.2 Overview of Similar Experimental Facilities and Their Results

Various natural circulation test facilities have been built to analyze stability of single- and two-phase flow. The systems vary in scale and geometry and many of them are related to testing natural circulation in a reactor core after unplanned shut down, loss of power, or loss of flow accidents. Some systems are designed to model natural circulation reactors such as Dodeward BWR due to the appearance of instabilities during startup and have attempted to determine methods for minimizing the appearance or duration of these flow instabilities. A summary of many of these experiments is presented in Tbl. 2.2.

Table 2.2: Overview of two-phase natural circulation facilities from Prasad et al. (2007)

| Test Facility | Configuration | Features |
|---|---|---|
| *DESIRE (IRI, Delft University Netherlands)* | A scaled facility for Dodewaard NCBWR. Uses Freon as working fluid. Possibility to adjust local friction at core inlet and riser exit. Variable riser length. | Radially asymmetric power distribution, which can be used to compare the 3D thermal hydraulic and CFD codes. Has artificial neutronic feedback. |
| *CIRCUS (IRI, Delft University Netherlands)* | A full height scaled model of Dodewaard reactor. Four electrically heated fuel channels and four bypass channels and one common riser. Flexibility in the use of number of risers and facility to adjust inlet friction and subcooling. | Designed to study the thermal hydraulic stability of a natural circulation BWR at low-pressure conditions typical for start-up. |
| *PANDA (Switzerland)* | A large scale thermal hydraulic test facility with six cylindrical pressure vessels. The installed power is 1.5 MW generated by a bundle of heater rods. | Designed for 10 bar and 200 °C. |
| *CLOTAIRE (CEA, France)* | Developed to study two-phase flow phenomena in the secondary side of PWR steam generators. Can simulate steam/water at a pressure of 75 bar with the use of Freon 114. | With slight modifications, the test facility can be used to BWR studies. |
| *PUMA (Purdue University, USA)* | Design consists of four parallel channels in the core with bypass channels. Detailed instrument system. Electrical heating mechanism. | Designed to simulate the transient response following various LOCA scenarios and to simulate transients where the pressure is below 1.03 MPa. |
| *SIRIUS-N* | A reduced scale test facility which resembles a typical NCBWR. The loop consists of two channels, two chimneys, an upper plenum, a downcomer, a subcooler and a preheater. | Can simulate accurately the regional and core wide instabilities of BWRs. Equipped with void feedback reactivity simulation facility. |
| *CAPCN (Argentina))* | Test facility with full height relative to CAREM reactor and a volume scale of 1:280. The operating pressure is 12 MPa and maximum power of 300 kW. | Simulate the dynamic phenomena of CAREM reactor coolant system near normal operating conditions. |
| *ITL (BARC, India)* | Full height test facility with a volume scaling of 1:452. It has a design pressure of 100 bar and temperature 315 °C. | Designed in BARC, India, to simulate natural circulation phenomena in Advanced Heavy Water Reactor (AHWR). |
| *PLC (BARC, India)* | A parallel channel (four channels) test facility developed by BARC. PLC has a design pressure of 20 bar and temperature 220 °C and can operate at 200 kW. | Can simulate steady-state behavior of AHWR with channels at same or different powers. Artificial neutronic feedback simulation. |
| *NCTF (IIT Bombay, India)* | A 1/4th length scale test facility resembling AHWR. It consists of two loops with four risers and two steam drums representing the four loops of AHWR. | Designed and fabricated in IIT Bombay to study the dynamics of AHWR. Studies on single and multiple channels, and integrated system studies can be carried out. |

### 2.2.1 Parametric Effect Studies for Stability

The primary reason for such experimental facilities is to determine operational areas of stability and methods for dampening or eliminating instability and oscillatory behavior, and to validate model predictions for stability. Many of the systems use power, pressure, and inlet subcooling as primary methods for characterization of the facilities' stable operating ranges.

Natural circulation systems often see instabilities in the form of density wave oscillations due to the coupled nature of mass flow with pressure, void fraction, and power. Often the region of stability is classified by a power vs subcooling plane and commonly non-dimensionalized into the Phase Change-subcooling plane for effective comparison with other facilities. The phase change-subcooling plane indicates stability of a thermal-hydraulic system with regard to Type I and Type II DWO and Ledinegg instabilities. Type I DWOs exist along the single-phase line at lower mass qualities, while type II DWOs reside at higher power and/or subcooling (Furuya et al. (2005b) and Ambrosini et al. (2000)).

Researchers used various tests to determine regions of stability. These researchers found that the envelope of stability's size and location on the phase change-subcooling plane can be affected by a system's operating conditions. Manera and van der Hagen (2003) found in the CIRCUS facility that the unstable region in the phase change-subcooling plane increases in size with power and that increased pressure decreases the size of the instability envelope. Guanghui et al. (2002) showed similar results with regard to power increasing the region of instability, although increased pressure did not decrease the size of the region of instability. Furuya et al. (2005a) also showed similar results to that of Manera and Guanghui et. al. on the SIRUS-N facility with regards to the effects of system pressure, heat flux, and subcooling. They also performed an in depth analysis on the type of instabilities occurring in the system and determined that DWOs are the dominate instability in their NC loops. The size of the region can also be affected by inlet and outlet frictional losses and pressure (Kim and Lee (2000), Manera and van der Hagen (2003), and Prasad et al. (2007)). The researchers mentioned did not show if the water inventory levels had an affect on the system behavior. RCCS type facilities will undergo inventory changes during operation, which can result in changes to the observed behavior for different frictional losses, external pressures, and power levels.

Boil-off effects are unique to natural circulation systems that are being utilized as a safety system during power outages. When the WRCCS reaches two-phase flow the water inventory is slowly boiled off in order to continue to remove decay heat from a reactor pressure vessel. Evaluations of water level on a natural circulation loop were performed at AES-2006 Protective Envelope Design for the Leningrad Nuclear Power Plant Site by Bakhmet'ev et al. (2009) and it was determined that the level had little effect on performance until the tank was nearly empty and the liquid loop was broken. At that point, the system experienced hydraulic shocks due to the reintroduction of water to the system. In other tests performed with varying pressure and power at higher water levels no shocks were formed although oscillations did occur at lower powers. The experiment did not have the ability to measure void fraction in the system for analysis of the operating mode during hydraulic shocks and did not determine the type of instabilities that occur when water was depleted.

Lisowski et al. (2014) studied the WRCCS extensively and determined that water inventory has a significant effect on the behavior of the system. While the system is losing inventory due to evaporation and flashing there is a period of oscillatory flow, that results in thermal oscillations in the piping network wall temperature. At lower inventory levels, when there is not a fully liquid

path for the water to follow (ie the loop is broken), the system experiences geysering due to a disconnect between the chimney outlet and downcommer inlet. This effect is similar to the flow excursions experienced by Bakhmet'ev et al. (2009). These instabilities can cause damage and fatigue to the system, shortening the operational lifetime of the cooling system. Lisowski et al. (2014) identified the types of oscillations or instabilities occurring during each operating regime in the WRCCS that arise as a result of liquid level changes in the storage tank based off changes in pressure, temperature, flow rate, and limited void fraction measurements. The void fraction in his analysis was measured using an optical probe, which only gives a single point measurement and can not truly evaluate the void in antisymmetric or annular flows. Without full measurements of the void, it is difficult to absolutely classify the change in voiding behavior due to the decreasing hydrostatic head. Thereby making it difficult fully evaluate the cause of the transition between different flow regimes. It was proposed that the voiding behavior changes due to a transition in the location of void formation. This analysis is restricted to observing changes in the optical probes measurement, phase shift of temperatures in the chimney region, and fluctuations in the differential measurement over the chimney.

Table 2.3: Overview of two-phase natural circulation testing.

| Test Facility | Configuration | Instrumentation | Parametric Studies |
|---|---|---|---|
| *UW 1/4 RCCS facility (Lisowski (2013))* | Asymmetric natural circulation with complex chimney | Pressure, Temperature, Flow Rate, and Point Void Fraction | Water Level, Power, Pressure, Orifice |
| *CIRCUS (Manera et al. (2005a))* | Asymmetric natural or forced circulation with simple chimney | Pressure, Temperature ,Flow Rate, and Area Void Fraction with gamma tomography and WMS | Power, Subcooling, and Pressure |
| *AES-2006 passive heat removal system (Bakhmet'ev et al. (2009))* | Asymmetric natural circulation with complex chimney | Pressure, Temperature, Flow Rate, and Mechanical Vibration | Power, Pressure, and Water level |
| *SIRIUS-N (Furuya et al. (2005a))* | Symmetric natural circulation with simple chimney | Pressure, Temperature, and Flow Rate | Power, Subcooling, and Pressure |
| *semi-closed experimental loop (Kim and Lee (2000))* | Semi-Symmetric natural circulation with simple chimney | Pressure, Temperature, Flow Rate, and void fraction from visual methods | Power, Pressure, Subcooling, and Orifice |
| *ANL 1/2 scale RCCS Facility (Lisowski et al. (2015))* | Asymmetric natural circulation with complex chimney | Pressure, Temperature, Flow Rate, and void fraction point measurements | To be completed 2018 |

Lisowski identified the most prominent oscillatory flow region in the UW-WRCCS facility as hydrostatic head fluctuations. The primary tool for analysis of hydrostatic head fluctuations was comparing pressure drop in the chimney and mass flow rate, which shows an elliptical relationship which is an indication of the presence of hydrostatic head fluctuations (Lisowski (2013)). However, it is more common to use a comparison of the driving pressure and the kinetic pressure to determine the operating trajectory. The measured pressure drop in the WRCCS measures a hydrostatic head change as well as the frictional drop, while the driving force is strictly a measure of the void fractions effect on driving the system (Manera et al. (2005a) and Furuya et al. (2005a)). Calculating the driving pressure requires knowledge of the void fraction in the chimney and Lisowski did not have the ability to measure total area void fraction at the exit of the chimney at the time of his experiments.

An overview of previous two-phase natural circulation testing is presented in Tbl. 2.3 and summarizes the instrumentation and tests performed at various facilities as well as a simple description of their geometry. Many of the facilities did not study the effects of liquid level on instability formation and the few that did lacked full information on the boiling boundaries and void fraction. The testing presented in this work is attempting to fulfill that void through the addition of wire mesh sensors for measurement of area void fraction. Wire mesh sensors and gamma tomography have been used in past experiments for full measurement of void fraction during instabilities such as those by Manera and van der Hagen (2003) at the CIRCUS facility, although the system geometry is simpler and therefore resulted in a different flashing behavior. The additional instrumentation in the WRCCS is expected to aid in the analysis of the mechanisms behind the change in flashing behavior in the RCCS experiment.

# 3 RCCS EXPERIMENTAL FACILITY AT UW

The RCCS experiment at University of Wisconsin - Madison is a scaled facility for the study of the effectiveness of the the decay heat removal design. The prototype was scaled to 1/4 height and a 5° slice. Various sensors were installed throughout the facility for both point and high-fidelity tomographic measurements of the system's operating parameters during all operating states. During each test a standard operating procedure is followed in order to acquire consistent and comparable results.

## 3.1 Facility Overview

The WRCCS test facility was designed to evaluate thermal hydraulic behavior in the full scale natural circulation facility. The full scale design is too large to be easily built and evaluated, so a scaling method was developed in conjunction with Argonne National Laboratories in an attempt to preserve all relevant non-dimensional numbers thought to be of importance for natural circulation. In addition to scaling considerations, the system was designed to be reconfigurable for operation under various scales if necessary and to allow implementation of a variety of instrumentation. The geometry in the WRCCS is unique and more advanced instrumentation such as wire mesh sensors were utilized in the current study of its evolving behavior.

### 3.1.1 Scaling

Scaling of experimental facilities can be a challenging task in order to accurately model the expected effects in a full scale system. The water-cooled RCCS at UW-Madison was scaled in height, due to the large space requirements a full scaled system would require. The same or very similar scaling methodology for the water-cooled RCCS has been applied on three different air-based RCCS experimental facilities: Argonne National Laboratories' (ANL) National Shutdown Test Facility (NSTF), Korea Atomic Energy Research Institute's (KAERI) PMR200 RCCS, and UW-Madison's ARCCS test facility. The scaling methodologies between ANL's 1/2 scale experiment and the UW 1/4 scale experiment are the same, while KAERI chose a slightly different methodology (C.P. Tzanos (2006) and Bae et al. (2014b)). The different scaling heights between ANL and UW allows for direct comparison of the scaling effects, while the differing methodology between KAERI's 1/3 scale experiment and UW's 1/4 scale experiment allow for closer comparison of the methodologies effect on the system's integral responses. Air-based RCCS facilities do not undergo phase change, so comparison of the two-phase dynamics have yet to be

validated. However, ANL is currently undergoing a transformation to the water-cooled RCCS, which can be used for direct comparison of scaling effects on the water-cooled RCCS.

The scaling laws developed for the afore mentioned facilities follow closely the derivation of energy and momentum equations and corresponding similarity relationships for natural circulation loop scaling developed by Ishii and Kataoka (1984). He determined that all the similarity parameters can not be met for both the single-phase and two-phase operating regimes. In the single phase operating regime he attempted to maintain the proper event timescale using geometry arguments ($t_o = l_R/u_R = 1$), but these arguments fail in the two-phase regime when trying to satisfy other similarity groups. This occurs because Ishii attempts to maintain the phase change number ($N_{pch} \propto (h_{out} - h_{in})/h_{fg}$) and the subcooling number ($N_{sub} \propto (h_f - h_{in})/h_{fg}$), which are known to be strong indicators for the occurrence of instability in a two-phase system. Ishii's analysis assumes the fluid is heated using heater rods inside the system, which is not the case for RCCS applications where the risers containing the transfer fluid are heated radiatively. From the perspective of the fluid, the heat source has little effect, however a radiative load allows for the study of the cavity wall temperatures which are important in determining the effectiveness of the RCCS system. Therefore, further analysis is performed to determine the effects of the radiative heat load on the risers and its effects on the system. KAERI put more emphasis on this effect when scaling their device than ANL or UW.

***UW-RCCS scaling***

RCCS scaling laws for the UW facilities were developed jointly with Argonne National Labs and UW-Madison for use in the NSTF, UW-WRCCS, and UW-ARCCS facilities. Researchers used a two-tier scaling method based on the Ishii method that scales the system height, but preserves the system's fluid temperature rise as well as operating pressure for steady-state conditions (C.P. Tzanos (2006)). The scaling ratio for the experiment to the prototype is shown in Eq. 3.1, where $\Psi$ is the parameter in question, such as height, heat flux, or a non-dimensional group. The subscript R will represent the scaling ratio for all states henceforth. The desired similarity relationships for single phase and two-phase flow in the RCCS are shown in Eq. 3.2 and Eq. 3.3 respectively and defined in Tbl. 3.1 and the reference C.P. Tzanos (2006). These non-dimensional groups are as follows in order from left to right, top to bottom: temperature ratio number, time ratio number, Stanton number, Rayleigh number, Biot number, cavity convective number, cavity radiation number, Froude number, Richardson Number, single phase friction number, two-phase Froude number, two-phase friction number, orifice number, and the drift flux number. It was determined that not all could be satisfied when scaling the system height, but the best attempt is described briefly below. A full discussion of the scaling can be found in the references (C.P. Tzanos (2006) and Lisowski (2013)).

$$\Psi_R = \frac{\Psi(model)}{\Psi(prototype)} = \frac{\Psi_m}{\Psi_p} \tag{3.1}$$

$$N_t = T^* = St = Ra = Bi = N_C = N_r = F\,r = Ri = F = 1 \tag{3.2}$$

$$N_{F\,r} = N_{fi} = N_O = N_d = 1 \tag{3.3}$$

The scaling laws were derived using a non-dimensional form of the momentum and energy fluid equations. These gave rise to a set of non-dimensional numbers upon which the similarity argument was applied and used for scaling the system. The system fluid properties were set as the prototype dictated, therefore maintaining thermo-physical properties including densities, thermal expansion coefficients, heat capacity, etc. The remaining parameters to be scaled are functions of the physical length scales, which have an implications in the thermo-hydraulic phenomena present in the RCCS.

The scaling laws are based on the assumption that the fluid temperature rise in the heated section of the scaled RCCS is equal to the prototype and the system height will be scaled down. An energy balance over the fluid is shown in Eq. 3.4. It suggests that an adjustment to the system height (`) will force a modification of the heat flux ($q_{00}$), azimuthal dimensions ($\xi$ and $A_o$), and/or the velocity ($u_o$) in order to hold similarity (Eq. 3.5).

$$\Delta T_o = \frac{q_o'' \xi \ell}{u_o \rho_o A_o C_P} \tag{3.4}$$

$$\Delta T_{oR} = \frac{q_{oR}'' \xi_R \ell_R}{u_{oR} A_{oR}} = 1 \tag{3.5}$$

Using non-dimensional similarity groups derived from the momentum and energy equations one can determine scaling effects associated with setting the temperature rise to unity. The Richardson or Froude number (Eq. 3.6), which is a ratio of potential to kinetic energy, was set to unity because natural circulation is dominated by gravitational effects. Henceforth, this method will be referenced as the Richardson scaling methodology.

$$Ri_R = \left( \frac{g \beta \Delta T_o \ell}{u_o^2} \right)_R = \frac{\ell_R}{u_{oR}^2} = Fr^{-1} = 1 \tag{3.6}$$

Maintaining the Richardson number results in a velocity scaling equal to $\sqrt{\ell_R}$. This has consequences in most non-dimensional hydraulic numbers. The first relating to the system dynamics is the time ratio number, which measured the thermal time response of the riser walls to the system flow (Eq. 3.7). It is desirable to maintain this value at unity, but that requires reducing the riser wall thickness ($\delta_{iR}$). This could result in loss of mechanical strength in the experimental facility, so its scaling value was arbitrarily set to unity. It also becomes difficult to get acquire piping with a thickness less than schedule 40. This results in slowing the time response of the system walls, but the time response of instabilities will be quicker because the velocity is not scaled exactly with the length.

$$T_R^* = \frac{\ell_R}{u_{oR} \delta_{iR}^2} = \sqrt{\ell_R} \tag{3.7}$$

In addition to setting the pipe wall thickness ratio to unity, the remaining azimuthal dimensions (hydraulic diameter and flow cross sectional area) were set to unity. This then scales the heat load ($Q_R$) and heat flux ($q_R''$), by $\sqrt{\ell_R}$ and $1/\sqrt{\ell_R}$ respectively according to Eq. 3.5. Scaling in this way results in a reduction in the Reynolds number and other heat transfer related quantities.

This will result in a slower thermal mechanical response, but a faster fluid response compared to the full scale design, so it is important to ensure that laminar and turbulent flow regimes are maintained between the model and prototype systems. At saturation with an expected fluid

temperature rise in the heated test section of 3 K, the corresponding Reynolds number is on the order of 30 000. This causes the system to remain in the fully turbulent regime, faster flows will only increase this. At low temperatures, the single-phase performance could be affected as the Reynold number drops to approximately 4000, which is near the transitional regime and will have an affect on heat transfer and friction in the RCCS. The final scaling ratio for all the non-dimensional groups are shown in Tbl. 3.1. A majority of the non-dimensional groups are reduced in the scaling of the RCCS with the exception of the heat flux, which needs to be scaled up in order to keep the temperature ratio number at unity. The friction numbers for both single and two-phase are not listed because they can be adjusted to unity with appropriately placed orifices.

***Scale Comparison***

The UW and ANL facilities use the same scaling methodology, while KAERI chose a different method based on heat transfer in the cavity as apposed to in the fluid. Their scaling methodology is presented in Bae et al. (2014b) and Bae et al. (2014a) and is primarily based on the cavity heat transfer effects as opposed to the fluid effects with the intention of scaling the system height. This results in the primary similarity parameters being the Rayleigh and Plank numbers in the cavity, where W is the cavity width between the RPV and risers, $T_c$ is the cavity temperature, and T is the temperature rise of the riser wall temperature, $\sigma_B$ is the Stefan-Boltzmann constant (Eq. 3.8 and Eq. 3.9). Both values can not be satisfied so they chose to use the Plank number as the primary parameter, because radiation should dominate heat transfer in the reactor cavity.

$$Pl = \frac{k\Delta T}{W\sigma_B T_c^4} \tag{3.8}$$

$$Ra = \frac{g\beta\Delta T W^3}{\alpha\nu} \tag{3.9}$$

Plank scaling results in a system where the structural temperatures are equal to the prototype system, but fluid temperatures are shifted. The applied heat flux is then scaled directly by $\grave{}_R$, while the azimuthal dimensions are equal to the prototype. This results is a system that has the same geometrical scaling as the UW air-based RCCS facility (scaled height and unchanged azimuthal dimensions) and ANL facility with the exception that the applied heat flux in *P l/Ra* scaled tests is lower than in the UW facility for a comparable test. A summary of the as built facilities is presented in Tbl. 3.2. Due to the same dimensional scaling (scaled height and unscaled azimuthal geometry) it is possible to directly compare the effects of the different scaling methodologies for heat loads.

Comparisons between air-based facilities have been performed in an INERI test series in conjunction between the three laboratories, but testing using KAERI's Plank scaling methodology required very low flow rates. These were unachievable in the UW facility due to integral flow instabilities, and therefore the results were inconclusive for Plank scaling. Richardson based scaling tests were successful at all three facilities and resulted in useful scaling data. Riser air temperatures were similar between the systems, but the duct wall temperature in the UW facility was significantly larger. This is attributed to a shorter distance between the heaters and risers and the lack of a reflector on the back side of heated cavity in the UW facility (Lisowski et al. (2016)).

***Other Scaling Methodology***

Commonly a power-to-volume scaling methodology is used for nuclear power plant test facilities because it has the advantage of preserving the event time scale. This method was first derived by Zuber (1980) for scaling nuclear test facilities for testing accident conditions. The method requires

the facility to adhere to the similarity conditions presented in Eq. 3.10. The first condition states that the same fluid conditions are necessary. The second is the power-to-volume scaling condition and states that scaling the power (Q) requires an equal scaling of the volume $(\forbidden{V})$ and therefore the flow rate by S. The third condition states that the height in both systems must be preserved in order to maintain pressure, gravity and friction effects in the energy and momentum equations for the scaled facility. The final condition states that friction between the model and prototype must be the same. Distortions in any of the parameters results in distortions in the experimental data.

$$\begin{aligned} P_R = \rho_R = h_R = 1 \\ Q_R = \forbidden{V}_R = \dot{m}_R = S \\ \ell_R = 1 \\ \left(\frac{\xi}{A_c}K\right)_R = 1 \end{aligned} \tag{3.10}$$

Table 3.1: Scaling parameters. Set parameters are in the first section and derived parameters are in the lower section.

| **Variable** | **Scaling Ratio** | **Value for $\ell_R = 0.25$** |
|---|---|---|
| Temperature Rise | $\Delta T_{oR} = 1$ | 1.000 |
| Reference Temperature | $T_{oR} = 1$ | 1.000 |
| Hydraulic Diameter | $D_R = \delta_{yR} = 1$ | 1.000 |
| Flow Area | $A_{oR} = 1$ | 1.000 |
| inner pipe thickness | $\delta_{iR} = 1$ | 1.000 |
| Froude number | $(N_{Fr})_R = \frac{\ell_R}{u_{oR}^2} = 1$ | 1.000 |
| Fluid Velocity | $u_{oR} = \sqrt{\ell_R}$ | 0.500 |
| Drift Flux Number | $N_{dR} = \frac{V_{gjR}}{u_{oR}} = \ell_R^{-0.5}$ | 2.000 |
| Drift Velocity | $V_{gjR} = 1$ | 1.000 |
| Time Ratio number, outer | $T^*_{oR} = \frac{\ell_R}{u_{oR}} = \sqrt{\ell_R}$ | 0.500 |
| Richardson number | $(Ri)_R = \frac{\ell_R}{u_{oR}^2} = 1$ | 1.000 |
| Heat Flux | $q''_R = \ell_R^{-0.5}$ | 2.000 |
| Reynolds Number | $(Re)_R = \left(\frac{\rho u_o D_h}{\mu}\right)_R = \sqrt{\ell_R}$ | 0.500 |
| Heat Transfer Coefficient | $h_R = \ell_R^{0.4}$ | 0.574 |
| Stanton number | $St_R = \frac{h_R \ell_R}{D_R u_{oR}} = \ell_R^{0.9}$ | 0.287 |
| Cavity Radiation number | $(Nr)_R = \frac{T_{oR}^4}{D_R \ell_R} = \sqrt{\ell_R}$ | 0.500 |
| Temperature Ratio number | $(Nt)_R = \frac{Q_{oR}}{u_{oR} A_{oR}} = 1$ | 1.000 |
| Biot number | $(Bi)_R = h_R = \frac{h_R \delta_{iR}}{k_R} = \ell_R^{0.4}$ | 0.574 |
| Friction Number | $N_{fi} = \sum \left(f\frac{L}{D} + K\right)_R = 1$ | 1.000 |

Vijayan and Austregesilo (1994) and Nayak et al. (1998) tested the validity of the power-to-volume scaling methodology for natural circulation facilities. They determined it is difficult to satisfy all the requirements of the power-to-volume methodology. Vijayan and Austregesilo (1994) stated that steady state phenomena can be accurately scaled and tested, but transient and stability behavior

is significantly effected when the hydraulic diameter is modified. Nayak et al. (1998) found similar results and also stated the scaling is best performed on systems where the diameter is affected minimally, such as those with multiple individual channels.

The power-to-volume scaling methodology allows for simulation of transient and steady state behavior which is desirable for the RCCS facility. The RCCS has multiple flow channels which makes it suited for the power-to-volume scaling method, but the one-to-one height requirement can be difficult to achieve. The RCCS was studied in order to investigate possible transient behaviors, their causes, and mitigation if possible.

Table 3.2: Scaled dimensions for ANL, UW, and KAERI air-based RCCS facilities.

| Parameter | Full Scale | ANL ($Q_R = \sqrt{\ell_R}$) | UW ($Q_R = \sqrt{\ell_R}$) | KAERI ($Q_R = \ell_R$) |
|---|---|---|---|---|
| $\ell_R$ | 1.0 | 0.5 | 0.25 | 0.3 |
| Q [kW] | 920 | 35.5 | 12.5 | 7.5 |
| Riser height $\ell$ [m] | 15 | 7.5 | 3.76 | 4.5 |
| Heated Length [m] | 13.5 | 6.82 | 3.51 | 4.05 |
| Number of Ducts | 220 | 12 | 6 | 6 |
| Air Temperature Rise [°C] | 98 | 98 | 98 | 98 |
| Flow Rate per Duct [$\mathrm{kg\,s^{-1}}$] | 0.042 | 0.03 | 0.021 | 0.013 |

The Richardson/Froude scaling methodology preserves the qualitative features of the full scale facility, however the system time scale is perturbed. This is not an issue if the qualitative features of the full scale facility are still present. Analysis on scaling effects for static instability are presented later in section 6.2.2.

Table 3.3: WRCCS dimensions referenced to tank inlet as shown in Fig. 3.1.

| **Location** | **Indicator** | **Value** | |
|---|---|---|---|
| Riser Inlet | $Z_{riser,i}$ | 6.085 | m |
| Riser Outlet | $Z_{riser,o}$ | 0.573 | m |
| Core Inlet | $Z_{core,i}$ | 5.624 | m |
| Core Outlet | $Z_{core,o}$ | 2.500 | m |
| Tank Outlet | $Z_{tank,o}$ | 0.833 | m |
| Tank Total | $Z_{tank}$ | 2.000 | m |

Table 3.4: WRCCS piping and insulation material properties

| **Material** | **Uses** | **Conductivity at** 100 °C | |
|---|---|---|---|
| SS304L | network piping | 16.200 | W/m-K |
| Pyrogel XL | heated enclosure walls | 0.023 | W/m-K |
| Zircal-18 | heated enclosure walls | 0.070 | W/m-K |
| Carbon Steel | heated enclosure walls | 33.000 | W/m-K |
| K-flex | Piping insulation | 0.038 | W/m-K |

### 3.1.2 Dimensions and Materials

The UW WRCCS facility is a 1/4 height scaled facility according to the scaling laws presented based on the Ishii method. It is an open loop asymmetric natural circulation facility including an elevated water storage tank, a downcomer for water supply to the heated test section, a heated

enclosure test section to represent the outside of a reactor pressure vessel and cavity walls, and an adiabatic chimney (Fig. 3.1). The system is completely closed with the exception of a steam outlet at the top of the tank, where the steam is condensed and stored as a final reference for water inventory losses.

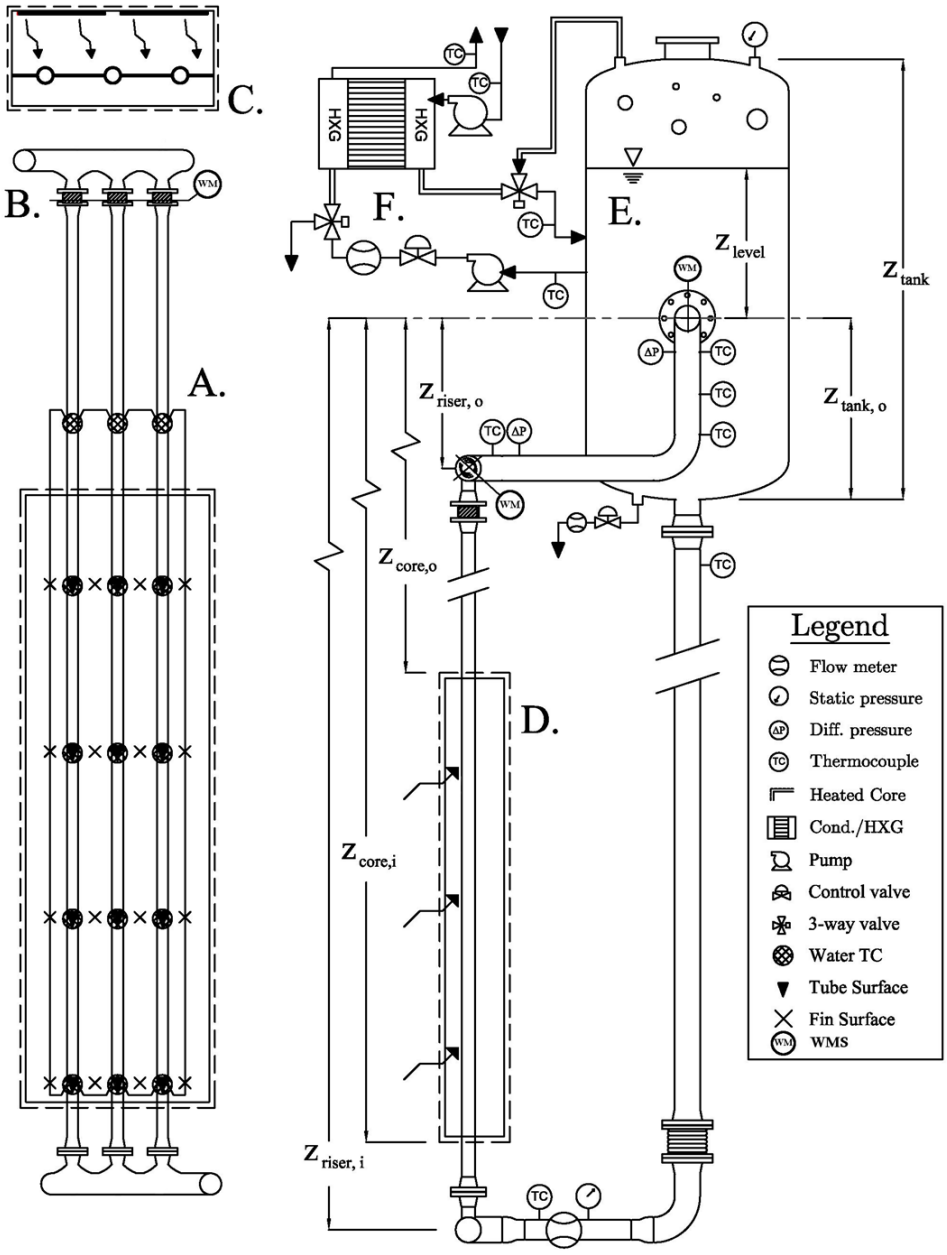


Figure 3.1: WRCCS elevation drawing dimensions are located in Tbl. 3.3. A: Test section, B: Outlet header, C: Heated enclosure (top view), D: Heated cavity (front view), E: Water storage tank, F: Condenser/Heat removal loop. Thermocouple elevations are located in appendix E. Only a single uncompensated differential pressure measurement is available, the locations on the diagram represent the tapping points for the measurement.s (Lisowski et al. (2014)).

The piping network is constructed from SS304 schedule 40 4" piping, while the heated fin consist of 3 schedule 40 2" pipes welded together with a 1/4" SS304L plate. Flexible hosing is used for connection with the heat exchanger/condenser and varies from 1/2" to 3/4" inner diameter. The heat exchange network is used for condensing steam during two-phase operation and as a heat removal system during single phase operation.

The heated enclosure contains thirty-six 1250 W plate heaters arranged in a 4 X 9 grid. The plate heaters are 12" X 6" rectangles arranged vertically (Fig. 3.2). The heaters are capable of a total maximum output of 45 kW or 27 kW/m$^2$, which is equivalent to 6.8 MW or 13.5 kW/m$^2$ in the full scale RCCS. The heaters are divided into four control zones which allows for the opportunity to test power shaping in both the axial and azimuthal directions.

The heated enclosure and piping are insulated in an attempt to maintain an adiabatic piping network. Reduction in these losses makes it easier to accurately model the behavior of the system and ensures as much energy is stored in the fluid as is possible. The heated enclosure is insulted with layers of Pyrogel and Zircal-18 sheet insulation. The piping network and tank are wrapped in a K-flex foam insulation. A summary of the material properties is shown in Tbl. 3.4.

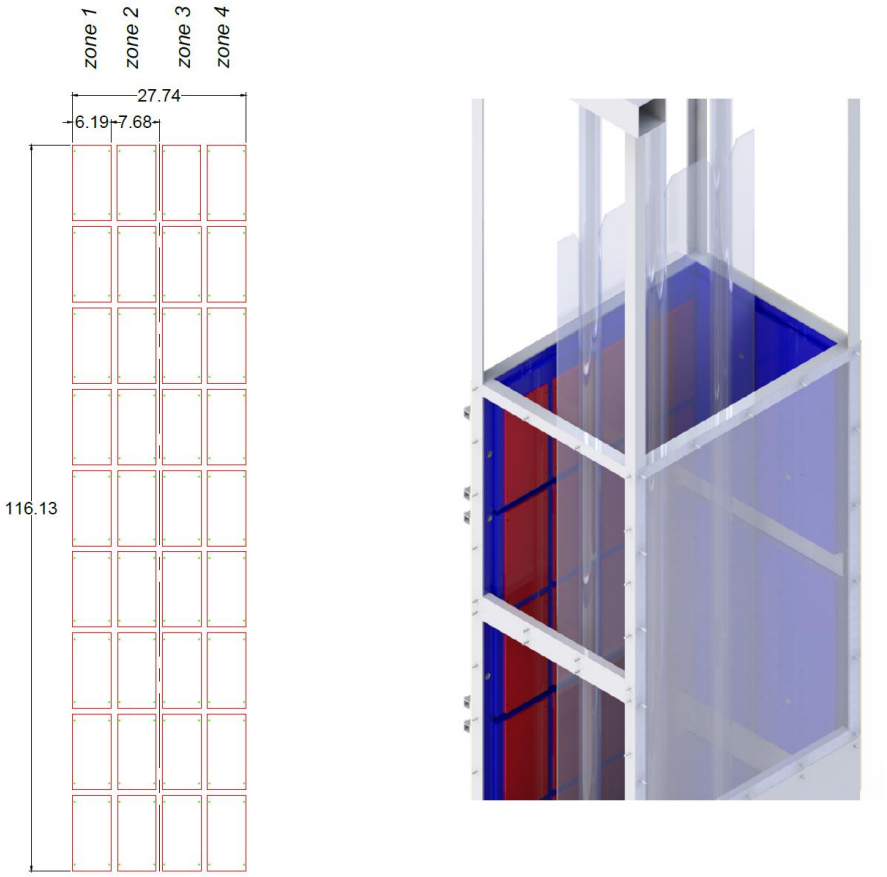


Figure 3.2: WRCCS heated enclosure showing plate heater orientation. Dimensions in inches.

In addition to heater control, the system can operate in forced flow and 1/6 scale. Forced flow is achieved by installing flexible tubing and pumping water from the tank directly into the downcomer for purposes of characterization of the system. Performing 1/6 scale testing requires

disabling the uppermost heaters, thereby reducing the total heat load on the test section. This can be used for testing effects on the RCCS stability due to hydrostatic head pressure. Scaling in the UW facility will also be validated by Argonne National Laboratories' NSTF after their conversion to a water-based RCCS.

## 3.2 Instrumentation

Various sensors are distributed throughout the RCCS in order to gain insight to the flashing phenomenon present in natural circulation systems. Instrumentation includes thermocouples, pressure transducers, flow meters, and wire mesh sensors (Fig. 3.1). Sixty-four thermocouples are distributed around the system in key locations. Primary thermocouples are located at the inlet and outlet headers of the heated section, throughout the chimney where flashing primarily occurs, and within the tank. Structural temperature sensors are placed on the riser tubes, rise conduction plate, and heater box walls.

System control and operations are performed with an NI C-RIO control system. Data acquisition and heater control is performed on a custom built LabVIEW program that runs the NI hardware. The main NI component is a cRIO-9024 containing multiple modules including: 64 thermocouple ports (NI-9213), 32 digital outputs for solid state relays (NI-9476+NI-9923), 16 differential analogue inputs (NI-9205), and 16 analogue outputs (NI-9264). The analogue outputs are used to control 4 Control Concepts microFUSION single phase SCR power controllers that control the four heating zones in the WRCCS.

### 3.2.1 Pressure and Flow

Primary metrics for system evaluation lie in the flow rate and pressure drop measurements throughout the system. Heat removal is a function of the mass flow rate which is a direct function of the frictional losses and driving forces in the WRCCS. The purpose of WRCCS research is to evaluate the two-phase phenomena and its effects on the system behavior. Therefore, it is important to measure the pressure drops across any two-phase regions. The system also undergoes inventory loss and pressurization due to steam production and flashing, so quantifying the loss is important for repeatability between tests.

***Mass flow***

The system is equipped with an electro-magnetic flow meter at the lowest elevation in the system just before water enters the heated test section. Placing the flow meter before the heated section prevents two-phase effects from entering meter and causing errors in the measurement. The flow meter is a FLOCAT IFC 090 and factory calibrated. The meter is generally set to measure from 0 to 80 gpm for all tests, but is capable of measuring in both flow directions if needed (-40 to 40 gpm). The absence of flow reversal in the system up to this point makes this unnecessary. The flow in the system is usually in the lower 25% of the meter's scope so error is kept to a minimum during tests.

***Pressure Measurements***

Three pressure transducers are installed in the system for measurement of hydrostatic gage pressures and differential pressure at various points. The information from these measurements quantify the evolving behavior of the system during flashing and the boundary conditions for each test.

Differential pressure is measured across the chimney region from the exit of the risers to the tank inlet, where a majority of two-phase effects are found in the system. These measurements reflect the formation of vapor and changes in the hydrostatic head due to density fluctuations in the chimney region.

Two hydrostatic gage pressure transducers are located in the WRCCS. The first is placed at the base of the system to measure water level and pressurization in the gas space. The second pressure transducer strictly measures the gas space pressure. The difference in the two yields a water level measurement that can be used to classify the amount of inventory boiled-off or drained during a test.

### 3.2.2 Void Fraction - Wire Mesh Sensors

Vapor formation (and therefore void fraction) in and above the heated risers is the primary quantity that affects the natural circulation driving force during two-phase low mass quality flows and its characterization is necessary in order to fully characterize the WRCCS operation state. A variety of methods have been employed to measurement of the void fraction, but the error produced is generally large and difficult to quantify. Typically void fraction can be measured using capacitance, conductance, optical, ultrasonic, or radiative methods (Boyer et al. (2002)).

The UW-WRCCS facility employs wire mesh sensors for the measurement of void fraction. These sensors measure the conductivity the fluid which can be correlated to the amount of steam and liquid water in the sensor. Under certain conditions, the sensors can also measure interfacial area, gas bubble velocity, and bubble size. An in-depth discussion on the instruments is presented in appendix D and a small summary on their operation is presented below.

***WMS operation theory***

Wire Mesh Sensors (WMS) in their current form were developed by Prasser and are designed for measuring phase fractions and visualizing phases in two-phase flows, where the phases have a significant difference in conductivity (Prasser et al. (1998)).

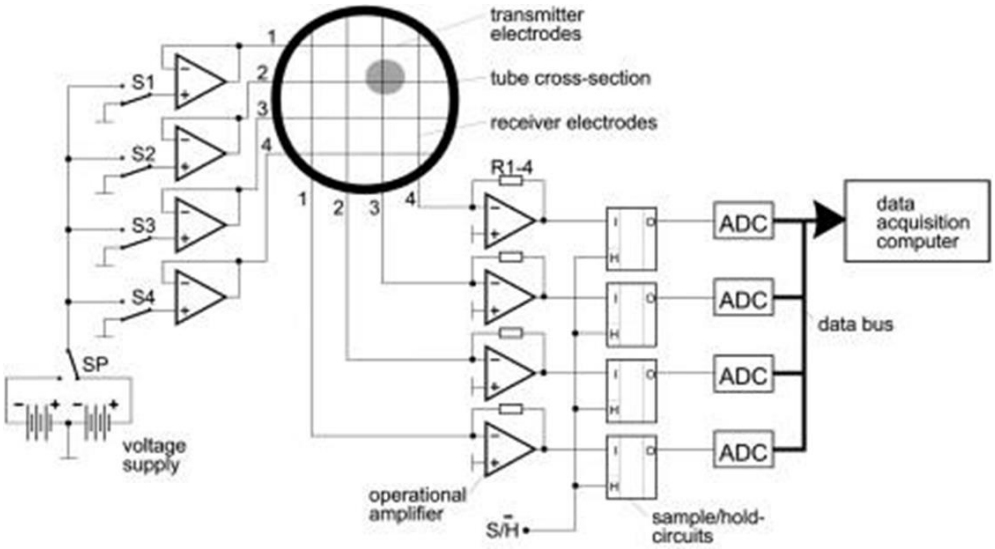


Figure 3.4: Wiring schematic for wire mesh sensors. Transmitters on the left supply a current to the electrodes sequentially and are measured by the receivers on the right (Pietruske and Prasser (2007)).

The WMS and their accompanying electronics used in this work have been supplied by the University of Michigan (Manera et al. (2006)). The WMS are conductivity measurements and unlike other intrusive void fraction measurements, a grid of sensors is employed instead of a single probe. This grid divides the flow into multiple cubic conductivity cells that are essentially measured instantaneously. This results in sliced images of the void fraction as it passes through the sensor. The WMS installed in the WRCCS are 16X16 grids of wires arranged in two parallel layers. Each layer consists of 16 wires oriented perpendicularly to the second layer with a fluid gap between them (Fig. 3.3).

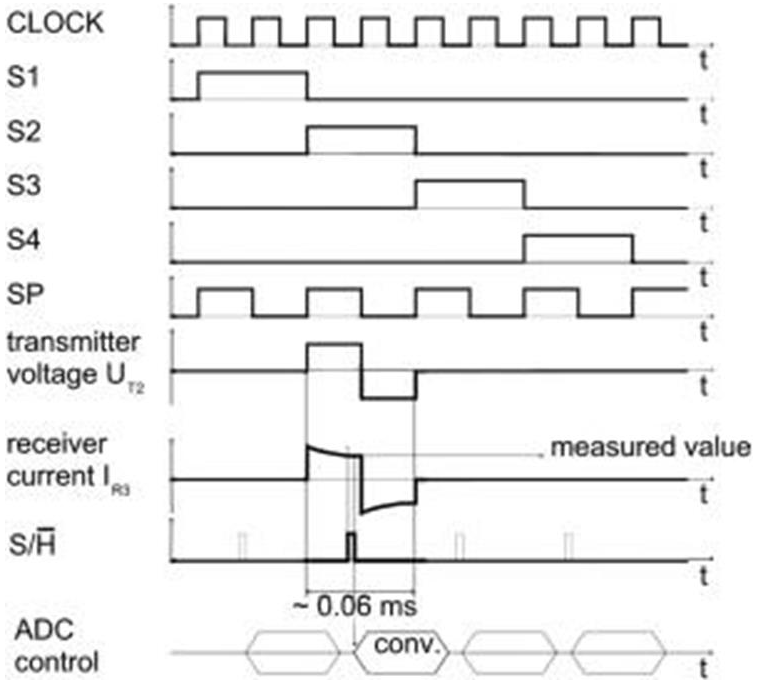


Figure 3.5: Wire mesh sensor timing for current pulses during operation and subsequent sampling. Labels are defined in the previous figure (Pietruske and Prasser (2007)).

Current flows from one layer through the fluid to the second layer and changes in the measured current correspond to a change in the conductivity of the fluid. The current pulses are sent sequentially through each wire at a rate of 6 µs per wire in one layer of the mesh sensor as demonstrated in Fig. 3.4 and Fig. 3.5. The currently installed sensors therefore take approximately 100 µs to measure a single slice of the flow. The current pulse along each wire is alternated in either direction to eliminate charge build up in the electrodes. Current in the receiver electrodes is constantly measured and sent to an analog to digital converter and stored for later analysis.

Temperature and salinity of the water can cause changes in the WMS conductivity measurements, so the sensors need to be calibrated for temperature if large shifts occur during measurements as described by Manera et al. (2006). A base calibration where the piping is fully filled with water at a temperature near to saturation is done every test to account for changes in salinity from test to test; these values are used as a maximum conductivity measurement that essentially identifies the liquid phase in comparison to the steam phase. Data from the WMS provides insight into the type of flashing phenomenon that occurs in the RCCS under two-phase operation.

The as build dimensions of the WRCCS WMS are shown in Tbl. 3.5. The sizes correspond to the wires transverse pitch ($\delta x$ and $\delta y$ assuming z is in the flow direction) and the axial pitch (space between sensing wires in z direction). The 4" sensors are located in the entrance and exit of the

larger chimney piping, while the 3 layer 2" sensors are located 4.5" before the exit of the risers. The wires are 0.125 mm in diameter, so one sensing layer results in a flow area reduction of 3.25% or 1.62% for the 2" and 4" sensor respectively. The associated pressure drop therefore can be considered negligible.

### 3.2.3 Uncertainty

Device uncertainty is determined and minimized to guarantee sufficient resolution in order to measure desired quantities in the UW-WRCCS facility. The equipment previously mentioned and their operational regimes are listed in Tbl. 3.6.

Table 3.5: RCCS WMS dimension

| Sensor | Transverse Dim. [mm] | Axial Dim. [mm] | Sensing Layers |
|---|---|---|---|
| 4" sensor | 6.059 | 1.905 | 1 |
| 2" sensor | 3.108 | 1.58 | 2 |

Table 3.6: Instrumentation in the WRCCS and their associated errors, see appendix D for details on error in the void fraction measurement.

| Measurement | Equipment | Range | | Uncertainty | |
|---|---|---|---|---|---|
| Temperature | Omega Type K Thermocouple wire | 1,250 | °C | ±0.75% or 2.2 | °C |
| Temperature | Omega Type K Thermocouple probe | 1,250 | °C | ±0.4% or 1.1 | °C |
| Temperature | Omega Type K Thermocouple prob sp. lim. | 1,250 | °C | ±0.2 | °C |
| Diff. Pressure | DP Harp EJA120A | 0-6 | inH2O | <0.2 | % |
| Hydrostatic Pressure | Siemens SITRANS P | 0-20 | psig | <0.5 | % |
| Gas Space Pressure | Siemens SITRANS P | 0-1 | bar | <0.5 | % |
| Flow Rate | Flocat IFC 090 | ±600 | l/min | ±1 mm $s^{-}{}_{1}$ and ±0.2 | % |
| Area Void Fraction | Wire Mesh Sensor | 0-1 | [-] | <10.5* | % |

Thermocouples have a range of errors associated with them, this is due to a recalibration process for some probe-type thermocouples. The WRCCS contains surface welded and probe type K thermocouples. The factory error for thermocouple wire for surface mounting is set at 2.2 ◦C. However, thermocouple probes used in the WRCCS have a special limit of error of 1.1 ◦C and are re-calibrated against a platinum RTD thermocouple in a circulating water bath to further reduce the error. The platinum RTD probe has an associated error of 0.2 ◦C and through the use of a linear regression fit between the measured type K probe temperature and the RTD probe temperature the error in the Type K probes is reduced to approximately that of the RTD probe.

The type K thermocouples also have a variety of time responses in the system due to various probe configurations. A majority of thermocouples are 1/8" diameter ungrounded probes which have a time response on the order of 0.5 s, which is sufficient for analysis of stable flows. In the header near the wire mesh sensors three grounded thermocouples are inserted that have a time constant of approximately 0.35 s, which enables measurement of faster temperature transients due to alternating fluid and steam across the thermocouple. The faster response time also assists in calibration of the WMS when there are large temperature transients that cause variation in the conductivity of the water. In the chimney a single exposed thermocouple is installed with a time

constant of 0.15 s for enhanced detection of void formation from alternating wetting and drying of the thermocouple tip.

Wire mesh sensor error is more challenging to quantify due to the measurements dependence on layer separation, mesh pitch, and void fraction disturbance due to the sensor. The spatial resolution of the sensor can be varied depending on the users purpose; the 4" WMS has square sensing areas each covering 4.35% of the total pipe area, so voids that are smaller than this go unmeasured. Finer mesh pitch or non-uniform pitch can result in greater disturbances to the void and thus increase or decrease the measured void fraction by slowing the vapor velocity by 20-40% due to increased friction at room temperature. Wangjiraniran et al. (2003) state that the error can be reduced at higher gas velocities and potentially at higher pressure and temperatures. The slowing of the void would not necessarily increase the area void fraction measured in a single sample, but would potentially increase the resonance time of the vapor and thereby increasing the measured time averaged void in the system. Currently the WMS that detects void in the chimney is not equipped to measured vapor velocity, so the estimated error is uncertain. The disturbance to the vapor from this slowing effect has been observed by Wangjiraniran et al. (2003) to be resolved 4δ past the WMS, where δ is the distance between layers. In the WRCCS, δ is approximately 1/8 to 1/16 inch so the void is restored before contact with any geometrical changes in the piping.

Uncertainty in WMS is a difficult quantity to asses due to limitations in the methods for its assessment. Through validation with secondary data sets it was determined that the WMS are accurate to within approximately 10%. Many of the secondary validation data sets used radiative methods, which have a maximum uncertainty of approximately 10-15% plus a possible unknown, but positive bias due to bubble dynamics as they pass through the sensing region. Trained neural networks have been shown to decrease the error of radiative void measurements significantly, but details on uncertainty of the secondary sensors in many of the validation sources are left unclear. The WMS have an additional inherent uncertainty that is affected by the physical parameters of the sensor (axial and transverse pitch), these have been shown to have an effect of less than 5% on the measured void fraction. A reduction in surface tension is expected to reduce these effects and can be achieved through an increase in fluid temperature. Bubble size measurements can only be accurately determined when they are larger than the mesh pitch, but there is still some uncertainty until approximately 3 times the size of the mesh pitch. Multiple sources estimate this at 10-25% error when compared to HSC data sets, which have limited accuracy for non-spherical or densely packed bubbles. Error in velocity measurements are entirely dependent on flow conditions. Velocity measurements have been shown to be best for the bubbly to slug flow transition, although the lower liquid velocities can lead to greater deceleration of the bubbles in the sensor.

## 3.3 Experimental Procedure

WRCCS testing occurs over a two or more day testing period depending on desired testing results and initial water conditions. Data is collected from the system when the heaters are active and during cool down periods, but not during preparation prior to the test.

***Pre-Test***

- Prepare the system with desired initial water volume and conditions (ie valve closure, orifices...)
- Filter water in the system with forced flow if it is not freshly filled with clean 18 MΩ water

***1 Day Prior***

- Recheck initial water volume for constancy and due to losses from filtering
- Check instrumentation for proper readings including initial pressure transducer readings and any open thermocouples
- Initialize data recording in LabVIEW, labeled by test number
- Set desired ramp conditions and begin heater ramp
- Allow system to preheat approximately 8-10 hours until desired preheat temperature is reached
- Shut down heaters and open tank access port to prevent vacuum formation

***Test Day***

- Initiate forced flow to return system back to an isothermal state
- Close all external valves and ports to RCCS except the steam vent
- Relabel recording file name for test day and start second data collection
- Set heater ramp power and rate
- Start heater power ramp
- Open cold line and start condenser pump when system reaches approximately 90 °C and set acquisition rate to at least 10 Hz
- Run test until desired two-phase phenomenon is observed
- Shut down heaters

# 4 UWRCCS FACILITY CHARACTERIZATION

The University of Wisconsin-Madison WRCCS facility is characterized by multiple modes of operation that are dependent on initial and boundary conditions including but not limited to water level, pressure, and orifice configurations to ensure repeatability. Primary operational variables include power level and shape, water level, and frictional loop effects. Previously, the WRCCS has been characterized for power level and shape effects as well as water level, but the focus of this work is on integral loop hydraulic effects when these state variables perturbed. Natural circulation facilities have been shown to be highly dependent on geometry and material selection due to their dependence on frictional losses. Small changes in the frictional losses can affect the occurrence and magnitude of two-phase flashing modes, while having minimal impact on single-phase flow. Characterization of the base flow behavior in the UW facility allows for study of perturbations such as pressure and increased frictional losses on system performance.

## 4.1 Nominal Behavior

The WRCCS facility operates over a two-day testing period for general tests due to the time required to heat the facility and to reduce strain on the operator. The first day of testing preheats the water over approximately 9 hours to about 90 °C. During this period the system undergoes stable single-phase flow. Overnight the power is shut down. The water begins to cool and becomes stratified with cooler fluid in the piping network and hotter fluid residing in the tank where there is larger thermal mass. The second testing day starts by pumping the preheated water through the loop in order to return the system to an isothermal condition and reduce the possibility of oscillatory effects that can occur when natural circulation is started with a stratified system. Upon reaching an isothermal state as defined by the temperatures in the inlet and outlet of the test section equalizing; the pump is shutdown and the heaters are ramped up in power over a 1-hour period.

The working fluid then rises in temperature until reaching saturation at the highest elevation in the chimney. Flashing begins and the system is held at power until the desired test conditions are fulfilled.

Described below is a characteristic data set detailing the phenomena observed during a typical WRCCS test. Included is the calculated system energy throughout the test period along with relevant temperature, pressure, and void fraction measurements. The data set is taken from Run 116, which operated with an electric heater input of 15.2 kW, a gas space pressure of 4.8 kPa, and 60% tank water volume.

### 4.1.1 Mass Flow Rate

The mass flow rate is a primary metric for evaluation of instabilities including their formation and decay. Mass flow in the WRCCS follows a predictable sequence of events for each test after determination of the initial operating mode at the start of two-phase flow. The timing of these operating modes, including duration and occurrence, is dependent on the system's boundary conditions including external pressure and insertion of additional frictional losses.

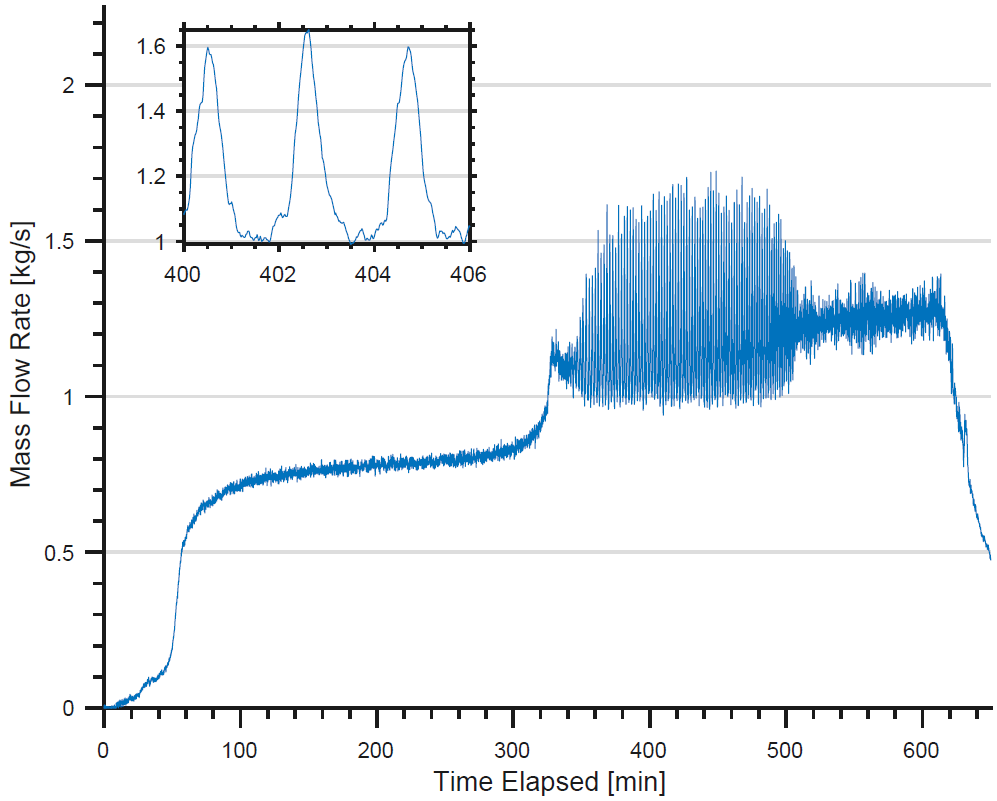


Figure 4.1: Mass Flow rate for run 116

At the beginning of a test after the heaters reach the desired power over a period of 60 min, thermal equilibrium between the structure and fluid is reached and steady single-phase flow is established (approximately 100 min). During this time the fluid temperature is steadily rising until saturation is reached at the exit of the chimney. At this point flashing begins to occur and a sharp increase in flow rate is observed due to an increase in the buoyancy force (approximately 325 min). The flow then evolves from a short period of steady flashing into an oscillatory regime. The flow oscillates

by ±25% of the mean flow rate with a decreasing period centered around two minutes. Eventually, the mean mass flow rate reaches approximately 1.25 kg $s_{-1}$ and the flow rate stabilizes, but constantly increases until the power is shut down at approximately 600 min (Fig. 4.1). Fluid oscillations of large magnitude and/or frequency can result in cyclic mechanical fatigue in the RCCS facility. As the system is scaled up, the magnitude of these oscillations are expected to scale and must therefore be considered in the final design of the RCCS. It is beyond the scope of this thesis to fully analyze the mechanical degradation due to these oscillations, but the magnitude and void fraction associated with these oscillations are analyzed and available for future studies into their effect on mechanical loading.

### 4.1.2 Temperature

Temperature in the WRCCS is a coupled response between the heater power and natural circulation mass flow rate in the system. Classification of the test, in regards to energy of the fluid and heat removal performance, is performed using temperatures at the inlet and outlet of the risers (Fig. 4.2a). They show a steady rise in temperature until saturation at the chimney exit is achieved. Flashing in the system maintains temperatures at a steady level, but small oscillations (± 0.5 ◦C) in the temperature are observed due to oscillations in the mass flow rate. Thermal couples located in the fluid are sheathed, but their associated time response in water (0.3 s) is insignificant compared to the duration of the oscillations. The fluid temperature in the heated cavity maintains a steady linear increase in the axial direction after saturation at the chimney exit is reached (Fig. 4.2b). The chimney and tank temperatures exhibit additional fluctuations overladed on the primary thermal fluid oscillations due to an alternating presence of steam and liquid passing over the thermocouple tip. These fluctuations are damped out in the tank due to the large water volume acting as a buffer between the flashing phenomena in the chimney and the water supply to the downcomer (Fig. 4.3).

The oscillations in the chimney temperatures exhibit a phase-shift due to system delay. The RCCS facility operates at low flow rates, so the propagation of temperature through the system is noticeably delayed. This in turn delays feedback mechanisms in the RCCS, which results in the sustained oscillations observed in the system. The travel length from the inlet to the exit of the chimney is approximately 2.2 m with an average flow rate of 0.2 m s−1, which results in a total travel time of approximately 11 s. This exactly corresponds to the phase shift between the peak of the fluid temperature oscillations (Fig. 4.3). This phase-shift also represents the significance of the adiabatic chimney in stability of the RCCS.

Delays between the travel of fluid from the heated section to the exit of the loop result in a delayed feedback when the fluid flow rate changes in the RCCS. This phenomenon results in self-sustained oscillations. As voiding begins to increase in the chimney, the flow rate also begins to increase due to the drop in hydrostatic head pressure, but the inertia of fluid in the system slows this flow rate increase. The increase in the flow rate results in a decrease in the enthalpy rise of the fluid in the riser, but the fluid that has already exited the heated section remains at a higher enthalpy due the previously lower flow rate. This hot fluid then propagates through the chimney eventually causing a further increase in the void production, thereby increasing the flow rate further. Eventually the lower enthalpy fluid propagates to the flashing point at the end of the chimney resulting in a lower voiding rate. This results in a reduced flow rate. The reduced flow rate allows for a larger enthalpy rise in the heated section and a delayed increase in the void fraction, repeating the process and resulting in the observed oscillations.

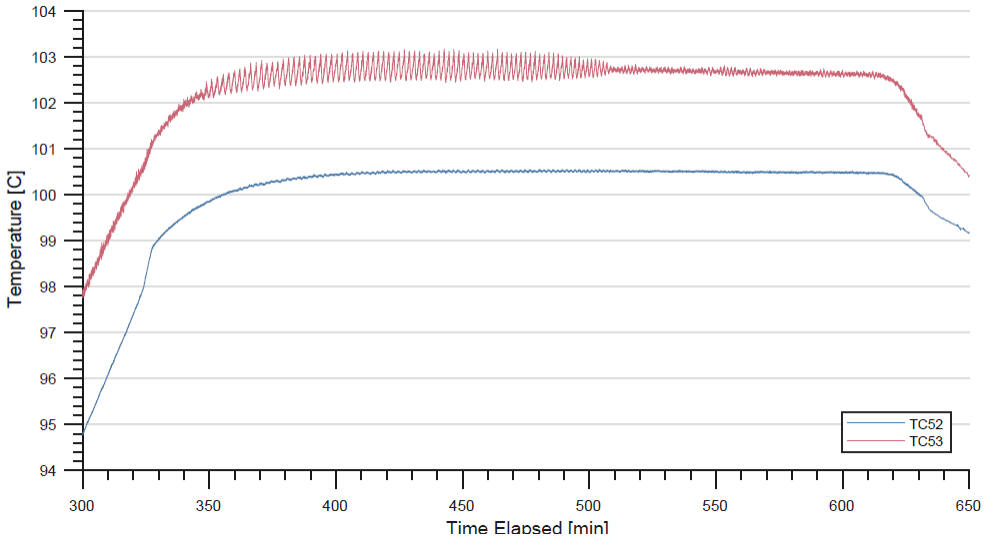


(a) Inlet and outlet header temperature surrounding the heated cavity

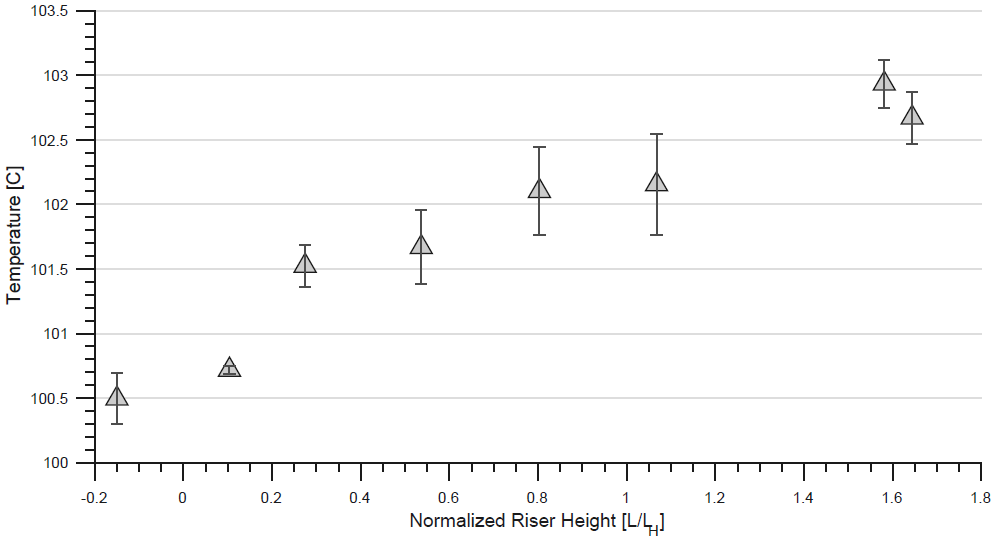


(b) Temperature rise in the risers from the inlet header to the outlet header. Location is normalized by heated riser height.

Figure 4.2: WRCCS temperatures at various locations for Run 116.

Oscillatory behavior in the flow rate due to voiding can result in changes in the structure temperature. These thermal oscillations result in fatigue, a shortened mechanical lifetime, and a loss of system efficiency. The thermal oscillations in the structure can be damped under low frequency oscillations by conducting the temperature evenly throughout the structure or neglected at higher oscillatory frequencies when the transfer rate between the fluid and the mechanical system is too slow to respond to the fluid temperature oscillations. These thermal oscillations have a small magnitude in the RCCS test facility and therefore are expected to have little effect of the structure, but at higher flow rates and/or oscillatory magnitudes they could become significant.

Efficiency issues from oscillations due to changes in the heat transfer rate between the structure and the fluid can not be directly measured in the RCCS due to lack of instrumentation, but an indication of the change in the heat transfer coefficient can be determined by a change in the structure temperature that is inconsistent with the change in fluid temperature due to the energy

conservation equation (Eq. 4.1). The applied heat rate ($\dot{Q}$) is constant and if the temperature difference between the fluid (Tf) and the pipe surface (Ts) is also constant it can be inferred that the heat transfer rate is constant. Data from the RCCS shows that the magnitude of thermal oscillations in the pipe wall are greater than the magnitude of oscillations in the center of the fluid, therefore there is a loss in the heat transfer rate between structure and fluid (Fig. 4.4). The oscillating fluid temperatures are not present until after exiting the test section, most likely due to strong radial temperature gradients. The lower magnitude of the thermal fluid oscillations could also be due to the thermal inertia of the adiabatic walls upon exiting the heated section of the risers. As the fluid temperature changes due to a varying heat transfer coefficient, the walls can dampen any sudden changes by reintroducing or removing heat from the fluid. Thermal oscillations are present in the tube surface, but not the conducting plate between risers (Fig. 4.5). This can cause added stress at the weld between the conducting plate and riser tube structure, although the thermal oscillation magnitude is small and this is unlikely.

$$Q = hA(T_S - T_f) \tag{4.1}$$

### 4.1.3 System Energy

Test performance is characterized by an energy balance over the test section (heated core) in order to determine heat removal efficiency (Eq. 4.2) of the WRCCS. This enables designation of any periods of operation where the system is less efficient or unable to perform adequately due to instability formation or flow reversal. During startup, the fluid begins to flow and the thermal mass of the structure is heated. Around 150 min the WRCCS structure's thermal mass reaches equilibrium with the fluid temperature and steady single-phase flow is observed. During this period the system displays steady heat removal (Fig. 4.6).

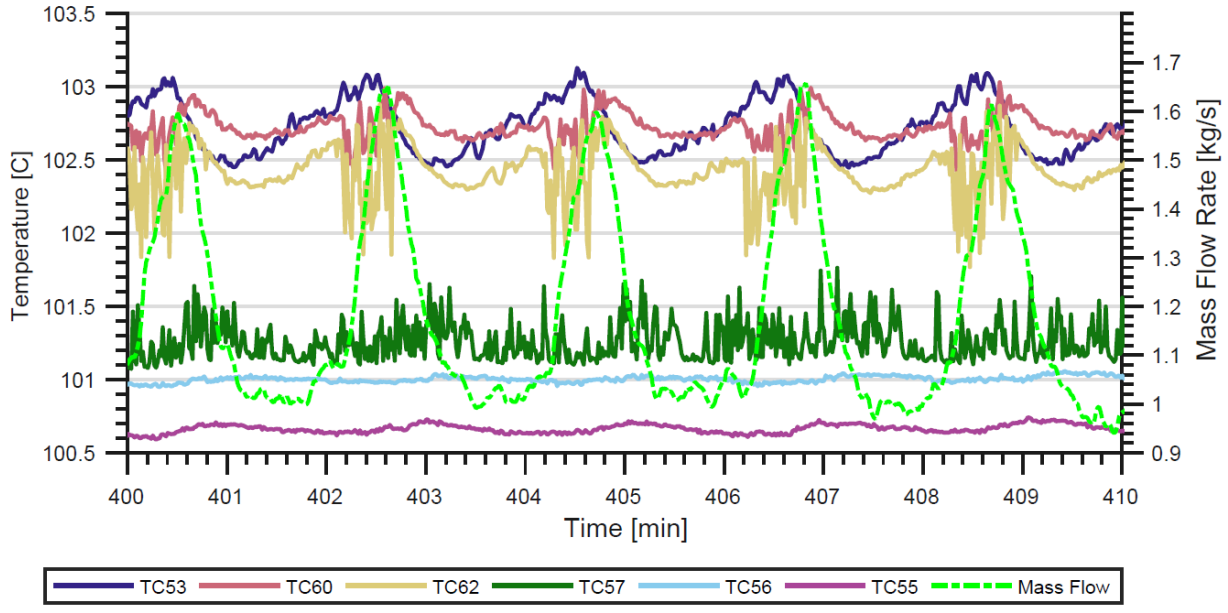


Figure 4.3: Chimney and tank temperatures during flow oscillations. Tank thermocouples 55-57 from lowest to highest elevation. TC53 is the chimney entrance. TC60 is the chimney exit. TC62 is located just before the chimney's final elbow.

At 325 min the fluid reaches saturation and flashing begins to occur in the chimney. The increased driving force causes an increase in mass flow and consequently an increase in heat removal. The

flow then enters a region of oscillatory behavior in both the temperature and flow rate, which is represented by oscillations in the energy balance. A phase shift between the mass flow and temperature readings at the inlet and the temperature reading at the outlet header creates these oscillations in energy. Filtering the data with moving time average presents a more accurate representation of the energy absorbed by the fluid and allows for classification of the system's efficiency during the oscillations. Ideally the outlet temperature data would be shifted back in time, but the varying flow rate in the system makes this more difficult with little payoff.

$$Q = mC_p^{\cdot}(T_{outlet,header} - T_{inlet,header}) \tag{4.2}$$

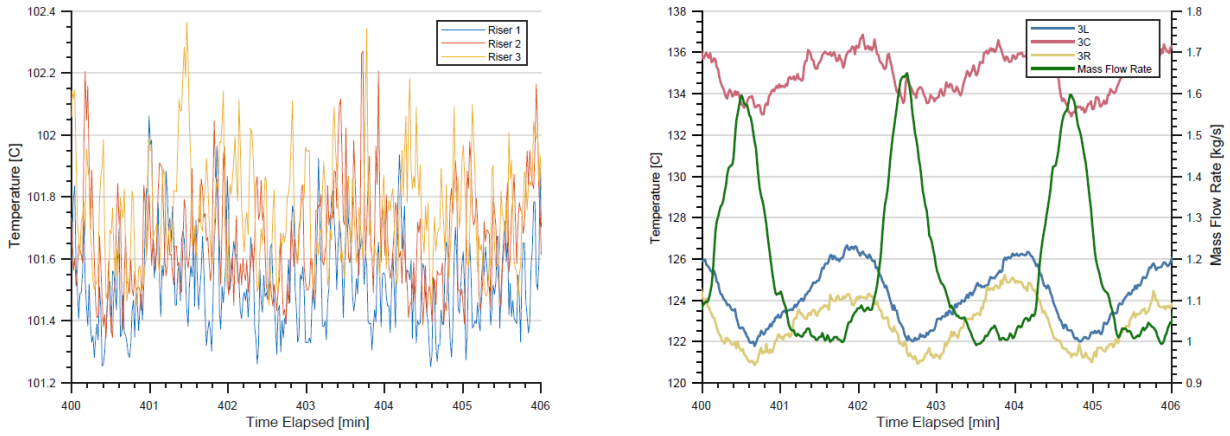


Figure 4.4: Thermal oscillations in the fluid (left) and pipe wall structure (right) at the middle of the heated test section. The magnitude of oscillations are greater in the pipe wall and nearly non-existent in the center of the risers.

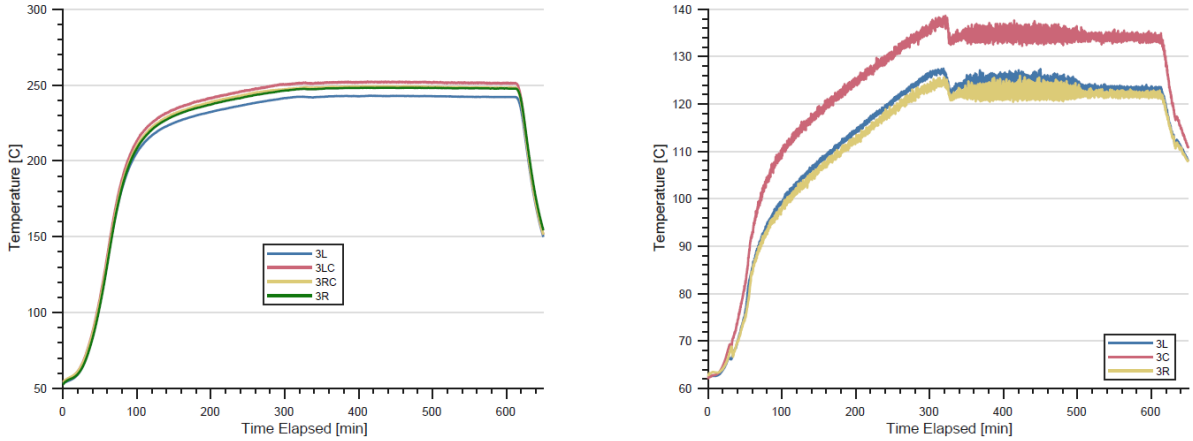


Figure 4.5: Riser conducting fin (Left) and tube (Right) temperatures over the course of the test. L = left, C = Center, R = Right, number indicates TC elevation (e.g. 3 is the middle of the heated section).

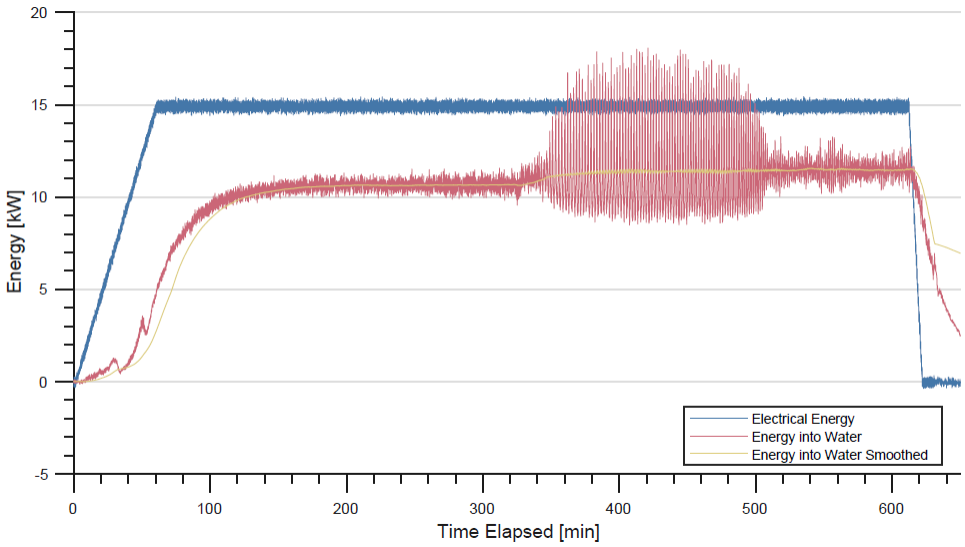


Figure 4.6: Energy balance over the heated core of the WRCCS that details the energy removed from the test section by the working fluid. Included is the electrical input energy, the time averaged energy, and the unaltered energy calculation.

### 4.1.4 Pressure

The WRCCS is equipped with two different gage pressure measurements: differential and hydrostatic. The hydrostatic pressure transducers measure the hydraulic head pressure of the system and the gas space pressure, while the differential pressure is a measurement across the chimney region (see chapter 3 for exact locations). These measurements are helpful in describing flow behavior, flow transitions, and quantifying external effects on the system.

***Hydrostatic Pressures***

Two static pressure measurements are taken to describe the varying state of the WRCCS as the system drains and/or pressurizes. Hydrostatic pressure at the base of the system describes the water level and any elevated pressure effects that arise from steam production in the tank. The gas space measurement solely measures the rise in tank pressure due to steam production. From these measurements, one can determine the water level in the system and its change during testing (Eq. 4.3). Where ρ is the average fluid density, g is the acceleration due to gravity and P is the measured hydrostatic pressure.

$$h = \frac{P_{static} - P_{gas}}{\rho g} \tag{4.3}$$

The static and gas space pressures have very similar features (Fig. 4.7). Upon reaching saturation both pressures rise due to pressurization of the tank. Eventually the steam production rate is equal to the venting rate and the pressure remains steady. During oscillatory flow, steam is not injected into the tank at a steady rate causing the gas space pressure to oscillate along with the flow.

Evaporation of the working fluid causes the water level in the system to drop (Fig. 4.8). The initial water level, as measured by a visual level gauge, and input power are the only parameters the operator has direct control over, so it is expected that a drop in water level is one of the primary

causes for behavioral changes in the system. The level is measured at the start and end of every test along with the integral condensation volume that is collected in a separate storage tank.

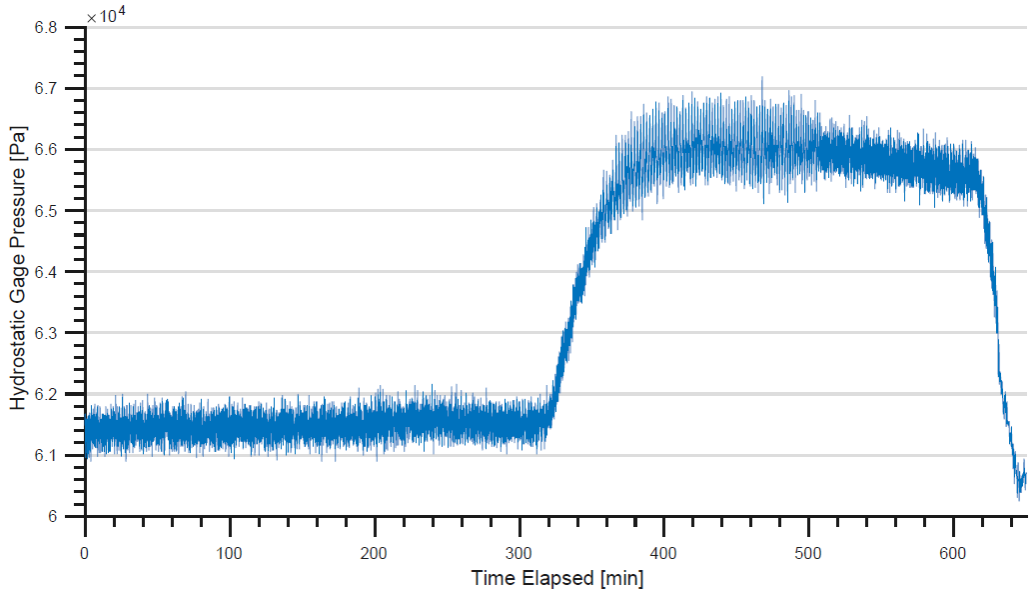


(a) Hydrostatic head pressure

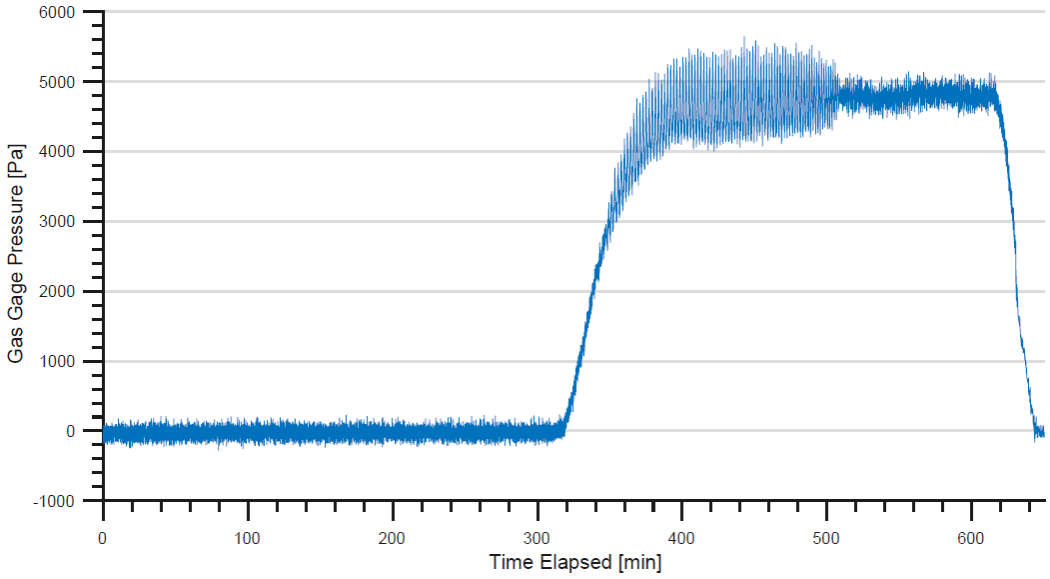


(b) Tank gas space pressure

Figure 4.7: System hydrostatic pressures during Run 116 (Q = 15.2 kW, Tank level = 60%)

### *Differential Pressure*

Differential pressure measurements in two-phase flow allow for classification and/or identification of the flashing phenomena. In order to study any effects from flashing in the WRCCS a differential pressure measurement is recorded across the chimney between the outlet header and the tank inlet (Fig. 4.9). This is a single uncompensated differential pressure measurement with impulse tubbing tapped at the inlet and outlet of the chimney, as shown in Fig. 3.1. The measurement is set to zero at room temperature (20 ◦C) and zero flow. Two-phase phenomena that is expected to have

significant effects on the flow phenomena is expected to pass through this region. The measurement also covers an elevation change, so density changes between the siphon points can have an effect on the measurement.

The differential pressure measurement exhibits a behavior similar to the mass flow measurements. Initially the differential pressure steadily increases due to the non-linear relationship between density and temperature, where the latter is constantly increasing until saturation is reached. Upon reaching saturation oscillations form in the differential pressure similar to those seen in the mass flow measurements. When the flow stabilizes, the differential pressure follows suit. However, the signal fluctuates greater than the mass flow rate due to the presence of void formation in the chimney.

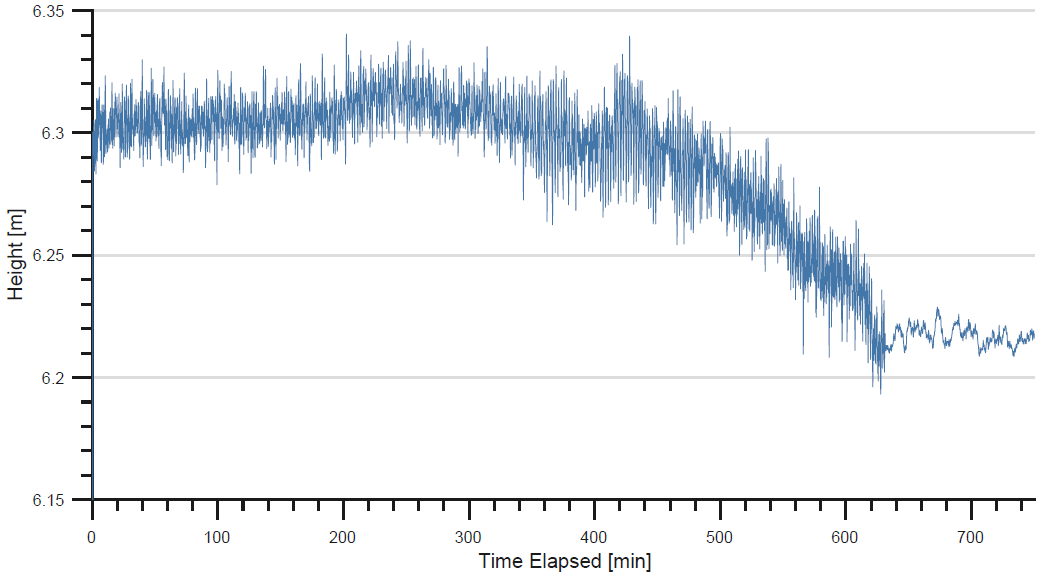


Figure 4.8: System water level measured from the entrance to the risers

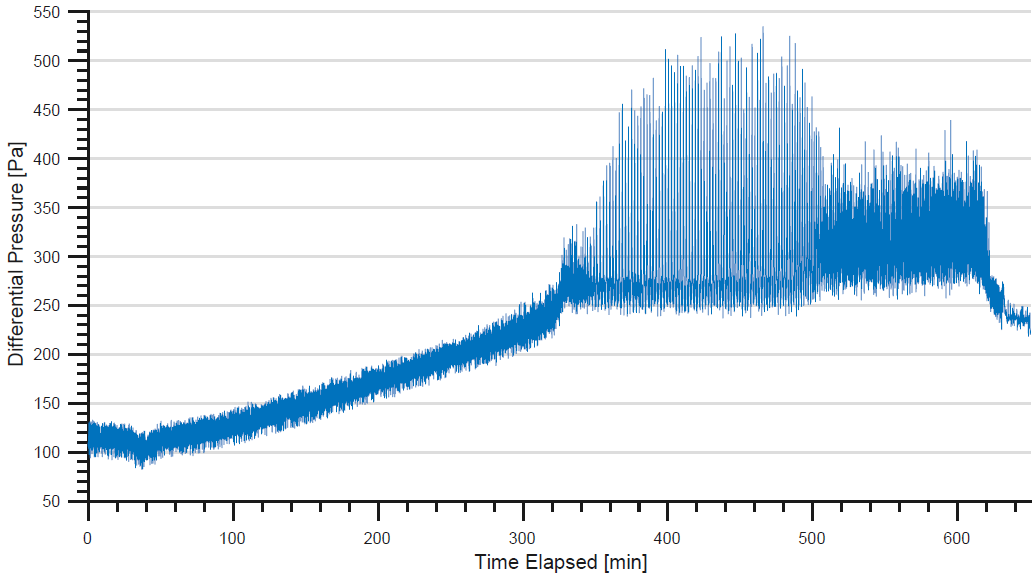


Figure 4.9: Differential pressure across the chimney

### *Differential Pressure and Mass Flow*

Mass flow and differential pressure across the chimney appear to present similar oscillations, but closer observation reveals some notable distinctions. Pressure is a quantity that can respond relatively instantaneously to changes in density or void, while mass flow has to overcome inertial changes. This feature allows observation of small fluctuating phenomena in the differential pressure due to voiding that are damped in the mass flow rate. Overlaying the measurements during the two phases of operation (large oscillations and stable flow) show these differing effects (Fig. 4.10).

Large oscillations in mass flow occur slowly over two minute periods and have smooth continuous evolution. The differential pressure tells a different story: within each oscillation there are numerous fluctuations indicating larger slugs that form along with continuous vapor production. The fluctuations occur over small 10-15 second periods and cause the average differential pressure to increase. The increase in average differential pressure indicates an increase in mean voiding, which causes the mass flow to overcome inertial effects and increase in speed. Upon reaching stable flow the large spikes in pressure and mass flow are damped, although the average differential pressure is higher which indicates an increase in void fraction in the chimney.

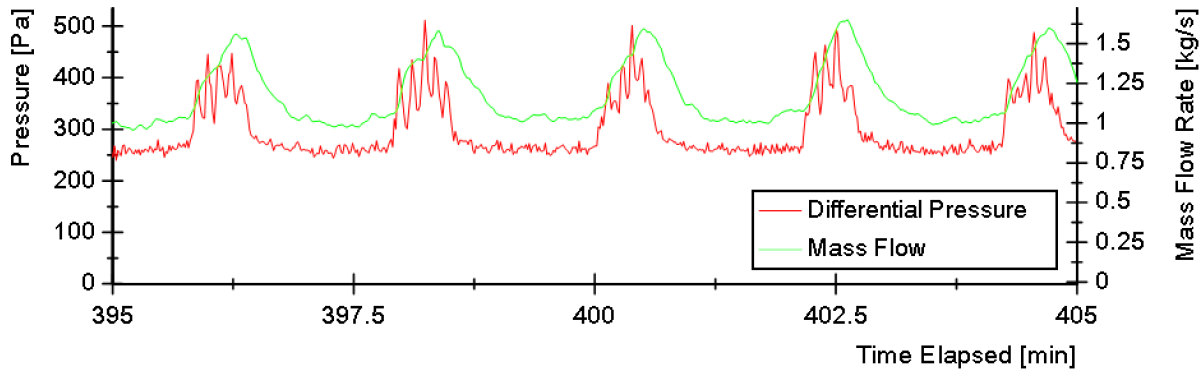


(a) large oscillations

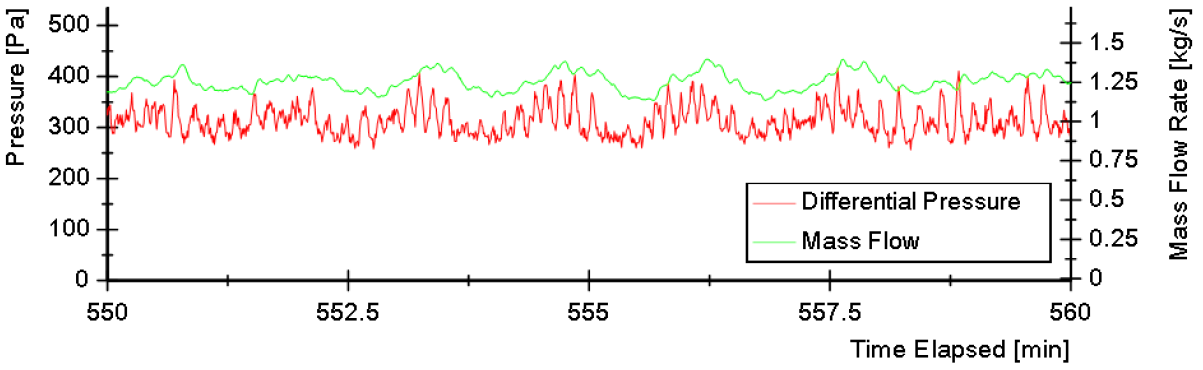


(b) stable flow

Figure 4.10: Scoped view of mass flow rate and differential pressure

### 4.1.5 Voiding

Wire mesh sensors (WMS) have the ability to visualize voiding phenomenon in closed piping and paired with other sensors can give insight into the type of boiling phenomenon occurring in a system. Void fraction measurements were taken at the exit of the chimney for both flashing regions (large oscillations and stable flow) and compared with differential pressure measurements, mass flow rates, and temperature oscillations.

***Large Oscillations***

Oscillatory effects seen in the mass flow rate and differential pressure are further verified by void fraction measurements. WMS measurements are collected at a rate of 160 Hz for 150 s, which is 50% longer than the average oscillation period. This is shown in Fig. 4.11 where an image of the instantaneous void is on the left and its evolution through time is on the right. During an oscillation, one can observe that void is continuously formed and that the void fraction has a similar qualitative profile as the differential pressure.

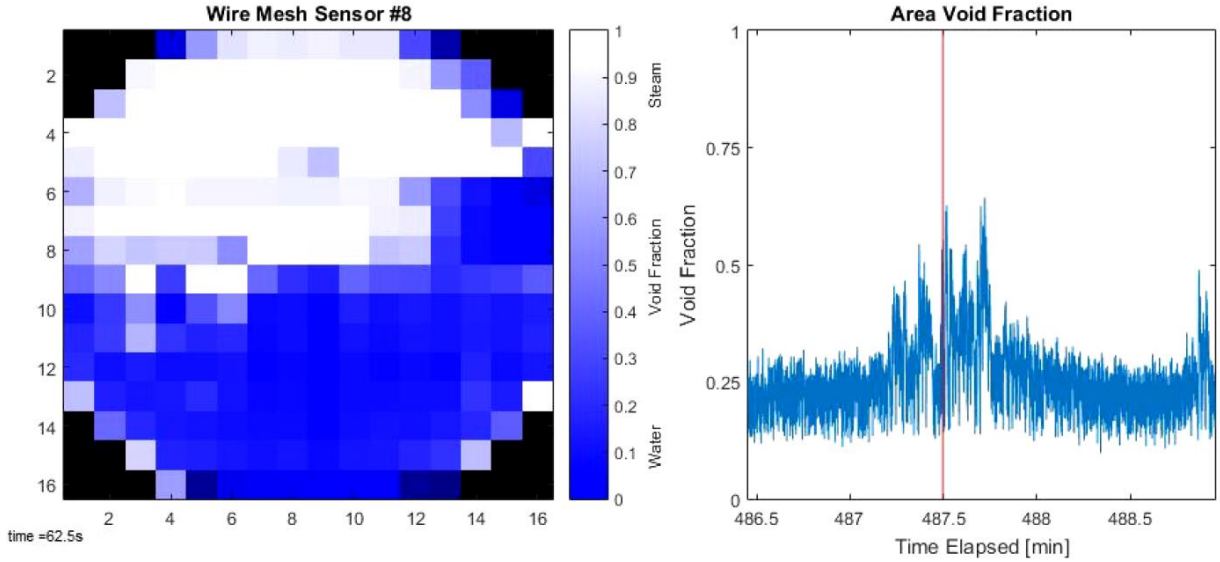


Figure 4.11: WMS data at the chimney exit during large oscillations. Left: flow visualization during voids. Right: Void variation during sample period

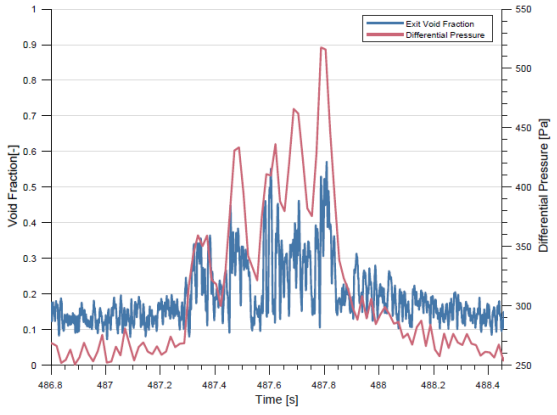


Figure 4.12: Void fraction and differential pressure over the chimney

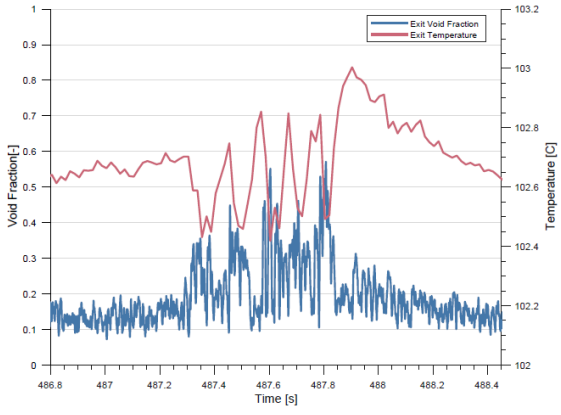


Figure 4.13: Void fraction and chimney temperature comparison

Comparing void fraction to differential pressure shows that the spikes in differential pressure occur with the presence of large slugs leaving the chimney (Fig. 4.12). Temperature correlates with void fraction in the same manner, but temperature decreases whereas differential pressure increases (Fig. 4.13). This suggests that steam is passing over the probe tip and the low heat transfer coefficient of the steam relative to water allows heat to conduct along the probe to the pipe wall resulting in a temperature drop. The formation of excess void also increases the frictional losses in the chimney.

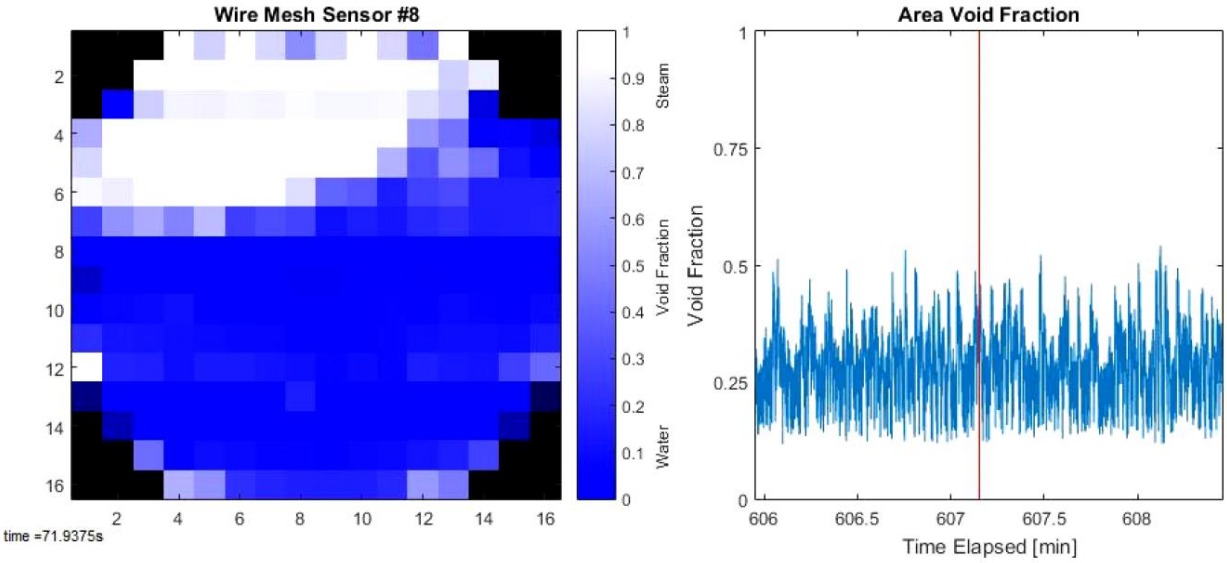


Figure 4.14: Left: area void fraction during stable flow. Right: change in void over time

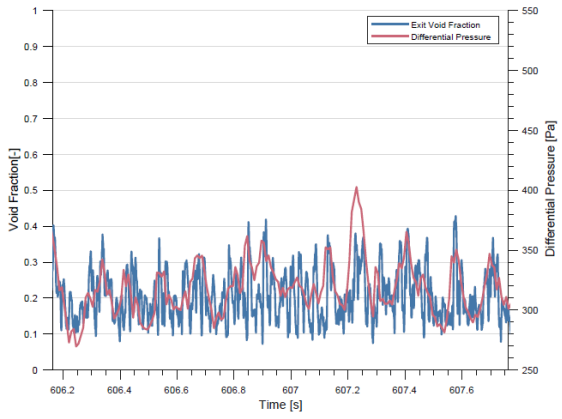


Figure 4.15: Differential pressure and void fraction in the chimney during stable flow

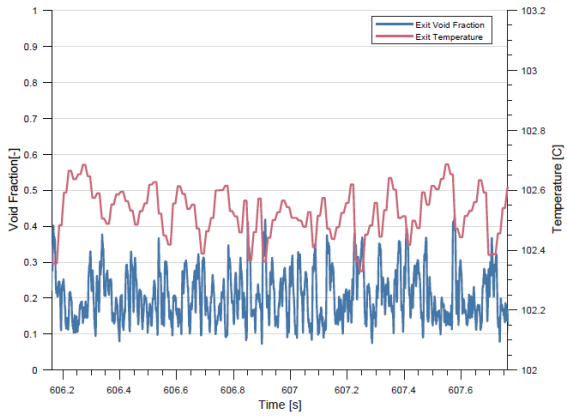


Figure 4.16: Temperature and void fraction in the chimney during stable flow

At this point, it is of interest to examine some features of voiding in an adiabatic system with oscillatory flow. Lisowski et al. (2014) determined through the use of phase-shifts in temperature that the voiding front is propagating through the chimney as the tank volume decreases. They showed that stability is achieved when the voiding front is located in one of the horizontal sections of the chimney and that oscillations are due to an instability called “Hydrostatic Head Fluctuations”. The theory behind these instabilities is that vapor is collected in a natural circulation facility in a horizontal component and when the buoyancy head increases the flow rate sufficiently

the vapor can be flushed out. Experimentally, WMS show that the system is continuously voiding passing through the chimney, so the likelihood of significant vapor entrapment may be questionable. Manera and van der Hagen (2003) showed experimentally in a two-phase natural circulation facility with wire-mesh sensors that the flashing front is propagated upward and downward during a single flow oscillation that occurs in BWR startup conditions at atmospheric pressure. This in turn caused the flow rate to increase and a corresponding delayed decrease in the system enthalpy. They also showed that the process operated in a non-equilibrium state, so superheated fluid of approximately 2 ◦C to 3 ◦C didn't flash until reaching a nucleation site present at flanges in the system. In either case, it is likely that the flashing front in the RCCS is migrating downward leading to an increase in void fraction with a decreasing hydrostatic head.

***Stable Flow***

Following the oscillatory behavior is a region of stable flow. The WMS data shows that fluctuations in the void fraction are now minimal (Fig. 4.14). Void fraction in the system remains stable, which results in a stable mass flow rate. The temperature and pressure in the chimney fluctuate from their mean values, but this is due to the slightly fluctuating void fraction (Fig. 4.16 and 4.15).

## 4.2 Heat Losses

Heat losses in the WRCCS are classified into two groups: losses within the heated enclosure, and losses between the network piping and the exterior environment. Losses from the heated enclosure are used to classify the efficiency of the heater box and give insight into the amount of energy available for steam production. Losses in the network piping are used to balance system energy with the amount of steam produced.

### 4.2.1 Heater Box and Riser Losses

Losses in the heater box were calculated using an energy balance on the fluid between the inlet and outlet headers (Eq. 4.4). The calculation uses thermocouple data from the inlet and outlet of the heated enclosure and the mass flow rate. The difference between the energy into the water and the power into the heaters is a combined effect from conductive and convective losses through the heater box walls and infiltration of air into and out of the heated enclosure.

$$\dot{Q} = \dot{m} C_p (T_{out} - T_{in}) \tag{4.4}$$

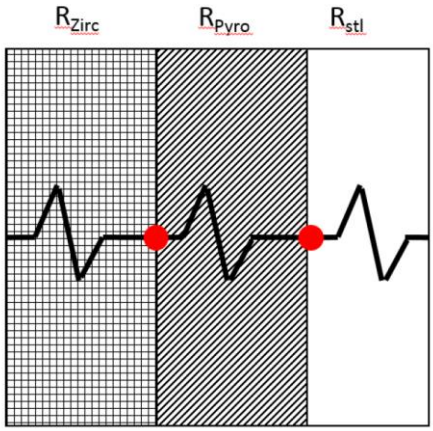


Figure 4.17: Thermal resistance network for the heated enclosure

Losses via conduction through the heater box walls were calculated with a 1D energy balance that can be simply described as a thermal resistance problem. The resistance network for the heated enclosure walls is shown in Fig. 4.17. The wall temperature on the inside and outside of the box is known via thermocouples placed on the inside and inferred thermal imaging scans of the outside.

Table 4.1: Heat loss overview for losses inside the heater box.

| Mechanism | Energy [kW] | Proportion | Mechanism | Energy [kW] | Proportion |
|---|---|---|---|---|---|
| Fluid | 11.89 | 79.76% | Infiltration | 0.73 | 4.91% |
| Walls | 1.91 | 12.80% | Structure | 0.33 | 2.21% |
| … | | | … | | |

Knowledge of the wall temperatures allows for direct calculation of the heat flux through the walls without assumed convection coefficients. Material properties for Pyrogel, Zircal-18, and Carbon Steel were taken from the manufacturers (Zircar (2005); Aspen Aerogels (2015); MatWeb (2017)). The temperature drop through the wall was assumed to be constant across the entire heater box. This assumption was made due to limited knowledge of the internal wall temperatures along the axial direction of the heater box. The external wall temperatures rise by 10 ◦C between the bottom and top of the heated enclosure, while internal fin temperatures rise by 50 ◦C. The thermocouples placed on the internal walls of the heated enclosure are located at the axial center of the box and temperatures of the risers in the heater box rise linearly along the axial direction. Therefore, it can be assumed that the thermocouple data is a rough approximation of the average internal wall temperature. The 1D conduction equations are as follows:

1. Conduction through Zircal-18 insulation

$L = thickness \quad k_{zirc} = Conductivity\ [Zircal] \quad A = surface\ area$

$$R_{cond,zirc} = \frac{L}{k_{zirc} A} \tag{4.5}$$

2. Conduction through Pyrogel insulation

$L = thickness \quad k_{pyro} = Conductivity\ [pyrogel] \quad A = surface\ area$

$$R_{cond,pyro} = \frac{L}{k_{pyro} A} \tag{4.6}$$

3. Conduction through carbon steel

$L = thickness \quad k_{stl} = Conductivity\ [steel] \quad A = surface\ area$

$$R_{cond,stl} = \frac{L}{k_{stl} A} \tag{4.7}$$

4. Total conduction resistance

$$R_{cond,tot} = R_{cond,zirc} + R_{cond,pyro} + R_{cond,stl} \tag{4.8}$$

5. Heat loss through walls

$$q_{loss} = \frac{T_{wall,i} - T_{wall,o}}{R_{cond,tot}} \tag{4.9}$$

In addition to conduction through the walls there is conduction from the heated box to the structure and infiltration of air into the box, which is assumed to account for the rest of the losses. Infiltration by air is expected to be small and could be classified by the resonance time of air in the heated

enclosure, but this is difficult to determine without knowing the temperature rise of the air in the enclosure. The residence time for air varies from 6.63 min to 9.95 min with a temperature rise of 200 ˚C to 300 ˚C respectively. These temperatures were chosen based on measured surface temperatures in the RCCS. This results in a low fluid residence time in the heater box, so it is assumed that there may be extra structural losses that have not been evaluated. A summary of losses are presented in Tbl. 4.1.

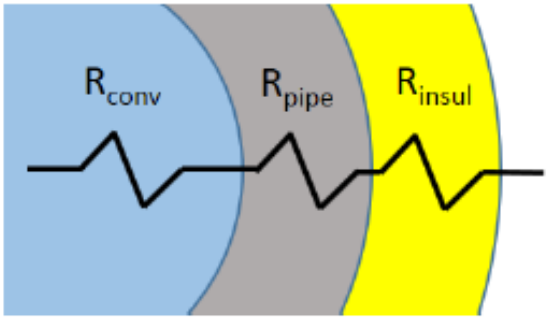


Figure 4.18: Thermal resistance network for the network piping.

### 4.2.2 Piping Network Losses

Losses in the piping network were calculated very similarly to the heated enclosure losses. Data for the internal fluid temperature and external air temperature were known so a thermal resistance network was formed (Fig. 4.18). Insulation and piping mechanical properties were taken from the manufacturers data sheets.

Convection was neglected in calculations for the heater box losses due to availability of wall temperatures, but no information for internal wall temperature is available for the network piping. Therefore, convective heat transfer coefficients were calculated using a correlation for the Nusselt number with available system data for mass flow and temperature of the fluid. The calculations for thermal piping losses are as follows:

1. Convection from water to SS304 piping

$L = piping\ length \quad h = convection\ coefficient \quad R_{pipe,i} = pipe\ radius$

$$R_{conv,water} = \frac{1}{h\ 2\pi R_{pipe,i} L} \tag{4.10}$$

2. Conduction through SS304 piping

$R_{pipe} = Pipe\ Radius \quad k_{pipe} = Conductivity\ [SS304] \quad L = pipe\ length$

$$R_{cond,pipe} = \frac{ln(R_{pipe,i}/R_{pipe,o})}{2\pi L\, k_{pipe}} \tag{4.11}$$

3. Conduction through Kflex insulation

$R_{insul} = Insulation\ Radius \quad k_{insul} = Conductivity\ [Kflex] \quad L = pipe\ length$

$$R_{cond,insul} = \frac{ln(R_{insul,i}/R_{insul,o})}{2\pi L\, k_{insul}} \tag{4.12}$$

4. Total resistance (4.13)

$$R_{tot} = R_{conv,water} + R_{cond,pipe} + R_{cond,insul}$$

5. Heat loss through piping

$$q_{loss} = \frac{T_{fluid} - T_{insul,o}}{R_{tot}} \tag{4.14}$$

6. Convection coefficient using Dittus-Boelter correlation for the Nusselt number (Nu)

$Re$ = *Reynolds number* $Pr$ = *Prandlt Number*

$k$ = *conductivity water* $D$ = *pipe diameter*

$$Nu = 0.0265\ Re^{0.8} Pr^{0.3} \tag{4.15}$$

$$h = Nu\ \frac{k}{D} \tag{4.16}$$

Comparing the energy input into the water from the heater box with the losses in the network piping yields the energy utilized in steam production. Using data from Run 116 one can compare the predicted steam production rate with a calculated steam production rate based on the total volume of condensed steam and the boiling time. The measured piping loss is calculated with an energy balance from the tank to the inlet header, similar to the calculation of energy into the water as it flows through the heater box. These results show that the predicted values for steam production are nearly equal to the measured ones (Tbl. 4.2). Large error exists in the measured and calculated piping losses due to error in the thermocouples. The temperature change in the piping due to losses is small (approximately 0.5 ◦C), so error in thermocouple data (±0.2 ◦C) can create large variations in the energy calculation.

Table 4.2: Heat loss in the piping network outside of the heated enclosure.

| Mechanism | Measured | Calculated | Error |
|---|---|---|---|
| Fluid Energy | 11.893 kW | - | - |
| Piping Loss | 1.986 kW | 1.595 kW | 19.69% |
| Steam Energy | 10.043 kW | 10.298 kW | 2.54% |

## 4.3 Testing Overview

Testing on the UW-WRCCS includes a variety of perturbations to the standard operating state; these include perturbations in pressure, water volume, and inlet throttling. These perturbations modify the stability of the UW-RCCS facility and allow for a deeper understanding of the mechanisms that initiate oscillations and instabilities. A summary of the tests performed and analyzed in the following chapters are presented below in Tbl. 4.3.

Table 4.3: Testing overview for analysis of instabilities and oscillations observed in the UW-WRCCS.

| **Purpose** | **Type** | **Power [kW]** | **Tank Levels** |
|---|---|---|---|
| *Inventory Repeatability* | Two-Phase | 15.19 | 70% 60% 55% |
| *Natural Pressurization (1.05, 1.08, 1.15 bar)* | Two-Phase | 15.19 | 60% |

| | | | |
|---|---|---|---|
| *Natural Pressurization and Accelerated Drain (1.15bar)* | Two-Phase | 15.19 | 80% |
| *Fully Orificed Risers (1/2, 1/4, 1/8 flow area)* | Two-Phase | 15.19 | 80%, 70%, 60% |
| *Partially Orificed Risers (1/8 flow area)* | Two-Phase | 15.19 | 80%, 70%, 60% |
| *Asymmetric Power Shaping* | Single-Phase | 7.27, 9.91 | 80% |

# 5 Experimental Results

The UW-WRCCS has undergone numerous experiments in order to analysis the envelop of stability. The system's operation under ordinary conditions has been characterized in the past by Lisowski (2013). In the following sections, the system's stability is assessed experimentally through several perturbations to the operating conditions and potential operating scenarios. The facility was perturbed by passively pressurizing the gas space, throttling the inlet resistance to the individual risers in various configurations, and varying the tank water level. Two additional operating scenarios that could cause system instabilities were tested: instantaneous loss of pressure and tank water refill. The experimental data acquired in these experiments were used to characterize the boiling location in the RCCS as well as the operating state as defined by the Phase Change-Subcooling plane.

## 5.1 Elevated Pressure Tests

Elevated pressure in natural circulation systems has been shown to increase stability in adiabatic flashing in previous research (Lisowski (2013), Manera and van der Hagen (2003), and Furuya et al. (2005a)). Theory has predicted that the oscillations in the flow are due to the low pressure head on the system and an elevated pressure could increase the stability of the system. Slight pressurization occurs naturally in the system gas space due to a balance between the rate of steam production and the outflow of steam to the condenser through a gate valve. Varying the closure of the outlet gate valve leads to a passive method for system pressurization used by Dr. Lisowski in addition to forced pressurization of the RCCS in his initial efforts on characterizing performance of the slow drain transient in a WRCCS (Lisowski (2013)).

### 5.1.1 Pressurization Method

The elevated pressure tests were performed by restricting the outflow of steam to the condenser with a gate valve as shown in Fig. 5.1. The reduction in the outflow area increases flow resistance and in order to maintain equilibrium between the steam production rate and the steam outflow rate the pressure in the system must increase. Pressurized tests were categorized by the fraction of area left open in the gate valve henceforth referred to as $\beta$. $\beta$ was calculated geometrically using the valve closure, which based on rotations of the valve handle and the points in which the valve is in the fully closed and fully open positions. The amount of closure then corresponds to some elevated pressure beyond normal operation, which is the ultimate boundary condition for each test.

A summary of the initial test conditions are shown in table 5.1. In all cases, the initial tank water volume was set to 60% with an electrical input power of 15.2 kW. The tank level was measured using a visual level gage on the outside of the tank and compared with the initial static gage pressure as measured by a hydrostatic pressure transducer located at the inlet to the risers. Water quality was maintained between tests by ensuring that the conductivity of the fluid was less than

10.0 ± 0.1 µS as measured by a hand-held Extech EC400 at the start of each test. All parameters with the exception of the steam outlet restriction were held constant.

### 5.1.2 Observed Effects

Elevated pressure testing has resulted in behavioral deviation from the standard test data. Higher pressure testing results in a higher overall system temperature and reduction in the fluctuating mass flow and differential pressure values.

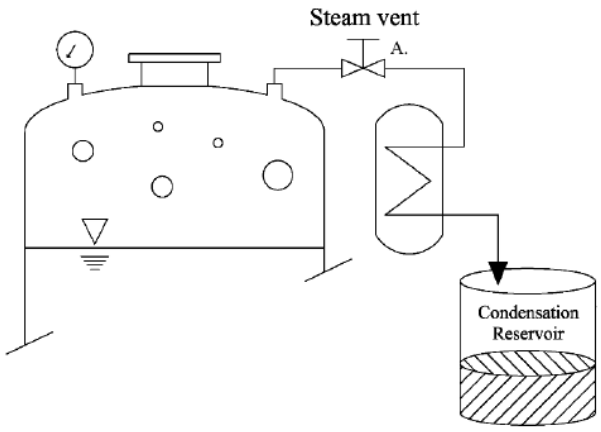


Figure 5.1: Gate valve location on top of the water tank (Lisowski (2013))

Table 5.1: Overview of initial conditions for elevated pressure tests

| Test Number | Tank Volume | Power [kW] | Open Valve Area ($\beta$) | Initial Static Gage Pressure [kPa] |
|---|---|---|---|---|
| Run 108 | 60% | 15.188 | 1.00 | 61.52 |
| Run 118 | 60% | 15.188 | 0.42 | 61.38 |
| Run 113 | 60% | 15.188 | 0.31 | 61.24 |
| Run 117 | 60% | 15.188 | 0.26 | 61.51 |
| Run 111 | 60% | 15.188 | 0.21 | 61.42 |

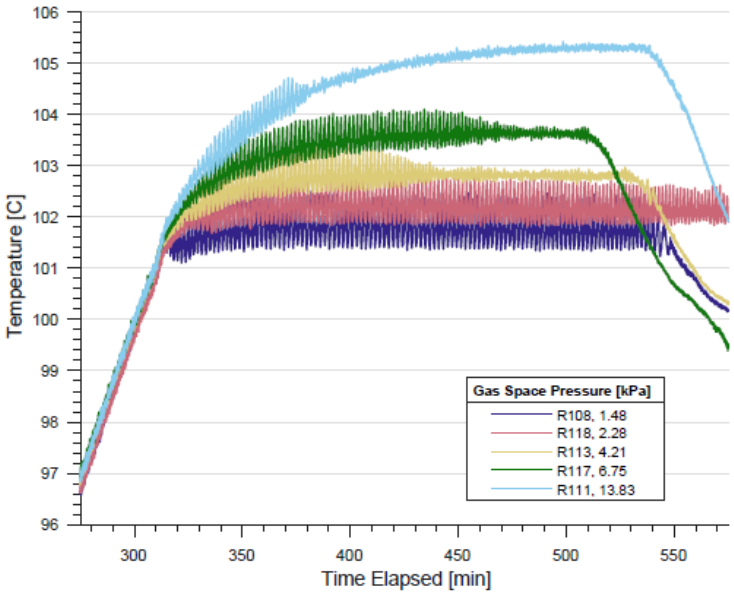


Figure 5.2: Outlet riser temperatures for elevated pressure tests. Temperature rise from inlet to outlet is equal for all tests**.**

### *Temperature Changes*

Higher than normal operating temperatures have been observed in the higher pressure cases (Fig. 5.2). System temperatures rise with pressure, but the fluid temperature rise between the inlet and outlet of the heated risers is approximately constant between tests. It can be shown that the overall temperature rise is due to an increase in the system saturation temperature if the inlet and outlet riser temperatures are normalized by the saturation temperature in the uppermost point of the chimney for the various pressures (Fig. 5.3). This shows consistency between tests and that saturation temperature is the limiting factor behind RCCS operation capabilities.

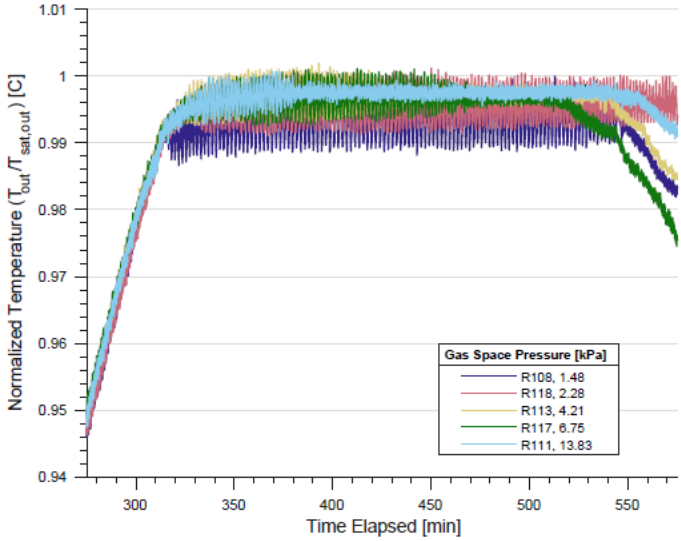


Figure 5.3: Inlet and outlet riser temperatures under elevated pressures and normalized by saturation temperature in the uppermost chimney piping.

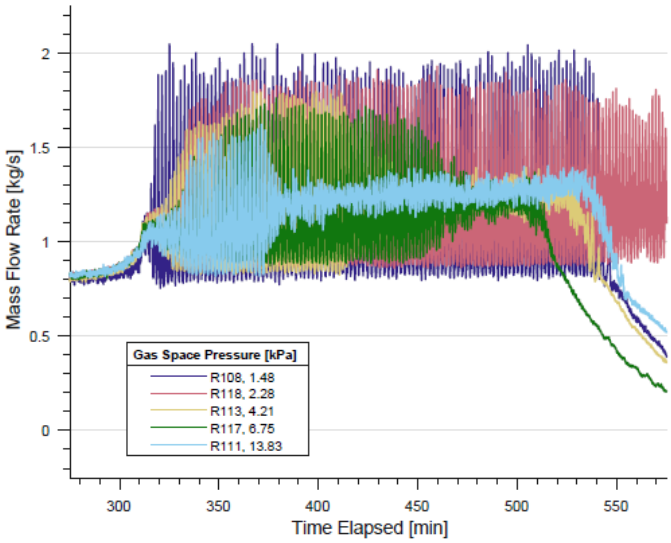


Figure 5.4: Mass flow oscillation magnitude with a change in gas space pressure. The data has been time shifted to align the beginning of the oscillations.

### *Oscillatory Changes*

Oscillatory phenomenon in the mass flow exhibits a reduction in magnitude with an increased gas space pressure. As pressure in the system is increased, the magnitude of the mass flow oscillations decreases as shown in Fig. 5.4. The increased pressure in the gas space ranges from 2000 Pa to 14 000 Pa (or 2 - 14% above atmospheric), which is equivalent to raising the water level in the tank by 0.26 m to 1.48 m respectively. In previous tests with variations in tank water level by Lisowski (2013) it has been shown that the large oscillations only form when the system has a tank volume between 70%-55% and that these oscillations increase in magnitude until the flashing phenomenon changes from oscillatory flow to stable flow. Higher gas space pressures result in an increase in vapor density similarly to higher tank volumes, which results in a more stable flow. However, the increase in gas space pressure also results in a change to the system boundary conditions by raising the tank surface temperature to a higher saturation point. The oscillations also appear to generally decrease in duration as the pressure is increased, although the mean observed mass flow rate is not changed to the same degree that changes in the tank volume cause. The differences due to the pressurized case are made clearer in a forced drain test over the entire RCCS operating range.

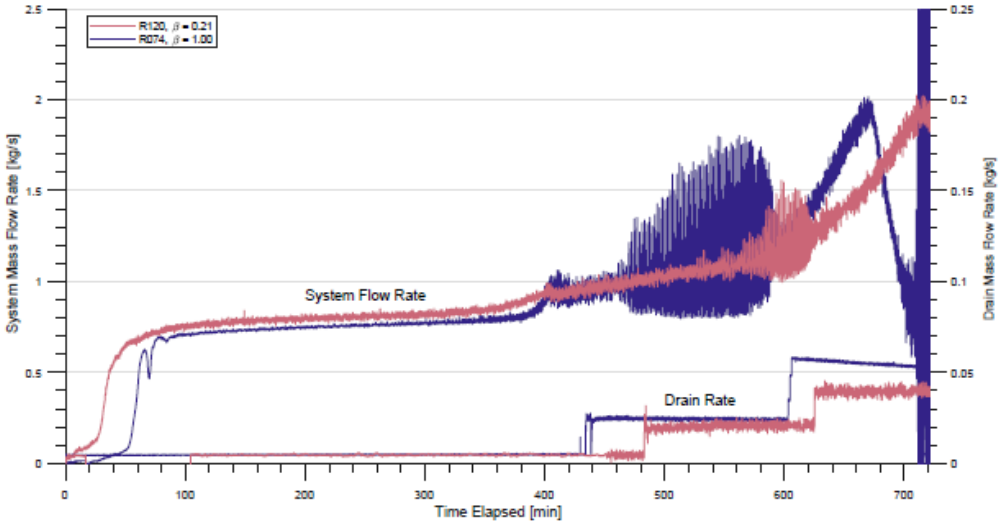


Figure 5.5: Forced drain comparison between Run074 (forced drain at standard conditions) and Run120 (forced drain at elevated pressure).

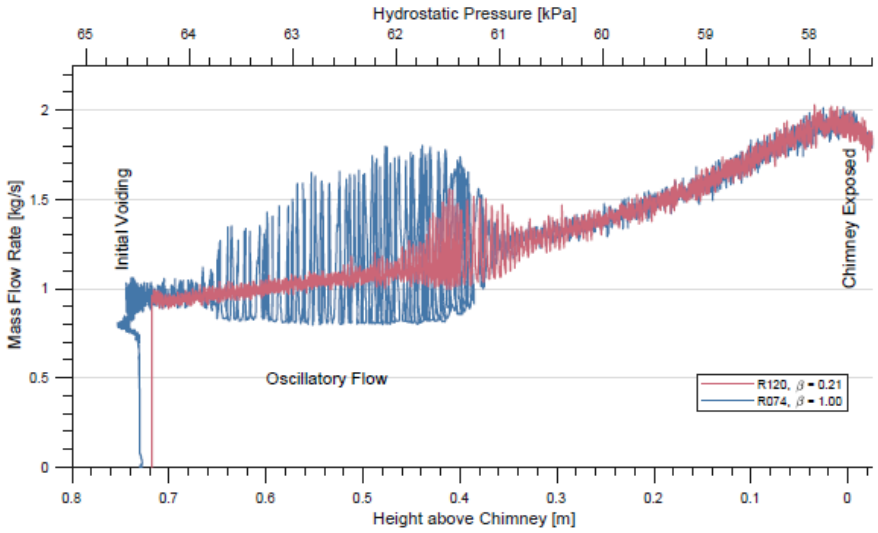


Figure 5.6: Forced drain tests plotted against tank volume height and hydraulic gage pressure for observation of behavioral shifts. Run074 at normal operating pressure and Run120 at elevated operating pressure of approximately 10 kPa to 15 kPa).

### 5.1.3 Forced Drain Under Elevated Pressure

Forced drain tests are performed on the RCCS in order to observe hydraulic behavior over a wide range of tank volume levels with a reduced testing time and to validate the absence of hysteresis effects that could occur from testing each volume separately. A forced drain test has been performed previously under normal operating conditions, where the tank volume went from 80% to 20%. The extended range allows for gas space pressure to stabilize before any oscillatory behavior is observed. A second forced drain test has been performed with a pressurization similar to run 111, with a $\beta$ of 0.21.

Forced drain tests are performed by heating the system to saturation and then draining fluid from the tank to accelerate the tank depletion. The system is operated in the normal fashion, but upon

reaching steady-state two-phase flow fluid is drained directly from the base of the water storage tank in addition to the release of steam produced from flashing. This accelerates the change in water level allowing the full tank to drain over the course of several hours as opposed to days. Further details of this procedure can be found in Lisowski (2013) and Lisowski et al. (2014). This particular test was performed under elevated pressure conditions in order to observe any shifts in behavior from the atmospheric test.

Forced drain tests at both atmospheric and elevated pressure show the same qualitative behavioral zones as described previously by Lisowski et al. (2014) (Fig. 5.5). There are notable changes in the magnitude and duration of these behaviors, in particular during boiling incipience and the large oscillation region. The drain rate in the two tests varies slightly, but the two can be easily compared by plotting the two systems not in time but by tank level (Fig. 5.6).

***Incipient Boiling***

Upon reaching saturation (around 400 min) flashing begins to occur in the adiabatic chimney for both tests. In previous testing, including pressurized and atmospheric, there is an immediate jump in the mass flow rate upon initial formation of void in the chimney due to the instantaneous increase in the buoyancy force. The elevated pressure test shows no such increase, the only indicator of the start of flashing is a small change in the slope of the mass flow rate curve and an increased temperature in the condenser inlet. The absence of the jump in mass flow indicates that the voiding rate in the system is lower than previous experiments or that the location of voiding has migrated to the chimney outlet so that its effect on the flow rate is dampened. The flow pattern has been shown in previous tests with the WMS to be a stable form of either bubbly or stratified flow in the chimney. The transition between stable flow and and large oscillations for both tests is very similar in that the oscillations begin to form with no other apparent shifts in behavior.

***Large Oscillations***

The greatest difference in performance for the two tests arise of the large oscillation region. The elevated pressure test shows significant dampening in the large oscillation magnitude. The higher pressure oscillations also begin at a lower water level than in the atmospheric forced drain test. These dampened oscillations have been shown previously in the pressurized tests, specifically Run 111. It has been empirically observed that this transition corresponds to a mean increase in flow rate to approximately 1.2 kg/s, which occurs between a tank volume height of approximately 65% to 55%. A theory is presented in the following chapter as to the nature of the transition between stable and oscillatory flow as well as a method for prediction of the instability.

### 5.1.4 De-pressurization Testing

Operation under increased pressure can result in de-pressurization events and subsequent flashing of inventory due to higher operation temperatures. A test was performed in which the system was allowed to pressurize and reach a new steady-state. The exit restriction valve was then fully opened resulting in a quick de-pressurization of the UW-WRCCS facility.

The increased pressure in the RCCS facility is the result of passive pressurization due to an exit restriction. The pressurization tests completed thus far were not tested more than 15% above atmospheric pressure, as such the severity of the test is limited. The pressure release resulted in a single flow excursion, which allowed the system to cool to standard operating conditions for the new pressure boundary condition (Fig. 5.7). The system then continued to operate normally at the new boundary condition. The flow excursion experienced was not larger in magnitude than the

oscillations normally operating in the facility, but the rise time of the excursion was larger than is typical for the oscillations.

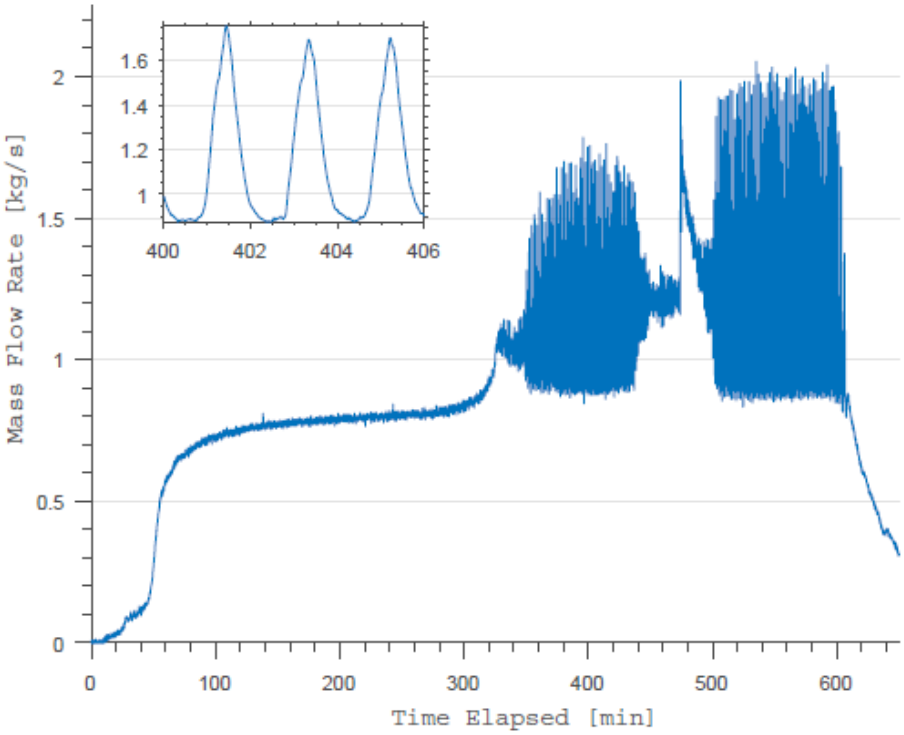


Figure 5.7: De-pressurization test with 60% tank volume from $\beta$ = 0.21 to $\beta$ = 1

### 5.1.5 Summary

Various elevated pressure tests were performed on the WRCCS by restricting the steam outflow to the condenser. Under these test conditions the pressure in the system gradually increases upon reaching saturation until an equilibrium state is reached. The magnitude of mass flow oscillations is reduced at the elevated pressures for a given tank water height. Prior to the large oscillations, as seen in the forced drain test, the flashing behavior is modified most likely due to a change in the location or amount of voiding occurring within the system. A summary of test results is presented below in table 5.2 and Fig. 5.8.

## 5.2 Orificed Flow Results

Inlet throttling has been found to reduce the magnitude and/or occurrence of instabilities in forced and natural circulation and has been validated with experimental facilities and modeling efforts (Ishii (1971) and Boure et al. (1973)). The UW RCCS experiment has attempted to study the effects of orificing in the past through insertion of a flow restriction to 1/16 total flow area at the end of the downcomer before flow is split into the risers (Lisowski (2013)). The results showed complex parallel channel interaction and potential voiding in the risers as indicated by fluctuations in thermocouple measurements that were more severe than the standard oscillatory behavior observed in water level testing. These results are in contention with the expected increase in stability that other researchers have observed. Therefore, the current system has undergone orificed flow testing with flow restriction to 1/2, 1/4, and 1/8 of the total cross-sectional area in each of the risers.

Orifices in the RCCS were designed to be inserted directly into the riser inlets for more flexibility in regards to symmetric and asymmetric orificing configurations between the risers. The orifices themselves

were designed similarly to those used for flow velocity measurement (Fig. 5.9). The inner opening is cut to reduce the flow to 1/2, 1/4, or 1/8 of the total flow area and the specified orifice dimensions are described in table 5.3. Loss coefficients for each orifice were experimentally measured in the RCCS using differential pressure across the system and the mass flow rate. The experimental data points were fitted to the form loss equation (Eq. 5.1), which resulted in a measurement of the overall system loss coefficient (Fig. 5.10). This equation defines $A$ as the full pipe cross-sectional area as opposed to the orifice inner cross-sectional area. The orificed loss coefficient can then be estimated by subtracting frictional and minor losses from the measured value as shown in Eq. 5.2.

Table 5.2: Overview of pressurized tests results. All recorded pressures are gage pressures. $P_{gas}[kPa]$ includes hydraulic system head and gas space pressure due to stability of the measurement. $P_{head}[kPa]$ is the static hydraulic head pressure on the system prior to saturation.

| Test | Run 108 | Run 118 | Run 113 | Run 117 | Run 111 |
|---|---|---|---|---|---|
| | | | *Initial Conditions* | | |
| $\beta[-]$ | 1.00 | 0.42 | 0.31 | 0.26 | 0.21 |
| $P_{head}[kPa]$ | 61.52 | 61.38 | 61.24 | 61.51 | 61.42 |
| | | | *Oscillation Region* | | |
| $\overline{\dot{m}}[kg/s]$ | 1.122 | 1.178 | 1.173 | 1.146 | 1.263 |
| $\dot{m}^{0}[kg/s]$ | 0.375 | 0.318 | 0.256 | 0.266 | 0.0417 |
| $\overline{P}_{gas}[kPa]$ | 63.00 | 63.66 | 65.45 | 68.26 | 75.25 |
| $P_{gas}^{0}[Pa]$ | 514.9 | 502.3 | 442.37 | 485.2 | 161.5 |
| $\overline{P}[Pa]$ | 301.27 | 316.76 | 305.22 | 310.68 | 337.8 |
| $P^{0}[Pa]$ | 104.86 | 90.64 | 73.14 | 69.08 | 44.40 |

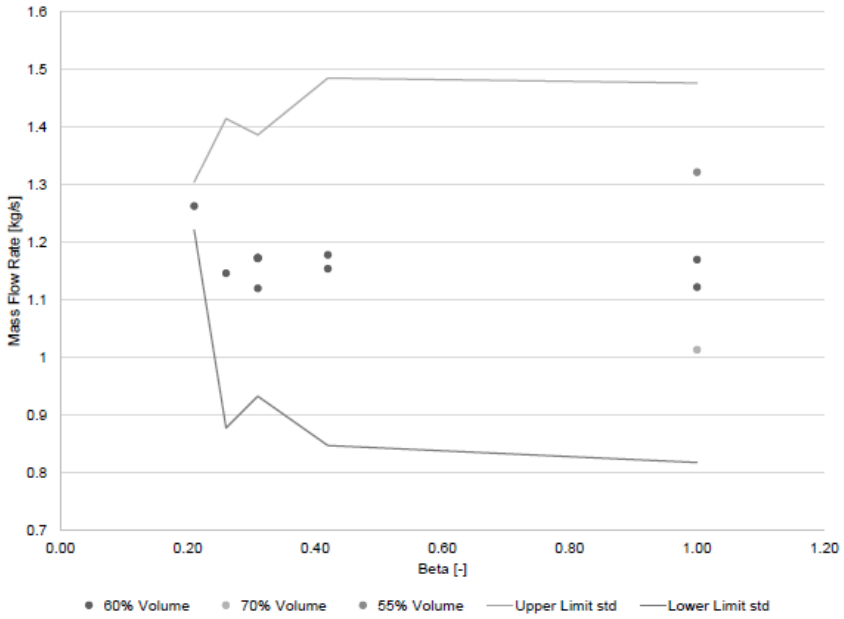


Figure 5.8: Summary of pressurized tests. The upper and lower limits are representations of the oscillatory magnitude for a given pressurization, as determined by the standard deviation of the flow rate when oscillations were present.

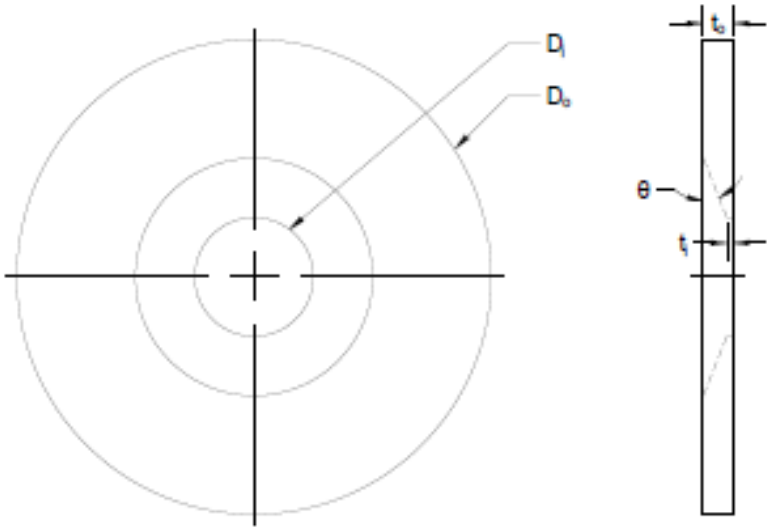


Figure 5.9: Orifice design

Table 5.3: Orifice Dimensions in millimeters(inches)

| Size | $D_i$ | $D_o$ | $\theta$ | $t_i$ | $t_o$ |
|---|---|---|---|---|---|
| 1/2 | 38.13(1.501) | 104.65(4.120) | 45° | 1.30(0.051) | 6.15(0.242) |
| 1/4 | 26.62(1.048) | 105.16(4.140) | 45° | 0.76(0.030) | 6.07(0.239) |
| 1/8 | 18.80(0.740) | 104.93(4.131) | 45° | 1.09(0.043) | 6.12(0.241) |

$$\Delta P = K_{in}\frac{1}{2}\rho v^2 = K_{in}\frac{\dot{m}^2}{2\rho A^2} \tag{5.1}$$

$$\Delta P_{orf} = \Delta P_{meas} - \Delta P_{fric} - \Delta P_{minor} \tag{5.2}$$

The theoretical value for orifice loss in inviscid flow can also be derived and estimated with the Bernoulli and Conservation equations (Eq. 5.3) solved across the orifice with no gravitational effects.

$$p_1 + \frac{\rho v_1^2}{2} = p_2 + \frac{\rho v_2^2}{2}$$
$$\rho_1 v_1 A_1 = \rho_1 v_1 A_2 \tag{5.3}$$

Where, subscripts 1 and 2 represent the quantities in the pipe prior to the orifice and at the orifice inner diameter respectively. Solving for the pressure drop as a function of the mass flow rate results in Eq. 5.4.

$$\Delta P = \left(\frac{\sqrt{1-\left(\frac{A_2}{A_1}\right)^2}}{A_2}\right)^2 \frac{\dot{m}^2}{2\rho} \tag{5.4}$$

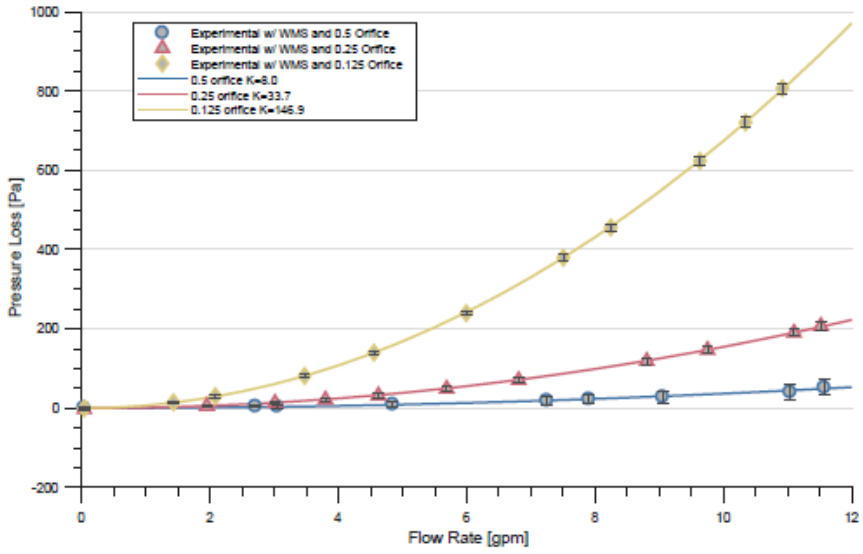


Figure 5.10: RCCS orificed flow loss coefficients

In order to account for the Vena Contracta that occurs after passing through the orifice a discharge coefficient ($C_d$) is multiplied by $A_2$ and is calculated according to Eq. 5.5 (Miller (1996)). The first half of Eq. 5.4 is then defined as the theoretical orifice loss coefficient (Eq. 5.6) by defining $\beta$ as the ratio of $A_2$ to $A_1$ and modifying the form to be analogous to other loss terms. The resulting values are shown as a function of $\beta$ in table 5.4.

$$
\begin{aligned}
C_D &= C_{D,\text{inf}} + \frac{b}{Re^n} \\
C_{D,\text{inf}} &= 0.5959 + 0.0312\beta^{2.1} - 0.184\beta^6 \\
b &= 91.71\beta^{2.5} \\
n &= 0.75
\end{aligned}
\tag{5.5}
$$

$$
\Delta P_{orf} = \left( \frac{\sqrt{1-\beta^2}}{C_D \beta} \right)^2 \frac{\dot{m}^2}{2\rho A_1^2} = K_{orf} \frac{\dot{m}^2}{2\rho A_1^2} \tag{5.6}
$$

Table 5.4: Orifice loss coefficients ($K_{orf}$ ) for various restrictions calculated theoretically and compared with the experimental measurement.

| $\beta$ | Theory | Integral Measured |
|---|---|---|
| 0.5 | 5.4 | 8.0 |
| 0.25 | 33.9 | 33.7 |
| 0.125 | 156.7 | 146.9 |

### 5.2.1 Predictive Modeling with MELCOR

MELCOR modeling of the UW - RCCS facility has been performed in the past in order to predict system performance and stability. Oh (2015) used and extended the model originally developed by Troy Haskin for prediction of two-phase stability (Lisowski et al. (2011)). The model qualitatively predicts continuously unstable behavior, however the as built facility only exhibits oscillations at certain tank volumes and flow rates under normal two-phase operating conditions. Quantitatively, the model predicts oscillations at twice the frequency and greatly over-predicts the magnitude at standard operating conditions. However, the model could still potentially be used to predict qualitative changes in system oscillations due to orificing.

MELCOR is a 1D system level engineering code developed for studying and predicting sever accident conditions in light water reactors (SNL (2010)). This includes core decay, thermal-hydraulic effects, and potential fissile release. The code is designed to run quickly on large scale models compared to computation fluid dynamics (CFD) models, because a solution is formed by dividing the system into bulk parameter control volumes connected by 'pipes'. Whereas, CFD uses significantly smaller meshes and allows for tracking of 3D flow structures and heat transfer phenomena. An evaluation with a best-estimate thermal-hydraulic code such as TRACE may be the next step for better accuracy, but a MELCOR model is already available for study of the RCCS facility. The MELCOR code was used to develop a 1D thermal-hydraulic model of the UW-RCCS facility and tested with the various inlet orificing conditions mentioned above. MELCOR is a lumped parameter 1D two-fluid model with flow regime dependent correlations. The applied boundary conditions consist of a reduced heat load equivalent to the measured heat load into the fluid via experimental data and an atmospheric gas space pressure with a time-dependent control volume for removing steam produced in the model. The nodalization scheme for the RCCS facility was implemented as shown appendix G. Further details of MELCOR's operation are beyond the scope of this thesis; for specific details see the reference (Oh (2015)).

The MELCOR model was tested at the most severe orificing case (reduction at the inlet of each riser to 1/8 total flow area) with multiple configurations. The first test case with all risers equally orificed exhibits a large transient instability occurring as the system reaches saturation. Shortly after formation, the large oscillations subside and leave small oscillations that are typical of the MELCOR model without orificing, but not the experimental facility (Fig. 5.11). The large oscillations depict parallel channel instabilities that include negative flow in a select riser and a procession of flow between the risers, which has never been observed in the RCCS facility due to voiding occurring in the chimney as opposed to the risers. The integral system mass flow rate is always observed positive in the model and the experimental facility. The presences of different riser flow rates is due to the presence of voiding in the risers, which has yet to be shown in the RCCS. The WMS present at the end of the risers can validate this observation and also measure gas velocity. If the gas velocity is assumed to follow the liquid velocity, the presence of negative flow in the risers can be captured and quantified.

Asymmetric orificing in the risers results in similar, but significantly more unstable phenomena than the fully orificed case. Two different asymmetric cases were tested in the model: risers 1 and 3 orificed with riser 2 open, and riser 1 orificed with riser 2 and 3 open (Fig. 5.12). In these cases the unorificed riser(s) showed significantly higher flow rates, as expected in order to balance the pressure drop between the risers, while the orificed risers experienced voiding and complex parallel channel interaction. The integral behavior of the system exhibits significantly larger oscillations that increase in magnitude as more risers are left unorificed.

On the left of Fig. 5.12, two risers are orificed, while the third act like a bypass. During large oscillations, riser 1 and 2 exhibit negative flow as seen in the previous test case, however the second riser is unorificed and therefore its velocity can not be measured with the current instrumentation in the RCCS facility. The flow rates in the two orificed risers operate out-of-phase with each other during a system wide flow oscillations as shown in the fully orificed test case, while the unorificed riser's flow rate oscillates with the integral oscillations with the exception of the negative flow. The risers are all in phase when the large oscillations decay away, although the change is less prominent than in the fully orificed test case.

On the right of Fig. 5.12, a test case is presented with a single riser orificed. Similarly to the previous cases, negative flow is observed but only in one of the open risers. Other phenomena is similar to the previous case, but the magnitude of the oscillations are increased.

Unlike the fully orificed case these two test cases have no clear distinction between the phase-change oscillations and "stable" oscillations. The overall magnitude of the oscillations slowly decreases as the tank drains, as opposed to the unorificed case where there is a sudden change between the oscillatory modes. This occurs because voiding always occurs in the orificed riser(s), which leads to an oscillating driving force. This phenomena can be measured with the riser exit WMS, unfortunately there is no integral flow rate measurement at the riser inlets for verification of the WMS velocity measurements.

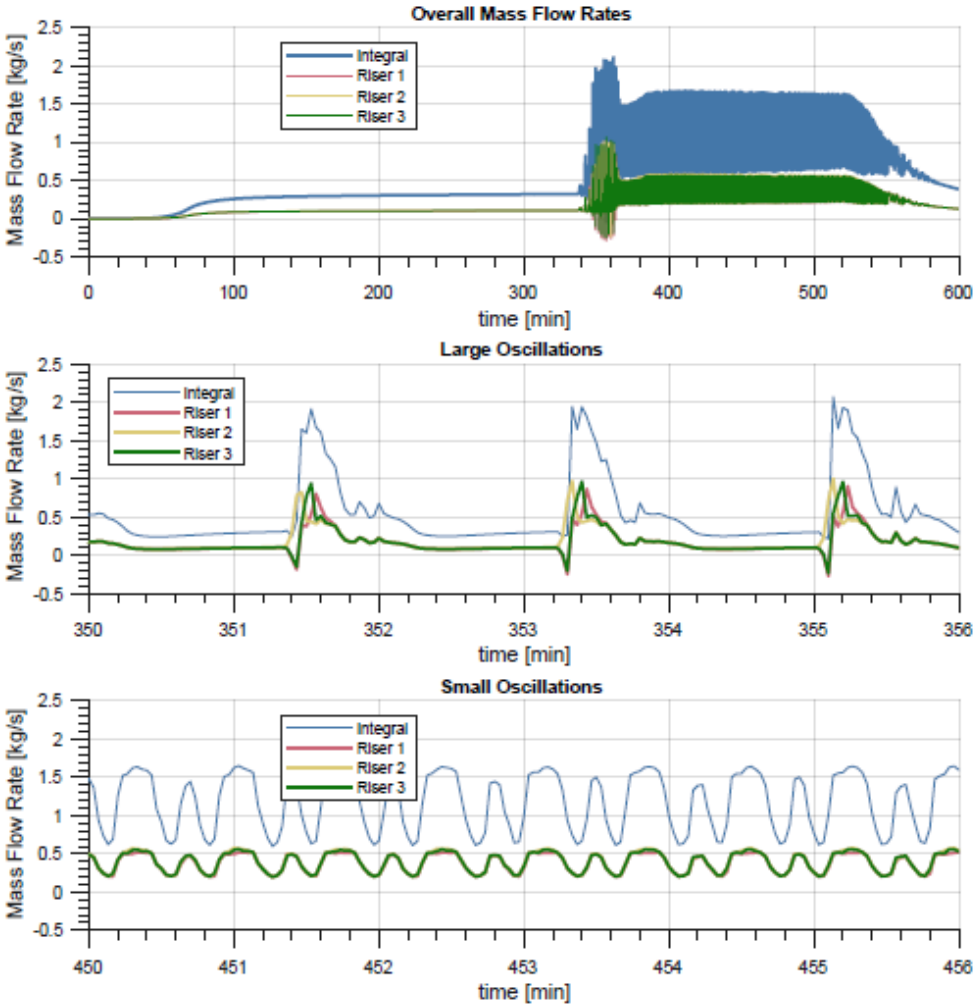


Figure 5.11: Predicted flow oscillations using a MELCOR model of the UW-RCCS facility with all risers orifiecd to 1/8 total flow area.

### 5.2.2 Full Flow Restriction

#### *1/2 Flow Restriction*

Inlet throttling to 1/2 total flow area represents a case with limited effects on the system due to the low loss coefficient. The mass flow rate data shows that the system exhibits similar phenomena seen in the unperturbed case (Fig. 5.13). At high tank volumes (80%) the system operates with a stable flow rate and as the tank level decreases the mean mass flow rate increases and oscillations start to form. These oscillations have a period of approximately two minutes, which is similar to the unperturbed test data. Voiding is only observed at the end of the chimney as seen in the unperturbed tests. The small pressure drop induced by the orifice also causes the oscillatory behavior to persist longer than is normal in previous parametric studies on the tank volume effects in the UW-WRCCS.

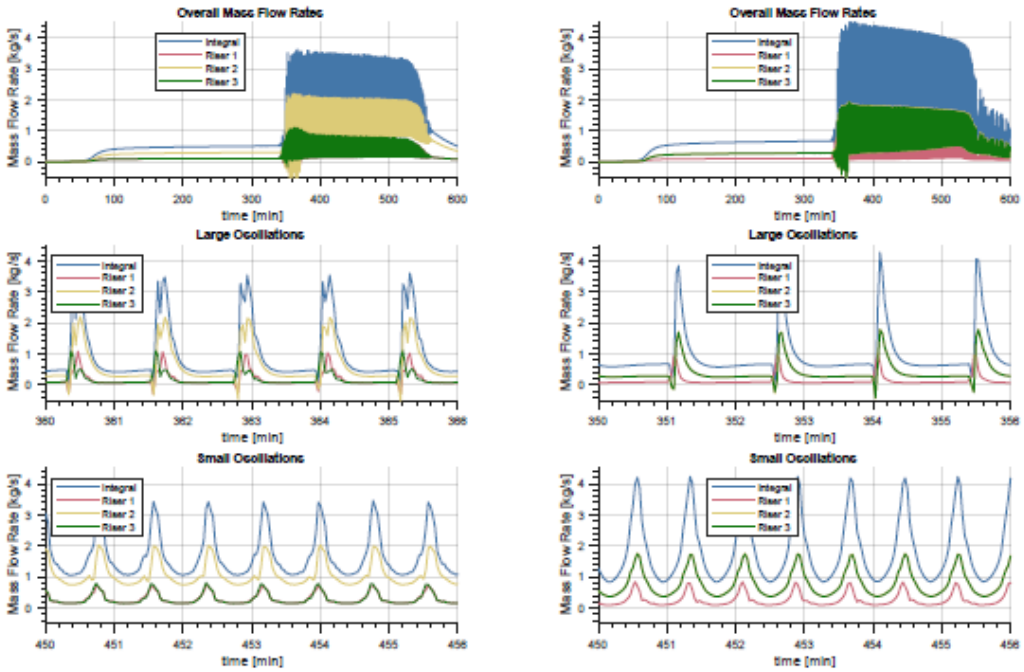


Figure 5.12: Asymmetric orifice cases with 2 risers orificed (left) and with 1 riser orificed (right) to 1/8 total flow area.

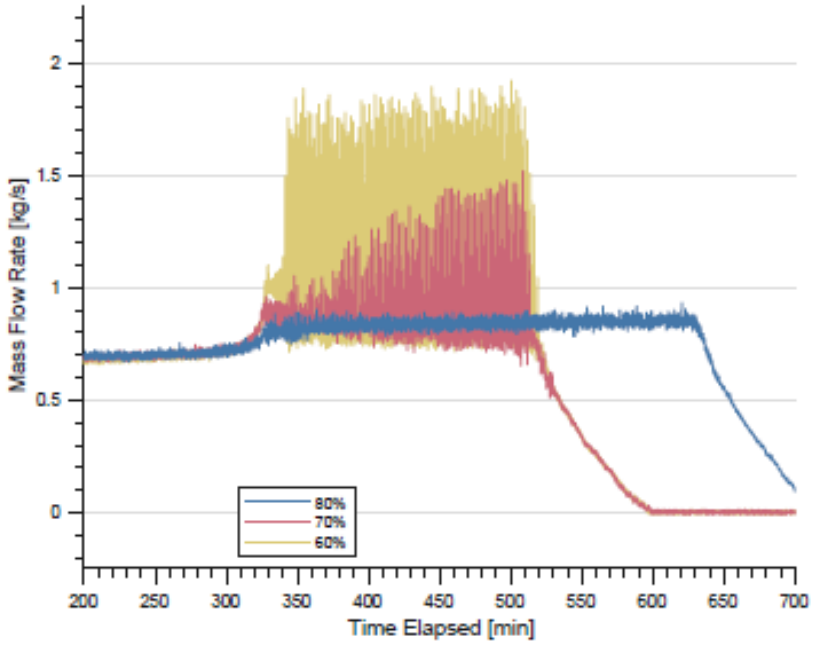


Figure 5.13: 1/2 area flow restriction for 60%, 70%, and 80% initial tank volumes.

### *1/4 Flow Restriction*

Restriction to 1/4 flow area represents the first major deviation from the unperturbed tests. The system exhibits unstable oscillations until low tank volumes (Fig. 5.14). These oscillations are quicker than the previously seen instabilities, which is unusual because in previous tank volume experiments the oscillations increased in frequency with an increase in flow rate and the average flow rate in this test is less than previous experiments. These particular oscillations occur with a

period of approximately 100 s, which decreases with tank volume. The oscillations are also 50% larger than those in the unperturbed or 1/2 orificed flow cases. This represents a decrease in stability as seen previously by Lisowski (2013). However, the fluid temperature oscillations in the risers are in-phase in the present case whereas Lisowski's data showed fluid temperature oscillations out of phase between the risers. This discrepancy is most likely due to the location of the orifice plates, the current scheme restricts flow directly into the risers whereas Lisowski restricted flow into the inlet header which may have caused a supply/demand issue that resulted in out-of-phase oscillations. This in turn causes unequal two-phase losses between the risers more so than in the present case.

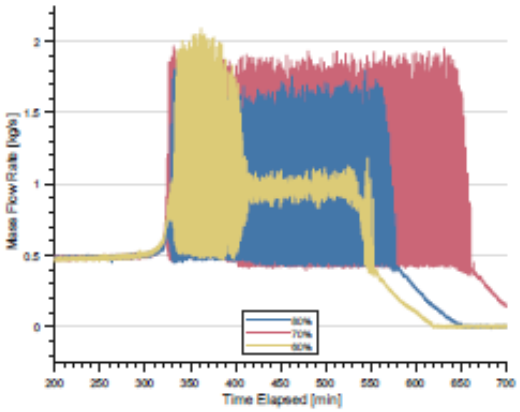


Figure 5.14: 1/4 area flow restriction for 60%, 70%, and 80% initial tank volumes.

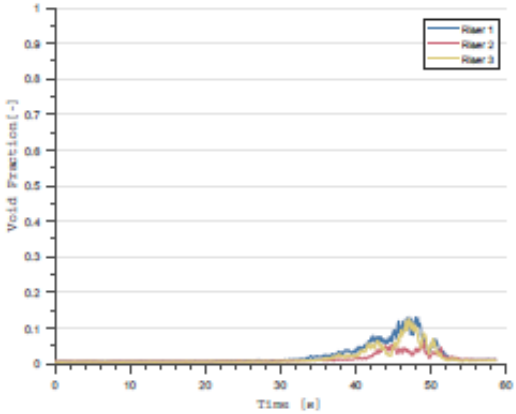


Figure 5.15: Void fraction at the exit of the RCCS risers during one oscillation with 1/4 area flow restriction and 70% initial tank volume at approximately 340 min. Magnitude of the void fraction decreases at later times.

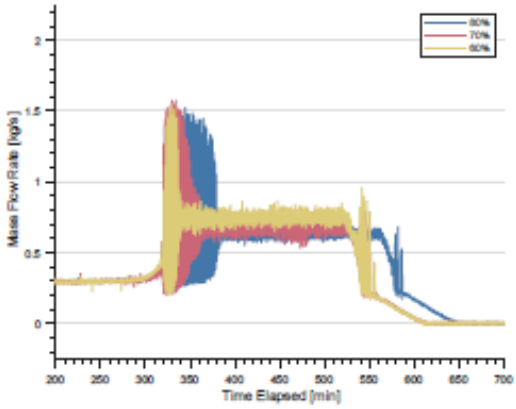


Figure 5.16: 1/8 area flow restriction for 60%, 70%, and 80% initial tank volumes.

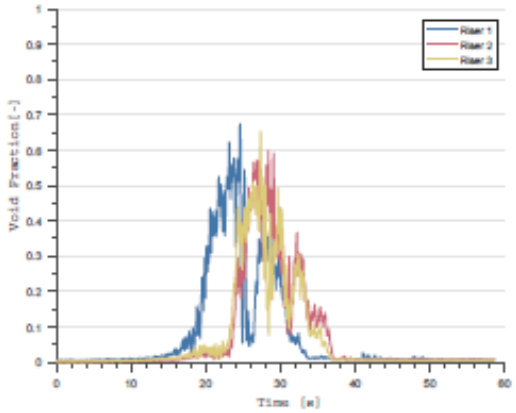


Figure 5.17: Void fraction during one oscillation at the exit of the RCCS risers with 1/8 area flow restriction at 60% initial tank volume at approximately 325 min.

Voiding in the RCCS changes with the increased inlet throttling. In previous tests voiding was restricted to the end of the chimney, but the WMS have revealed voiding in the risers before the exit header (Fig. 5.15). The presence of void at a lower elevation in the system indicates an increase in the overall driving force due to a lower mean fluid density earlier in the loop, this results in the

increased oscillatory magnitude and frequency. This could also be the indication of a different instability occurring the RCCS, which will be discussed later.

***1/8 Flow Restriction***

Stability is achieved with flow restriction to 1/8 total cross-sectional area. The system exhibits flow oscillations upon reaching saturation, which quickly diminish and give rise to stable flashing flow (Fig. 5.16). The stable two-phase regime is characterized by a lower flow rate than previous tests due to the pressure drop imparted by the orifice plate. The oscillations present at the single- to two-phase transition have the fastest observed period of approximately 80 s.

Voiding in the 1/8 orificed case reveals a large change in the system's dynamics. Stable flow is marked by constant voiding in the chimney exit as seen in previous tests, but the unstable oscillations present in the system are marked by a unique voiding behavior (Fig. 5.17). Voiding begins to occur in the risers in succession during each oscillation. Therefore, indicating that the overall flow rate in each riser is likely out-of-phase with its neighbors. However, all of the riser voiding does occur during a single system wide oscillation. The corresponding oscillatory magnitude is slightly smaller than those present in the 1/4 orificed case. When the oscillations die away, the system returns to saturated flashing at the end of the chimney, which can be explained by a steady-state model shown in following chapter.

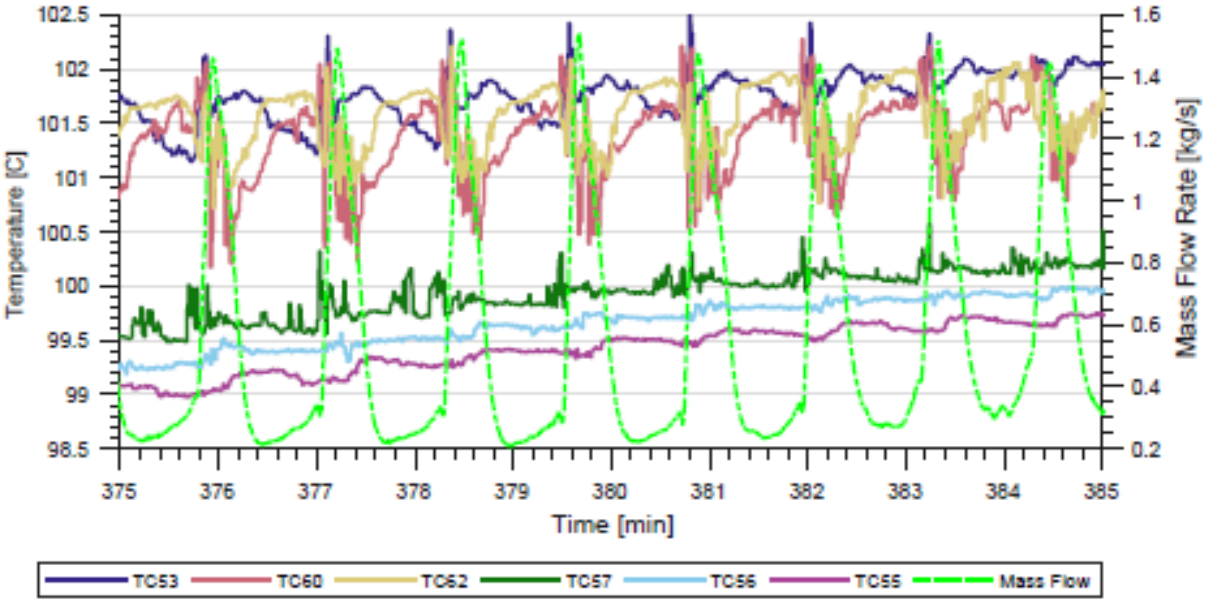


Figure 5.18: Fluid temperature oscillations in the chimney and tank. Chimney inlet (TC53) is 180° out of phase with the chimney outlet (TC60). TC62 is located slightly upstream of TC60. TC55, 56, and 57 are tank temperatures from lowest to highest elevation with TC57 0.23 m above the chimney exit centerline.

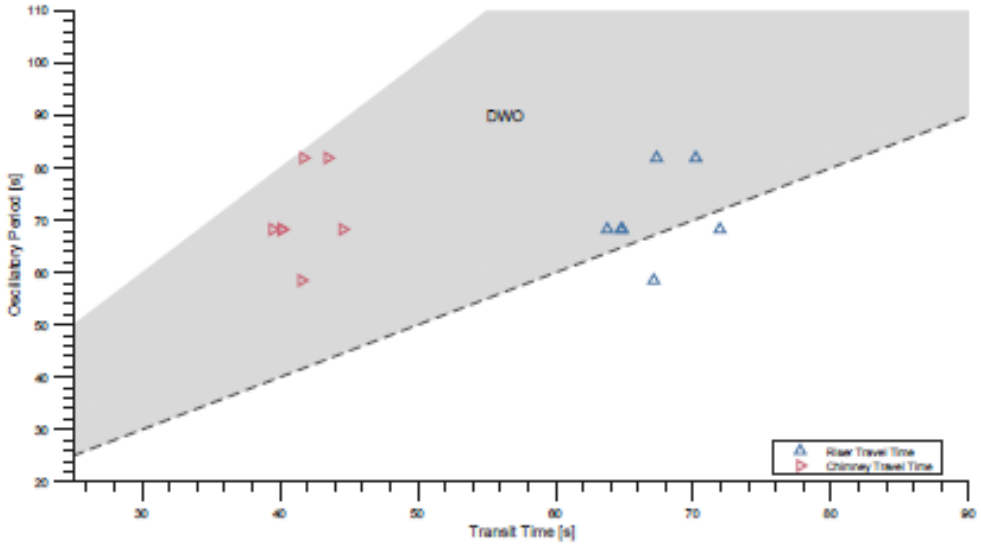


Figure 5.19: fluid packet transit time and oscillatory period comparison in relation to expected transit time from the exit of the heated core and from the exit of the risers to the exit of the chimney for density wave oscillations.

Transient oscillations that occur upon reaching saturation are expected to be a different type of instability than those seen in the unorificed cases. The instabilities result in 180° out-of-phase temperature oscillations in the chimney region (e.g. TC53 vs TC60)(Fig. 5.18). This can be an indication of self-sustained density wave oscillations (DWO), but can also be the indication of hydrostatic head fluctuations as shown by Lisowski (2013). The primary indication of a DWO is the relationship between transit time and the oscillatory period. Boure et al. (1973) suggests that DWOs occur on a period of 1 to 2 times the transit period through the entire adiabatic chimney. Other researchers suggest similar transit timing, but claim it is relative to the two-phase travel length (Fukuda and Kobori (1979)). An analysis of the transit time through the chimney during the large oscillations show that the travel time of the two-phase flow is in between 1 to 2 times the oscillatory period (Fig. 5.19). The flashing location during the oscillations is difficult to measure, but WMSs indicate voiding is occurring before the exit of the risers. Meaning that the flashing point could be anywhere between the exit of the heated core and the entrance to the risers. The two-phase travel time then corresponds to the expected time for DWOs, indicating that they are the cause of oscillatory behavior upon reaching saturation under orificed flow conditions. The transient oscillations end when the tank water surface temperature reaches a steady-state value just below saturation and the system subcooling is at a minimum.

The presence of voiding in the risers allows for further analysis of steam velocity and bubble size distribution. WMS are able to recover this information using algorithms presented in appendix D. Superficial velocities (Eq. 5.7) show that the void is traveling significantly faster than the bulk integral liquid velocity which ranges from 0.09 m s−1 to 0.13 m s−1 in the single-phase region as determined from the inlet header measurement. Interestingly, the flow rate is shown to reverse in one riser for a short period as the voiding and velocity in the adjacent risers increases (Fig. 5.20). This result is in qualitative agreement with the MELCOR analysis, although the velocity and void fraction in risers 2 and 3 are more in phase than MELCOR predicted. The measured bubble sizes as given in Eq. 5.8 also increase with an increase in total void fraction, this results in a transition between bubbly and slug or churn flow in the risers. This information gives valuable insight into

modeling and selection of appropriate void fraction correlations, which can have a drastic effect on the calculated mass flow rate in low mass quality natural circulation systems.

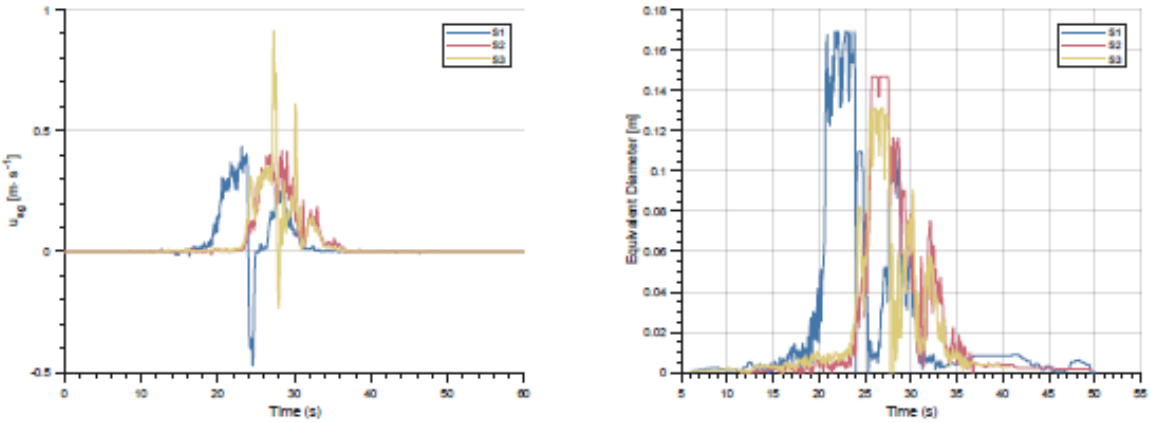


Figure 5.20: Time averaged riser gas superficial velocities (left) and bubble sizes (right) during a single flow oscillation. Calculated velocity and bubble size for each frame consist of an average over all bubbles present during each measurement frame.

$$u_{sg} = < \alpha > v_g \tag{5.7}$$

$$D_{eq} = \left(\frac{6V}{\pi}\right)^{1/3} \tag{5.8}$$

Vapor velocity during the transient oscillations show an unexpected negative flow rate. This flow is only observed in a single riser at a time, whereas the other risers exhibit upward flow. This negative flow is an indication of a complex parallel channel interaction due to asymmetry between the risers and is expected to be the primary cause for the density wave oscillations. The negative flow in the risers occurs immediately after a very large slug exits the riser. This results in a reduced buoyancy force in the riser relative to the neighboring risers. The drop in driving pressure causes stagnation and flow reversal in order to replace the volume previously filled by the vapor. The larger driving force in the adjacent risers reduces the effective supply at the riser inlet, which is why the suction effect occurs at the riser outlet. The fluid in the riser is then doubly heated allowing for voiding to continue. The flow reversal also reintroduces void that exited the riser, which increases the buoyancy force in the riser. These effects restore upward flow very quickly, which is why the downward flow only last for a brief period (approximately 3 seconds).

### 5.2.3 Special Orificing Cases

Uneven orificing represents cases where the inlet throttling is not consistent between the risers. This can occur in a full scale system if individual risers need to lengthened in order to route around features of the RPV. The increased resistance in individual risers will cause a larger enthalpy rise and lower mass flow rate relative to the neighboring risers. This can result in voiding in the selected risers, whereas the adjacent risers experience single-phase flow. Tests in the RCCS were carried out for two separate cases:

1. Symmetric orificing with riser 1 and 3 orificed to 1/8 flow area and riser 2 open.
2. Asymmetric orificing with riser 1 orficed to 1/8 flow area and risers 2 and 3 open.

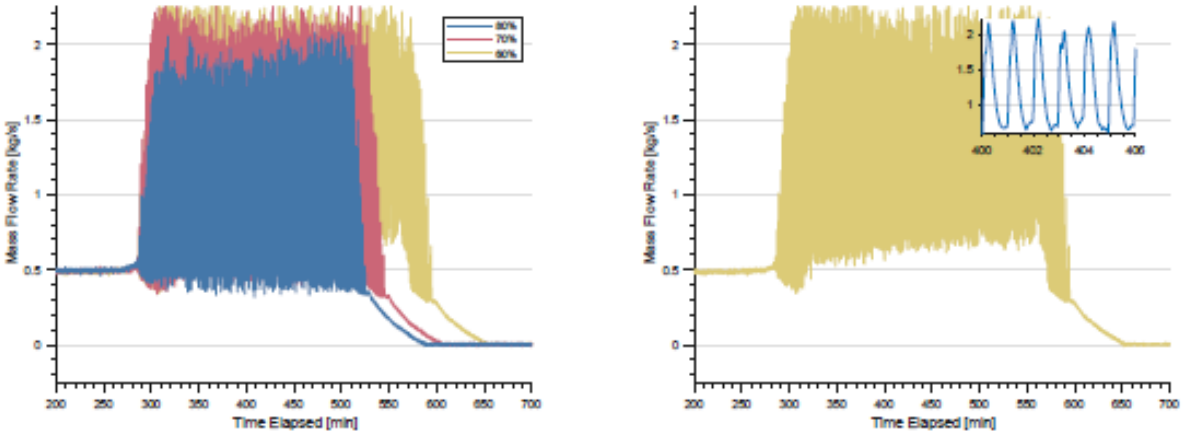


Figure 5.21: Mass flow rate oscillations under symmetric orificing conditions with riser 1 and 3 orificed and riser 2 open for various initial tank volumes, with 60% initial tank volume shown separately on the right.

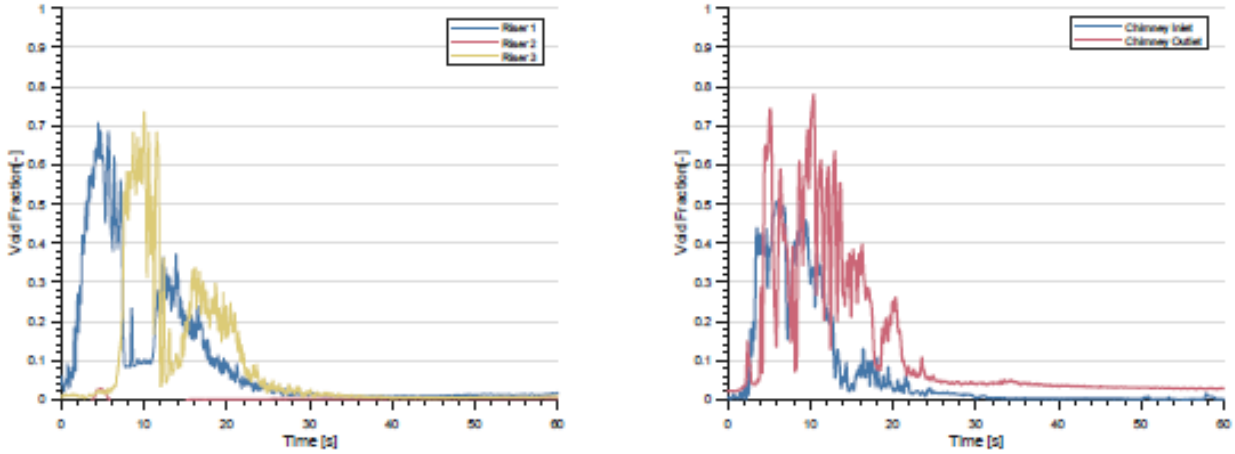


Figure 5.22: Void fraction in the risers (left) and chimney (right).

***Case 1***

Case 1 depicts a system with two heavily orificed risers surrounding an open flow path. The system responds by producing large magnitude oscillations (1.75 kg $s^{-1}$) for the full duration of system operation (Fig. 5.21). These oscillations are the largest seen in the system and increase in magnitude as the tank drains until 60% tank volume, when the oscillatory magnitude starts to decrease because the minimum flow rate increases. The oscillations occur with a period of approximately 62 s, which is also the fastest period observed. This oscillatory period is expected, because the integral system flow rate is faster due to the presence of an unorificed riser.

Void fraction in case 1 is similar to the fully orificed 1/8 flow restriction case (Fig. 5.22). Riser 1 and 3 start voiding, while riser 2 remains filled with single-phase liquid. Mixing between the channels occurs in the chimney and causes dampening of the overall void fraction due to the subcooled liquid from riser 2. However, as the fluid rises through the system the drop in hydrostatic head causes the introduction of more vapor as seen in previous tests. The riser voiding is out-of-phase between the risers similar to the 1/8 orificed case.

Stability in case 1 is not achieved as observed in the 1/8 fully orificed case. This behavior is due to variation between the saturated liquid in the orificed risers and subcooled liquid in the open riser. During flow oscillations, the orificed risers reach saturation and begin to void. This causes an increase in the buoyancy force for the individual riser followed by an increase in buoyancy for the integral system as the void exits the riser and enters the chimney. Oscillations are then observed in the integral system with out-of-phase oscillations occuring in the individual risers. The increased flow rate in the unorificed riser never allows it to reach saturation, this asymmetry causes perpetual oscillations at all tank levels even after the tank temperature reaches a steady-state value.

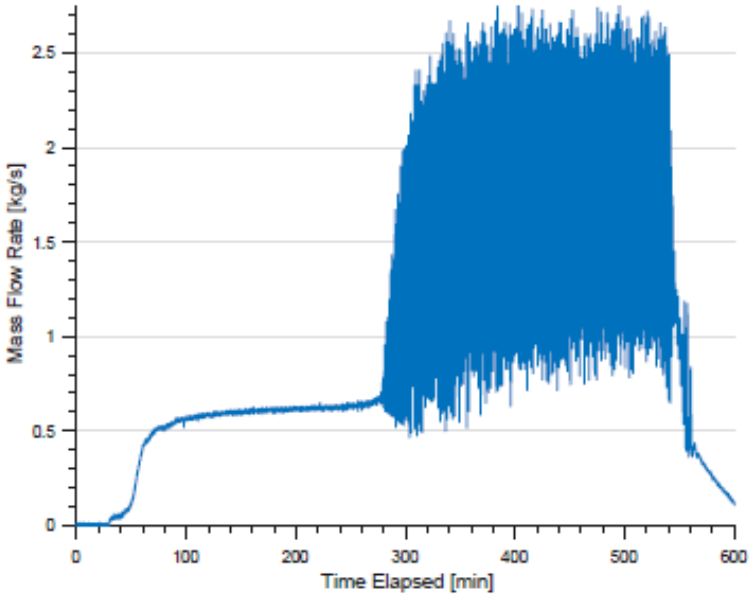


Figure 5.23: Mass flow rate oscillations with a single orificed riser.

***Case 2***

The second case represents a system where one riser is orificed. The mass flow rate oscillates continuously throughout the test, but exhibits multiple transients that affect the overall system performance (Fig. 5.23). Upon reaching saturation oscillations similar to those in the 1/8 restriction case occur. These then go through a transitional period where bimodal oscillations occur (Fig. 5.24). Finally, a different oscillatory mode is dominate and sharp changes in void occur in the risers along with continuous oscillations in the chimney (Fig. 5.25).

The bimodal oscillations occur as the system transitions from the DWO seen in the 1/8 orificed case to the oscillatory behavior seen in case 1. Voiding in riser 1 occurs due to the higher enthalpy rise compared to the adjacent risers. The localized flow increase results in oscillatory voiding. When voiding enters the chimney the integral system flow rate begins to oscillate as well. Eventually the tank temperature reaches steady-state and the system oscillations stabilize to those shown in Fig. 5.25. Unlike the MELCOR prediction, the oscillatory behavior in case 2 is not larger in magnitude than that of case 1. The two cases are approximately the same in magnitude, however case 2 does have slightly faster oscillatory period due to the faster integral flow rate.

### 5.2.4 Summary

Orificed flow has been shown to both increase and decrease system stability. At low inlet orificing the system is shown to be perpetually unstable with large magnitude oscillations, which result in

constant thermal oscillations that could challenge structural integrity of an RCCS. High inlet orificing results in a stable system assuming transient oscillations that occur until the tank temperature reaches a steady-state can be sustained. Prediction of the inlet loss required to reach a stable steady-state system can be estimated with phenomenological modeling described in the following chapter.

Transient oscillations due to the introduction of orifices in the RCCS result in new phenomena including voiding in the risers and negative flow rates. This phenomena was qualitatively predicted with MELCOR, however the magnitude of the instabilities were greatly overestimated. Experiments show that the oscillations are not as severe as predicted and therefore final RCCS designs do not need to accommodate such a large mechanical load potentially resulting in cost savings. More sophisticated two-phase analysis may be better able to capture the qualitative and quantitative features experimentally observed in the RCCS facility.

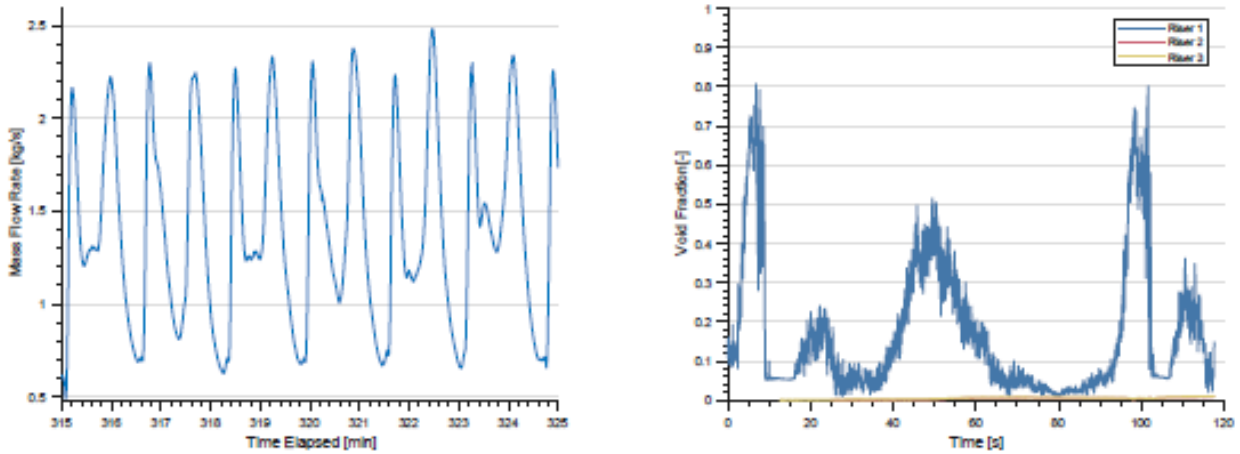


Figure 5.24: Bimodal oscillations during the transition from phase change oscillations to "steady state" oscillations. Void fraction time begins at approximately 318.4 min.

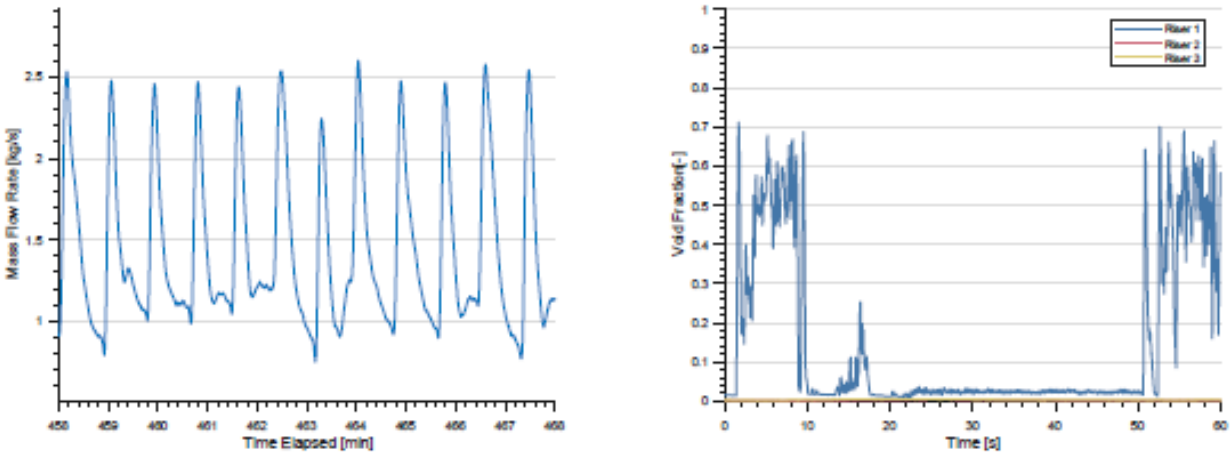


Figure 5.25: "Steady state" oscillations occurring after 350 min. Void fraction time begins at approximately 462 min.

## 5.3 Transient Tank Refill

The RCCS facility is designed to supply cooling to the reactor cavity until the tank water supply is depleted. The Electric Power Research Institute (EPRI) designates that passive safety systems are required to last 72 hours after an unplanned shutdown without operator interaction (EPRI (2014)). Therefore, the RCCS tank must be sized to accommodate enough water to boil-off for that duration. The operation of the RCCS can be extended by refilling the tank inventory after operating for the extended period for which it was designed. A test was performed to ensure that the refill procedure doesn't cause any new instabilities due to the mixing and/or stratification of temperatures with the insertion of room temperature fluid to the saturated system.

The test was designed to refill the tank inventory from 60% tank volume to 80% tank volume after flow oscillations were developed at 60% tank water volume. Water was pumped directly into the storage tank at a constant rate until the set level was reached. Upon which the system was allowed to reach saturation again and resumed normal operation. The mass flow rate in the system is shown in Fig. 5.26. Normal flow oscillations are observed until the refill fluid is introduced into the system at 409 min. The system quickly stops oscillating and becomes subcooled. Eventually the tank is filled to 80% at 421 min and the system slowly returns to saturation with the introduction of single-phase flow oscillations. Flashing begins to occur in the chimney as observed in the normal 80% tank volume tests. The test is then shut down, because normal voiding operation is expected to continue until the tank drains completely as seen in the forced drain tests.

Single-phase flow oscillations are observed following the system refill. The oscillations occur due to alternating cold and hot fluid packets are being circulated around the loop. When hot fluid is in the risers and cold fluid enters the downcomer there is a larger gravitational pressure difference between the channels. This applies a greater driving force causing a flow excursion. The loop is then flooded with cold fluid lowering the flow rate and entering a reheat period. This repeats until the system temperature is equalized around 500 min. Eventually the system is returns to saturation at 560 min and normal operation continues. If the system is naturally pressurized there will be a potential loss of pressure and a flow excursion will occur as shown in previous sections. Introduction of orificing is expected to cause the introduction of DWO upon reaching saturation a second time.

Tank refill is shown experimentally to have a minimal impact on the system performance. Introduction of the cold refill fluid causes a large drop in the riser wall and fin temperature of approximately 20 °C. This can result in thermal stresses in the structural components of the RCCS. As long as these stresses are accounted for in the construction of the RCCS, the facility can continue to function indefinitely.

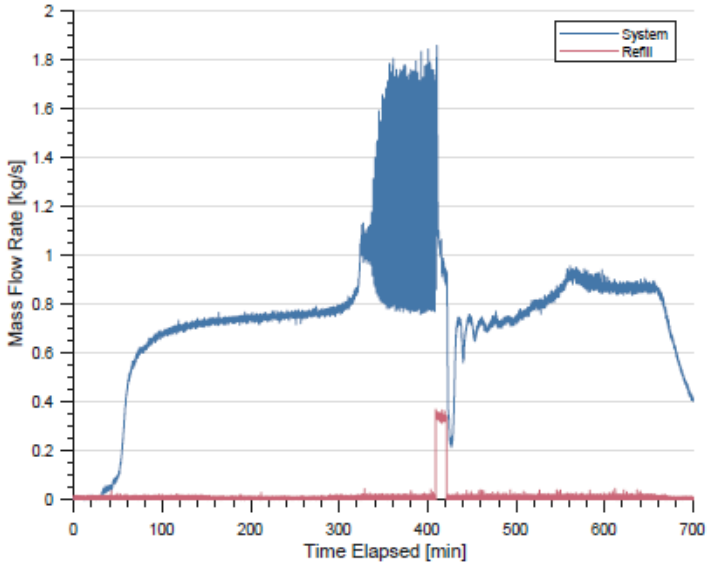


Figure 5.26: System mass flow rate during tank refill test.

## 5.4 System Flashing Location in Standard Oscillations

Variation in the flashing location in natural circulation systems can occur with different testing conditions including but not limited to pressure, power, and geometry. In natural circulation systems with adiabatic chimneys flashing occurs as the fluid rises in the chimney and reaches a saturation point due to the dropping hydrostatic pressure. Previous experimentalists have used glass piping to observe the flashing phenomenon and any changes that occur in its behavior, but small changes in the frictional losses due to a changes in surface material in a natural circulation system can have a large impact on the flow rate and oscillatory phenomenon. Through the use of a variety of instrumentation including thermocouples and wire mesh sensors in an opaque piped system with the unique WRCCS geometry it is possible to determine where the flashing is occurring.

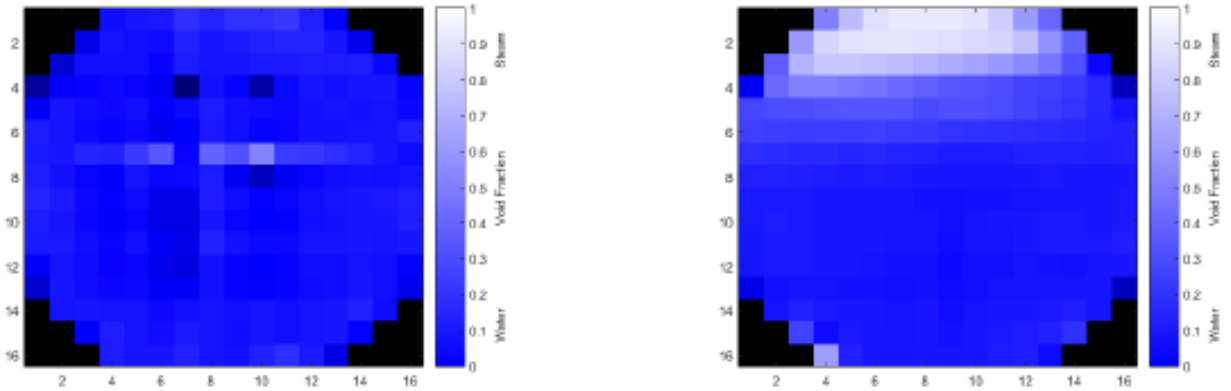


(a) WMS 4 located at the header exit (b) WMS 5 located at the chimney exit

Figure 5.27: Time averaged WMS data during pressurized tests, x and y axes represent wires in the WMS. The sensors are inside a 4" diameter pipe. Small deviations in figure a are due to fluctuations in the distance between the wires in the sensor.

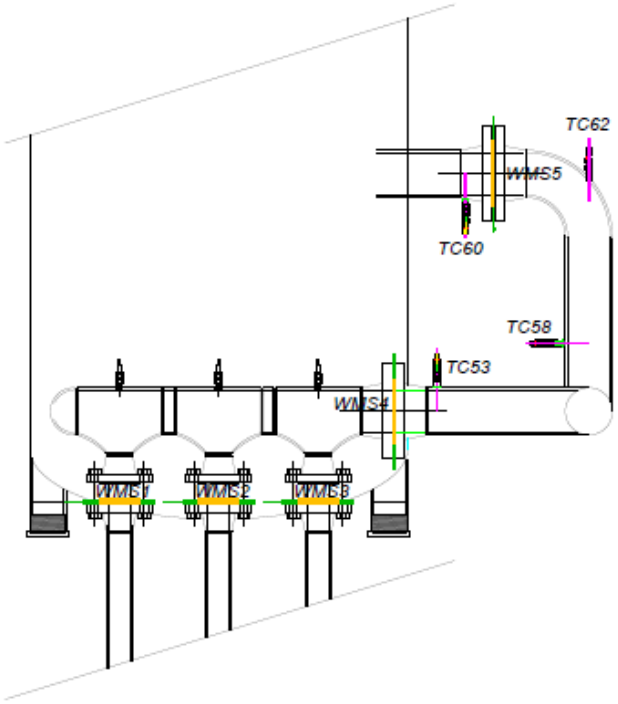


Figure 5.28: Chimney network diagram with thermocouple and WMS locations. 3 layer WMS are located in the risers while 2 layer WMS are located in the 4" chimney piping. Thermocouples are all located in the center of the piping.

### 5.4.1 WMS Data on Flashing Location and Performance

WMS are located at various locations in the adiabatic chimney including the riser exits, header exit, and tank inlet. Measurement of voiding at these locations can be used narrow down a specific area in the system where voiding naturally occurs. The WMS have shown that the under standard tests such as Run 116 with a heat input of 15.188 kW and $\beta$ = 0.31 the void is only present at the exit of the chimney (Fig. 5.27). The expectation is that the voiding occurs during a drop in the hydrostatic head, which narrows the search area to the final vertical portion of the RCCS (Fig. 5.28).

### 5.4.2 Liquid Temperature Oscillations

Thermocouples are more densely populated in the chimney and can provide further insight to the boiling location from small fluctuations in temperature due to alternating convection coefficients from the steam and liquid water phases. However, the temperature data cannot provide any indication in the type or amount of voiding like the WMS. In the chimney thermocouples are placed at the same locations as the WMS and additional thermocouples have been placed in the final vertical portion of the chimney (Fig. 5.28).

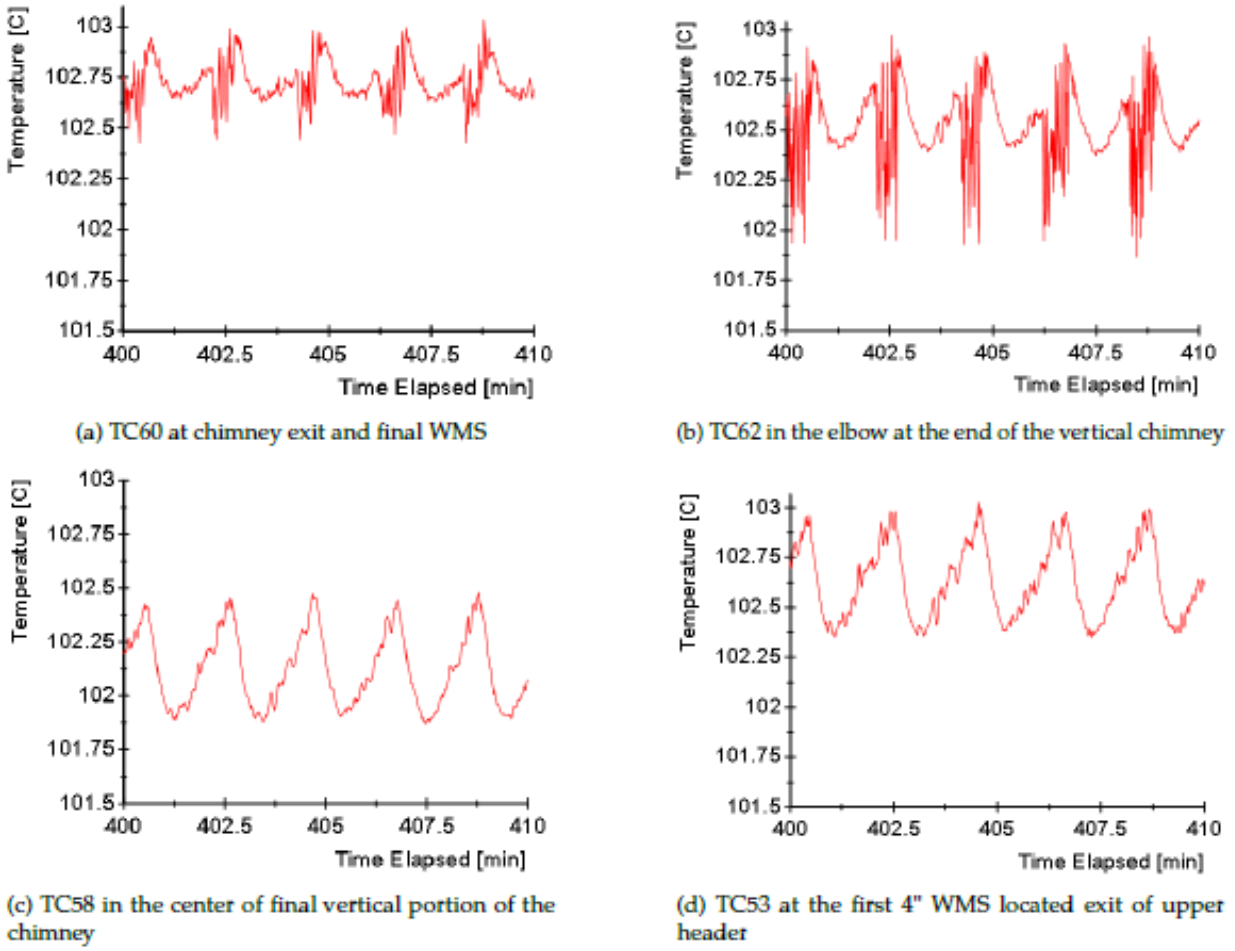


(a) TC60 at chimney exit and final WMS

(b) TC62 in the elbow at the end of the vertical chimney

(c) TC58 in the center of final vertical portion of the chimney

(d) TC53 at the first 4" WMS located exit of upper header

Figure 5.29: Chimney thermocouple data for Run 116. Higher frequency temperature oscillates in the signal at upper elevations due to flashing in the chimney.

The data from these thermocouples are shown in Fig. 5.29. The temperatures in all 4 thermocouples are nearly equal due to insulation of the chimney, although some error exists due to error in the thermocouples calibration against an RTD probe. Thermocouples at higher elevations show increased noise; more specifically drops in the temperature during a mean temperature rises. Electrical noise is not attributed as the source of fluctuations because the fluctuations only occur at the final thermocouples in the chimney. These drops suggest the measurement of different phases due to different convective heat transfer coefficients between the phases. When steam passes over the thermocouples a measurable drop in temperature occurs due to the low heat transfer coefficient of steam compared to water, allowing heat to conduct out of the probe to the mechanical structure. The oscillations in the temperature are phase-shifted due to the time of travel between the thermocouples. The fluctuations in the temperature only correspond to the largest instantaneous voids measured with the WMS, which also suggests that the base voiding phenomenon is occurring on nucleation sites along the piping walls, flanges, or weld points and not in the center of the piping where the thermocouple resides.

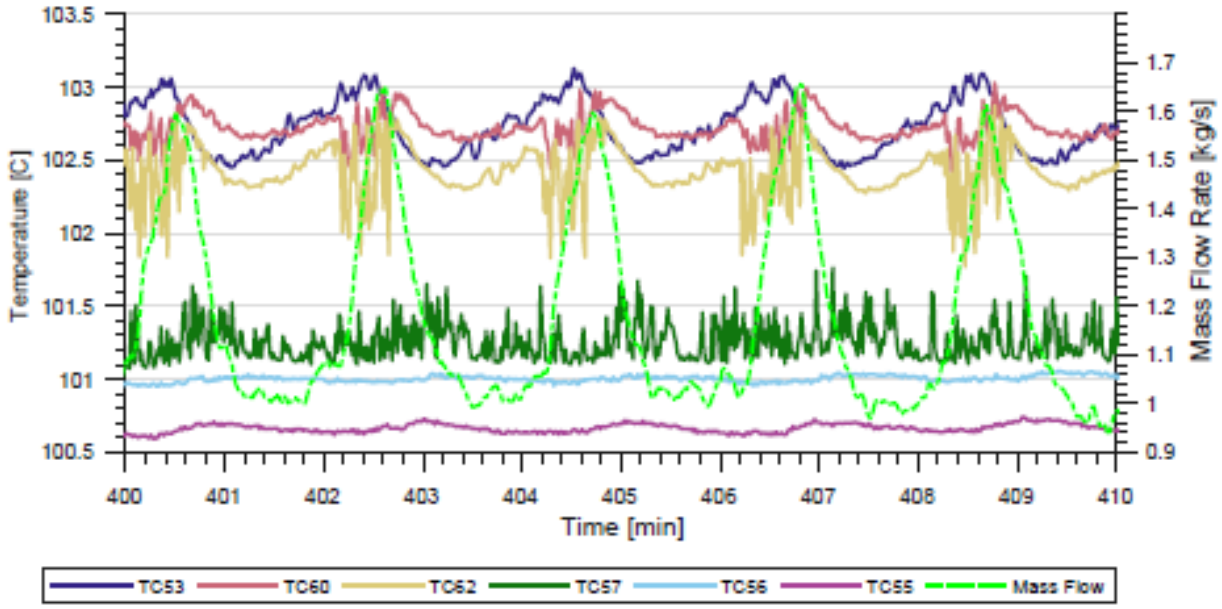


Figure 5.30: Mass flow rate and temperature data for the chimney region of the WRCCS.

The thermocouples show smaller fluctuations as the fluid travels further into the chimney due to fluid mixing effects. TC58 also measures a lower temperature than the other chimney thermocouples due to a calibration error or radial temperature gradients in the flow. TC62 shows the largest fluctuations due to it being an exposed probe, which has a faster response time compared to the grounded probes. Upon reaching TC60 the fluid has some time to mix which causes the mean and fluctuating minimum temperature to be higher than the other thermocouples. The difference could also occur due to temperature gradients across the flow causing hotter fluid to rise to the upper half of the pipe while cooler fluid settles on the bottom of the horizontal pipe.

***Mass Flow Relation to Temperature Oscillations***

Mass flow rate in the system is a direct function of the flashing phenomenon due to feedback effects from pressure changes in the driving and frictional forces. Therefore, when the mean void fraction is at a maximum, the mass flow rate should also be at a maximum. The maximum void fraction occurs when the temperature is at a maximum at the location where flashing is initiated. So, the mass flow rate should be in-phase (or slightly delayed due to fluid inertia) with the temperature oscillations at the location in the RCCS where flashing is initiated. Overlaying the mass flow rate with the chimney temperatures results in an in-phase alignment between the mass flow and TC62, which corresponds to the temperatures in the final elbow of the chimney (Fig. 5.30). Prior to this location (TC53) the oscillations peak slightly before the mass flow rate. This suggests that TC62 must be closest to the systems saturation and voiding point.

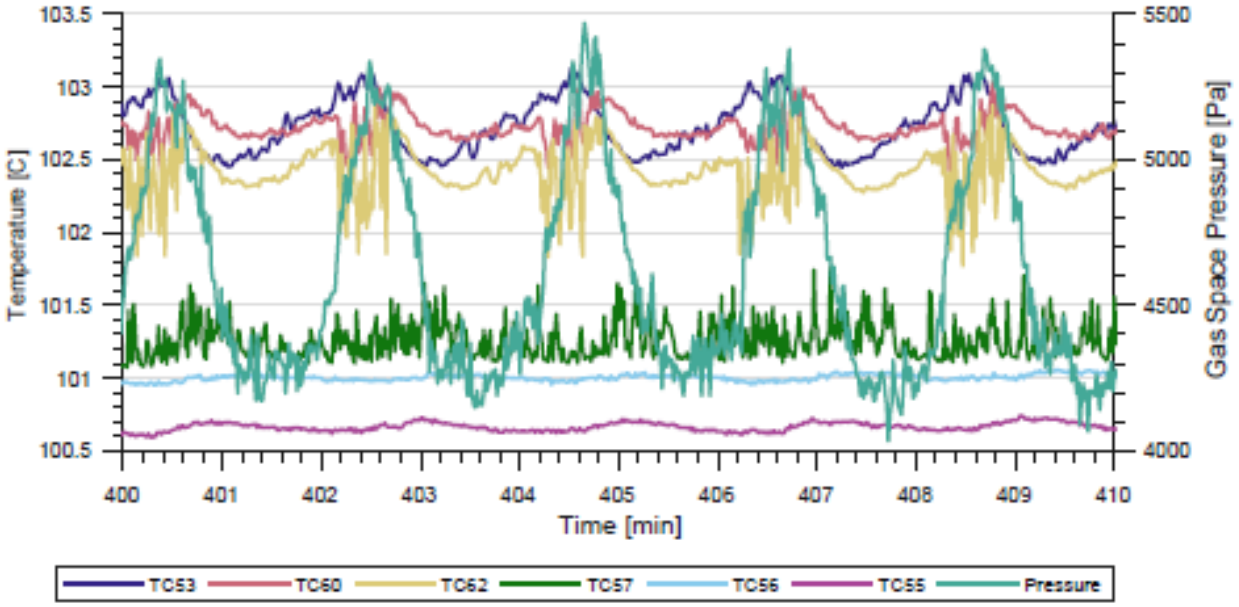


Figure 5.31: Gas space pressure and chimney temperature relationship

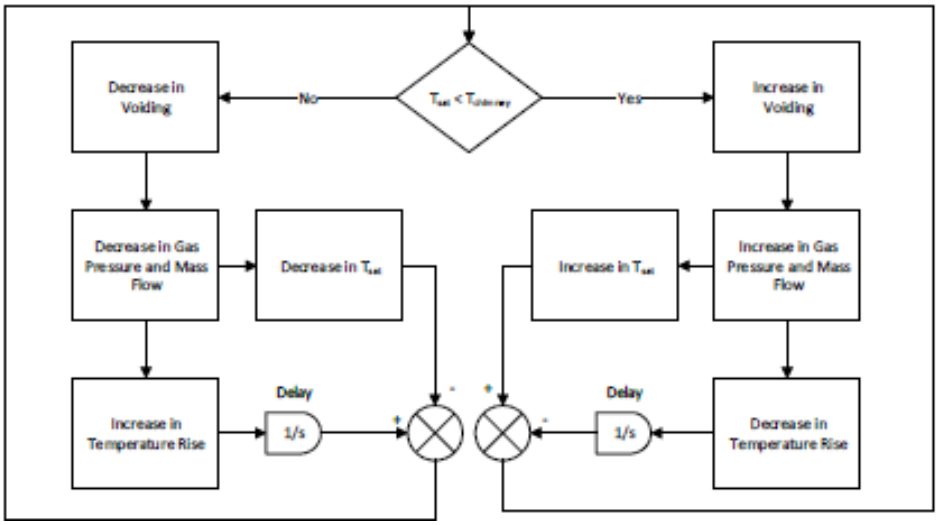


Figure 5.32: Operation flow diagram for oscillation feedback

***Tank Pressure Effects on Oscillations***

Oscillations occur in the WRCCS chimney fluid as a response to pressure and temperature changes. When the WRCCS reaches saturation voiding begins to occur and remove energy from the system, thus system temperatures are maintained at a steady-state for the duration of flashing assuming operating conditions do not change. In the WRCCS, flashing events causes an ejection of steam into the tank gas space. The release of steam from the tank is limited by the exit valve. When the rate of steam injection increase above the vented steam rate a temporary increase in the tank gas space pressure occurs (Fig. 5.31). This pressure rise translates into an increased saturation temperature, which requires the system temperature to rise in order to continue flashing and removing energy. The amount of voiding also increases due to a phase lag in the system, causing a mass flow rate increase with the pressure rise. The increase in mass flow rates results in a delayed decrease in the chimney temperature due to the time lag between the entrance to the heated section

and the flashing location in the chimney. Eventually the saturation temperature rise is greater than the temperature in the chimney generated by the mass flow rate causing a halt in the rising behavior. The delayed temperature effect due to the higher mass flow rate is observed by a decrease in the chimney temperature. During this time the tank pressure equilibrates with the reduced flashing rate. Eventually the system temperature rises enough from the lower mass flow rate to induce increased flashing as described before. The phenomenon is then repeated resulting in the observed flow rate oscillations as detailed in the operational diagram in Fig. 5.32.

***Saturation Location***

The analysis thus far can be verified by comparing saturation temperatures with fluid temperatures in the chimney at various locations and its evolution as pressure in the system changes. Saturation temperature was calculated using a polynomial fit for pressure and temperature, where pressure at each point was calculated as shown in Eq. 5.9. $\rho$ is the average fluid density, g is gravitational constant and h is the height from the sensor location to the elevation of interest. The temperature in the chimney at TC60 closely follows the saturation temperature until the peak of the oscillation where the saturation temperature rises above the liquid temperature (Fig. 5.33). At this point, the total voiding must decrease due to there being less fluid at the saturation temperature. This suggests that a variation in the initial voiding point occurs such as moving further downstream, because WMS data shows that there is constant voiding during all points of the flow oscillation. Data for mass flow rate and temperature in the forced drain test at higher pressures even suggests that the flashing may be occurring at the chimney exit right before the tank.

$$P_{head} = P_{static} - \rho g h \tag{5.9}$$

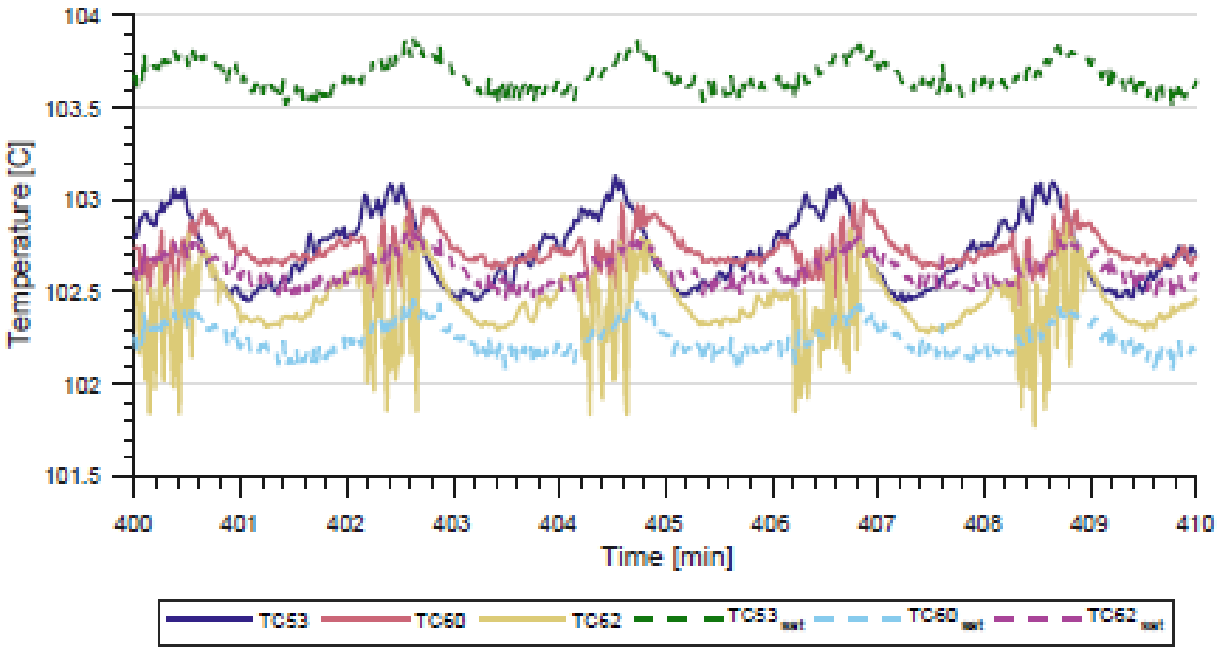


Figure 5.33: Saturation and chimney temperature relationship

### 5.4.3 Summary

Flashing in the WRCCS during normal operating conditions occurs in the adiabatic chimney region of the system and is expected to vary location during the mass flow oscillations. This phenomenon is indicated by a change in temperatures in the chimney with respect to the saturation temperature during flow oscillations. The voiding in the chimney also exhibits spikes that can be verified with the wire mesh sensors and the shorter period oscillations present in the temperature data in the final elbow of the chimney.

## 5.5 Subcooling Analysis

Natural circulation and flow boiling systems are often characterized by their operating point within the subcooling plane for purposes of stability. The plane is a non-dimensional method that classifies a system's operating point based on the channels subcooling and input power. This plane is used because those are expected to be the primary operator controlled values in a thermal hydraulic system. Multiple researchers have investigated instabilities using linear or nonlinear stability analysis in order to define stable regions of operation on the subcooling plane (Ishii (1971) and Nayak et al. (2007)). These models then offer guidance in the design of stable thermal-fluid systems.

### 5.5.1 Subcooling Plane

The subcooling plane is formed from two non-dimensional numbers: phase change number and the subcool-ing number. The phase change number is a ratio of the power into the fluid and the vaporization enthalpy; it is sometimes referred to as the Zuber or flashing number (Eq. 5.10) (van der Hagen et al. (2000)). The subcooling number is the ratio of fluid subcooling at the inlet to the vaporization enthalpy (Eq. 5.11).

$$N_{pch} = \frac{h_{out} - h_{in}}{h_{fg,out}} \frac{\rho l - \rho g}{\rho g} \quad (5.10)$$

$$N_{sub} = \frac{h_{f,out} - h_{in}}{h_{fg,out}} \frac{\rho l - \rho g}{\rho g} \quad (5.11)$$

Where h is the enthalpy and $\rho$ is the density. Subscripts **in** and **out** refer to the inlet and outlet of the channel, while **l** and **g** refer to the liquid and gas phase respectively. The subscript **f** refers to the saturated fluid value. $h_{fg}$ is the enthalpy of vaporization.

Equating the two non-dimensional numbers results in a comparison between the outlet liquid enthalpy and the saturated enthalpy. If the outlet enthalpy is greater than the saturation enthalpy, it indicates that there is enough power to result in flashing or boiling behavior in the system. In Fig. 5.34, the operating point is continuously calculated over an entire RCCS test, because the system undergoes a slow transient due to the evaporation of water inventory. The combined effect from flow oscillations and inventory loss results in the varying operating point, so a single data point for each test would be an insufficient characterization of the data. The figure shows the system approaching saturation ($x$ = 0). Upon reaching saturation the operating point begins to

migrate along the zero quality line. The dropping outlet temperature due to the drop in hydrostatic head causes the outlet enthalpy and saturation enthalpy to drop while the vaporization enthalpy increases. The shift causes the downward diagonal migration of the operating point slowly over time. Flow oscillations are reflected by the oscillations in the phase change number due to oscillations in the enthalpy rise of the system.

The system's operating region can vary as the system is perturbed. The RCCS has been parametrically studied by perturbing the system using water volume, pressure, and inlet throttling. These can have an effect on the location in the subcooling plane. Pressure and water volume have very little effect on location in the subcooling plane; the operating flow rates and temperatures are very similar and hence the system only migrates slightly along the $x = 0$ line. However, orificing has been shown to cause the presence of new instabilities and a large shift in the system flow rate, so it is useful to compare its effect on the system operating region.

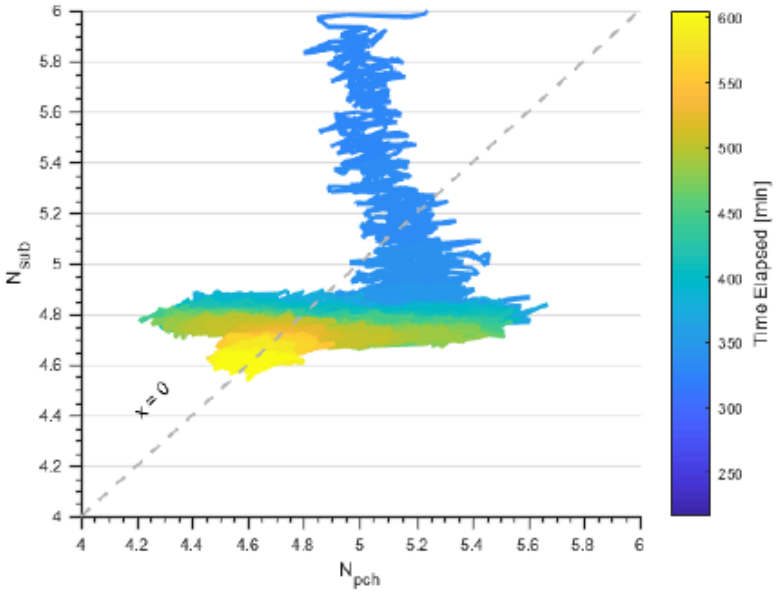


Figure 5.34: Subcooling plane for Run 116 (tank volume = 60%, Power = 15.2 kW)

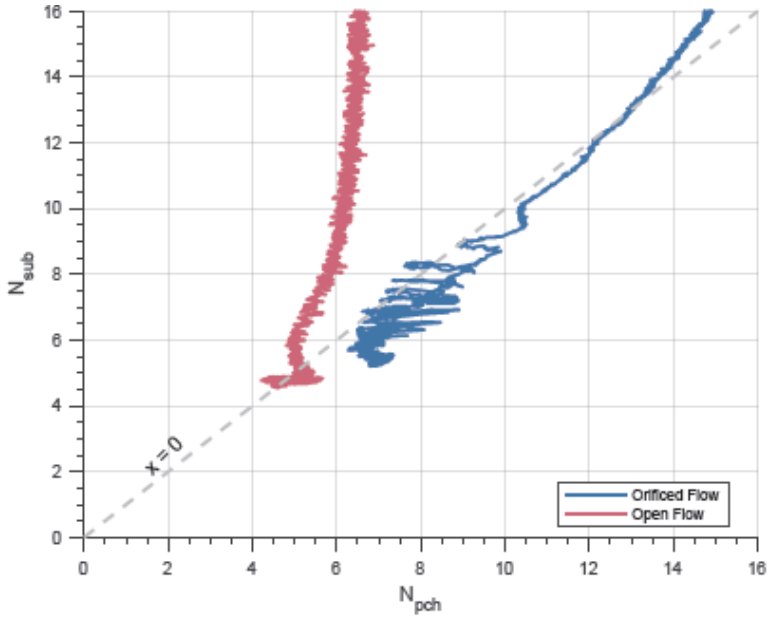


Figure 5.35: Subcooling plane comparison between orificed flow and unorificed flow

Orificing results in much larger subcooling due to the lower flow rate before flashing begins. This lower flow rate is accompanied by a significantly larger enthalpy rise in the RCCS until the system reaches saturation (Fig. 5.35). Orificed flow operates near the $x = 0$ line similarly to the unorificed case. The oscillatory magnitude in orificed flow is significantly larger than unorificed flow and it is represented by much larger oscillations in the phase change number. The overall domain operated in during orificed flow is also much larger than in unorificed flow. This occurs due to the large shift in the system enthalpy rise when the system changes from single- to two-phase flow. Upon reaching two-phase flow, the system takes approximately 20 min to transition to stable flashing. The system then operates in approximately the same location on the map for the rest of the test ($N_{pch} = 7$ and $N_{sub} = 5.5$).

### 5.5.2 summary

Plotting the migrating operating point of the RCCS can help to determine the bounds of stability with enough data points, but the results shown here do not give a conclusive indication of the stability envelope. Stability maps for DWOs formulated by Ishii (1971) and Nayak et al. (2007) can be compared with the RCCS data to determine to assist in validating the identification of instabilities or oscillations in the RCCS. Their stability maps are generally functions of the inlet velocity, because they were designed for forced flow BWRs whereas the RCCS has a variable flow rate as the system transitions from single to two-phase flow. This can cause changes in the results of the stability analysis' application to the RCCS. Their maps are also formulated with multiple assumptions that may or may not be valid for the WRCCS facility. Ultimately a more sophisticated or entirely different analysis is required in order to determine the source of instabilities and oscillations in the UW-WRCCS facility.

# 6 PHENOMENOLOGICAL MODELING

Experimental results described in the previous chapter led to some interesting findings on the stability of the UW-RCCS facility. Oscillations can be damped or eliminated with the introduction

of increased pressure or inlet throttling. The oscillations are also shown to be a function of the system flow rate and therefore the tank volume. This chapter evaluates this phenomenon using simple models of the RCCS facility.

Three models were employed in this classification of the WRCCS. The first model evaluates the system's steady-state response to various boundary conditions and inputs based directly on measured experimental data, in particular the measured void fraction. The model also acts as a sensitivity analysis of the system to different perturbations and designed to provide bounds on the expected behavior. The second model is an independent steady-state drift flux model of the RCCS in order to evaluate static instability limits in the system. This model in particular evaluates the possible presence of Ledinegg instabilities and relaxation instabilities. The final model is the application of the Ishii linear stability model to the RCCS in order to characterize the dynamic system response. This model is meant to indicate the presence of a DWO in a thermal-fluid system, but its applicability is limited as discussed below.

## 6.1 Operational Limits Model

WRCCS testing over different pressure regimes has shown that the mass flow rate during every test slowly increases over long-term testing (hours) as the tank water level decreases due to water flashing and evaporating (Fig. 6.1). This behavior can be understood by considering a steady-state momentum balance over the system with inputs for thermal energy into the water, gas space gage pressure, and void fraction in the upper chimney network. Parametric studies with this model for qualitative behavior and comparison to the experimental data suggests that the variation in mass flow is due to an increase in the void produced in the chimney region of the WRCCS. The model also calculates bounds for the mass flow behavior of the system and can be used as a predictor for future tests with heat load variation, changes in the frictional drops, or changes in scale; e.g. the WRCCS test facility under design and construction at Argonne National Labs.

Modeling the WRCCS was accomplished by dividing the flow loop into discrete control volumes. Within each control volume a pressure was determined based on temperature, pressure head, flow rate, and in the case of two-phase flow, the void fraction. These inputs resulted in a computed pressure drop around the flow loop that was balanced with the driving buoyancy force in order to calculate the mass flow in Eq. 6.1 shown below. Subscripts **c** and **h** represent the cold and hot side of the loop, while the subscripts **1Φ** and **2Φ** represent the single- and two-phase pressure losses. The integral is taken from the lowest elevation of the loop up to the elevation where the two sides of the loop close again (Fig. 6.2).

$$\Delta P_{Driver} = \int (\rho_c - \rho_h) dh = \Delta P_{1\Phi} + \Delta P_{2\Phi} \tag{6.1}$$

where

$$\Delta P_{1\Phi} = \sum_i^n f_i \left(\frac{L}{D}\right)_i \frac{\dot{m}^2}{2\rho_i A_i^2} \tag{6.2}$$

$$\Delta P_{2\Phi} = \left(\frac{\dot{m}}{A}\right)^2 \left(\frac{x^2}{\alpha\rho_g} + \frac{(1-x)^2}{(1-\alpha)\rho_l}\right) + f\left(\frac{L}{D}\right) \frac{\dot{m}^2}{2\rho_l A^2} \Phi_{lo,tt} \tag{6.3}$$

$$\frac{1}{\sqrt{f}} = -2LOG\left(\frac{2.51}{Re\sqrt{f}} + \frac{\varepsilon}{3.72D}\right) \tag{6.4}$$

$$\dot{Q} = \dot{m} C_p \Delta T \qquad (6.5)$$

The single-phase losses described above in Eq. 6.2 consist solely of major frictional losses using the Colebrook equation for the friction factor (fi); where A is defined as the pipe cross-sectional area. ρ is the density of the fluid. L/D is the length to diameter ratio of the pipe. The single-phase loss equation also describes minor losses from pipe bends, sudden expansion, and sudden contraction when DL f is combined into a single loss coefficient (K). Those coefficients are determined from the literature or analytically for the flow restrictions as shown in the previous chapter for orificing. The subscript i represents the individual control volumes of the flow loop and are divided by elevation and instrumentation, namely thermocouple locations, as shown in Fig. 6.2. The two-phase drops shown in Eq. 6.3 consist of the acceleration drop and the frictional drop in terms 1 and 2 respectively, where x is the quality and α is the void fraction. The subscripts l and g represent the saturated density of liquid and gas respectively. The frictional drops were calculated using the Martinelli-Nelson parameter Φlo,tt. The Colebrook equation is used for the frictional loss coefficient and is shown in Eq. 6.4, where Re is the Reynolds number and ε is the pipe roughness (Colebrook (1939)).

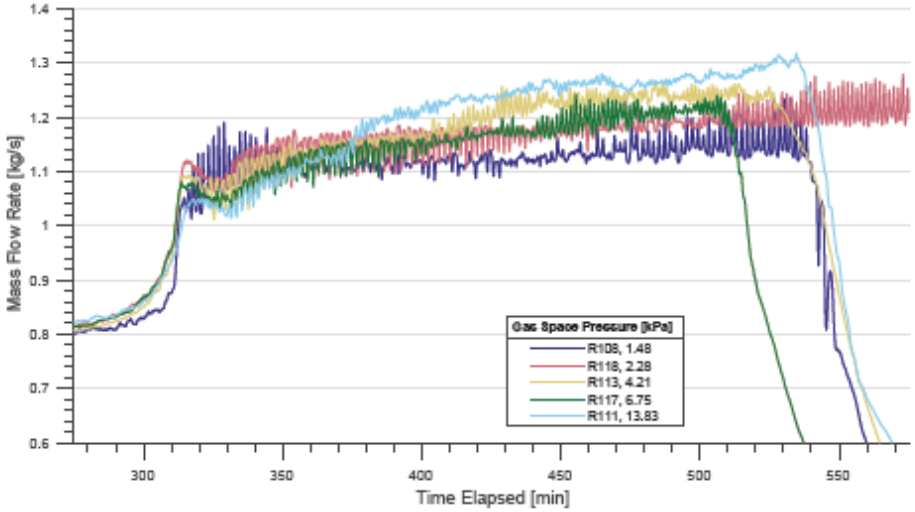


Figure 6.1: Mass flow rate from pressurized tests smoothed via moving average filter

Initial testing of the model required inputs including temperatures at the inlet and outlet of the risers, gas space pressure in the tank, and a time average void fraction. The model assumes that the area void fraction input, usually taken from WMS data, is uniform throughout the last horizontal section in the chimney before entering the tank. The inability to measure the start point of void formation at this time led to this assumption. However, based on differential pressure, temperature, and measurements from WMS in the chimney it can be deduced that voids form in the elbow entering the uppermost horizontal part of the chimney piping network. The primary metric for evaluation of the model is the mass flow of the system, although any of these states (mass flow rate, pressure head, void fraction, and temperature) can be calculated with the other three as inputs. Later revisions of the model for parametric studies assumed that the temperature of the chimney was at saturation and applied an energy balance over the risers (see Eq. 6.5) to calculate the temperature rise in parallel with the mass flow rate of the system. This replaced the temperature input with an energy input to the water (Q), because it is state variable controlled by the operator during testing. This makes the model easier to compare with test data. This also

enabled a more efficient method for the study of individual effects that were expected to cause the mass flow to increase during testing and to find operational mass flow limits under various conditions.

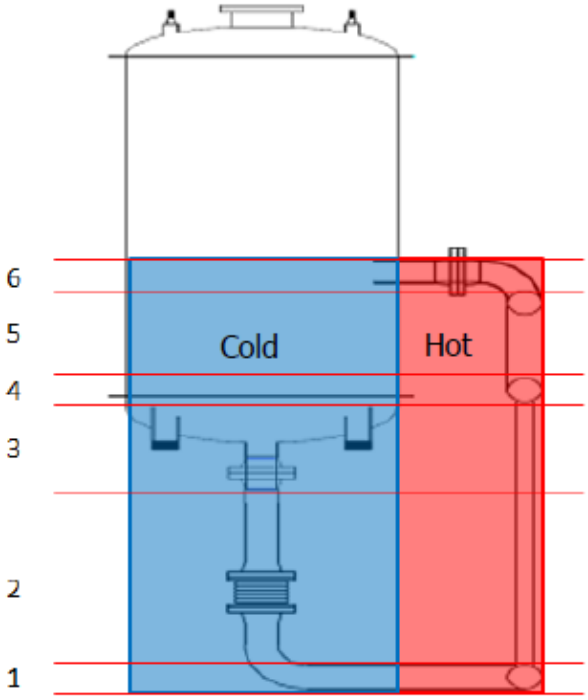


Figure 6.2: Control volume separation for momentum balance with horizontal lines and designation of cold(blue) and hot(red) sides of the RCCS loop. (not to scale)

### 6.1.1 Model Verification and Adjustments

The model was compared to a particular test (Run 116) with $Q_{thermal}$= 10 kW and slightly elevated pressure in order to evaluate behavior of the loop with different void fractions. The single phase friction factor was tuned to match the calculated single phase mass flow rate to that of the measured test data by setting the mass flow rates equal to each other in the single phase region between t=200-350 min (Fig. 6.3). From this, a friction factor could be calculated and applied to the Colebrook equation. Before comparison with the model the Colebrook equation predicted a friction factor of approximately 0.018, while measured data predicted a value of 0.029. The error could be due to increased roughness in the pipes from the flanges used for instrumentation ports and other connections that were not accounted for in the model. The measured value was equated with the Colebrook equation to solve for a new roughness value of 0.69 mm, which is significantly larger than the accepted value for stainless steel piping of 0.015 mm. This new roughness value was used in all simulations. Calculated results assuming only single phase flow using data from Run 116 as inputs is shown below in Fig. 6.3 (light blue). It shows that the model performs well, but clearly underestimates the mass flow when saturation is reached and two-phase flow occurs in the chimney region of the RCCS loop. This is due to neglecting the increase in the driving buoyancy force that a small amount of void produces. The model shows that the single-phase region has an almost perfect correlation with the measured data. Upon reaching the two-phase region the model under predicts the flow rate at the minimum flow in each oscillation; this suggests that there must be constant void production as seen in the WMS and at certain times there is a

spike in the production which causes the mass flow to oscillate. The predicted mass flow rate is also shown to have a negative slope upon reaching saturation instead of rising like the measured data; indicating that the rise seen must be the result of a change in the two-phase behavior. Oscillations in the data at the beginning of the test (0-60 minutes) are due to inconsistent inputs. Energy was input into the model as a constant, but during the first 60 min of the test the system is ramping up in power so Eq. 6.5 generates odd behavior in the mass flow rate.

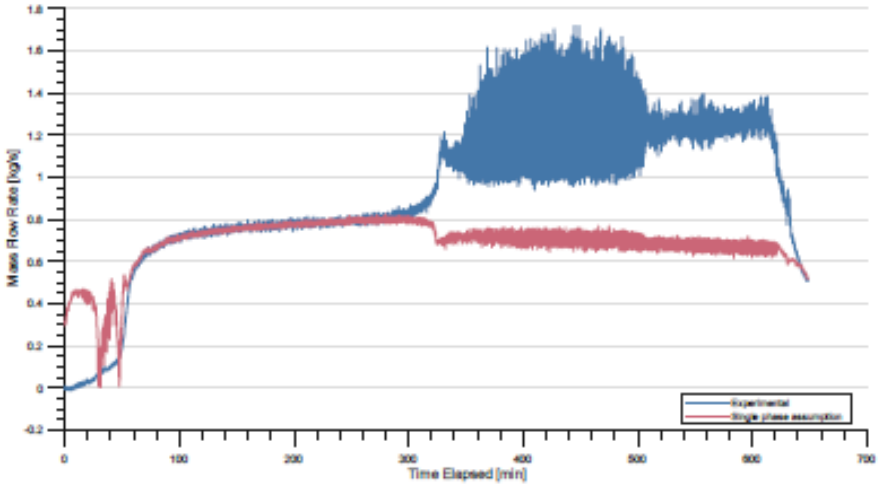


Figure 6.3: Mass flow rate from run 116. Measured data compared with a single phase flow rate calculation

Through the use of the wire mesh sensors (WMS) in the chimney one can determine the local void fraction and use this as inputs for estimating the mass flow oscillation magnitude.WMSs have shown that the void fraction oscillates between 9% and 70% during integral flow oscillations as shown in Fig. 6.4. Inputting WMS data into the simulation yields the results for two-phase flow at various assumed void fractions as shown in Fig. 6.5. As shown, the calculated values bracket the experimental data, although the calculated mass flow rate with an assumed void fraction of 62% is much higher than the maximum mass flow in the measured data. The over prediction in mass flow is due to this being an operating point model which essentially assumes that each input is independent of all others, so a 62% void fraction has its full effect on the mass flow and does not have to overcome any inertial changes in the system. In reality the spike in void fraction only lasts for approximately 5 seconds while the average flow oscillation has a period of 2 minutes. The total volume of the void in the spike is unavailable, but can be estimated using time averaging and the integral system mass flow rate. Velocities evaluated in orificed flow can also be used as an approximation of vapor velocity. It can be concluded that the mean flow rate increase is due to a mean increase in the void fraction that is depicted in the WMS data in Fig. 6.4. The mean void fraction increases to approximately 25% when the flow rate increases. This value more accurately bounds the data (Fig. 6.5).

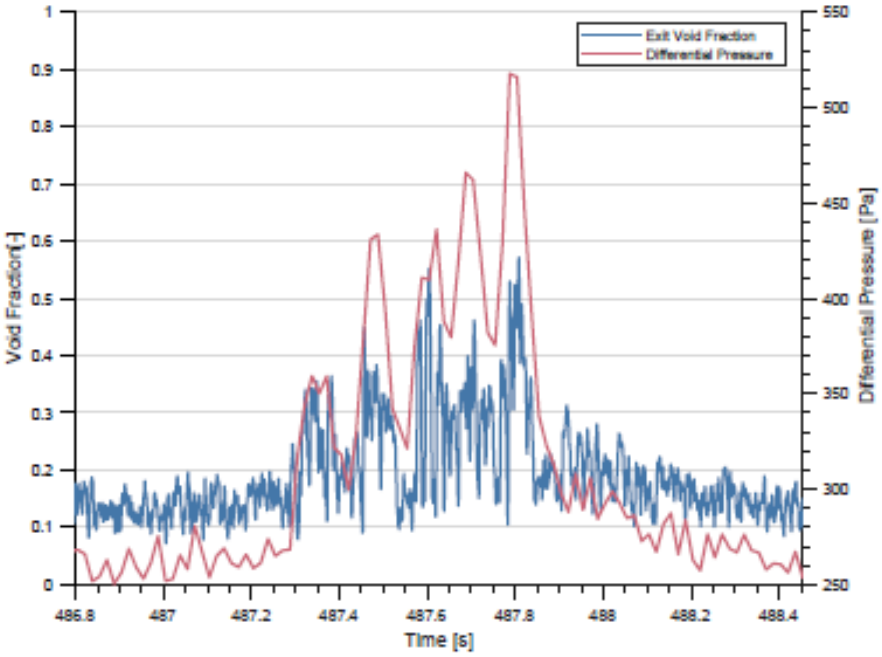


Figure 6.4: Wire Mesh Sensor data during a flow oscillation

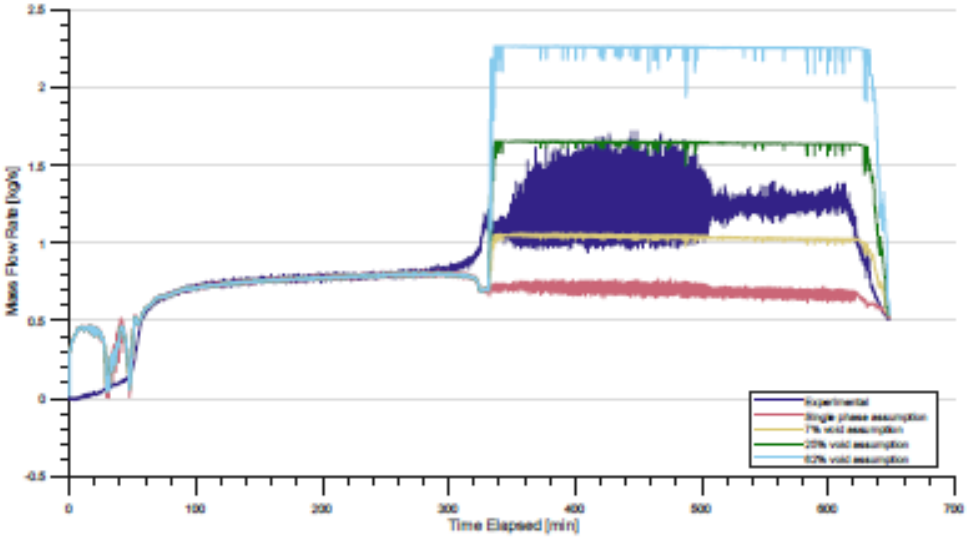


Figure 6.5: Comparison of calculated mass flow with 7%, 25%, and 62% assumed void fraction with the measured mass flow rate from Run 116.

### 6.1.2 Model Parametric Analysis

Comparing the model to experimental data led to reasonable estimates of the time averaged void fraction and mass flow rate limits during tests. However, further analysis of the model was used in order to explain the gradual rise in mass flow during the drain transient and the peak void fraction of nearly 70% observed with the WMS. During model validation testing it was shown that the calculated mass flow for both single-phase and constant void fraction tests slightly decreases during each test run, whereas the physical system shows a measurable increase in the mass flow rate. Therefore, a series of parametric studies were performed in order to analyze the effects of

system pressure head, thermal input power to the water, and void fraction on the system performance to determine the primary cause for the flow rate increase and the limits on this behavior.

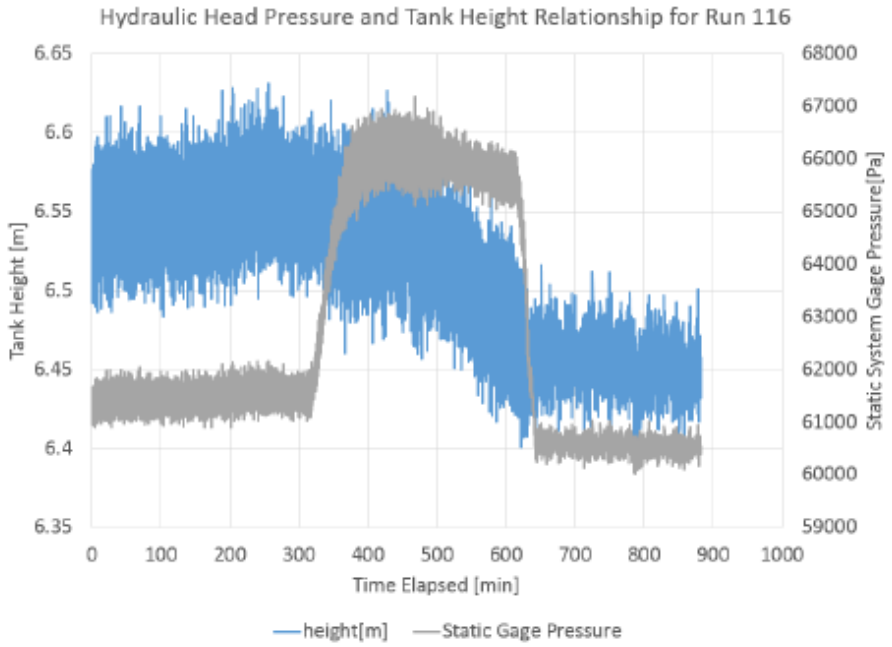


Figure 6.6: Pressure and tank height change during Run 116 (60% tank volume and slightly elevated pressure). Tank height decreases due to evaporation of the water inventory. The increase in hydrostatic pressure is due to steam production causing an increase in the gas space pressure.

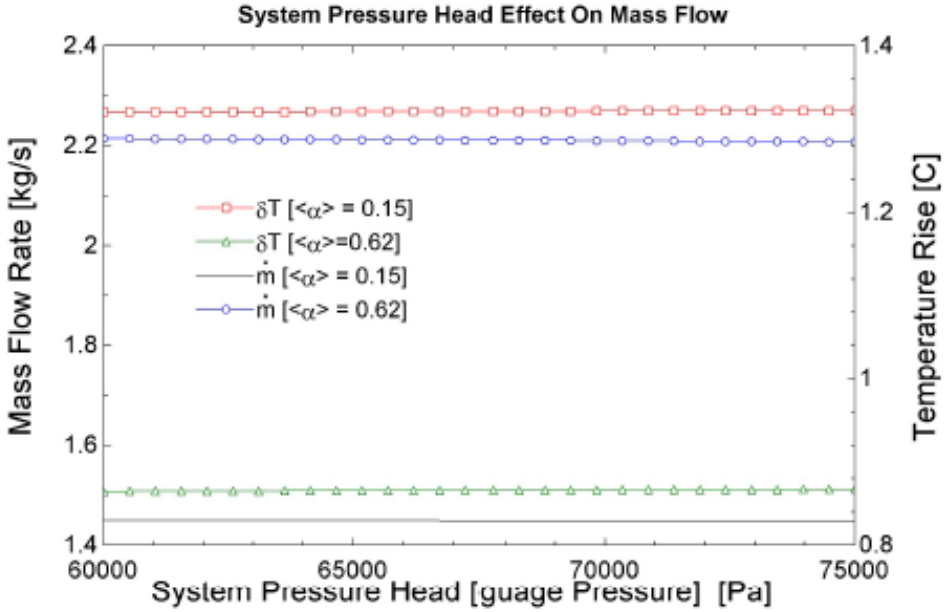


Figure 6.7: Parametric pressure head analysis with Q=10 kW and $\alpha$ = 20%

***Pressure Head Variation***

Experimental tests show the static pressure head (ambient gas space and hydraulic head pressure) dropping due to evaporation and flashing of the water inventory as shown in Fig. 6.6. This behavior was modeled with a constant void fraction of 15% and 62% with a thermal heat load on the water of 10 kW (Fig. 6.7). The decrease in the pressure head shows minimal change in mass flow under constant void fraction. The drop in pressure does cause a small change in the saturation temperature, but it is not enough to cause significant changes in performance. The overall effect to the mass flow rate as a direct result of the hydraulic head pressure drop appears to be minimal compared to the measured change in the filtered experimental data. This suggests that the average voiding must be increasing; possibly due to a time lag between system temperature and a decrease in saturation temperature.

***Power Variation***

Total thermal power input into the fluid has been shown in previous studies to affect the behavior and stability of the system. Varying the power is expected to increase the T of the system and therefore increase the driving force and mass flow rate. Shown in Fig. 6.8 are the results from the model for varying the thermal power into the water with a constant void fraction of 0.25 and 0.62. The pressure head was maintained at a gage pressure of 66.5 kPa along with the assumption that the fluid at the top of the chimney was at saturation. The results show that increased power does cause an increase in the system T, but does not have a substantial effect on mass flow. As shown the mass flow rate at low void fractions increases slightly more with power than at higher void fractions, which one would expect to lead to better stability of the system due to smaller variation in the flow rate with voiding. However, further testing is required to verify these effects.

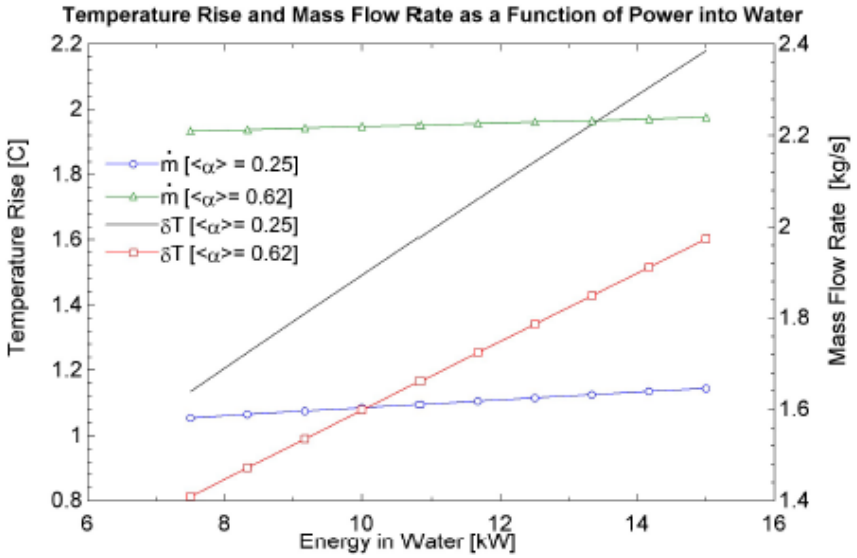


Figure 6.8: Parametric thermal power analysis with $P_{head}$ = 66.5 kPa (gage)

***Void Variation***

The absence of any significant effect on mass flow rate due to pressure variation alone led to the assumption that the loss of pressure head from evaporation and flashing must cause a change in the void fraction. Shown below in Fig. 6.9 is the calculated mass flow rate as a function of void fraction in the chimney exit with a constant pressure head of 66.5 kPa and energy input of 10 kW. Void fraction is shown to have a strong influence on the mean mass flow rate. However, the maximum effect on flow rate occurs around 70% void fraction, which corresponds to the peak

values seen in the WMS data. Further increases in the void fraction have diminishing returns on the flow rate. This suggests that the WRCCS has an operational region with void fraction below 70%. This peak location shifts with changes in the system frictional losses.

The peak void fraction occurs due to changes in the dominate pressure losses in the system. At low void fractions the major losses in the system are due to single-phase frictional losses, which are proportional to the mass flow rate in the system. Increasing void leads to increases in the driving pressure and two-phase losses in the chimney. Eventually two-phase losses dominate the system behavior as shown in Fig. 6.10a. The peak in mass flow occurs at a lower void fraction than the intersection between single- and two-phase losses, because the increase in the driving force due to increased voiding becomes less than the increase in two-phase frictional losses in the chimney. This is shown in Fig. 6.10b, which depicts the rate of change in pressure losses due to a change in void fraction normalized by the change in the driving force with void fraction. Data from the WMS appear to always follow the limits to void production based on Eq. 6.6 during flashing spikes as verified by the model.

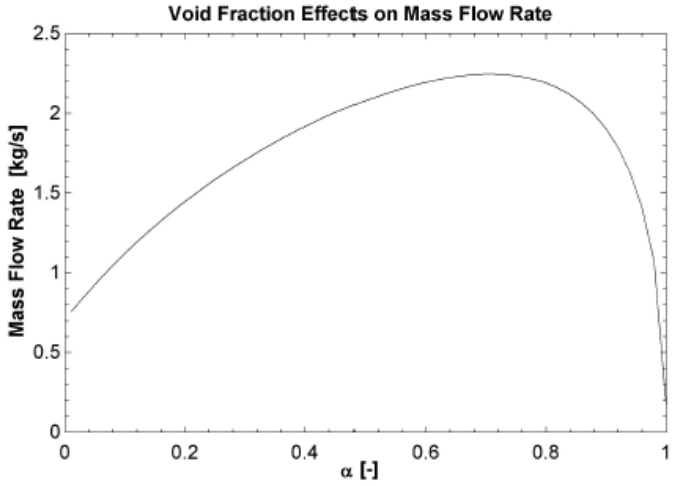


Figure 6.9: Parametric void fraction analysis with Q=10 kW and $P_{statichead}$ = 66.5 kPa (gage)

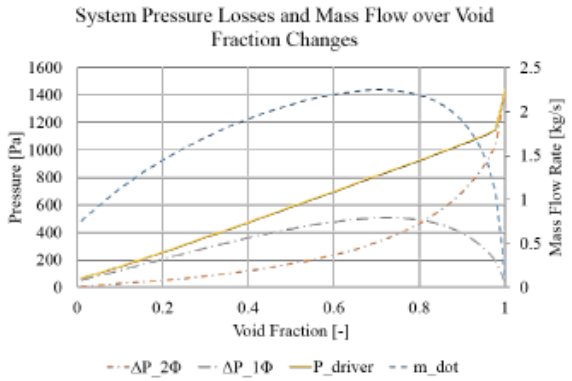


(a) Mass flow peak due to void fraction change and accompanying pressure losses at Q=10 kW and $P_{statichead}$ = 66.5 kPa (gage)

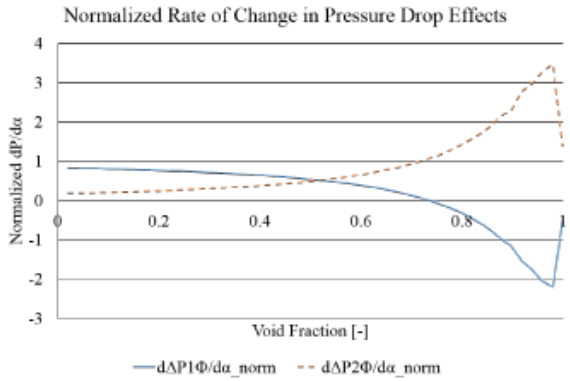


(b) Derivative of driving pressure and two phase pressure loss with void fraction normalized by the driving pressure

Figure 6.10: Peak mass flow due to voiding

$$max[\alpha]\ when,\ \frac{d\Delta P_{2\Phi}}{d\alpha} = \frac{d\Delta P_{Driver}}{d\alpha} \qquad (6.6)$$

Model results with mass flow as the varied parameter and all other parameters held constant were used to gain insight to the range of the base level void fraction that might cause the change in mass flow seen during each test. The results show that a deviation in the mean void fraction of 7% can cause the mass flow to change by as much as 0.2 kg $s_{-1}$ (Fig. 6.11). This change could occur during tests from either an increase in overall flashing or by varying where in the chimney the flashing is originating.

Comparisons between the measured mass flow rate and the calculated flow rate were performed using void fraction data produced from WMS. WMS data was collected during run 116 at three different times for 150 seconds at a sample rate of 160 Hz. The void measurements were time averaged and are shown in Tbl. 6.1 along with a calculated mass flow rate. The data shows that the time averaged void increases slightly during testing confirming the results from the model, but the time averaged void fraction yields a calculated mass flow that is higher than the mean measured mass flow. This could be due to the instantaneous short lived peaks in void artificially raising the time averaged void fraction. Another possible cause could be due to uncertainty in the void fraction measurement. The non-linear nature of the void fraction's effect on flow rate then leads to an error in the calculated increase of mass flow. A lower initial void fraction with a similar rate of change over time would yield a larger calculated increase in mass flow; thereby reducing error between the measured and calculated mass flow.

Void fraction can also be calculated instead of used as an input to the model using a Rouhani based drift flux model assuming the energy into the system is fully utilized to create steam and thereby maintains an energy balance throughout the system. This removes the models dependence on void data from the WMS, so that only operator controlled inputs (external pressure and power) are used in the model for calculation of the mass flow rate. The model then over predicts a void fraction of 0.58 to 0.596, which yields a mass flow rate of 2.20 kg $s^{-1}$ to 2.21 kg $s^{-1}$ for 10 kW input power and static head pressures from 67 kPa to 60 kPa. Experimental data shows that voiding this high only occurs at the peak of the oscillations and the measured mass flow rate does not achieve that speed until the water level is equal to the chimney exit as shown in forced drain tests Lisowski et al. (2014).

Table 6.1: Void fraction and calculated mass flow during Run 116

| Time Elapsed [min] | Time Averaged Void Fraction | Mass Flow Rate [kg/s] | Measured Mass Flow Rate [kg/s] |
|---|---|---|---|
| 365 | 0.2536 | 1.567 | 1.142 |
| 487 | 0.2589 | 1.581 | 1.210 |
| 513 | 0.2779 | 1.634 | 1.232 |
| Total Change | 0.0243 | 0.067 | 0.090 |

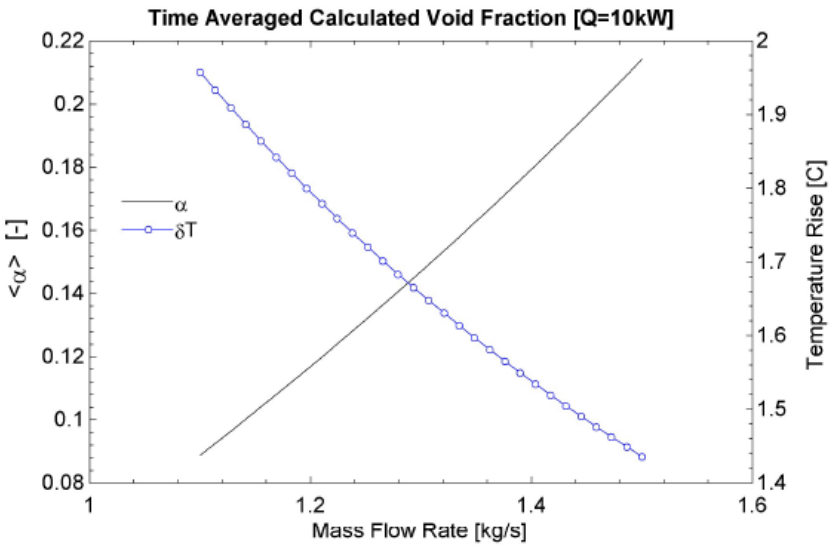


Figure 6.11: Parametric mass flow analysis with Q=10 kW and $P_{statichead}$ = 66.5 kPa

### 6.1.3 Summary

Mass flow changes in natural circulation come with variations in system performance and flow stability. Understanding the mechanism that causes the system to evolve can help to determine what causes flow oscillations and help to classify the ranges of flow stability. It has been shown experimentally that variations in the system pressure head on the RCCS leads to changes in the flow rate of 0.2 kg $s_{-1}$ (10-20%) over the course of a single test by increasing the void produced in the chimney by approximately 7%. Gradual changes in the mass flow suggest that it is based on an increase in the mean void fraction and that short time-scale spikes in the void fraction (seconds) do not immediately impact the mass flow. This phenomenon is represented by the smooth change in flow rate during oscillations in contrast with the sharp changes in differential pressure and WMS data indicating a pulse of steam.

The peak mass flow rate has been shown to be limited by the frictional losses in the two-phase region of the RCCS. The model shows that the driving force linearly increases with void fraction, but single-phase and two-phase frictional losses do not. The single-phase losses are directly proportional to the mass flow rate, while two-phase losses depend on void fraction and mass flow. At 70% void fraction the increase in two-phase acceleration and frictional losses in the chimney become greater than the increase to the driving force resulting in an imaginary and possibly unstable operating region at voiding greater than 70%.

The model requires further refinement for accurate predictions of the system wide behavior, but does show qualitative effects on the system. The model shows that power has a greater effect on flow at low void fractions and that an increase in power can potentially increase stability at the current operating conditions. Also shown was that the pressure alone does not affect the flow, but suggests that the decreases in pressure must cause an increase in void fraction that directly causes a change in the flow rate. Refinement in the form of better prediction of frictional changes in the model and better implementation of void prediction can be used to garner further insight in the performance of the RCCS.

## 6.2 Steady State Modeling for Static Stability

Steady-state modeling is a technique useful for the design of a thermal-hydraulic system. It predicts the expected flow rate, voiding, and flow regime. This allows for proper mechanical design of a system based on the expected operational limits of the system. This type of analysis is especially important in natural circulation (NC) due to the inability to directly control the system's operating point when on-line.

Steady-state modeling is able to identify Ledinegg flow excursion and Fundamental Relaxation instabilities in thermal-fluid systems. Ledinegg excursions were the primary points of failure with boilers in the early 1900's and were descried by Ledinegg's criterion (Eq. 6.7) (Ledinegg (1938)). His criterion states that if the rate of change of the characteristic pressure drop curve for the system is less than the rate of change of the driving pressure drop curve then the system will experience a flow excursion. In natural circulation the driving pressure is represented by the gravitational forces in the downcomer, whereas in a forced flow system this would be the pump power. The inability to directly change the driving force in a NC system requires the channel to be designed to operate in an instability free regime.

$$\frac{\partial \Delta P_{channel}}{\partial \dot{m}} - \frac{\partial \Delta P_{drive}}{\partial \dot{m}} \leq 0 \qquad (6.7)$$

### 6.2.1 Drift Flux Model

Multiple models exist for studying the two-phase phenomenon of thermal hydraulic systems including the two-fluid model, drift flux model, and homogeneous equilibrium model from most to least complex. The drift flux model was chosen to study the RCCS due to its extensive work on modeling dynamic instabilities in NC systems (Ishii (1971), Nayak et al. (2007), and Goudarzi and Talebi (2013)). This model has numerous options for the void fraction/drift model that have been studied for accuracy in a variety of systems including NC flows (Manera et al. (2005b), Chexal et al. (1991)). Drift flux also allows for extraction of the phase velocities, which can potentially be measured by WMS diagnostics if voiding occurs at a 3 layer sensor and exists in a bubbly or slug flow regime.

***Model Equations***

The standard 4-equation drift flux model derived in appendix C and rigorously by Ishii and Hibiki (2011) is presented below. The 1D field equations are a result of ignoring interfacial effects, turbulent effects, viscous stress, and internal conduction.

$$\frac{d\rho_m}{dt} + \frac{d(\rho_m v_m)}{dz} = 0 \tag{6.8}$$

$$\frac{d(\alpha\rho_g)}{dt} + \frac{d(\alpha\rho_g v_m)}{dz} = \Gamma_g - \frac{d}{dz}\left(\frac{\alpha\rho_g\rho_\ell}{\rho_m}\overline{V_{gj}}\right) \tag{6.9}$$

$$\frac{d\rho_m v_m}{dt} + \frac{d(\rho_m v_m|v_m|)}{dz} = -\frac{dp_m}{dz} + \frac{d}{dz}\left(-\frac{\alpha}{1-\alpha}\frac{\rho_\ell\rho_g}{\rho_m}\overline{V_{gj}}^2\right) - \rho_m g_z - \frac{f\Phi_{lo}^2}{2D}\rho_m v_m|v_m| \tag{6.10}$$

$$\begin{aligned}\frac{d\rho_m h_m}{dt} + \frac{d(\rho_m v_m h_m)}{dz} =& \left(v_m + \frac{\alpha(\rho_\ell-\rho_g)}{\rho_m}\overline{V_{gj}}\right)\frac{dp_m}{dz} + \frac{dp_m}{dt} + \frac{q''_W P_w}{A} \\ &- \frac{d}{dz}\left\{\alpha\frac{\rho_\ell\rho_g}{\rho_m}\overline{V_{gj}}h_{g\ell}\right\}\end{aligned} \tag{6.11}$$

Steady state modeling removes all time dependence from the field equations resulting in the two primary field equations for momentum and energy. Differential pressure in the energy equation is assumed to be only a function of the body forces (e.g. $dP/dz \approx -\rho g$).

$$\frac{d(\rho_m v_m|v_m|)}{dz} = -\frac{dp_m}{dz} - \frac{d}{dz}\left(\frac{\alpha}{1-\alpha}\frac{\rho_\ell\rho_g}{\rho_m}\overline{V_{gj}}^2\right) - \rho_m g_z - \frac{f\Phi_{lo}^2}{2D}\rho_m v_m|v_m| \tag{6.12}$$

$$\frac{d(\rho_m v_m h_m)}{dz} = -\left(v_m + \frac{\alpha(\rho_\ell-\rho_g)}{\rho_m}\overline{V_{gj}}\right)\rho_m g + \frac{q''_W P_w}{A} - \frac{d}{dz}\left\{\alpha\frac{\rho_\ell\rho_g}{\rho_m}\overline{V_{gj}}h_{g\ell}\right\} \tag{6.13}$$

***Constitutive Relationships***

Multiple constitutive relationships are required to solve the thermo-fluid equations these include an equation of state, a correlation for drift flux, a void fraction relationship, and frictional loss coefficient relationships.

***Equations of State***

The equations of state used in the model are summarized below and include the definitions of density and the corresponding mixed properties.

$$\rho = \rho(P, h) \tag{6.14}$$

$$\rho_m = \alpha\rho_g + (1-\alpha)\rho_\ell \tag{6.15}$$

$$v_m = \frac{\alpha\rho_g v_g + (1-\alpha)\rho_\ell v_\ell}{\rho_m} \tag{6.16}$$

$$h_m = \frac{\alpha\rho_g h_g + (1-\alpha)\rho_\ell h_\ell}{\rho_m} \tag{6.17}$$

***Drift Flux Correlation***

Manera et al. (2005b) showed the applicability of various drift flux correlations and determined that either the GE-Ramp or Dix correlation work well with adiabatic flashing flows as long as the

pipe diameter is not too large. The GE-Ramp equation was selected due to ease of implementation in the solution scheme.

$$\begin{aligned}
\alpha_2 \le 0.65 &\begin{cases} C_0 &= 1.1 \\ R &= 2.9 \end{cases} \\
\alpha_2 > 0.65 &\begin{cases} C_0 &= 1.1(1-\alpha_2)/0.35 \\ R &= 2.9(1-\alpha_2)/0.35 \end{cases} \\
V_{2j} &= R\left(\frac{g\sigma\Delta\rho}{\rho_1^2}\right)^{0.25} \\
\overline{V_{2j}} &= V_{2j} + (C_0 - 1)j \\
j &= v_m + \alpha\frac{\rho_\ell - \rho_g}{\rho_m}\overline{V_{2j}}
\end{aligned} \tag{6.18}$$

***Void Fraction Relationship***

Below is the relationship for void fraction and quality in a drift flux model, which is necessary for determining the mixed parameters. From continuity, $\rho_m v_m$ = const. and could be replaced with $\dot{m}$.

$$\alpha = \frac{x}{\rho_g}\left[C_0\left(\frac{x}{\rho_g} + \frac{1-x}{\rho_\ell} + \frac{\overline{V}_{gj}}{\rho_m v_m}\right)\right]^{-1} \tag{6.19}$$

***Friction Correlations***

This model uses a standard Darcy friction factor for laminar flow and the Churchill correlation for turbulent flow shown in appendix C. The transition regime is approximated using a ratio of the turbulent and laminar friction factors as shown below, where $Re_L$ = 2100, $Re_T$ = 4000, and $f_k$ is the friction factor for laminar ($L$) and turbulent ($T$) flow.

$$\begin{aligned}
f_{tran} &= f_L^c f_T^{1-c} \\
c &= \frac{Re - Re_L}{Re_T - Re_L}
\end{aligned} \tag{6.20}$$

Two-phase flow requires a proper two-phase multiplier to adjust the friction factor. In the case of the RCCS, the Friedel multiplier was chosen due to applicability at low pressure and $\mu_g/\mu_\ell < 1000$ (Friedel (1979)).

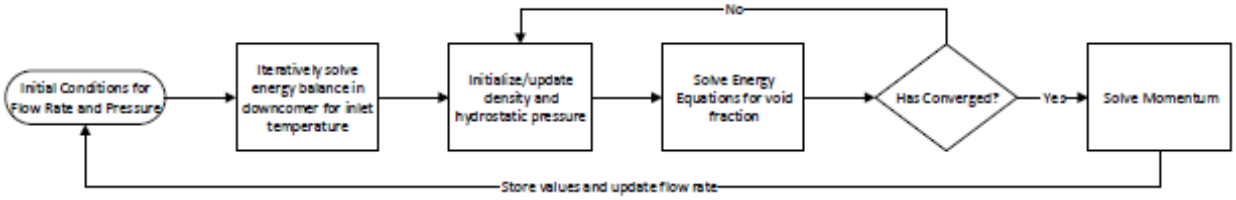


Figure 6.12: Solution methodology for steady-state characteristic pressure drop.

$$\Phi^2_{\ell o,Friedel} = E + \frac{3.24FH}{Fr^{0.0454}We^{0.035}}$$
$$E = (1-x)^2 + x^2\frac{\rho_l f_{vo}}{\rho_g f_{\ell o}}$$
$$F = x^{0.78}(1-x)^{0.224}$$
$$H = \left(\frac{\rho_l}{\rho_g}\right)^{0.91}\left(\frac{\mu_g}{\mu_l}\right)^{0.19}\left(1-\frac{\mu_g}{\mu_l}\right)^{0.7} \quad (6.21)$$
$$Fr = \frac{G_m^2}{gD_e\rho_{mc}^2}$$
$$We = \frac{G_m^2 D_e}{\sigma\rho_{mc}}$$
$$\rho_{mc} = \left(\frac{x}{\rho_g} + \frac{1-x}{\rho_l}\right)^{-1}$$

***Solution Methodology***

The solution was formed by solving the energy equation for quality and then the momentum equation for the system pressure drop as shown in Fig. 6.12. The energy and momentum equation are decoupled by neglecting all momentum terms with the exception of the body forces. This allows one to solve the energy equation and then apply the evaluated system parameters (void fraction, density, quality, and hydrostatic pressure) to the momentum equation.

The energy equation is simplified using the continuity equation, which states that $d(\rho_m v_m)/dz = 0$ and multiplying by the cross-sectional flow area. This results in an equation dependent $\dot{m}$. $q_{00}$, $V_{gj}$, $\rho_m$, and $\alpha$. $\rho_m$ and $V_{gj}$ are only functions of void fraction as defined previously with the constitutive relationships. $\dot{m}$ and $q_{00}$ are system inputs and defined by the experiment. Therefore, enthalpy is only a function of void fraction, for which a constitutive relationship has been previously defined. The constitutive relationship for void fraction is implicit and not directly dependent on enthalpy, however the energy equation can be converted to a mass quality equation using the definition of equilibrium quality (Eq. 6.22). This results in the energy equation show below in Eq. 6.23.

$$x_{eq}(z) = \frac{h_m(z) - h_\ell^{sat}(z)}{h_g^{sat}(z) - h_\ell^{sat}(z)} \quad (6.22)$$

$$x(z) = x_{in}(z) + \frac{P_W}{\dot{m}h_{\ell g}(z)}\int_0^x q''_W(z)dz - \frac{g}{h_{\ell g}}\left(z + \frac{A(\rho_\ell - \rho_g)}{\dot{m}}\int_0^z \alpha(z)\overline{V_{gj}(z)}dz\right) - \frac{A}{\dot{m}}\left\{\alpha\frac{\rho_\ell\rho_g}{\rho_m}\overline{V_{gj}}\right\}_z \quad (6.23)$$

The energy and void fraction constitutive relationship are solved iteratively, which yields the hydrostatic pressure, void fraction, and density profiles. These values are applied to the momentum equation and its constitutive relationships, yielding a solution for the pressure drop in the riser and chimney. This was performed over a range of mass flow rates and compared with the driving pressure drop calculated at those flow rates by solving the momentum equation in the downcomer. The point where these curves cross is the predicted system operating point under the applied boundary conditions and geometric inputs shown in table 6.2.

The problem's boundary conditions consist of an applied heat load, tank water level and tank gas pressure. The heat load can be applied directly to the energy equation and the tank water level affects the water properties in the loop. Gas pressure modifies the temperature of the tank and

therefore the inlet temperature to the risers. Many models set the inlet temperature directly and stability becomes a function of the subcooling number such as Ishii (1971) linear dynamic stability analysis. The RCCS inlet temperature is directly coupled to the loop parameters and needs to be calculated for each mass flow rate with a set tank gas pressure. The tank water surface temperature is assumed to be just below saturation. An energy balance over the downcomer is performed from the surface of the tank water to the inlet of the risers assuming the pipe surface temperature is approximately constant.

Table 6.2: Model boundary conditions and geometric inputs.

| Parameter | Value | Parameter | Value |
|---|---|---|---|
| *Boundary Conditions* | | | |
| Heat Load $Q$ | 11 kW | Tank Pressure $P_{gas}$ | 2000 Pa |
| Air Temperature $T_{inf}$ | 20 ˚C | Tank Water Level $L_{tank}$ | 0.36 m |
| *Geometric Properties* | | | |
| Inlet Loss $K_i$ | 1 - | Outlet Loss $K_o$ | 0.9 - |
| Length Downcommer $L_{dc}$ | 5.00 m | Hydraulic Diameter $D_i$ | 0.10 m |
| Heated Length $L_H$ | 3.12 m | Adiabatic Riser Length $L_{Hp}$ | 1.88 m |
| Adiabatic Chimney Length $L_{ch}$ | 0.68 m | Pipe Roughness | 20E-6 m |
| *Fluid Properties* | | | |
| Conductivity Water $k_w$ | 0.68 W m$^{-1}$ K$^{-1}$ | Conductivity Air $k_a$ | 0.026 W m$^{-1}$ K$^{-1}$ |
| Dyn. Viscousity Air $\mu_a$ | 184.6E-7 N s m$^{-2}$ | Heat Capacity Air $C_{p,a}$ | 1007 J kg$^{-1}$ K$^{-1}$ |
| Expansion Coef. Air $\beta_a$ | 2.5E-3 K$^{-1}$ | Specific Volume Air $v_a$ | 15.9E-6 m$_3$ kg$^{-}{}_1$ |
| Thermal Diffusivity Air $\alpha_a$ | 22.5E-6 m$_2$ s$^{-}{}_1$ | Heat Capacity Water $C_{p,w}$ | 4216 J kg$^{-1}$ K$^{-1}$ |

$$\frac{d(\Delta T)}{dz} = \frac{P_W}{\dot{m}C_p} h \Delta T \tag{6.24}$$

Where, $P_w$ is the wetted perimeter, $C_{p,w}$ is the heat capacity of water, and $h$ is the heat transfer coefficient. T is defined below with Ts being the external temperature and Tm being the fluid temperature.

$$\Delta T = T_s - T_m \tag{6.25}$$

Eq. 6.24 is solved for the temperature at the exit of the pipe, which is the inlet temperature to the risers

$$T_o = T_{inf} - (T_{inf} - T_{tank}) \exp\left(\frac{-1}{\dot{m}C_p UA}\right) \tag{6.26}$$

Where, $UA$ is the overall heat transfer coefficient, $T_{inf}$ is the air temperature, and $T_{tank}$ is the tank temperature. The overall heat transfer coefficient is defined below with convective heat transfer coefficients for air and water ($h_a$ and $h_w$) and their respective surface area for convection. $k_{ins}$ is

the conduction coefficient of the insulation on the outside of the piping with its corresponding length ($L_{dc}$) and inner and outer diameter ($D_i$ and $D_o$).

$$UA = \frac{1}{h_w A_{si}} + \frac{ln(D_o/D_i)}{2\pi k_{ins} L_{dc}} + \frac{1}{h_a A_{so}} \tag{6.27}$$

Convective heat transfer coefficients are determined using the Dettis Bolter correlation (Winterton (1998)) for water and the Churchill and Chu (1975) correlation for natural convection with air. The Churchill correlation is defined for external flow over a vertical plate, but can be applied to a cylinder when $D/L \geq 35/Gr_{1/4}$. This is condition is borderline acceptable in the RCCS downcomer.

$$h_{DB} = 0.023 Re^{4/5} Pr^{0.3} \frac{k_w}{L_{dc}} \tag{6.28}$$

$$h_{churchill} = \left( 0.825 + \frac{0.387 Ra_L^{1/6}}{\left(1 + \left(\frac{0.492}{Pr_a}\right)^{9/16}\right)^{8/27}} \right)^2 \tag{6.29}$$

Where the Rayleigh, Reynolds, and Prandtl number are defined below.

$$Ra_L = \frac{g\beta_a (T_s - T_{inf}) L_{dc}^3}{\nu_a \alpha_a} \tag{6.30}$$

$$Re = \frac{\rho v D}{\mu} \tag{6.31}$$

$$Pr = \frac{\mu C_p}{k} \tag{6.32}$$

The energy balance is solved iteratively with an initial guess for the pipe wall temperature, because the convection coefficient is dependent on the pipe surface temperature and mass flow rate. The downcommer outlet temperature and pipe surface temperature are evaluated at each iteration. The new surface temperature is applied to next iteration if the difference in surface temperature from the previous iteration does no meet an acceptable error criteria ( $T_{s,err} < 10^{-3}$). The evaluated channel inlet temperature is then used to determine the inlet enthalpy (hin(Tin, Pin)) that is required to solve the fluid energy equation.

### 6.2.2 Model Results

Modeling results exhibit stability for all possible mass flow rates (Fig. 6.13) according to Ledinegg's criterion. The channel operating curve has a positive slope at all points, while the driving curve due to pressure in the downcommer is always negative with an increasing mass flow rate. The system operating point occurs where the two curves cross. This occurs at a single point indicating that the system has one stable operating point and no possible Ledinegg instabilities. The mass flow rate is within 10% of the mean flow rate in the experimental facility. However, the experimental facility exhibits an oscillatory behavior between 55% to 65% tank volume, which is not explained by Ledinegg criterion. This indicates that an different instability is present.

Mapping the results from the steady state model to the Taitel and Dukler (1976) flow pattern map indicates that there is a possibility for a fundamental relaxation instability due to the operating trajectory intersecting with the boundary between stratified and bubbly/intermittent flow (Fig. 6.14). Traditionally fundamental relaxation instabilities are defined by a trip from bubbly or stratified flow to annular flow, whereas the current model shows a transition from stratified to bubbly/slug flow. The transition in flow regime causes a change in the system pressure drop and

an accompanying flow excursion. The accompanying pressure drop for this particular transition is small and generally neglected in forced flow, but the small overall pressure drop due to non-gravitational terms in NC flows can make this a significant contribution to the overall pressure drop curve. The present model is ignorant to flow regime changes and the accompanying pressure drop that comes with them. Addition of this phenomenon could result in the observation of multiple solutions on the pressure drop vs flow rate curve, but it is of the author's opinion that mapping the operational curve to the flow pattern map is sufficient. Nayak et al. (2003) used a flow pattern map with regime dependent void fraction and pressure drop correlations to predict transition instabilities. This method is highly dependent on the choice of void fraction models and did not have any experimental data to validate the model or presence of relaxation instabilities.

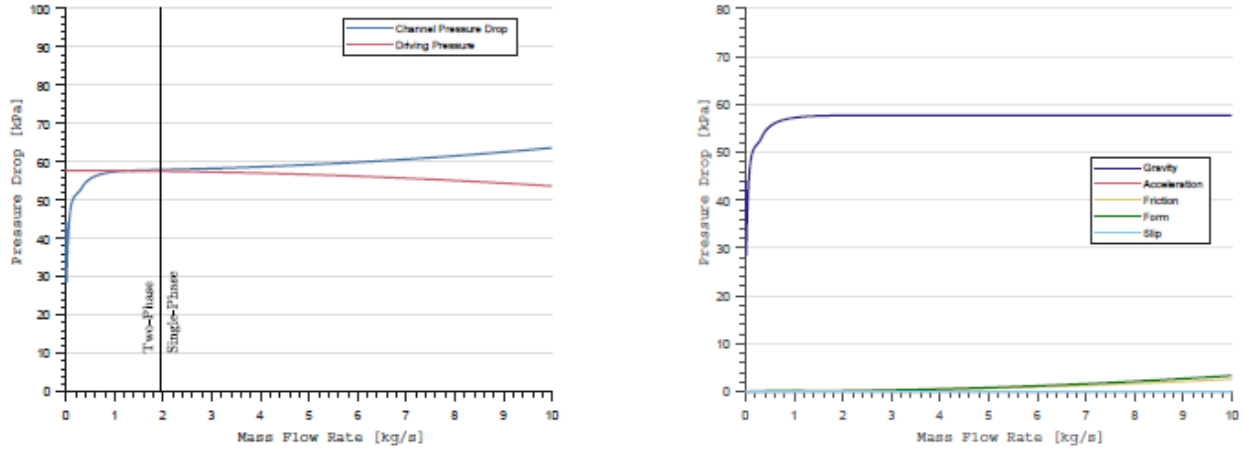


Figure 6.13: Steady state RCCS operational curve (left) and pressure components (right) showing stable operation at all possible operating points with the current operating point occurring at $\dot{m}$ = 1.23 kg $s^{-1}$. Overall pressure drop is dominated by gravity, although the downcommer gravity component is nearly equal to the channel gravitational component. ( $L_{water}$ = 0.36 m, $P_{gas}$ = 2000 Pa, $Q$ = 11 kW ).

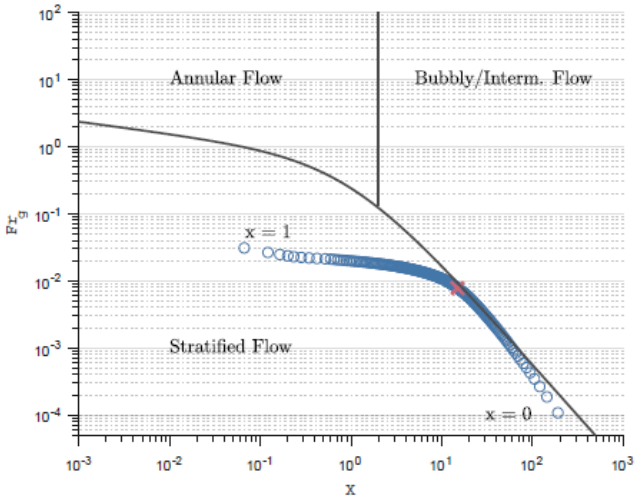


Figure 6.14: Steady state RCCS operational curve mapped to the Taitel and Dukler flow pattern map. Shows operation crossing the boundary between stratified and bubbly flow, where the red X represents the operating point ($\dot{m}$= 1.23 kg $s^{-1}$ ) at the specified conditions: $L_{water}$ = 0.36 m, $P_{gas}$ =

2000 Pa, and $Q$ = 11 kW. This particular flow pattern map is in a non-dimensional form using the Froude number ($F\ r_g$) and the Martinelli parameter (X).

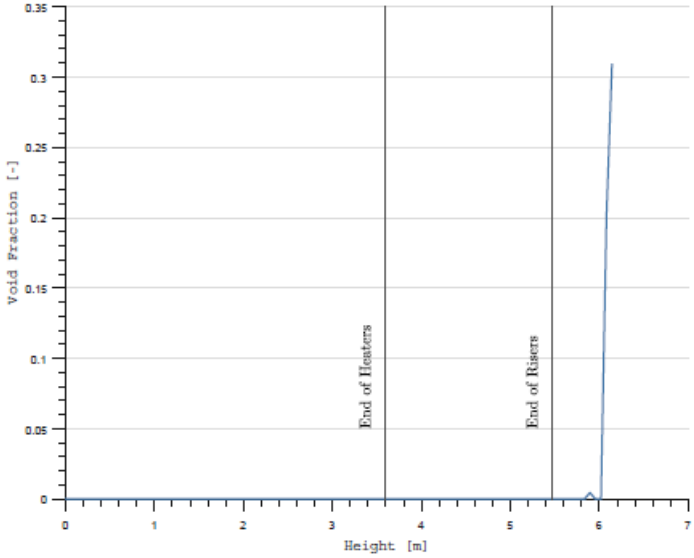


Figure 6.15: Predicted void fraction in the steady state model as a function of system height, with the end of the heated region and the end of the 0.05 m diameter risers marked with vertical lines. ( $L_{water}$ = 0.36 m, $P_{gas}$ = 2000 Pa, $Q$ = 11 kW ).

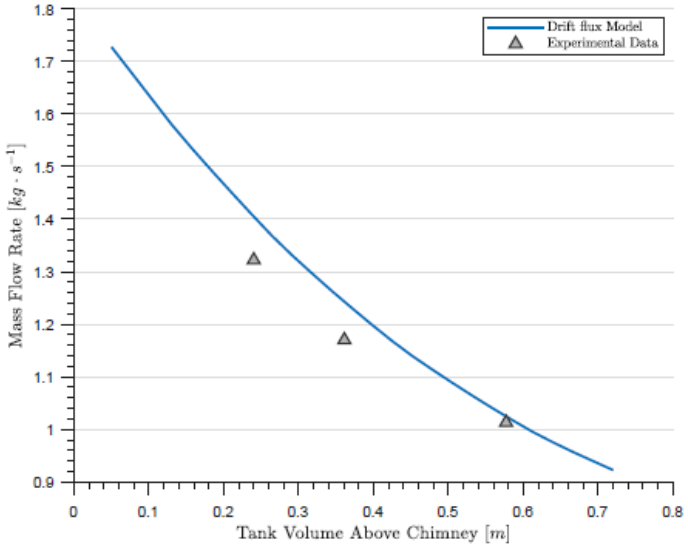


Figure 6.16: Flow rate vs. tank volume comparison between the steady state model and the experimental data. Error on mass flow rate is less than 0.2%.

System parameters including temperature rise and exit void fraction at the evaluated operating point ($\dot{m}$ = 1.23 kg $s^{-1}$) show good agreement with the experimental facility. The model qualitatively predicts that voiding begins in the chimney as seen in the experiment (Fig. 6.15). However, the exit void fraction is 32%, which is higher than the mean experimental results of approximately 20 to 25% and could contribute to the slight over estimation of th mass flow rate. The experimental value represents the time average over a single oscillation, which could be skewed depending on when the data was acquired during the drain transient. Data acquisition over

multiple oscillations is difficult due to the long oscillatory period and high frequency acquisition rate. Although, the data from the WMS do show that the flow is oscillating between stratified and bubbly/intermittent flow during the oscillatory period. Unfortunately the resolution of the WMS at the exit of the chimney is too large (6 mm) to distinguish between small individual bubbles, which would guarantee the transition between flow regimes. The temperature rise in the system is also under predicted by 22% with the model predicting 1.8 ◦C, whereas the experiment predicts 2.3 ± 0.7 ◦C. The oscillatory behavior of the system could also affect the measurement of the temperature rise due the phase shift between the inlet and outlet of the risers.

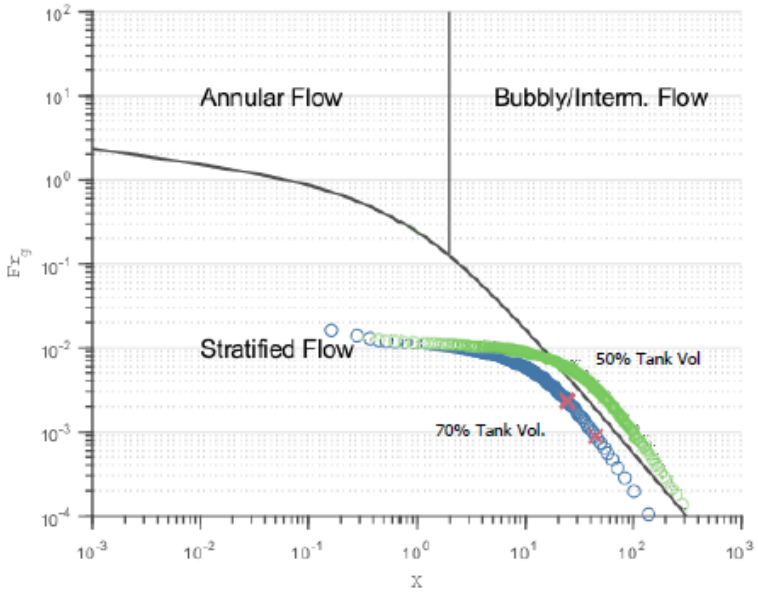


Figure 6.17: Operating curves for various tank volumes plotted on the flow patter map. Showing a possible transition from stratified to bubbly/intermittent flow. Red X indicate $1.25\,\mathrm{kg\,s^{-1}}$ at a higher $Fr_G$ and $1.68\,\mathrm{kg\,s^{-1}}$ a the lower $Fr_G$ value, these indicate the trajectory along the operating curve that accompanies an increase in flow rate.$K_{in} = 1$, $P_{gas} = 2000\,\mathrm{Pa}$, and $Q_{therm} = 11\,\mathrm{kW}$

***Parametric Results - Tank Volume***

Tank volume has been shown to be a dominate boundary condition on system wide flow stability. Experi-mentally it has been shown that there is an unstable region between 65% and 55% tank volume. Other tank volumes show stable operation with voiding restricted to the chimney region. Parametrically evaluating over a variety of tank volumes from 40% to 80% shows that there is an increase in the flow rate with a decrease in tank volume which is corroborated in the experimental data (Fig. 6.16).

As before, these operating points can be plotted along the Taitel and Dukler (1976) flow pattern map to predict the operating trajectory of the RCCS. As the tank volume increases, the system operating curve moves toward the left of the flow map and as the tank volume decreases it moves to the right (Fig. 6.17). The evaluated operating points generated from the system operating curves during a tank drain transient are then represented in Fig. 6.18.

The analysis shows the system crossing the boundary between stratified and bubbly/intermittent flow. This transition will cause a sudden change in the system pressure drop, resulting in a flow excursion. An increase in the flow rate in turn causes a delayed decrease in the channel outlet temperature. This reduction in system enthalpy results in decreased voiding and a shift to a lower mass flow rate back to the stratified flow regime. The process then repeats causing flow oscillations

described in detail in the previous chapter to continue until the system migrates completely into the bubbly/intermittent flow regime.

***Parametric Results - Inlet Orificing***

Inlet orificing has been shown experimentally to remove the oscillatory flow present in the unorificed case, however additional transient instabilities are present as the system reaches saturation and begins to flash. Modeling the effect of inlet orificing and applying it to the Taitel and Dukler (1976) flow map shows that the operating point migrates away from the flow transition boundary (Fig. 6.19). The is due to a decrease in the overall system mass flow rate. The model indicates that no flow transition exists in the system with increased inlet orificing as well as a more narrow operating regime, therefore increasing system operating stability. However, transient oscillations present upon reaching saturation when the system is orificed are not described by the steady-state model. This indicates that they must be dynamic instabilities and it is necessary to perform a linear or non-linear stability analysis to determine the operational range and/or type of the instabilities.

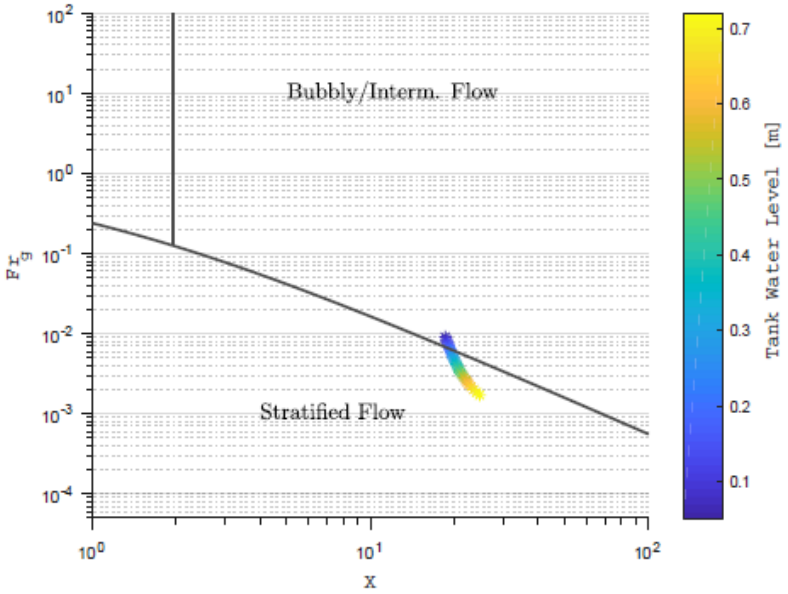


Figure 6.18: Operating point map during a tank drain transient (e.g. normal two-phase operation). Shows operation crossing from stratified flow to bubbly/intermittent flow.$K_{in}$ = 1, $P_{gas}$ = 2000 Pa, and $Q_{therm}$ = 11 kW

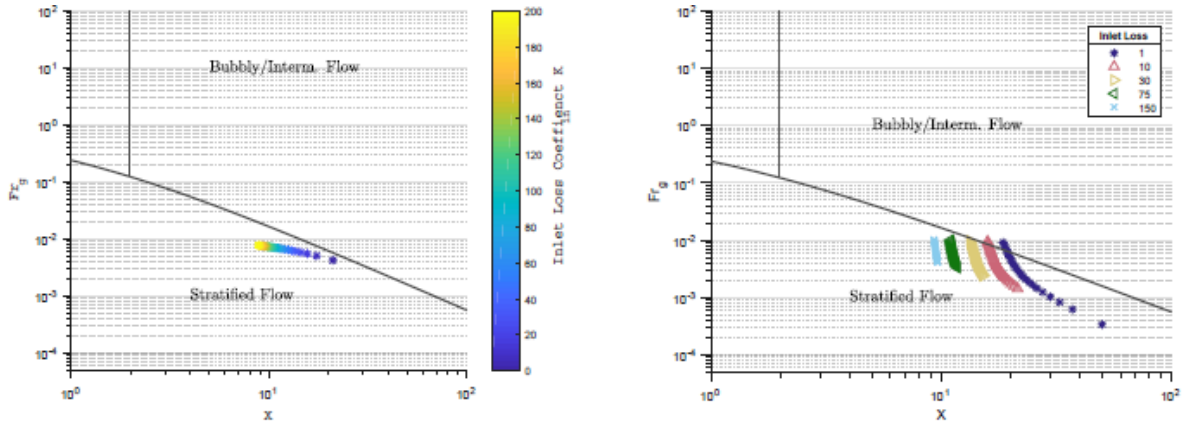


Figure 6.19: Operating trajectory due to changes in inlet loss coefficient. Showing the operating trajectory moving away from the boundary between stratified and bubbly/intermittent flow on the left at the following boundary conditions:$L_{tank}$ = 0.36 m, $P_{gas}$ = 2000 Pa, and $Q_{therm}$ = 11 kW The right plot depicts the systems entire operating curve as the tank drains from 1 m to 0.05 m above the chimney exit for specified inlet loss coefficients.

### *Parametric Results - Pressure Effects*

Increased pressure has been show experimentally to dampen the oscillatory behavior present in the RCCS, but the oscillations are still present in every pressurized test case. It is a simple matter to modify the boundary conditions of the model for several different gas space pressures. The model was varied from the standard unrestricted pressure case (approximately 2 kPa above atmosphere) to twice the highest pressure case (32 kPa gage pressure). This results in the operating curve reducing in length, but still traversing the boundary between stratified and intermittent flow (Fig. 6.20).

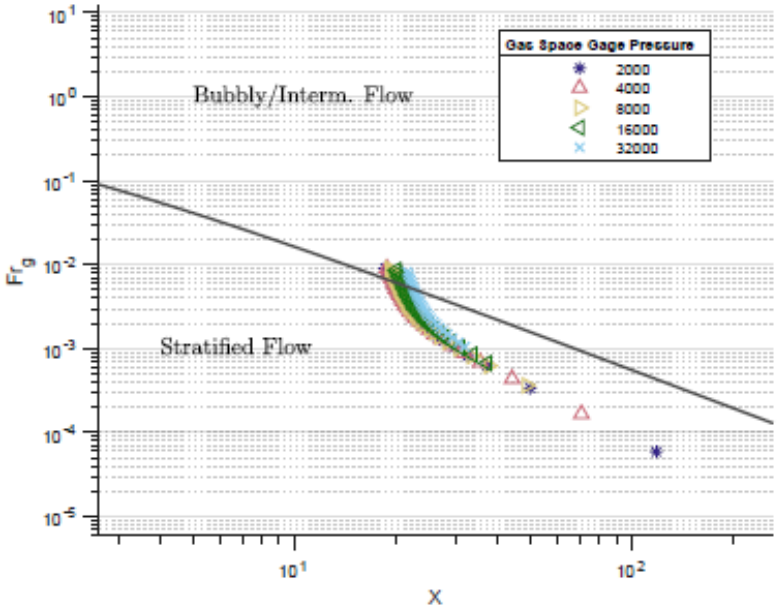


Figure 6.20: Model results for several different gas space gage pressures varying from the unrestricted outlet case to twice the pressure of the highest outlet restriction.

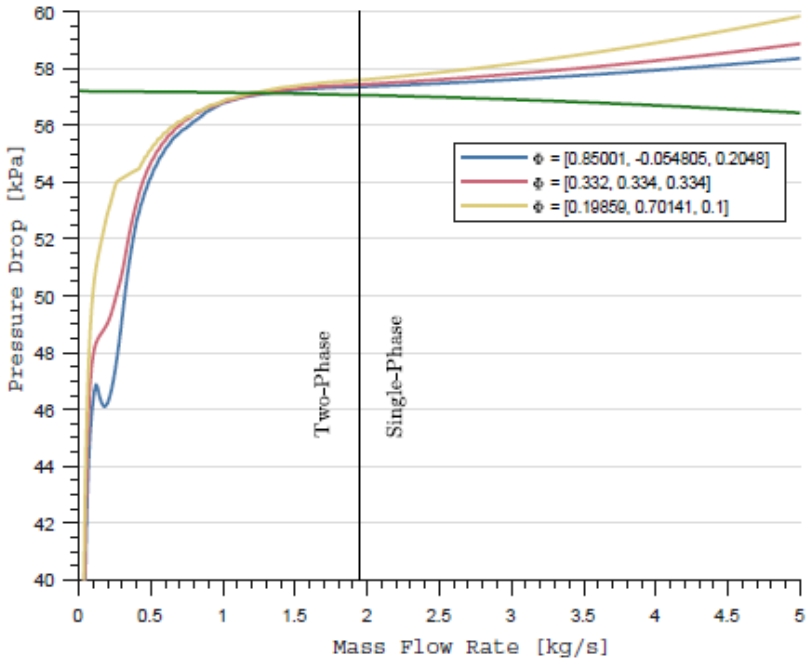


Figure 6.21: Parallel channel steady state modeling, showing limited channel deviation at the RCCS operating point and large deviations with potential instability at low flow rates. Each curve listed represents a separate operating case with flow branching fractions represented by Φ. $L_{tank}$ = 0.36 m, $P_{gas}$ = 2000 Pa, and $Q_{therm}$ = 11 kW.

### *Parallel Channel Effects*

Steady-state modeling can be extended to model the parallel channels that exist in the RCCS. Parallel channels can results in multiple steady-state operating modes due to flow difference in the risers. Modeling these requires solving a system of momentum and energy equations for each riser with the addition of Eq. 6.33 and substituting $\dot{m}_r = \Phi_r \dot{m}_{tot}$. $\Phi_r$ represents the branching fraction of flow into each riser, which is solved along with the momentum equations. These equations are then solved for Φ and *P* using a Newton-Raphson method.

$$\Delta P_1(\Phi_1 \dot{m}) = \Delta P_2(\Phi_2 \dot{m}) = \Delta P_3(\Phi_3 \dot{m})$$
$$\Phi_1 + \Phi_2 + \Phi_3 = 1 \qquad (6.33)$$

Predicted voiding at the RCCS normal operating point is restricted to the chimney, which results in limited effects on the flow with different branching fraction. The model predicts three different mass flow rate branching fractions (Φ) that result in steady state operation: all risers equal, procession of flow rates (i.e. small, medium, and large), and flow reversal in one riser with uneven flow in the other two (i.e. low flow riser and high flow riser) represent by a Φ less than zero. Each case results in very similar flow rates at the RCCS operating point with slight deviations due to overall system enthalpy changes that result in slight voiding changes (Fig. 6.21). The majority of deviation in flow rate occurs when voiding initiates in the riser channels as noted by the divergence of the characteristic curves at lower mass flow rates ($\dot{m}$ < 0.75). Operating in this regime can also result in Ledinegg instabilities as noted by the negative sloped curve, which also happens to correspond to a potential operating condition with flow reversal. It is also could also be possible

for the system to switch between operating curves in this low flow regime with the presence of a dynamic instability.

***Scaled Comparisons and Predictions***

Argonne National Laboratories is currently undergoing a transition from a 1/2 scale air-based to water-based RCCS test facility with the ultimate goal of validating scaling laws and expanding the testing capability of the RCCS experiments between universities and US national laboratories. This drift flux model has been shown to work well on the UW-RCCS test facility and it can be used for prediction of performance and stability in ANL test facility.

Physical dimensions of the National Shutdown heat removal Test Facility (NSTF) have been applied to the model for direct comparison with the UW facility. The exact dimensions are currently unavailable for public release, but have been shared with RCCS collaborators (Lisowski et al. (2015)). The 1/2 scale facility has some differences that can affect performance and scale validation between it and the UW 1/4 scale facility. The chimney in the NSTF facility is 13.5% longer than the heated core, where as the UW facility's chimney is 20% shorter than the heated core. The ANL facility also has 8 risers with a shorter pitch and smaller inner pipe diameter. The ratio of total flow area between the risers and chimney is still approximately unity. The model assumes heat is directly input into the fluid, so changes in the heat transfer surface do not affect the mode. However, changes in the azimuthal dimensions will cause changes in friction and therefore potential modifications to stability.

Tank volume has been shown to be a strong contributor to changes in performance and this does not change with scale. The mass flow rate in the system is expected to scale with $\sqrt{\ell_R}$ but that prediction fails when compared to the UW facility (Fig. 6.22). The flow rate of the NSTF is approximately 1.5 kg $s^{-1}$ faster than the UW facility at all tank volumes, whereas the expected scaled mass flow rate is 0.4 kg $s^{-1}$ to 0.7 kg $s^{-1}$ faster than the UW facility. The variation is likely due to changes in azimuthal dimensions and chimney head height.

The model also predicted the true 1/2 scale flow rate by doubling the vertical dimensions in the UW-RCCS. The predicted values are lower than the ANL facility and those predicted by the scaling law. However, at large tank volumes the prediction via the 1/2 scale model and the scaling law begin to converge. Clearly, this shows that there is some distortion between the scaled facilities, although this does not necessarily mean that qualitative flow features are not captured. The distortion between the scaling law and the 1/2 model prediction is likely due to lack of adherence to the scaling laws. The friction number $(\sum(fL/D+K)_R)$ between the facilities is not the same and will have a significant effect on the flow rate. It requires properly placed orifices in both the single- and two-phase regimes to account for the frictional pipe loss present in the larger system. This will cause a reduction in the UW facility flow rate and therefore a reduction in the scaling law values especially at larger flow rates. This would close the gap between the model and the prediction. The ANL facility has too many dimensional changes to properly quantitatively validate against the UW facility, but there is still potential to qualitative compare the observed instabilities their mechanisms.

The model allows for prediction of stability due to fundamental relaxation instabilities. The UW facility, as shown previously, crosses the boundary between stratified and intermittent flow, which causes low frequency oscillations. The true 1/2 scale facility depicts very similar behavior and essentially operates on the same operating trajectory. The NSTF models a slightly different behavior (Fig. 6.23). The operating trajectory runs parallel to the boundary between stratified and

bubbly/intermittent flow, improper selection of an inlet orifice can move the curve to coincide with boundary. This will potentially cause perpetual instability in the system. The operating trajectory is also migrating up and to the left toward the annular flow regime with increases in scale. A flow regime transition to annular flow will cause a much larger change in the system pressure drop and potentially very different operation of the RCCS. The full scale system should evaluated for flow regime changes to ensure the system operates in a single flow regime, especially when operating near the annular/bubbly/stratified transition.

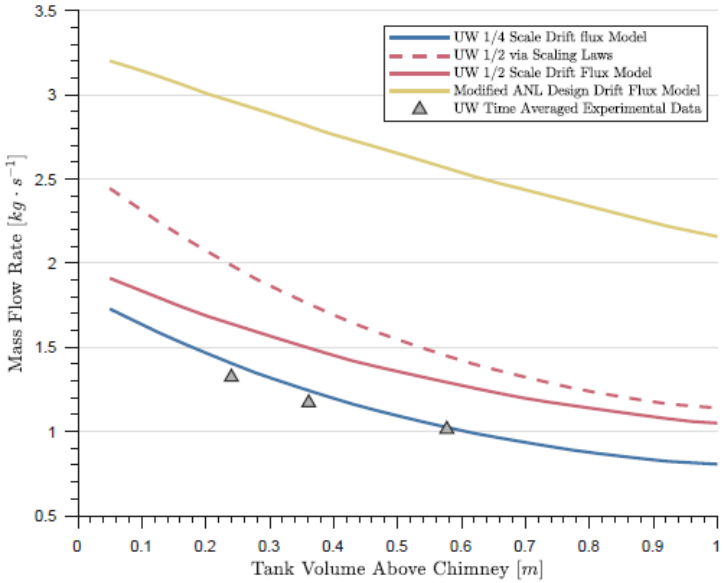


Figure 6.22: Comparison of mass flow rate as a function of tank volume for 1/2 scale NSTF and 1/4 scale UW RCCS facility

Static stability observed through these models do not guarantee a stable system; dynamic instabilities need to be modeled using either linear or non-linear control theory. It is possible to have sustained DWO's and other instabilities if operating under the right conditions. The RCCS is unique in that it always operates under a slow tank drain transient that can potentially move the system into and out of stable operating regimes.

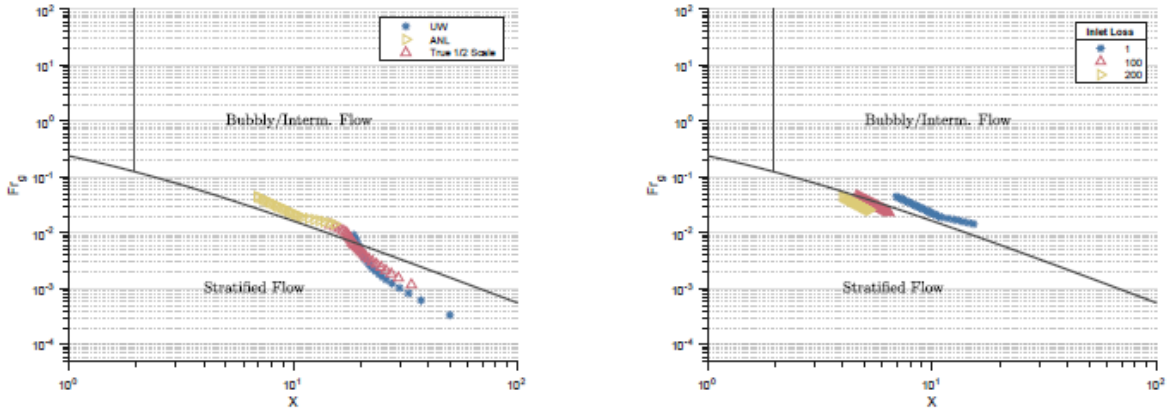


Figure 6.23: Comparison of operating regimes as a function of tank volume for 1/2 scale NSTF and 1/4 scale UW RCCS facility and the true 1/2 scale based on UW dimensions (left) as well as the effect of the inlet loss coefficient on the operating trajectory (right).

## 6.3 Ishii Density Wave Oscillation Stability

In an attempt to find closure and completeness on the study of the observed instabilities, the Ishii's stability map was applied to the RCCS geometry in order to determine initial limits of DWO instability. Ishii (1971) determined stability for BWR's by applying linear perturbation theory to the drift flux model (DFM), which is described in appendix C. Ishii chose the following set of boundary and initial conditions on density ($\rho$), pressure ($p_s$), enthalpy ($h$), and velocity ($v_{fi}$) in order to solve the DFM. Most parameters are defined with the system pressure ($P_s$) at the inlet to the heated section ($z = 0$) or at the boiling boundary ($z = \lambda(t)$).

$$\begin{aligned}
\rho_f &= \rho_f(p_s) && at \quad z = 0 \quad t \geq 0 \\
p &= p_s = const. && at \quad z = 0 \quad t \geq 0 \\
h_f &= h_1 = const. && at \quad z = 0 \quad t \geq 0 \\
v_f &= \overline{v}_{fi} + \epsilon e^{st} && at \quad z = 0 \quad t \geq 0 \\
h_f &= h_s(p_s) && at \quad z = \lambda(t)
\end{aligned} \tag{6.34}$$

Furthermore, several assumptions were made in order to simplify the solution.

1. Voiding begins in the heated core
2. Constant heat flux
3. Constant frictional loss
4. Downstream unheated region is neglected except for exit throttling ($K_e$)

These assumptions results in a characteristic system equation that is a function of multiple non-dimensional groups defined below. The most important parameters of the non-dimensional groups are the phase change number ($N_{pch}$) and subcooling number ($N_{sub}$). These parameters essentially represent the applied power and inlet temperature for the system respectively. From an engineering standpoint, a parametric study on the characteristic equation over all possible power and inlet temperature conditions would provide a stability map showing where the system can operate safely. The other non-dimensional groups represent boundary conditions and/or geometry, and are functions of the thermodynamic quantities or the inlet velocity. The final parameter $s$ is a complex number defined as $s = \alpha + i\omega$, which arises from the perturbation to the inlet velocity.

The solution to the characteristic equation can be formed using the D-partition method, which assumes $\alpha = 0$ thereby replacing $s$ with $i\omega$. The characteristic equation is then solved for all complex roots (Porter (1968)). The DFM results in infinitely many complex roots for a given $N_{pch}$ and $N_{sub}$. When both the real and imaginary components are zero the solution is said to be neutrally stable. The real component determines whether the system is damped and the imaginary component determines if an oscillatory solution is present, which is obvious if the root is applied to the velocity condition in Eq. 6.34.

Table 6.3: Similarity groups for Ishii stability.

| Non-dimensional group | Symbol | Definition |
|---|---|---|
| Froude Number | $N_{Fr}$ | $\frac{\overline{v}_{fi}^2}{g\ell_h}$ |
| Reynolds Number | $Re$ | $\frac{\rho_f \overline{v}_{fi} D}{\mu_f}$ |
| Subcooling Number | $N_{sub}$ | $\frac{h_f - h_{in}}{h_{fg}} \frac{\Delta\rho}{\rho_g}$ |
| Phase Change Number | $N_{pch}$ | $\frac{\dot{Q}}{\dot{m} h_{fg}} \frac{\Delta\rho}{\rho_g} = \frac{h_{out,h} - h_{in}}{h_{fg}} \frac{\Delta\rho}{\rho_g}$ |
| Drift Number | $N_d$ | $\frac{V_{gj}}{\overline{v}_{fi}}$ |
| Density Number | $N_\rho$ | $\frac{\rho_g}{\rho_f}$ |
| Geometric Similarity | $D^*, \ell_e^*, K_e, K_i, f$ | $\Phi^* = \frac{\Phi}{\ell_h}$ or non-dimensional constant |

### 6.3.1 Validity of Ishii's method for the RCCS

Two notable assumptions can cause an issue with the application of Ishii's stability map to the RCCS facility. Firstly, Ishii assumes that voiding begins in the heated section. Based on experimental data this is not valid for the RCCS. WMS show that the system tends toward voiding in the adiabatic chimney. The only time voiding occurs in the risers is during transient instabilities when the system is orificed, but this does not necessarily mean that voiding occurs in the heated section. Secondly, Ishii's general solution ignores the adiabatic chimney except for the the exit throttling coefficient. From an engineering standpoint, Ishii expects that this will not necessarily change the bounds of the unstable region, but the rate of growth/decay of the instabilities may be affected.

Based on Ishii's assumptions the model could potentially be used to determine instability under orificed conditions, which are when DWO instabilities are present in the RCCS. The solution is not valid for the RCCS when voiding occurs in the chimney exit. Ishii also developed the solution for BWR's in which the inlet velocity is controlled. In natural circulation the flow rate is highly dependent on void fraction in the system, therefore the onset of voiding whether stable or not changes the system operating point. This in turn causes the stability map to change, so it is necessary to plot multiple versions of the map in order to determine stability as the system approaches saturation.

### 6.3.2 Ishii stability in RCCS applications

The model developed by Ishii was solved using properties from the RCCS when orificed to 1/8 total flow area in all risers. The selected velocities come from experimental data and are varied from the single-phase flow rate to the stable two-phase flow rate. These values are presented in table 6.4.

Ishii performed several parametric studies on his model for typical BWR conditions. Based on Ishii's parametric studies, increases in the Reynolds number cause a small increase in the size of the unstable region. However, including the effects of the drift flux number (ie $V_{gj}$ 6= 0) compete against the Reynolds number causing the overall size of the unstable region to decrease with an increasing drift flux number. Ishii also showed that increased friction causes an increase in the size of the unstable zone. This effect competes with the increased flow rate, due to friction being inversely proportional to flow rate except in the transition region. Inlet and outlet throttling were

shown to have opposite effects on stability: increases in inlet throttling decrease the unstable region, while increases in exit throttling increase the size of the unstable region.

Table 6.4: Ishii stability input parameters.

| Non-dimensional groups | $\overline{v}_{fi} = 0.039$ | $\overline{v}_{fi} = 0.053$ | $\overline{v}_{fi} = 0.073$ | $\overline{v}_{fi} = 0.093$ |
|---|---|---|---|---|
| Froude Number | $4.25 \times 10^{-5}$ | $7.85 \times 10^{-5}$ | $1.37 \times 10^{-4}$ | $2.42 \times 10^{-4}$ |
| Reynolds Number | $1.36 \times 10^{4}$ | $1.85 \times 10^{4}$ | $2.45 \times 10^{4}$ | $3.25 \times 10^{4}$ |
| Drift Number | 11.65 | 8.57 | 6.49 | 4.89 |
| Density Number | $6.52 \times 10^{-4}$ | $6.52 \times 10^{-4}$ | $6.52 \times 10^{-4}$ | $6.52 \times 10^{-4}$ |
| $D^*$ | 0.0274 | 0.0274 | 0.0274 | 0.0274 |
| $K_e$ | 1.17 | 1.17 | 1.17 | 1.17 |
| $K_i$ | 146 | 146 | 146 | 146 |

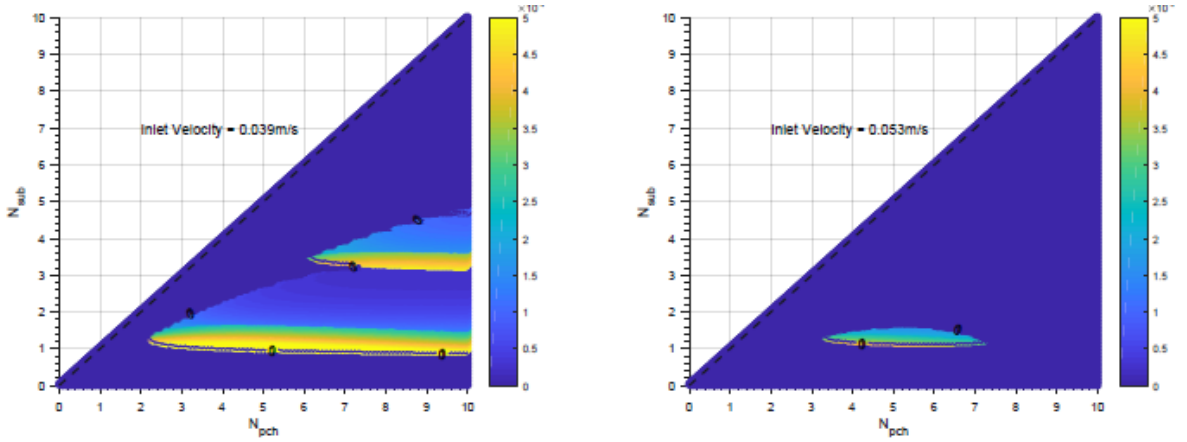


(a) $\overline{v} = 0.035$ (b) $\overline{v} = 0.053$

Figure 6.24: Ishii stability map for the RCCS with zero drift velocity. Input parameters are listed in tbl. 6.4. Colors represent the real part of the complex solutions, so negative values are stable and positive values are unstable. $\overline{v}_{fi} = 0.7$ and $\overline{v} = 0.93$ are not shown because all eigenvalues in the domain of interest have negative real components.

The results for cases with and without the drift flux number are shown below in Fig. 6.24 and 6.25 respectively. Both show the presence of an unstable regime that shrinks as the flow rate in the system increase. This is much more prominent in the RCCS than in the parametric studies performed by Ishii. Ishii tested BWR conditions, so the pressure was significantly higher than in the RCCS. This indirectly affects the stability curves by lowering the liquid densities and increasing the steam densities, thereby the decreasing the Reynolds number and increasing the Drift and Density numbers for a given inlet velocity. This caused the Froude number in Ishii's cases to be 2 orders of magnitude larger, even though the Reynolds numbers were approximately the same.

The operating zone for the RCCS has been shown in sec 5.5. The orificed test cases enter the two-phase region around a subcooling and phase change number of 13. With the introduction of voiding, the system quickly migrates along the $x = 0$ line to subcooling and phase change numbers of approximately 6-9. During this time, the flow velocity is also changing due to the production of void which causes a corresponding increase in the buoyancy force. According to the model without

including drift flux effects the system will immediately enter an unstable when it crosses the $x = 0$ line. This causes a density wave instability to occur, the flow rate increases and the unstable zone shrinks. The increased flow rate causes a decrease in the systems enthalpy rise and a halt to voiding. The system then oscillates across the $x = 0$ boundary until the mean flow rate is high enough to operate in an instability free zone. The model that includes drift flux effects predicts that no inabilities occur in the region of operation, but this is clearly not the case given the experimental data. This could be due to the underlying assumptions in the stability model which states that the drift velocity is constant. At the onset of voiding $V_{gj}$ is expected to be approximately zero, because the bubbles will be small and should have a velocity equal to the liquid velocity. As the bubble size increases the buoyancy of the bubble becomes a significant contribution to its velocity and hence the drift velocity will increase and begin to take effect on the system stability.

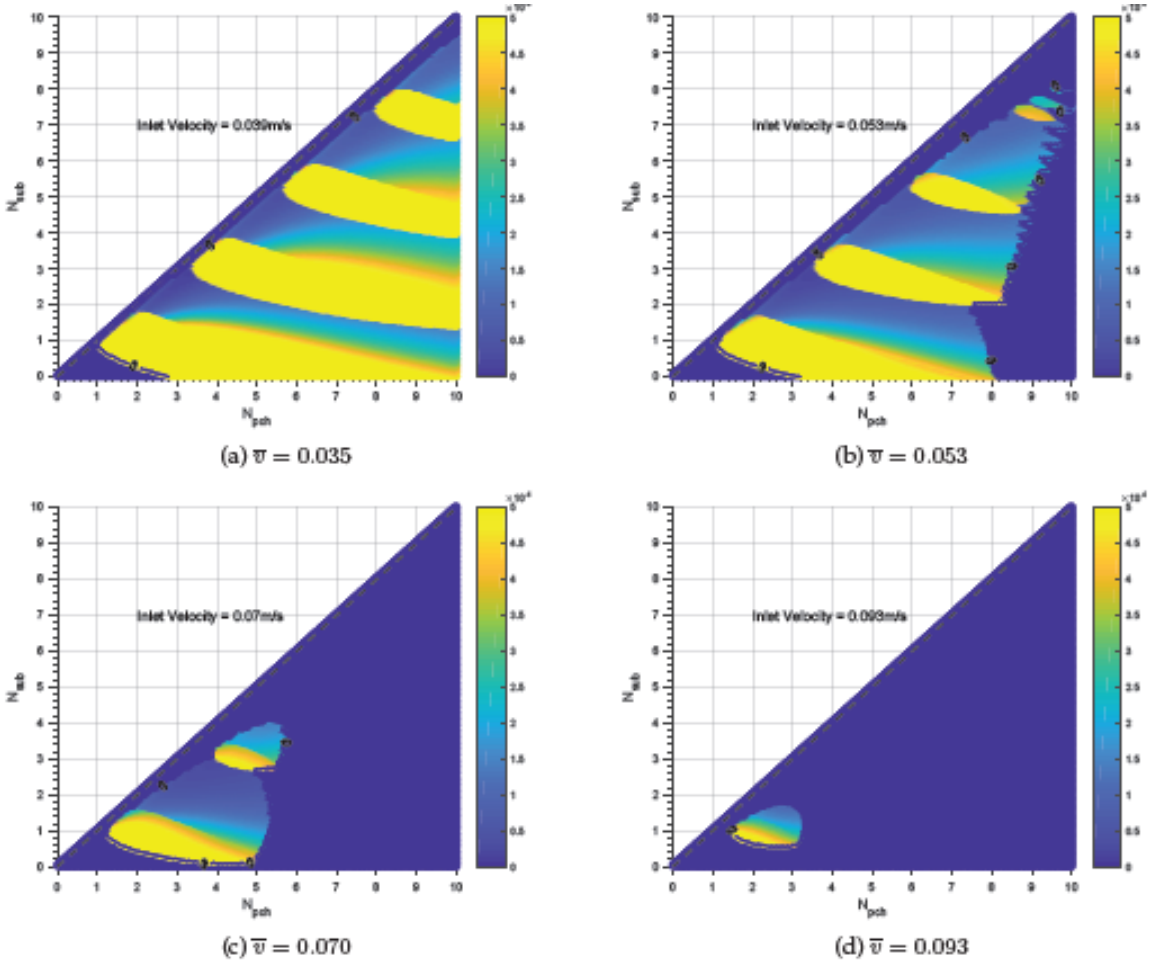


(a) $\overline{v} = 0.035$ (b) $\overline{v} = 0.053$

(c) $\overline{v} = 0.070$ (d) $\overline{v} = 0.093$

Figure 6.25: Ishii stability map for the RCCS with drift velocity calculated using the GE-Ramp model. Input parameters are listed in tbl. 6.4. Colors represent the real part of the complex solutions, so negative values are stable and positive values are unstable.

If we choose to apply the model to cases without voiding in the risers (e.g. unorificed flow), the stability map predicts unstable flow for almost all operating points. Unorificed flow operates at a higher velocity, but the absence of a large inlet loss coefficient increases the size of the unstable zone. The application of the model in these cases is not accurate, but does give a starting point until a proper model is formed. Further work needs to be done on this type of model for RCCS

type facilities in order to get an accurate stability map. The development of such a model is beyond the scope of this project.

### 6.3.3 Summary

Ishii's linear stability model based on the DFM allows for prediction of density wave oscillations in the RCCS for a narrow operating range. The model assume that voiding begins in the heated section of the system and neglects adiabatic flashing, therefore the model cannot predict instabilities when those parameters are met. The RCCS generally operates with adiabatic flashing that is not applicable to Ishii's model, but when orifices are installed the system does exhibit flashing closer to the heated core. In these cases, Ishii's model predicts that the system will exhibit density wave oscillations as soon as any void is produces at low flow rates. Experimentally, DWO are observed for a short period until the system's tank temperatures reach a steady-state, which result in the system operating at a steady state as indicated by the drift flux model. The DWOs predicted by Ishii's model are present, but the applicability of the model is questionable and not reliable. It is therefore suggested that a more sophisticated model be employed to analyze density waves oscillations in the RCCS facility.

# 7 PART I – CONCLUSIONS

Within the project 42 natural circulation tests were performed in the UW-WRCCS facility for studying and analyzing the stability and performance of the RCCS in order to make design recommendations for the full scale facility. Testing included repeatability tests after reconstruction of the heated enclosure, scoping tests for wire mesh sensor operation, pressurization tests, and orifice testing. The final goal from an engineering perspective was to evaluate the RCCS performance and derive recommendations for building a stable natural circulation cooling facility. Advanced instrumentation allowed for a deeper understanding of the mechanisms involved in the stability of the RCCS to further the validity of the design recommendations.

## 7.1 Overview of Results

The WRCCS facility underwent multiple parametric studies that resulted in a detailed empirical data set from which to analyze the system performance. This resulted in the development of a phenomenological model that helped to asses the system stability and determine the root cause behind the oscillatory behavior that occurs under normal two-phase operation.

### 7.1.1 Empirical Results

Testing under various perturbations to the RCCS facility resulted in changes in the stability of the integral system. Baseline system conditions consisted of atmospheric gas space pressure, 80% to 60% tank volume, 15.2 kW applied heat load, and no frictional perturbations in the system. This test case results in stable flashing until approximately 65% tank volume upon which a slow oscillatory behavior on the order of 2 min periods began to occur. Eventually the oscillations die away and result in stable flashing. Wire mesh sensors (WMS) were used to show that flashing only appeared at the end of the chimney, just before entering the tank. During the peak of the oscillations, the void fraction was observed to oscillate rapidly between stratified flow and intermittent voiding. Flashing during the trough of oscillations remained in a stable stratified regime. During stable flashing before and after the oscillatory regime stratified flow was observed.

However, the low resolution of WMS in the chimney (6 mm pitch) make it unclear whether the flow was purely stratified or stratified bubbly due to gravitational effects.

Tank volume was the first major effect observed to have influence on the stability of the RCCS. It was shown that tank volume influenced the presence of hydrostatic head fluctuations (Lisowski (2013)). It was further discovered that the RCCS operates under a slow transient during the entirety of its operation due to the evaporation of inventory in the tank, which then consequently changes the boundary pressure on the flow loop. This results in the constantly changing flow rate and therefore operating point.

Natural pressurization investigations lead to the discovery of a stabilization effect on system performance. Increasing the outlet loss coefficient between the water tank and the steam condenser causes a natural pressurization of the tank gas space. Increasing the gas space pressure lead to a reduction in the duration and magnitude of the flow oscillations and therefore a reduction in thermal oscillations in the RCCS structure. The pressure was parametrically varied between 5% and 15% above atmospheric pressure with a greater pressure resulting in greater stability. Greater pressures did not effect the integral mass flow rate, meaning that operating regimes were not varied, but they did result in an increase in system wide temperature. During a loss of pressure transient, flow excursions were observed, but the magnitude of the excursion was no greater than the oscillatory magnitude of the baseline tests.

Influence of inlet loss coefficients resulted in complete system stability and instability depending on the applied loss coefficient. It was observed at high inlet losses that the system was completely stable at all tank volumes. However, upon reaching saturation in the risers the system exhibits transient density wave oscillations until the tank temperature reaches a steady-state value just below saturation. Under some inlet losses the system was observed to be entirely unstable at all tank volumes. These oscillations were observed to be the more severe than the base case due to a higher magnitude and frequency and were a result of overlapping DWO and relaxation instabilities. Finally, the presence of one or more bypass risers resulted in completely unstable oscillations. These were the most severe with the highest magnitude and frequency of any other test throughout all of the RCCS testing campaigns.

### 7.1.2 Phenomenological Results

Steady-state drift flux modeling was used to analyze the mechanisms behind the instabilities present in the RCCS facility in order to help predict their occurrence and to develop a completely stable facility. Steady-state modeling is a commonly used to predict the performance of a facility and to avoid the occurrence of Ledinegg instabilities. Under natural circulation conditions the presence of these static instabilities can become the initiating event for dynamic instabilities. The phenomenological model was shown to accurately predict the experimentally time averaged mass flow rates at various tank volumes.

Static stability as predicted by this type of model is represented in the traditional sense by the presence of a negative $\partial P/\partial \dot{m}$. This behavior was not observed in the single-channel model. However, the parallel channel model did exhibit this behavior when voiding occurs in the risers, but the driving force when at saturation does not predict operation near this point. The model is ignorant to changes in the flow regime, and translating the operating curve for each possible tank volume under certain boundary conditions onto Taitel and Dukler's analytical flow pattern map results in the observation of a transition between stratified and bubbly/intermittent flow at certain tank volumes. A change in flow regime is accompanied with a small change in the frictional

pressure drop. The RCCS operates at a low quality mass fraction and an extraordinarily low frictional pressure drop compared to the gravitational pressure drop, so the small frictional pressure drop imparted by a change in flow regime can cause a relatively large change in the void fraction. This results in a large change in the gravitational pressure drop and therefore a corresponding change to the flow rate, which results in a shorter fluid residence time in the heated core. The exit fluid temperature drops, which results in lower voiding and therefore a lower mass flow rate. This causes the system to revert back to the stratified flow regime and resumes a reheat period. This behavior repeats until the system is able to transition fully into the bubbly/intermittent flow regime. When the transition is complete integral stability is observed experimentally. To this author's knowledge, the dynamic oscillations observed in the RCCS facility and similar natural circulation facilities have not been attributed to a flow transition instability in the literature.

Inlet orificing has an influence on the location of the system's operating curve in the Taitel and Dukler flow pattern map and the operating point on the $\dot{m}$ vs P curve. Increases in the inlet loss coefficient results in the migration of the operating point curve during a tank drain toward the stratified flow regime on the flow pattern map (Fig. 7.1). As the inlet loss coefficient increases, the size of the curve also decreases meaning that the system's operating point changes more slowly than under normal conditions. For improper selection of the orificing coefficient, the duration of the transition instabilities will be extended resulting in unstable behavior over a greater range of tank volumes. Whereas at larger inlet loss coefficients the operating curve remains entirely in the stratified flow regime and one would expect to have completely stable behavior. Inlet orificing to 1/8 total flow area results in stable flow at all tank volumes when the system reaches steady-state (i.e. the tank temperature stabilizes just below saturation) as expected via the model results.

Transient oscillations observed experimentally in the RCCS upon reaching saturation in the risers when orifices are installed are not captured by the steady-state model. These oscillations have been determined to be density wave oscillations with a parallel channel interaction component and therefore require a dynamic transient model to predict them. MELCOR was used as a predictive tool when performing inlet orificing tests and was able to capture the DWO that occurred upon reaching saturation in the risers. It is expected that a complete non-linear or linear stability analysis will be able to predict the occurrence of DWO in the RCCS an may be able provide a method for limiting their occurrence or magnitude when orifices are installed in the RCCS. Ishii (1971) linear stability model was applied to the RCCS and showed that there is an unstable regime upon reaching saturation at high subcooling numbers. This accounts for the transient DWO that occur in the RCCS upon reaching saturation in the risers, but the validity of the model is questionable and further analysis needs to be performed.

## 7.2 RCCS Design Recommendations

Results from extensive experimental campaigns on the RCCS have resulted in recommendations and guide-lines for the design of a full-scale RCCS and in general all natural circulation loops. These are as follows:

1. Validate designs with steady-state modeling and flow maps to ensure continuous operation in a single flow regime
2. Verify dynamic operating regime to avoid unstable transients
3. Passive pressurization can reduce unavoidable instabilities

Validation using a steady-state model and flow regime mapping can ensure that static instabilities are avoided. At atmospheric pressure, Ledinegg instabilities do not appear in the RCCS, because

gravitational effects are dominate. However, dynamic oscillations due to flow pattern transitions are likely, because small frictional losses can cause changes in the void production. Hence, it is imperative to avoid operation at the boundary between any flow regimes. The operation of the UW facility is able to avoid this by introducing inlet orificing. The future water-cooled NSTF at Argonne National Laboratories has an operating curve that follows the boundary between stratified and bubbly/intermittent flow. Modifying inlet orificing can force the system to operate fully on the bounding curve. Their facility can then be used to verify the validity of this effect. As their tank drain transient persists, the system should not exhibit the same instabilities present in the UW facility unless inlet orificing is adjusted to coincide with the flow regime boundary.

Dynamic instabilities, such as DWO, were only observed in the RCCS with an increase in the inlet orificing. This resulted in a migration of the system operating point through an unstable operating regime on the phase change - subcooling plane due to increased subsooling when operating in single-phase. Upon reaching saturation, the subcooling rapidly decreased causing traversal through an unstable DWO region. Careful selection of inlet orificing coefficient will change the size of the unstable region, but also the operating point of the RCCS. Numerical parametric studies can be used to derive an ideal operating location that limits the instabilities duration or occurrence in the RCCS facility. In cases where dynamic instabilities are guaranteed to occur increased gas space pressure has been shown to suppress the magnitude and duration of them. This has been validated with the oscillations that occur due to the flow pattern transition instability, but also in the literature for DWO.

## 7.3 Future Recommendations

Reactor Cavity Cooling Systems offer a unique system for studying various instabilities, transients, and two-phase instrumentation. The 1/4 scale facility was originally designed for validating the effectiveness of passive decay heat removal via RCCS type facilities under normal and accident conditions in high temperature generation IV reactors. Initial studies characterized the stability at various power levels and inventory volumes. Since then stability was further analyzed and validated using extended pressure testing and inlet throttling as well as 1D modeling efforts. From these efforts, additional future investigations have been identified.

1. Scaling validation
2. Detailed dynamic stability analysis
3. Validation of Wire Mesh Sensor Data
4. Nano-Particle stability perturbations

Scaling will always be a subject of contention for experimental facilities. The scaling methodology used in the RCCS facility, both at UW and ANL, has been questioned for scaling the height in a natural circulation facility. Some speculate through correspondence that this will have a strong effect on the natural circulation flow. While it does have an effect on the event time scale, it is expected to exhibit the same qualitative instabilities as the full scale design. It is therefore proposed to develop a detailed TRACE model of the RCCS facility. Assuming this model performs better than the previous MELCOR models it can be adjusted to numerically test the effect of different scaling methodologies. The model can be used to predict thermal-hydraulic phenomena in the 1/4, 1/2, and full-scale UW designs and validate the behavior seen in the UW facility. The model can also be used to compare with the power-to-volume scaling methodology, which is essentially a 5° slice fo the full-scale system without azimuthal or axial scalings. This can be used to validate the

experimental data gathered at the UW air- and water-cooled facilities as well as those at ANL and KAERI.

Stability analysis such as those performed by Ishii (1971) and Nayak et al. (2007) can be used to fully understand the dynamics of the RCCS facility. At this point, an accurate dynamic model of the RCCS has not been created. Ishii (1971) model has been used on the RCCS, but is has several assumptions that are not necessarily valid, such as assuming that voiding always begins in the heated core. This assumption naturally leads to assuming that the increase in steam quality is not a strong function of hydrostatic pressure (e.g. flashing doesn't occur in the adiabatic chimney). This is not valid for the RCCS, which naturally begins flashing in the chimney region. Many of the models also ignore parallel channel effects. These make a model significantly more difficult to solve, but could result in a dampening effect on some instabilities or the presence of additional parallel channel interaction instabilities. It is also the only way to assess dynamic instability in a case where the system has a bypass channel.

Wire mesh sensors have been used extensively in the RCCS for study of the instability mechanisms and to guide the formulation of models. They have been proven in the literature to be just as accurate as any other void fraction measurement, but they offer a direct tomographic visualization of the void fraction. This allows for quantitative measurement of the flow regime, individual bubble velocities, and individual bubble size distributions. The data allowed for measurement of negative gas velocities in the risers during DWO. This data can not be validated at this time without secondary flow measurements. It is therefore recommended to increase the instrumentation in the risers in order to validate the measurement of flow reversal under orificed conditions. The intrusive effect of WMSs on bubble velocity has been observed experimentally under room temperature, but analysis has not been performed for higher temperature. Numerical CFD studies could be performed to look at the WMS intrusive effects for a variety of conditions assuming the model can verify the experimental results that are available. Currently, there is no good way to validate the bubble size measurement via WMS beyond visual methods, which can not be applied with any accuracy for dense bubbly flows. The WMSs also require additional validation against properly characterized secondary measurements to quantify the accuracy of the sensor for all measurement methods and conditions.

Modifying water chemistry has been shown to dampen dynamic instabilities in other natural circulation facilities. The introduction of a suspension of nano-particles causes changes the heat capacity, density, and viscosity of the fluid. The viscosity in particular has been observed to decrease significantly at higher temperature, this causes a decrease in frictional effects and therefore an increase in the flow rate for a given set of boundary conditions. This in turn has been shown to dampen dynamic instabilities in single-phase natural circulation without changing the system's operating point and/or geometry as done with the insertion of orifices (Nayak et al. (2008)). It would be interesting to study the effects nanofluids have on the two-phase stability of the RCCS, especially during transient DWO with orificing and the flow pattern transition instabilities.

# PART II – UM RCCS SEPARATE EFFECT TEST FACILITY, EXPERIMENTS AND SIMULATIONS

# 8 UM SEPARATE-EFFECT TEST FACILITY

The Natural Convection Shutdown Heat Removal Test Facility (NTSF) (Vilim and Feldman, 2005; Tzanos, 2005; Farmer et al., 2005) has been recently built at Argonne National Laboratory (ANL) to enable a full scale simulation of the air-cooled RCCS, and to provide experimental support for the design and analysis of this system. The NTSF consists of a natural circulation loop with 12 risers facing a heater and connected with an upper plenum. The hot air exits the upper plenum through two pipes connected to the atmosphere. While full scale facilities are crucial to understand the overall system behavior and to provide validation data for thermal-hydraulic system codes, they are generally not the best suited for the validation of Computational Fluid dynamic (CFD) models. This because of the difficulties associated to high resolution instrumentation and accurate control of boundary conditions (velocity profiles, etc.).

In order to investigate the three-dimensional behavior of the air-cooled RCCS and complement the experimental and validation activities done at ANL and the University of Wisconsin, a scaled facility has been built at the University of Michigan within this project, aimed at the simulation of the upper plenum of the air-cooled RCCS. Our long-term objective is to build a CFD-grade experimental database by using advanced innovative instrumentation, and then to assess and improve the predictive capabilities of both system codes and CFD codes. A specific task of our objective is to advance the experimental studies carried out with the NTSF at the ANL, and further develop the predictive capabilities of computer models. Particularly, we propose to build a separate-effects scaled facility of the air-cooled RCSS upper plenum to address the issues of mixing in the hot plenum as a consequence of the interactions of multiple duct-jet flows. In the following sections, the scaling methodology used to downscale the separate-effects experimental model/configuration from the full-scale air-cooled NTSF is described. Accompanying CFD simulations to verify the scaling are presented as well. Details on the design of the facility are reported in section 8.2. The technical drawings are presented in the Appendix.

The facility is scaled to use water as working fluid instead of air. This simplifies the application of high resolution instrumentation. In addition, the experimental facility is adiabatic; the density of the jets entering the plenum can be adjusted by adding sugar and/or alcohol instead. In this way the uncertainties associated to heat losses are eliminated and a fully optically transparent experimental set-up can be realized. Boundary conditions (inlet flow rates and fluid density) for the risers are defined by scaling the experiments performed at the ANL NTSF facility.

The experimental facility has then been equipped with particle image velocimetry (PIV), and planar laser induced fluorescence (PLIF) to have measurement of the velocity field with high spatial and time resolution. A full characterization of the inlet conditions is performed using LDV (Laser Doppler Velocimetry). This is especially relevant if the data has to be used for the validation of CFD models. The advanced instrumentation will complement the experiments performed at ANL and will allow for deeper insight in the phenomena taking place in the RCCS upper plenum

## 8.1 Scaling analysis of the air-cooled RCCS

It should be noted that the objective of the UM separate effect test facility is to study characteristics of the ducts' flows when entering the plenum by using particle image velocimetry (PIV).

Therefore, the scaled-model is built to mimic the partial-length of the riser ducts and the outlet plenum.

### 8.1.1 Related studies in literature

As the scaled-model is built to characterize the fluid flow rises from the riser ducts into the plenum by natural convection, measured or observed parameters from the RCCS prototype are taken into account as the input, initial and boundary conditions in the scaled-model, for example, the Reynolds number, Froude number, momentum and buoyant energy.

These considerations simplify the study into a case of vertical buoyant jets, which can be commonly found in engineering applications, such as disposal of waste effluents from thermal, industrial, agricultural or domestic sources into the atmosphere or the hydrosphere (Yannopoulos and Noutsopoulos, 1990). Problems related to the study of buoyant jets usually require characteristics of jet entrainment rate, decay of jet velocity, density and temperature (Chen and Chen, 1979).

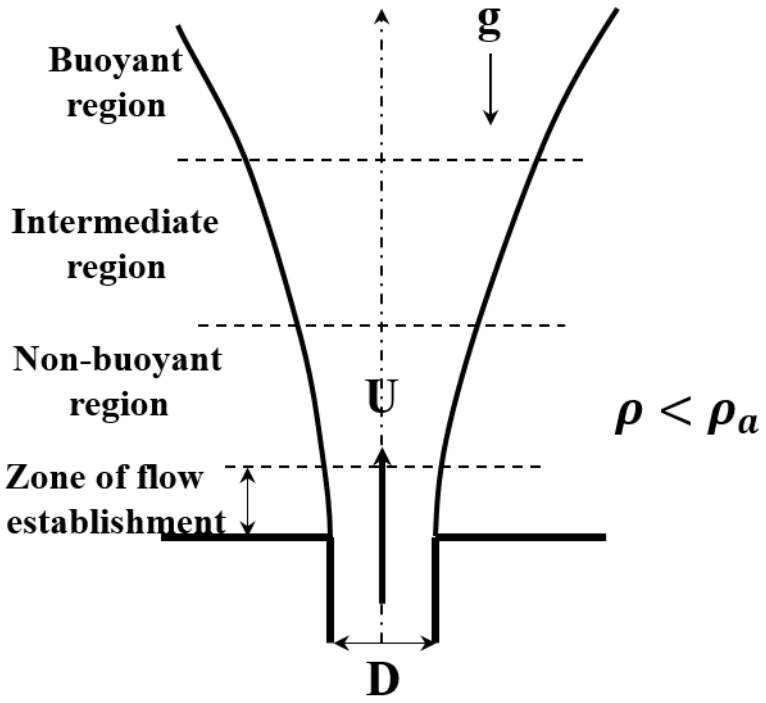


**Figure 8.1 Schematic of zones and regions of buoyant jet.**

Figure 8.1 shows a schematic of zones and regions of a vertical buoyant jet, which discharges the fluid of density $\rho$, kinematic viscosity $\nu$, from a slot of width $D$. The jet fluid flow has a velocity of $U$, vertically upwards into a large volume of fluid whose density is greater, i.e. $\rho_a > \rho$. Yannopoulos and Noutsopoulos (1990, 2006) discussed that the initial densimetric Froude number (Equation (2)), which expresses the ratio of momentum forces to buoyant forces, affects the flow field. Two extreme cases are driven by considering the fluid density difference $\Delta\rho'_m$, i.e. $Fr = \infty$ where buoyancy is absent, and $Fr = 0$ where the flow is driven by buoyancy only.

The characteristics of buoyant jets related to the cases of $0 < Fr < \infty$ are normally complicated and the flow field is usually distinguished by two regions (Chen and Chen (1979), Yannopoulos

and Noutsopoulos (1990, 2006)). The zone of flow establishment is located near the jet exit, where turbulence is not penetrated into the jet symmetry plane. Beyond the zone of flow establishment is the zone of established flow, where the whole flow field is turbulent.

Turbulent plane buoyant jets have been investigated by means of theoretical and experimental studies. Extensive studies on the buoyant jets can be reviewed in Tollmien (1926), Albertson et al (1950), Rouse et al (1952), Chen and Chen (1979), Yannopoulos and Noutsopoulos (1990, 2006), to name a few.

The study of scaled-model RCCS represents a more complex case where the riser ducts are model by multiple vertical buoyant jets discharging fluid flow into the volume of plenum. Depending on the spacing between the risers, interaction of vertical buoyant jets is probably expected. The initial, boundary conditions to the modeled risers and plenum are appropriately scaled from those in the RCCS prototype. Results obtained from the scaled-model will be considerably validated to those discussed in the study of interaction of vertical round turbulent buoyant jets by Yannopoulos and Noutsopoulos (2006).

### 8.1.2 Scaling of UM separate-effect test facility

The scaling methods are developed to preserve the flow dynamics that are present or observed in the regions of riser ducts' outlets and outlet plenum in the full-scale RCCS. Parameters governing the flow dynamics, including riser outlet Reynolds number $Re$, Froude number $Fr$, riser ducts momentum $M$ and kinematic buoyancy $W$, are considered. These parameters are defined as follow:

Reynolds number:

$$Re_m = U_m D_m / \nu_m \tag{1}$$

Froude number:

$$Fr_m = \frac{U_m^2}{g D_m \Delta\rho'_m} \tag{2}$$

Momentum:

$$M_m = \rho_m U_m^2 D_m^2 \tag{3}$$

Buoyant:

$$W_m = \Delta\rho_m U_m D_m^2 \tag{4}$$

Note that the subscript *m* indicates properties of the scaled-model. To preserve the flow dynamics of the scaled-model of the riser-plenum RCCS to be similar to those of the prototype RCCS, ratios of the values of a similarity group considered in the scaled-model and the values of the same group measured in the NSTF conditions must be identical. In the following analysis, the subscript R indicates the ratio of the parameters' values from the scaled-model and those from the prototype RCCS. This can be expressed as:

$$\Psi_R = \frac{\Psi(model)}{\Psi(prototype)} = \frac{\Psi_m}{\Psi_p} \tag{5}$$

Note that the fluid considered in the scaled-model is water-based while the fluid in the prototype RCCS is air. Therefore, the ratios

$$\nu_\Psi = {}^{\nu_{water}}/_{\nu_{air}} = 0.064, \text{ and}$$

$$\rho_\Psi = {\rho_{water}}/{\rho_{air}} = 829.075,$$

where $\nu_{water} = 1.004 \times 10^{-6}$ ($m^2/s$) and $\rho_{water} = 998.2071$ ($kg/m^3$); $\nu_{air} = 15.68 \times 10^{-6}$ ($m^2/s$), and $\rho_{air} = 1.204$ ($kg/m^3$).

The similarity conditions for the Reynolds number, Froude number, momentum and buoyant yield

$$Re_\Psi = \frac{U_\Psi D_\Psi}{\nu_\Psi} \quad (6)$$

$$Fr_\Psi = \frac{U_\Psi^2}{D_\Psi \Delta\rho'_\Psi} \quad (7)$$

$$M_\Psi = \rho_\Psi U_\Psi^2 D_\Psi^2 \quad (8)$$

$$W_\Psi = \Delta\rho_\Psi U_\Psi D_\Psi^2 \quad (9)$$

The similarity of Reynolds number gives $Re_\Psi = 1$, then

$$U_\Psi D_\Psi = \nu_\Psi = 0.064. \quad (10)$$

In case that the scaled-model is considered to maintain the fluid density difference in the prototype RCCS, i.e. $\Delta\rho'_\Psi = 1$, the Froude similarity yields $Fr_\Psi = 1$, or

$$U_\Psi^2 = D_\Psi. \quad (11)$$

The similarity of momentum gives $M_\Psi = 1$, then

$$U_\Psi^2 D_\Psi^2 = {1}/{\rho_\Psi} = 0.001206. \quad (12)$$

It can be seen from the equations (10) and (12) that to satisfy the similarity conditions, the scaled-model could not preserve the density difference as in the prototype RCCS.

Now, with an assumption that $\Delta\rho'_\Psi \neq 1$, the similarities of momentum and buoyant give $M_\Psi = 1$, and $W_\Psi = 1$. Considering the ratio ${M_\Psi}/{W_\Psi} = 1$ yields

$$U_\Psi = \frac{\Delta\rho_\Psi}{\rho_\Psi} = \Delta\rho'_\Psi \quad (13)$$

From the similarity of Froude number, $Fr_\Psi = 1$, then

$$D_\Psi = \frac{U_\Psi^2}{\Delta\rho'_\Psi} = U_\Psi = \Delta\rho'_\Psi \quad (14)$$

The similarity of Reynolds number, $Re_\Psi = 1$, gives

$$U_\Psi D_\Psi = \nu_\Psi \quad (15)$$

Using equations (10), (14) and (15), one can obtain the following conditions:

$$U_\Psi = D_\Psi = \Delta\rho'_\Psi = \sqrt{\nu_\Psi} = 0.2529 \quad (16)$$

This can be translated to

$$\left(\frac{\Delta\rho}{\rho}\right)_{water} = 0.2529 \left(\frac{\Delta\rho}{\rho}\right)_{air} \quad (17)$$

where $\rho$ is the fluid density, and $\Delta\rho = \rho_a - \rho$, with $\rho_a$ is the fluid density in the plenum.

Equations (16) and (17) allow us to determine the fluid properties, initial flow conditions and geometry of the scaled-model.

For instance, the fluid velocity at the risers' outlets and the cross-section of the riser will be scaled from those of the RCCS prototype with a factor of $f_{scale} = {}^{1}/_{0.2529} \approx 4$.

The maximum ceiling height of the plenum $H_m$ is considered to appropriately scale in order to preserve the penetration depth of the riser jets. Turner (1966) has studied the characteristics of the negative and reversing buoyant jets, and the author proposed a proportional relation of the jet height to the Froude number and characteristic diameter of the jet, as shown below

$$X_m = D_m Fr^{1/2} \tag{18}$$

Applying the scaling analysis and note that the similarity of the Froude number, $Fr_\Psi = 1$, one can find that

$$X_\Psi = D_\Psi = U_\Psi = \Delta\rho'_\Psi \tag{19}$$

Equation (19) indicates that the height of the plenum in the scaled-model can be scaled by the same factor $f_{scale}$.

Mi et al. (2000) have compared the centerline mean flow velocity and turbulence characteristics in differently shaped jets, and found that different geometries of jets yielded various mixing rate. Therefore, the aspect ratio of the riser duct, $AR_m = {}^{L_m}/_{D_m}$, is also maintained as in the RCCS prototype, i.e. $AR_\Psi = 1$. It is then translated to:

$$L_\Psi = D_\Psi \tag{20}$$

Additionally, this relation means to scale the hydraulic diameters of the rectangular riser ducts in the scaled-model to the RCCS prototype by the same factor as other properties.

Figure 8.2 illustrates a schematic of the scaled-model including the sections of the plenum, twelve (12) risers and two (2) exhausts. The number of risers is similar to that of the RCCS prototype. The cross-section of the riser, distances from the risers and exhausts to the plenum walls are scaled from the corresponding values in the RCCS prototype by $f_{scale}$.

### 8.1.3 Confirming CFD simulations – scaling

In this section, we present and compare numerical results obtained from the case of air flow in the plenum-riser of the ANL RCCS prototype and the case of water flow in the plenum-riser of the UM scaled-model.

To validate the scaling analysis, the air flow in the region of plenum-riser of the RCCS prototype and the water flow in the plenum-riser of the scaled-model are numerically produced. The calculations have been performed using the commercial CFD software StarCCM+. Note that the domain of plenum and risers are symmetrical, therefore only half of the simulation domain is calculated. The computational domains are built inside the StarCCM+ using the 3D-CAD Models. The generated meshes are polyhedral with prism layers on the risers' walls and plenum's wall (see Figure 8.3).

The calculations are steady, three-dimensional (3D) Reynolds Averaged Navier-Stokes (RANS). Turbulent calculations are performed using the Realizable *k*-ε two layer model with two-layer wall treatment. Iterative calculations are executed until the maximal normalized residuals of the continuity, x-, y- and z-momentum, turbulent kinetic energy *k*, and turbulent dissipation ratio ε converged to less than $10^{-4}$.

For the simulations of the RCCS prototype and the scaled-model, an inlet boundary condition with a uniform velocity, $W_{m-air} = 4W_{m-water} = 3.5$ (m/s), and turbulence intensity $I = 4\%$. The values of $W_{m-air}$ and $I$ are similarly taken from the measurements in the RCCS prototype. The Flow-Split Outlet boundary condition is assigned to the exhaust outlet, while the non-slip wall boundary condition is applied to the interior surfaces of the risers, plenum (except the symmetrical plane), and the exhaust.

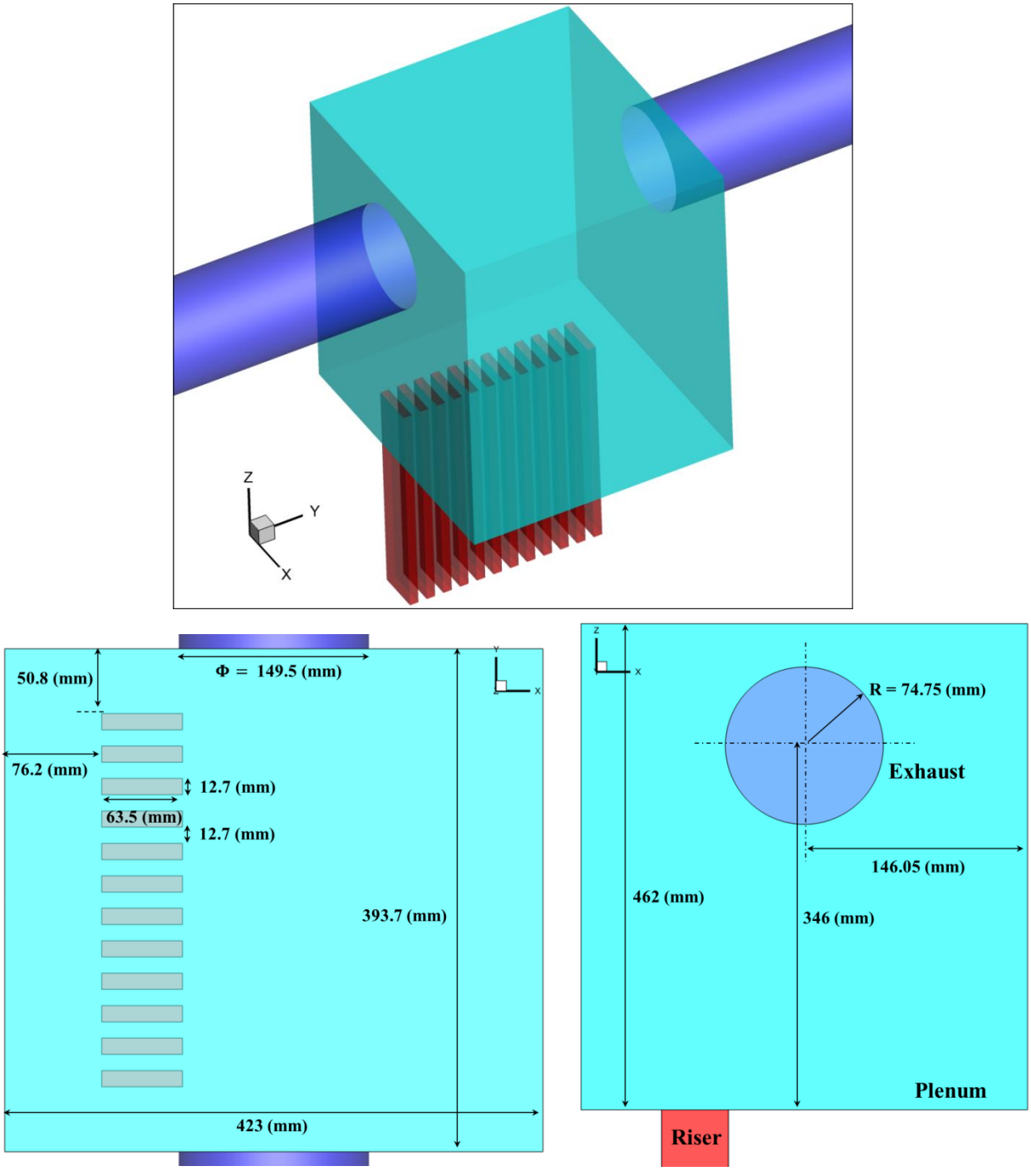


**Figure 8.2 Scaled model of risers and upper plenum (top), top and side view (bottom).**

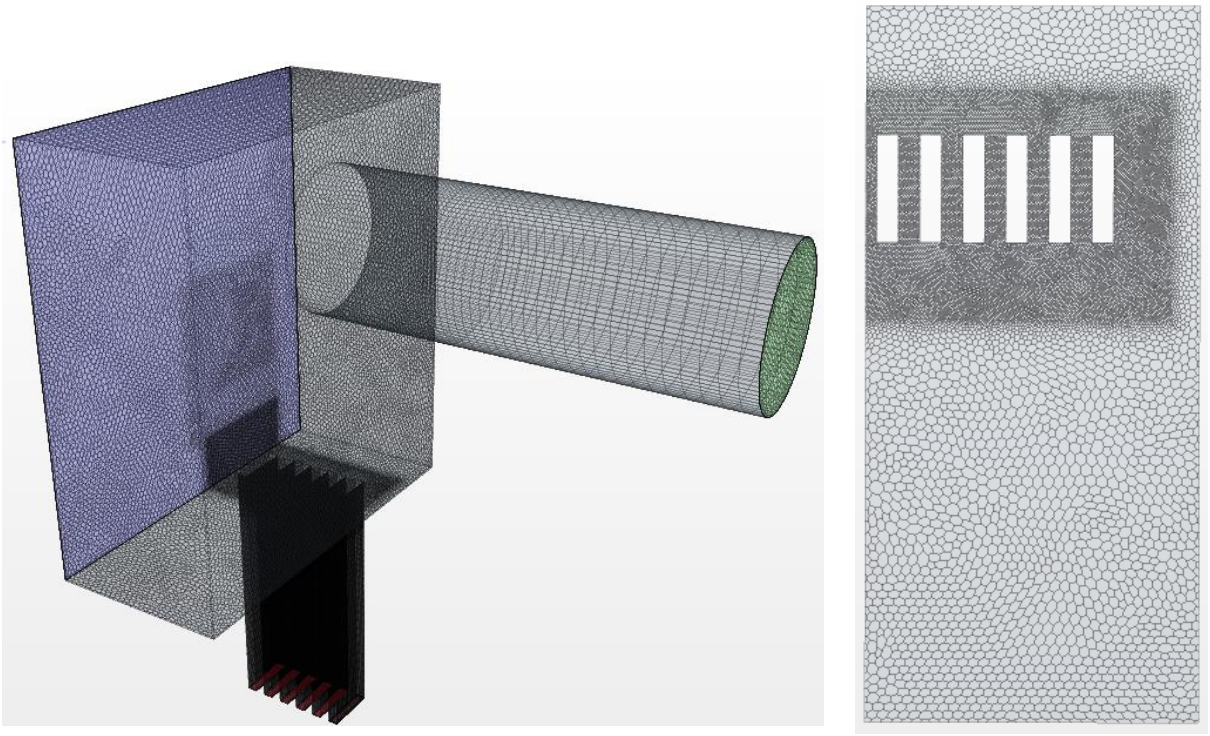

**Figure 8.3 Polyhedral mesh (left) generated for the plenum, risers and exhausts, and mesh on the bottom surface of the plenum (right).**

In Figure 8.4, we present the velocity streamlines calculated from the numerical results of the air-flow and water-flow in the plenum-riser of the RCCS prototype and scaled-model, respectively. Flow patterns from these figures are qualitatively similar where the risers discharged flows into the plenum form a large recirculation region before exhausting by the outlet.

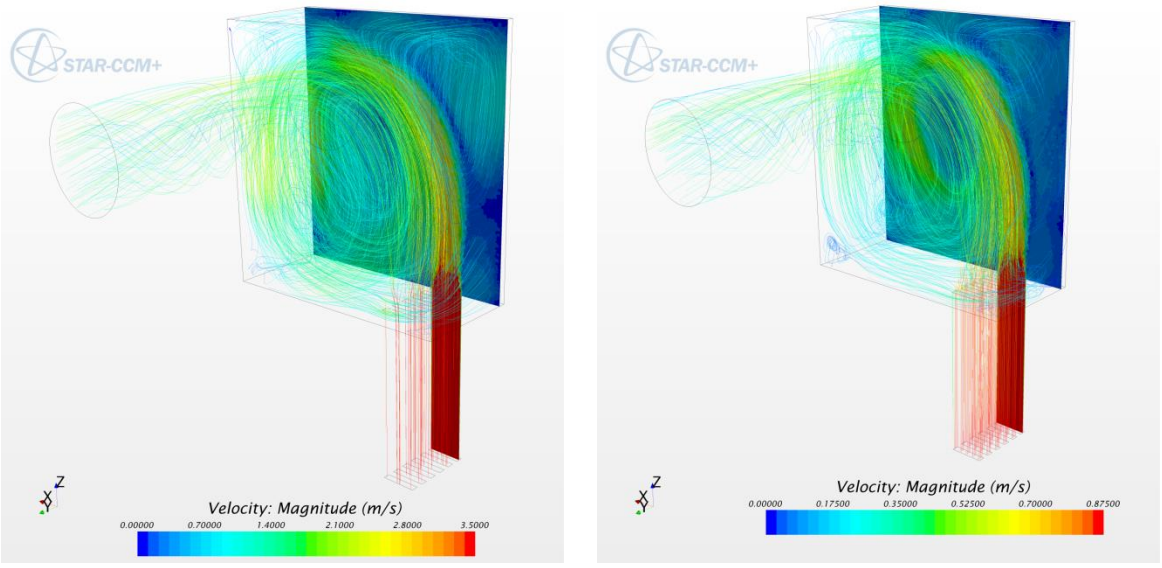


**Figure 8.4 Velocity streamlines obtained from the numerical simulations. Left: air flow in the plenum-riser of RCCS prototype. Right: water flow in the plenum-riser of scale-model.**

In Figure 8.5 and Figure 8.6, direct comparisons among the numerical results, i.e. velocity and turbulent kinetic energy profiles, from the RCCS prototype and the scaled-model are presented. Results are interpolated along 6 vertical-centerlines of the middle plane of the risers (*yz*-plane) and along 6 vertical lines of the middle plane of the plenum (*yz*-plane, $x = 0$). These profiles are normalized by the riser velocity, $W_m$. It can be seen that results from the simulations of the RCCS prototype and the scaled-model are in good agreement.

The results from the numerical simulations of the RCCS prototype and the scaled-model have confirmed the capability of the scaling analysis.

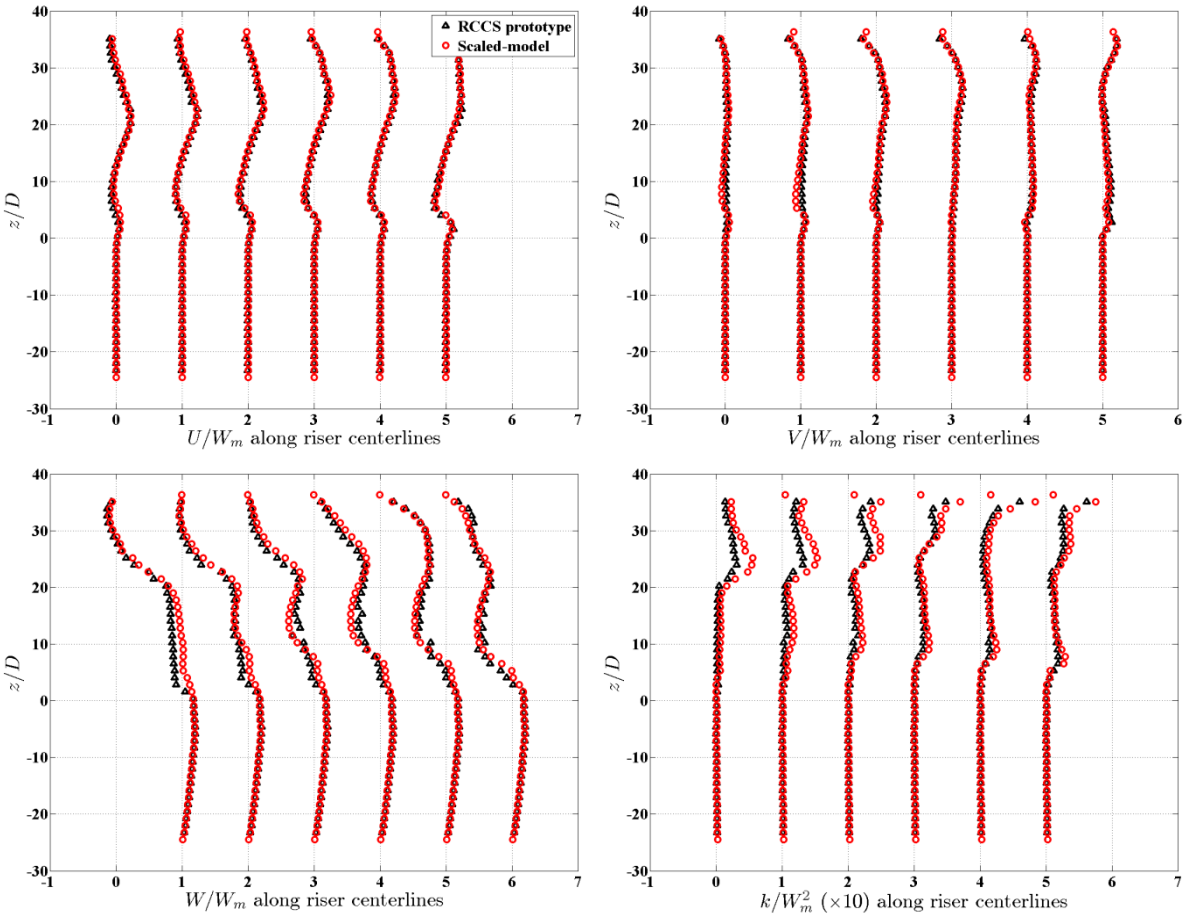


**Figure 8.5 Comparisons among velocities and turbulent kinetic energy obtained from the RCCS prototype and scaled-model simulations. Velocities are interpolated along 6 vertical-centerlines of the middle-plane of risers (yz-plane).**

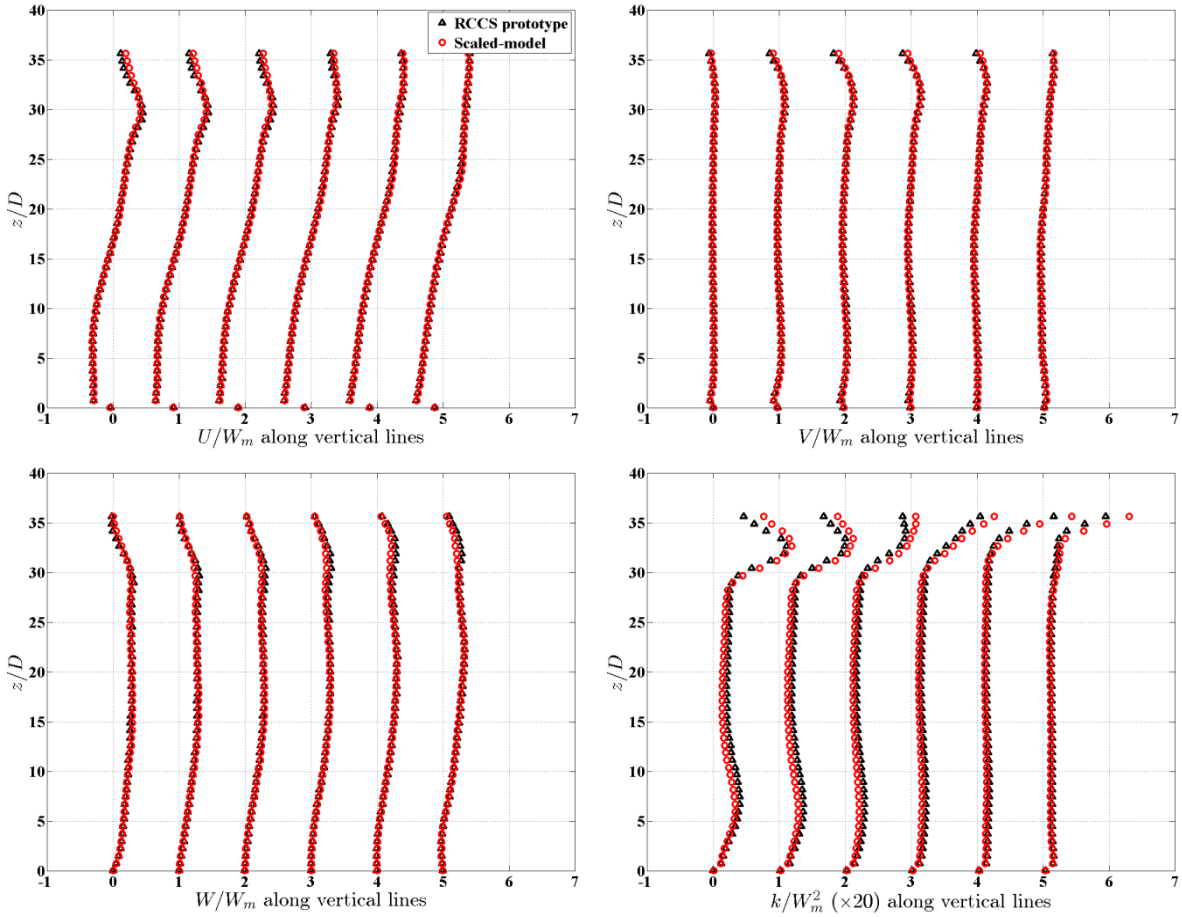


**Figure 8.6 Comparisons among velocities and turbulent kinetic energy obtained from the RCCS prototype and scaled-model simulations. Velocities are interpolated along 6 vertical lines of the middle-plane of plenum (yz-plane, x = 0).**

## 8.2 Design of the experimental set-up

An experimental facility of the water-based scaled-model, aimed at the investigation of the air-cooled RCCS upper plenum, has been designed following the scaling analysis presented in the previous section.

Geometrical dimensions of the scaled-model such as riser width, riser length, distance between risers, distance between risers and plenum wall are downscaled from those of the ANL facility by the factor $f_{scale}$. The facility is designed to include 6 riser ducts. Since the ANL facility includes 12 riser ducts, the physical dimensions of the upper plenum size are correspondingly downscaled and adjusted to maintain the similarity with the ANL RCCS facility. Because the number of the riser ducts has been reduced by a factor of 2, the cross-section of the exhaust pipes of the scaled-model facility is reduced by the same factor to reserve the same mass flow rate exiting the plenum.

Physical dimensions of the experiment facility at the University of Michigan are presented in the Appendix (dimensions are given in *mm*). In order to be able to investigate the effect of the riser ducts extension above the upper plenum bottom wall (similarly to the ANL RCCS facility), a removable bottom wall is placed on the rigid wall of the plenum. Legs with various heights are used as spacers and attached to the removable wall.

### 8.2.1 Confirming CFD simulations – reduction of number of risers

In this section, we present results obtained from the numerical simulations whose geometrical dimensions are taken from the experiment facility. These results confirmed that the flow patterns inside the experiment facility with 6 riser ducts followed and matched those from the numerical simulations of the scaled-model with 12 riser ducts shown in section 8.1.3.

Similar to the CFD calculations done to verify the scaling analysis, water flow in the experiment facility of the scaled-model are numerically produced. The calculations have been performed using the commercial software StarCCM+. Only half of the simulation domain is calculated because of the symmetrical geometry. Meshes are generated with polyhedral shapes and prism layers on the risers' walls and plenum's wall (see Figure 8.7).

The calculations are steady, three-dimensional (3D) Reynolds Averaged Navier-Stokes (RANS). Turbulent calculations are performed using the Realizable k-ε two layer model with two-layer wall treatment. Iterative calculations are executed until the maximal normalized residuals of the continuity, x-, y- and z-momentum, turbulent kinetic energy k, and turbulent dissipation ratio ε converged to less than $10^{-4}$.

Geometrical dimensions of the riser ducts and the plenum are shown in Figure 8.8. In order to investigate the effects of the plenum wall to the fluid flow discharged by the riser ducts, distances from the riser ducts to wall, noted by $r_w$, are adjusted so that the ratio, $\frac{r_w}{W}$, where W is the plenum width, is 0.12 and 0.24. Effects of the plenum wall to the duct flows discharged into the plenum volume have been done at the ANL RCCS air-based facility.

***a) Effects of plenum wall to riser duct flows:***

In this subsection, the CFD results corresponding to the case $\frac{r_w}{W} = 0.12$ and $\frac{r_w}{W} = 0.24$ respectively will be presented. Boundary conditions of the CFD calculations are assigned by using and scaling the measurements taken from the ANL RCCS facility (similar to those done in the section 8.1.3). The inlet boundary condition is assigned with a uniform velocity, $W_m = 0.875$ (m/s), and turbulence intensity $I = 4\%$. The Flow-Split Outlet boundary condition is assigned to the exhaust outlet, while the non-slip wall boundary condition is applied to the interior surfaces of the risers, plenum (except the symmetrical plane), and the exhaust.

It can be observed that the velocity streamlines shown in Figure 8.10 for the case of rw/w = 0.12 exhibit flow patterns similar to those from the CFD calculation of the scaled-model with 12 risers, which were illustrated in Figure 8.4(right). This similarity assures that the experiment facility with 6 risers can reproduce the main flow characteristics and patterns of the full-scale air-cooled ANL RCCS facility.

In Figure 8.10 (a), velocity streamlines of the scaled-model with a shorter distance riser-to-wall, i.e. case $\frac{r_w}{W} = 0.12$, reveal that the fluid flow is discharged by the riser ducts into the plenum volume and decelerated at a certain height, which indicates the penetration of the jet. The jet flow impinges to the plenum top wall where a large partial flow moves towards the farther wall and a small partial flow forms a reverse region at the corner of the closer wall. The larger flow has a greater kinetic energy and continuously moves along the vertical and bottom walls, forming a large circulation region in the central plenum volume, before exiting through the exhaust pipe.

In Figure 8.11 (a), the velocity streamlines for the scaled-model with a greater distance riser-to-wall, i.e. case $\frac{r_w}{W} = 0.24$, show similar trends as seen in Figure 8.10 (a). However, the greater gap

between the riser flows and closer wall creates a larger reverse region compared to that in Figure 8.10(a). Furthermore, in this case the jets have a greater penetration height. Velocity contours in the riser planes $y = 0.0127$ of both cases show the similar trends and patterns previously discussed. Turbulent kinetic energy contours however illustrate that the jet flows of the case $\frac{r_w}{W} = 0.12$ have a higher turbulent region at the maximum height. Velocity and turbulent kinetic energy contours in Figure 8.10 (c) and Figure 8.11 (c) reveal similar flow structures, excepting that jet height of the case $\frac{r_w}{W} = 0.24$ is shorter to that of the case $\frac{r_w}{W} = 0.12$. The greater the riser-to-wall distance seems to force the jet flows tilting out of it axis sooner than the case of shorter distance.

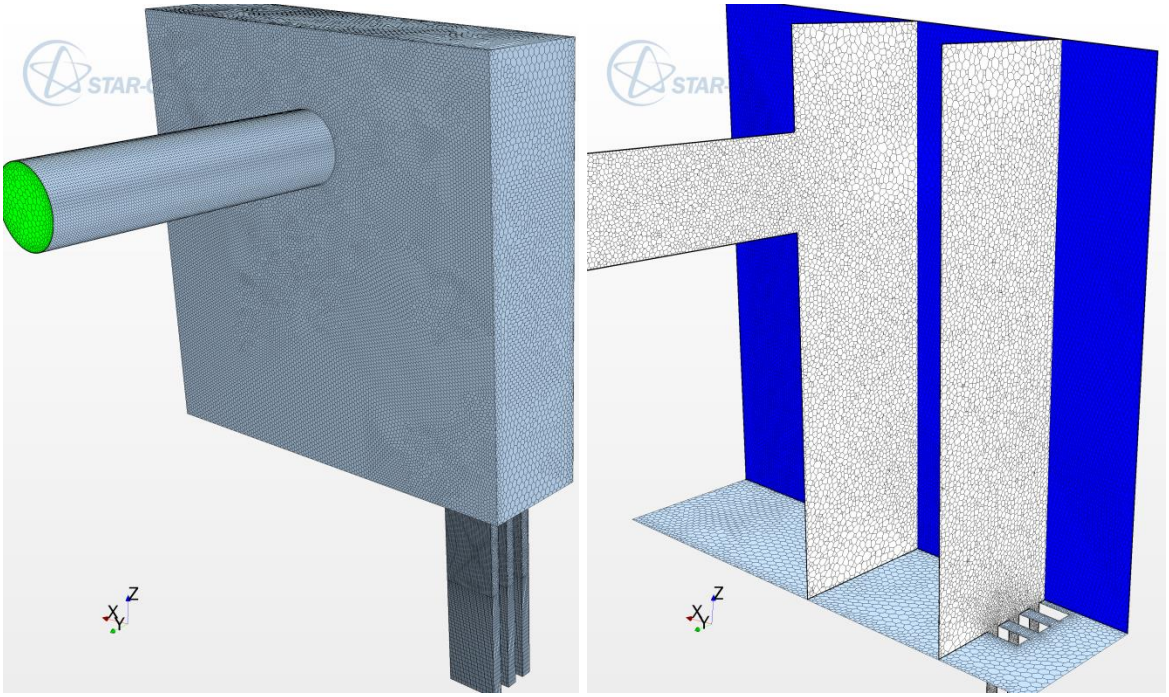

**Figure 8.7 Polyhedral mesh *(left)* generated for numerical simulations of the experiment facility of the scaled-model with 6 riser ducts, and mesh on selected surfaces of the scaled-model *(right)*.**

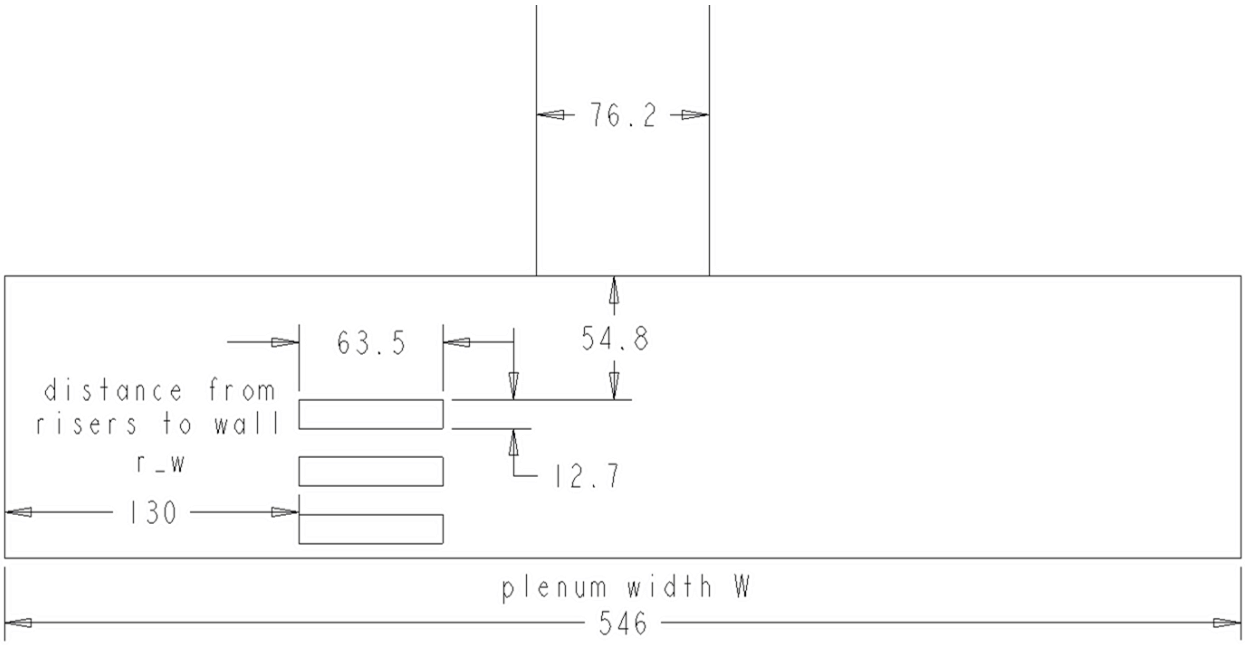


**Figure 8.8 Geometrical dimensions of the riser ducts and upper plenum applied to the CFD simulations. Ratios, between the distances from risers to plenum wall, $r_w$, and the plenum width, $W$, are $\frac{r_w}{W} = 0.12$, and 0.24.**

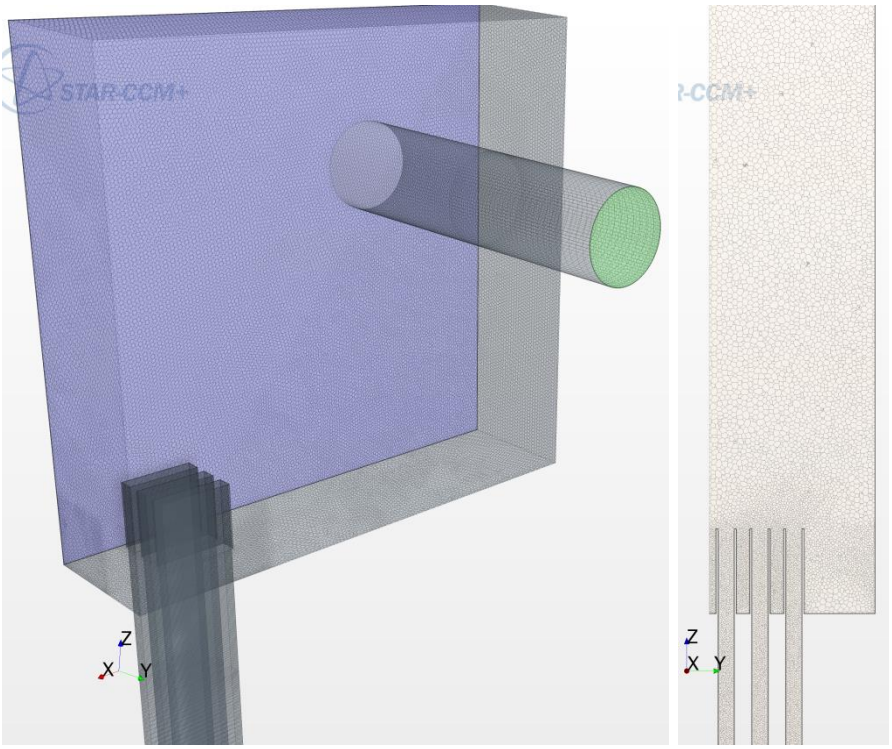

**Figure 8.9 Polyhedral mesh *(left)* generated for numerical simulations of the experiment facility of the scaled-model with 6 riser ducts, and risers are extended above the plenum bottom wall, mesh on riser ducts' middle plane *(right)*.**

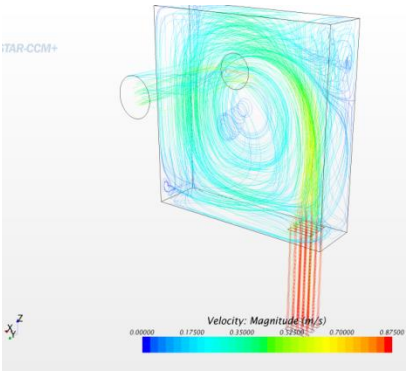


*(a)* Velocity streamlines

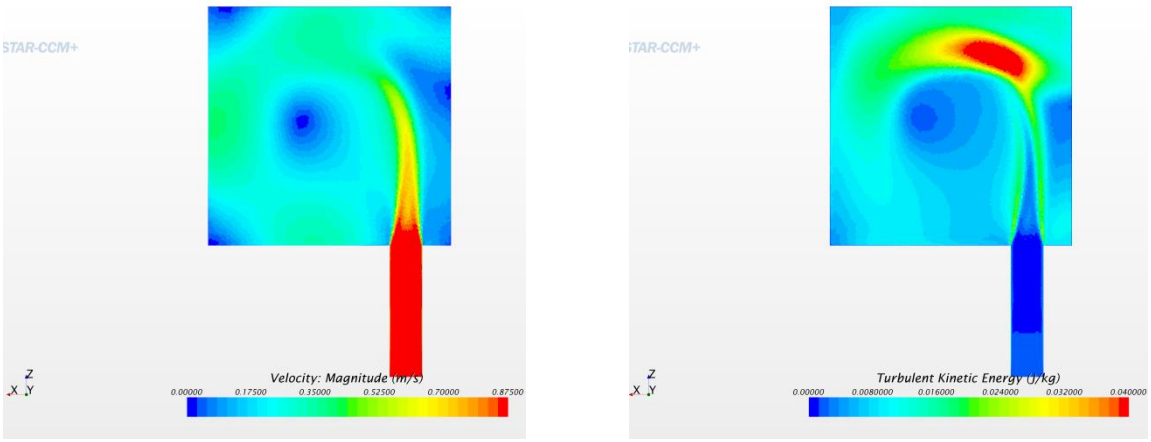


*(b)* Velocity and turbulent kinetic energy contour in the riser plane $y = 0.0127$

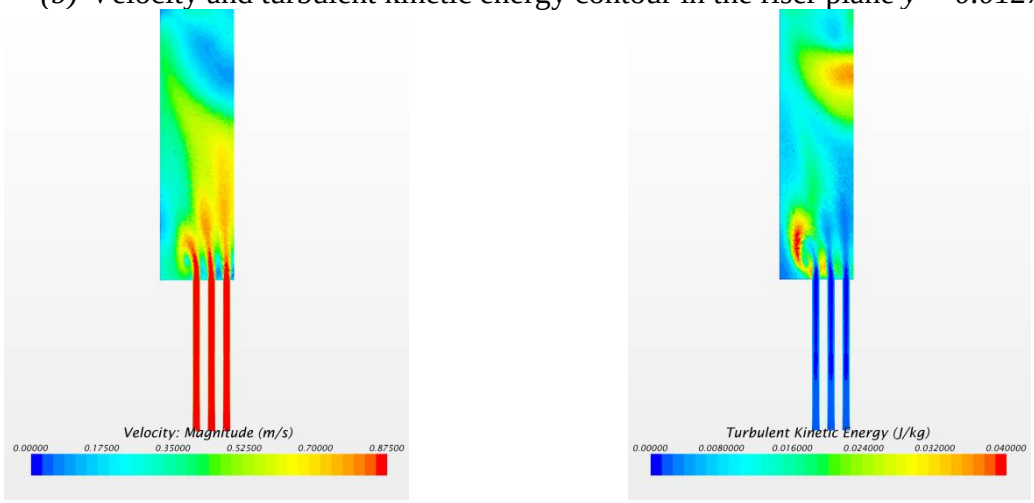


*(c)* Velocity and turbulent kinetic energy contour in the risers' middle plane

**Figure 8.10 Results obtained from the CFD simulations for the experiment facility of scaled-model with 6 risers, case $\frac{r_w}{W} = 0.12$. (a) Velocity streamlines, (b) results in the riser plane $y = 0.0127$, (c) results in the risers' middle plane**

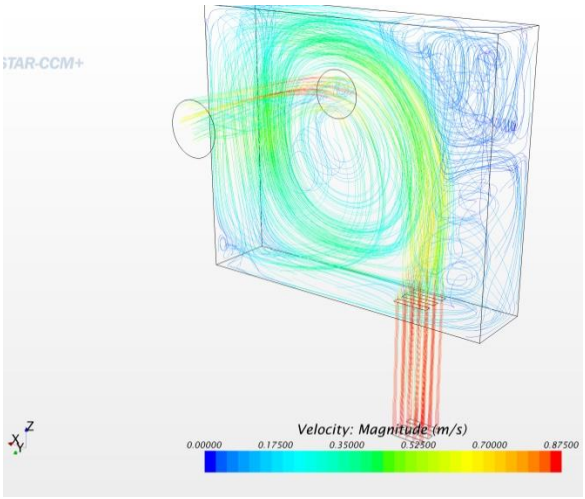


*(a)* Velocity streamlines

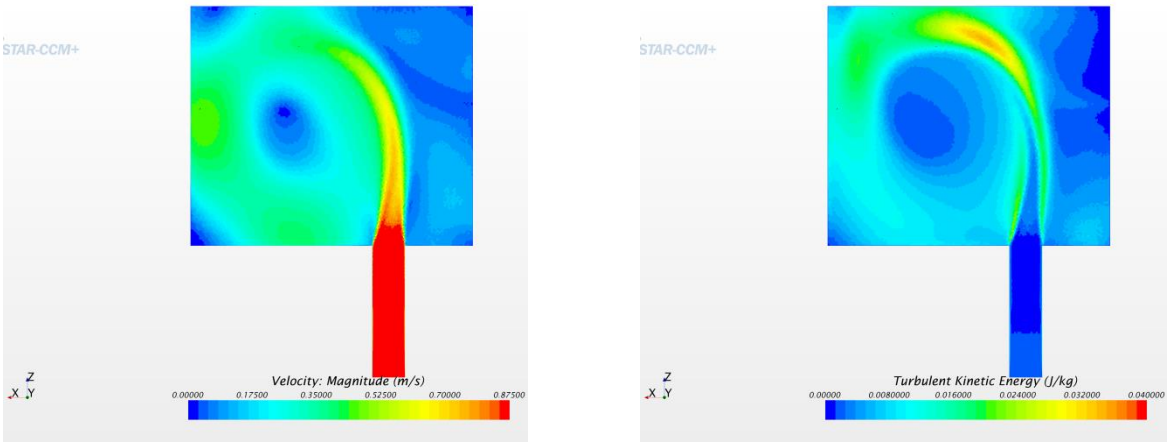


*(b)* Velocity and turbulent kinetic energy contour in the riser plane $y = 0.0127$

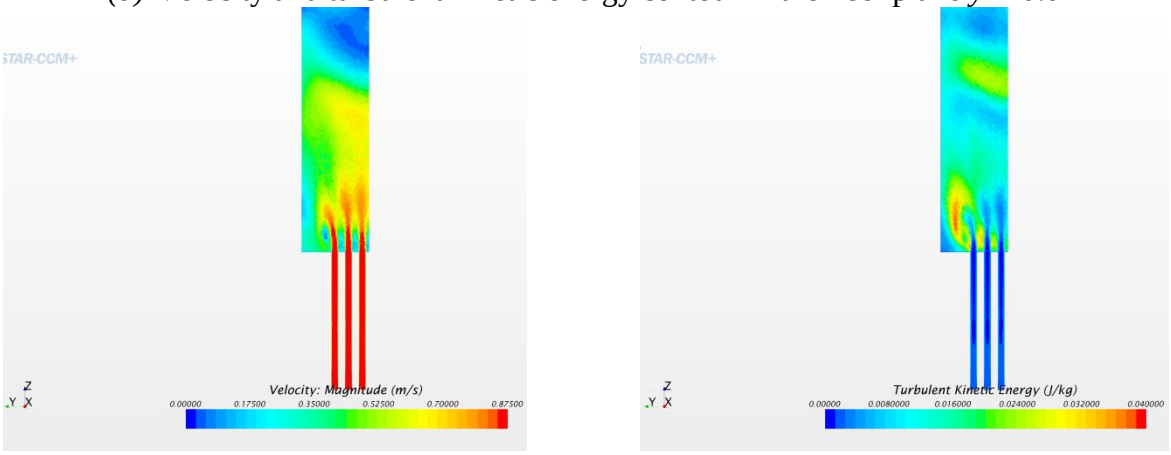


*(c)* Velocity and turbulent kinetic energy contour in the risers' middle plane

**Figure 8.11 Results obtained from the CFD simulations for the experiment facility of scaled-model with 6 risers, case $\frac{r_w}{W} = 0.24$. (a) Velocity streamlines, (b) results in the riser plane $y = 0.0127$, (c) results in the risers' middle plane.**

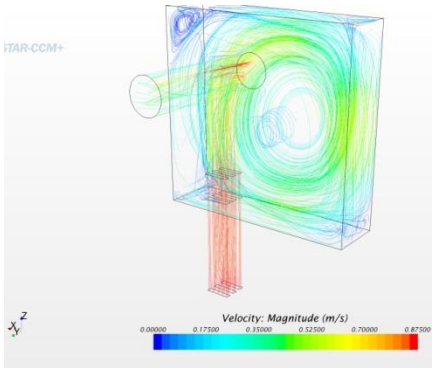


*(a)* Velocity streamlines

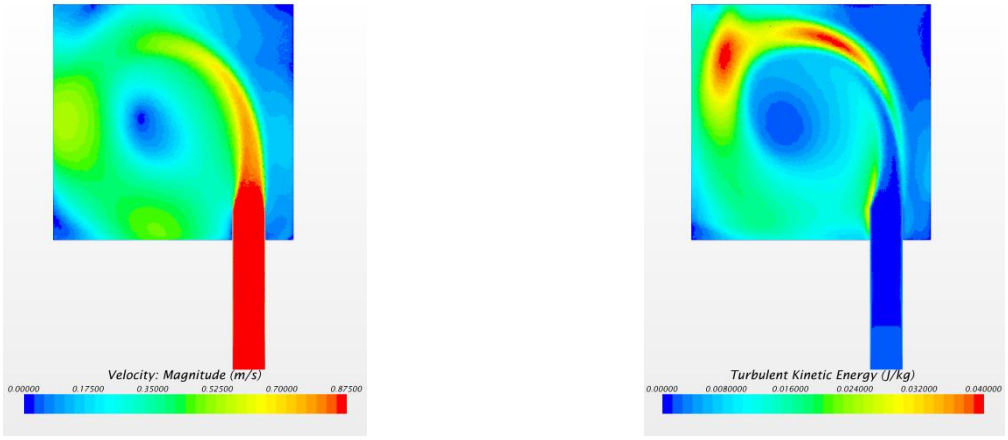


*(b)* Velocity and turbulent kinetic energy contour in the riser plane $y = 0.0127$

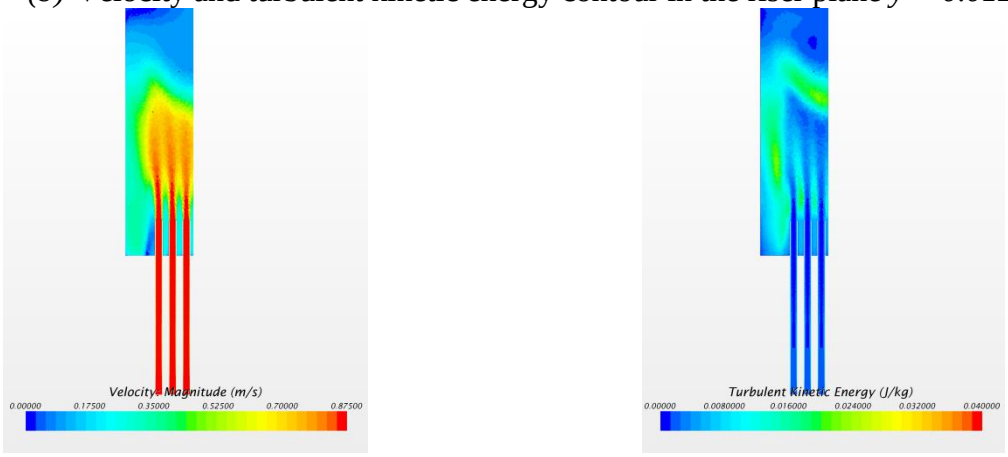


*(c)* Velocity and turbulent kinetic energy contour in the risers' middle plane

**Figure 8.12 Results obtained from the CFD simulations for the experiment facility of scaled-model with 6 risers extended higher than the plenum bottom, case $\frac{r_w}{W} = 0.12$. (a) Velocity streamlines, (b) results in the riser plane *y = 0.0127*, (c) results in the risers' middle plane.**

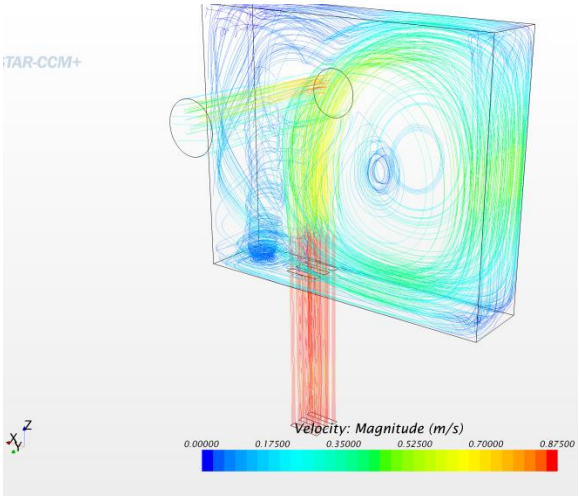


*(a)* Velocity streamlines

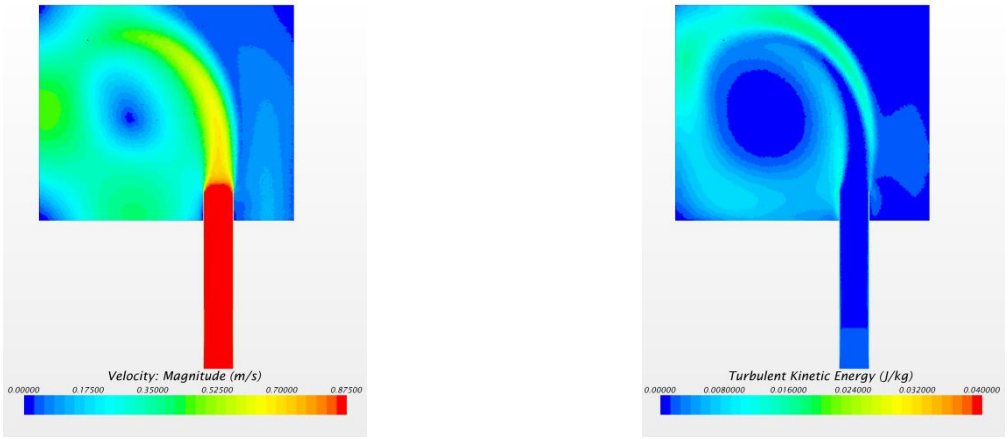


*(b)* Velocity and turbulent kinetic energy contour in the riser plane *y = 0.0127*

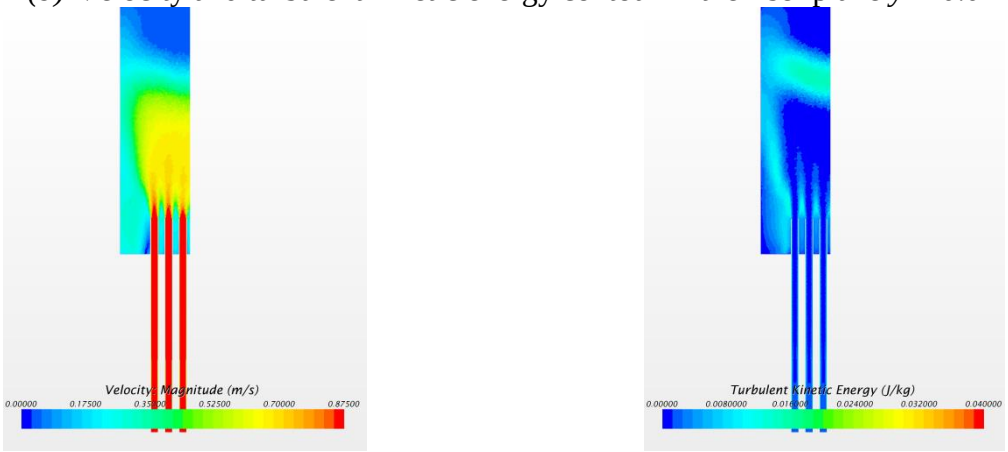


*(c)* Velocity and turbulent kinetic energy contour in the risers' middle plane

**Figure 8.13 Results obtained from the CFD simulations for the experiment facility of scaled-model with 6 risers extended higher than the plenum bottom, case $\frac{r_w}{W} = 0.24$. (a) Velocity streamlines, (b) results in the riser plane *y = 0.0127*, (c) results in the risers' middle plane.**

***b) Effects of extending the riser duct height above the plenum bottom:***

In this subsection, we present results from extending the riser duct one-width higher than the plenum bottom. The CFD calculations are done for $\frac{r_w}{W} = 0.12$ and 0.24. Boundary conditions such as the inlets of the riser ducts, exhaust outlets, etc., are assigned similarly to those described in previous sections. Because of the thickness of the riser walls (assumed to be 1 mm), the distance between two successive riser ducts is reduced by about 15.7% compared to the model with non-extending riser ducts. This reduction is expected to have negligible effects to the flow characteristics. Figure 8.9 illustrates the calculation domain and meshes for the experiment facility of the scaled-model with 6 risers generated with polyhedral shapes and prism layers on the risers' walls and plenum's wall.

Figure 8.12(a) and Figure 8.13(a) display the velocity streamlines from the CFD calculations of the experiment facility of scaled-model with 6 risers extended higher than the plenum bottom for the cases of $\frac{r_w}{W} = 0.12$ and 0.24. In general, the two flow configurations show similar large circulations in the central volumes. In Figure 8.13 (a) the effects of the larger distance riser-to-wall are clearly seen in the swirling region between the wall and riser ducts. In this case, the riser flows are discharged into the plenum volume, impinged to the top plenum wall and the mass flow rate is separated. The larger partial flow forms the main circulation zone, while the smaller partial flow reverses along the top wall and move downward to the bottom wall. When the downward flow reaches the bottom wall, it moves upward and creates a swirling tube that moves parallel to the risers' axes, before re-joining the large circulation to exit the plenum by the exhaust.

## 8.3 Construction of UM RCCS separate-effect test facility

The separate-effects scaled facility has been successfully built at the University of Michigan (UofM). A scheme of the facility is reported in Figure 8.14. The facility has been fabricated in transparent acrylics to allow access for optical laser measurements. The working fluid of the facility, i.e. water, is stored in two tanks of 400 liters and one tank of 2000 liters. The upper plenum of the test section has the inner dimensions of length × width × height = 470.6 × 249.3 × 462 ($mm^3$) and two exhaust pipes with an inner diameter of 76.2 (mm). A pack of six risers, whose distance between neighboring risers is $S_r = 12.7$ (mm), was attached to the bottom of the plenum. Each riser has a $D_1 \times D_2 = 12.7 \times 63.5$ ($mm^2$) cross section. The water flow is driven through a conditioning section with honeycomb grids and long channels to obtain a uniform water jet flow and to minimize the turbulence level. The axial length $L_{riser}$ of the risers is 800 (mm) yielding the ratio $L_{riser}/D_r$ = 38.1 ($D_r$ is the hydraulic diameter of the riser), which is sufficiently long for the flow to reach a fully developed state. Flow rates through the six risers are regulated by gate valves and accurately measured by turbine flow meters (Blancett 1100). The main components of the experimental facility are listed in Table 8.1, while photos of the setup are shown in Figure 8.15.

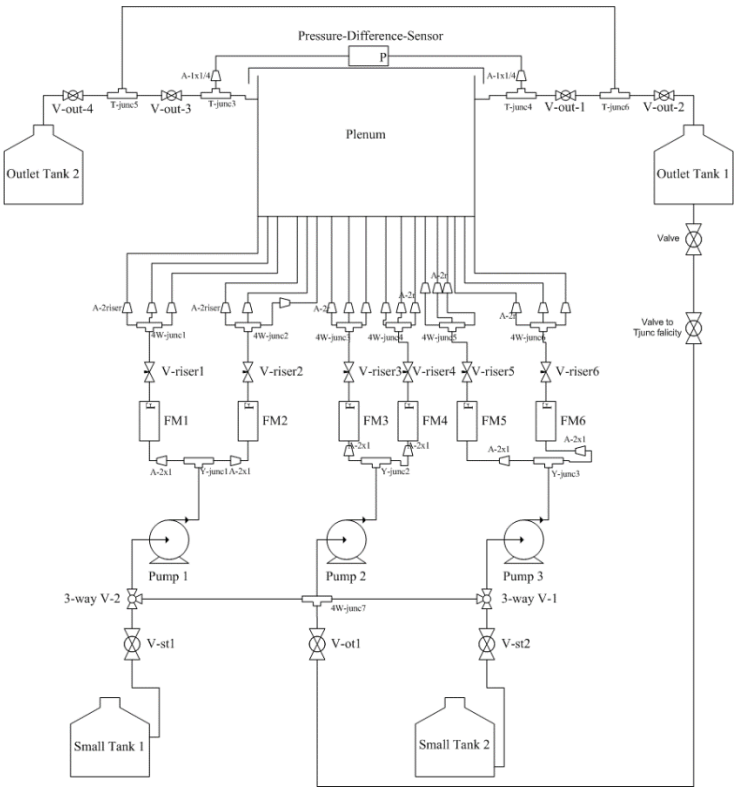


**Figure 8.14: Scheme of the UM Separate Effect RCCS facility**

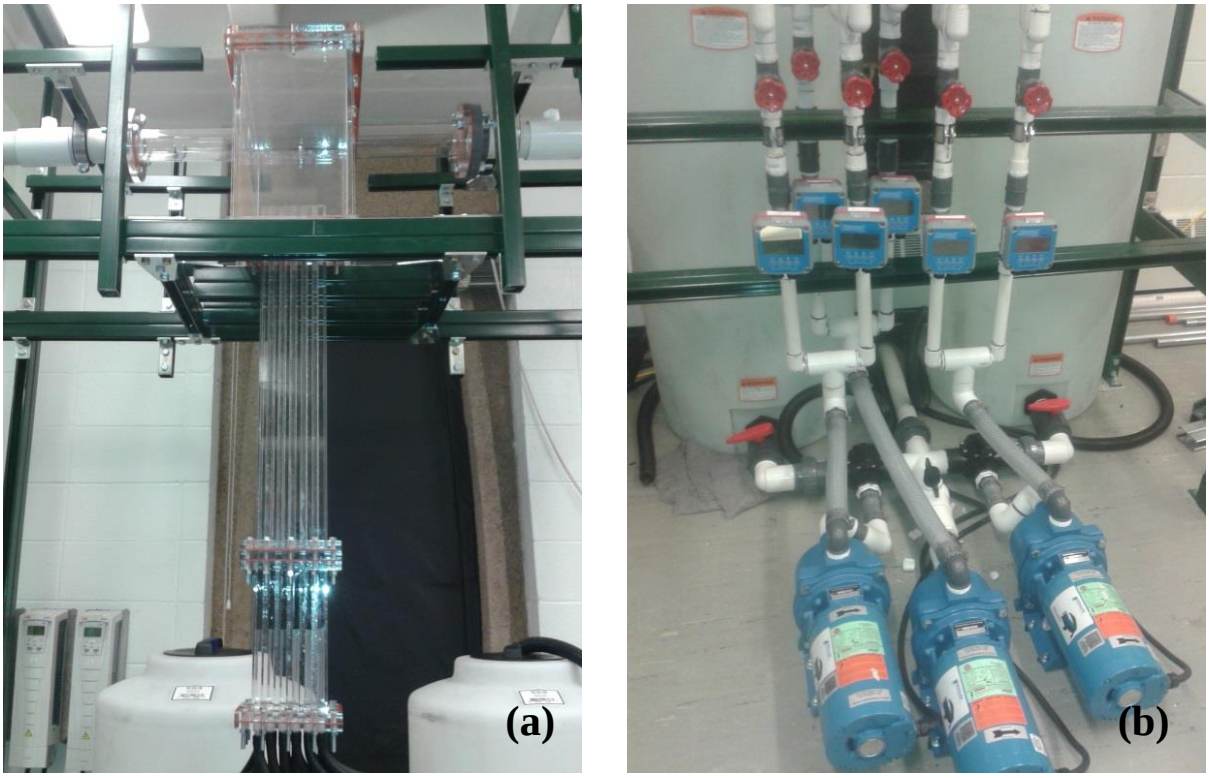


**Figure 8.15: (a) The separate-effects scaled facility with 6 risers vertically discharging into the upper plenum, (b) 3 water pumps and 6 turbine flow meters connected to the risers.**

**Table 8.1: List of main components in the RCCS facility scheme.**

| Main components | Code | Main components | Code |
|---|---|---|---|
| Plenum | | Flowmeter 3 | FM3 |
| Small Tank 1 | | Flowmeter 4 | FM4 |
| Small Tank 2 | | Flowmeter 5 | FM5 |
| Outlet Tank 1 | | Flowmeter 6 | FM6 |
| Outlet Tank 2 | | Valve to riser 1 | V-riser1 |
| Pump 1 | | Valve to riser 2 | V-riser2 |
| Pump 2 | | Valve to riser 3 | V-riser3 |
| Pump 3 | | Valve to riser 4 | V-riser4 |
| Valve to Small Tank 1 | V-st1 | Valve to riser 5 | V-riser5 |
| Valve to Small Tank 2 | V-st2 | Valve to riser 6 | V-riser6 |
| Valve to Outlet Tank 1 | V-ot1 | Valve to Outlet Tank 1 | V-out-1 |
| 3-way Valve 1 | 3-way V-1 | Valve to Outlet Tank 1 | V-out-2 |
| 3-way Valve 2 | 3-way V-2 | Valve to Outlet Tank 2 | V-out-3 |
| Flowmeter 1 | FM1 | Valve to Outlet Tank 2 | V-out-4 |
| Flowmeter 2 | FM2 | | |

## 8.4 Operation of the UM RCCS facility

In order to start up the RCCS facility, one can follow the below setups and adjust the main components in the system in order to have the desired experimental runs. In this report, two experiment setups are described and they can be considered as the base runs (see Figure 8.16 and Figure 8.17 respectively).

**a. Base run 1**: The RCCS facility uses water from the *Outlet Tank 1* and returns to the *Outlet Tank 1***.** The *Small Tank 1* and *Small Tank 2* are not used in this setup.

- The ball valve connected to the *Outlet Tank 1* should be OPEN.
- The valve connected to the T-junction facility should be OPEN.
- The valve *V-ot1* should be OPEN.
- Verify the directions of the two 3-way valves, i.e. *3-way V-1* and *3-way V-2*, in order to let the water goes through the *Pump 1* and *Pump 3*.
- Depending on the considered flowrates, one can adjust the pump power by regulating the frequency converter attached on the wall next to the RCCS facility.
- Each pump supplies the water to 2 risers whose mass flowrates can be regulated by the valves, noted by *V-riser1, V-riser2… V-riser6***,** and the corresponding values can be read by the flowmeters, i.e. *FM1, FM2…FM6*.
- The RCCS plenum has two exhaust outlets that are able to return the water to the *Outlet Tank 1* and *Outlet Tank 2*. On each side of the exhaust outlet, there are two valves, i.e. *V-*

*out-1* and *V-out-2* or *V-out-3* and *V-out 4*, that can be adjusted to modify the return flows. In the current experimental runs, the *V-out-4* is closed while the other three valves are open so that the outlet flows are returned into the *Outlet Tank 1*.

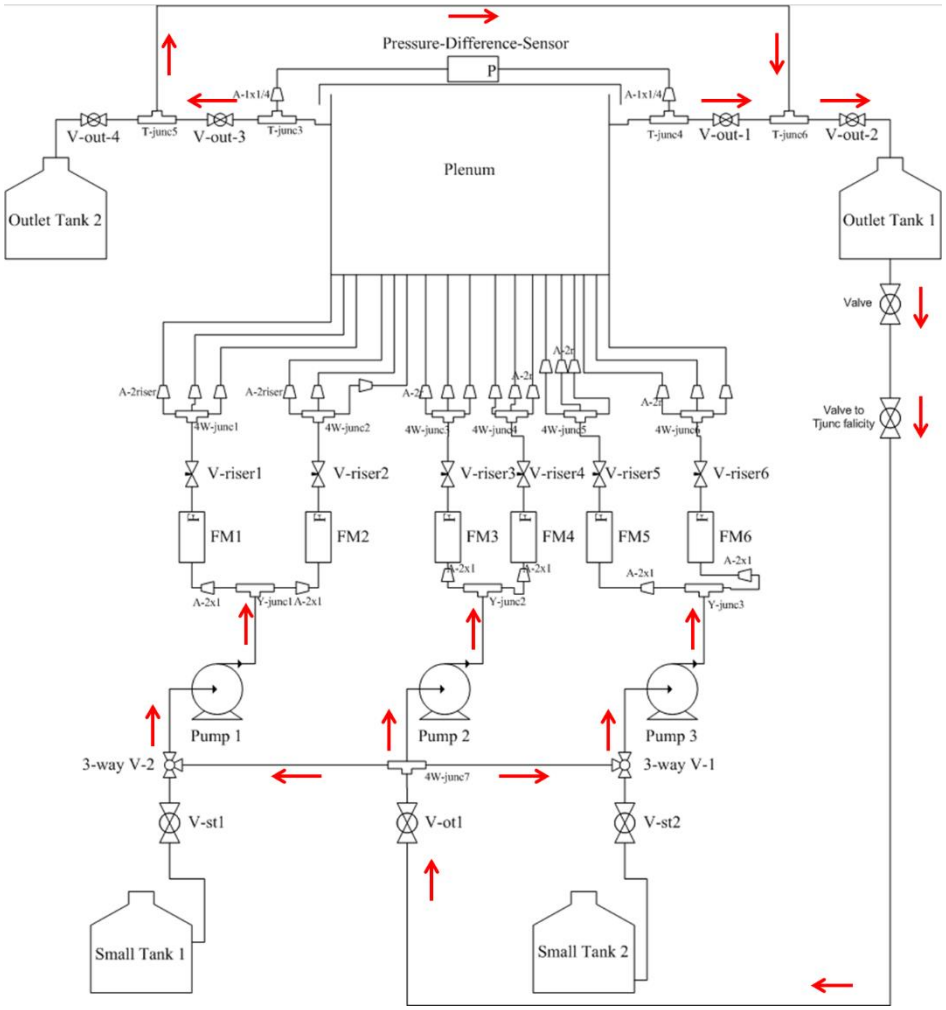


**Figure 8.16: Scheme of RCCS facility with flow direction for base run 1.**

**b. Base run 2:** The RCCS facility uses the water from the *Outlet Tank 1*, *Small Tank 1* and *Small Tank 2*, and returns to the *Outlet Tank 2***.** Water in the *Outlet Tank 1*, *Small Tank 1* and *Small Tank 2* can be adjusted to have different densities.

- The ball valve connected to the Outlet Tank 1 should be OPEN.
- The valve connected to the T-junction facility should be OPEN.
- The valves *V-st1***,** *V-ot1***,** and *V-st2* should be OPEN.
- Verify the directions of the 3-way valves, i.e. *3-way V-1* and *3-way V-2*, in order to let the water goes separately/isolately through the *Pump 1, 2* and ***3*** as desired.

- Depending on the considered flowrates, one can adjust the pump power by regulating the frequency converter attached on the wall next to the RCCS facility.
- Each pump supplies the water to 2 risers whose mass flowrates can be regulated by the valves, noted by *V-riser1, V-riser2… V-riser6***,** and the corresponding values can be read by the flowmeters, i.e. *FM1, FM2…FM6*.

For this setup, the *V-out-2* should be closed while the other three valves are open so that the outlet flows are returned into the *Outlet Tank 2*.

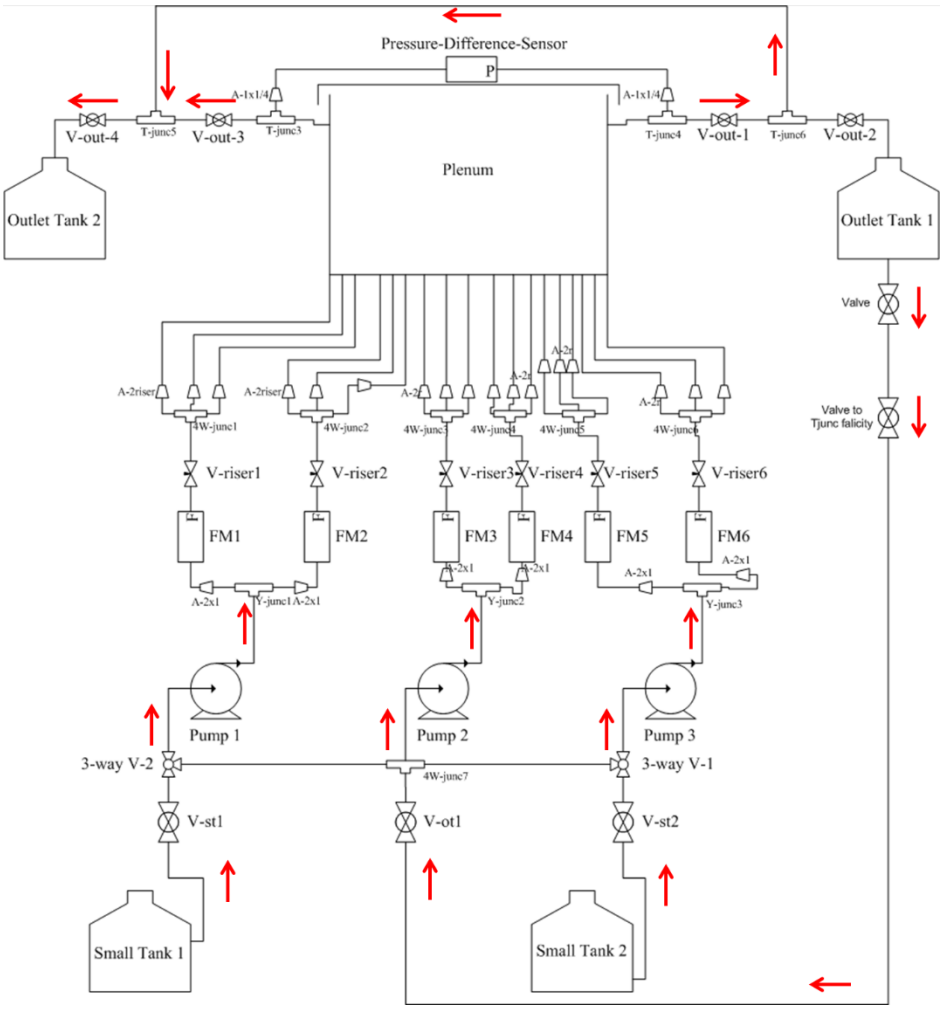


**Figure 8.17: Scheme of RCCS facility with flow direction for base run 2.**

# 9 RESULTS OF EXPERIMENTAL CAMPAIGN

Experimental tests have been conducted to study the flow characteristics of same density, turbulent risers vertically discharging into the plenum. Particle image velocimetry (PIV) measurements are performed along the central plane of the risers and the central plane of the plenum. Characteristics of the risers' flows inside the plenum are investigated to provide better understanding to the

behaviors of the RCCS system. Partial content of this report had been published in the proceedings of the NURETH 16 conference (see Nguyen, et al., 2015).

In the experiments presented in this report, tap water at room temperature was used as working fluid. Flow rates in each risers have been varied from 0.35 to 0.53 (l/s) yielding the mean velocities in the risers from 0.43 to 0.66 (m/s). The riser Reynolds numbers, which are based on the riser velocity $U_j$, the riser hydraulics diameter $D_r$, and the kinematic viscosity $\nu$, were $0.9\times10^4$ to $1.4\times10^4$. The *x, y* and *z* coordinates, respectively, represent the horizontal, vertical and spanwise directions. The origin of the coordinate system is at the bottom left corner of the plenum. The velocity components corresponding to the *x*, *y* and *z* directions are *U*, *V* and *W* for the time-averaged velocity and *u'*, *v'* and *w'* for the fluctuating velocity, respectively.

Particle image velocimetry (PIV) measurements have been performed on the RCCS facility with two configurations. In the first configuration (*c.f.* Figure 9.1 (a)), the risers were attached into the bottom wall of the plenum with an intrusion of 63.5 (mm). In the second configuration (c.f. Figure 9.1(b)), an acrylic plate with four attached spacers was placed on the bottom wall in order to make an additional bottom wall. Within this configuration, the outlet surfaces of the risers were at the same height of the bottom wall and discharged the water flow into the plenum.

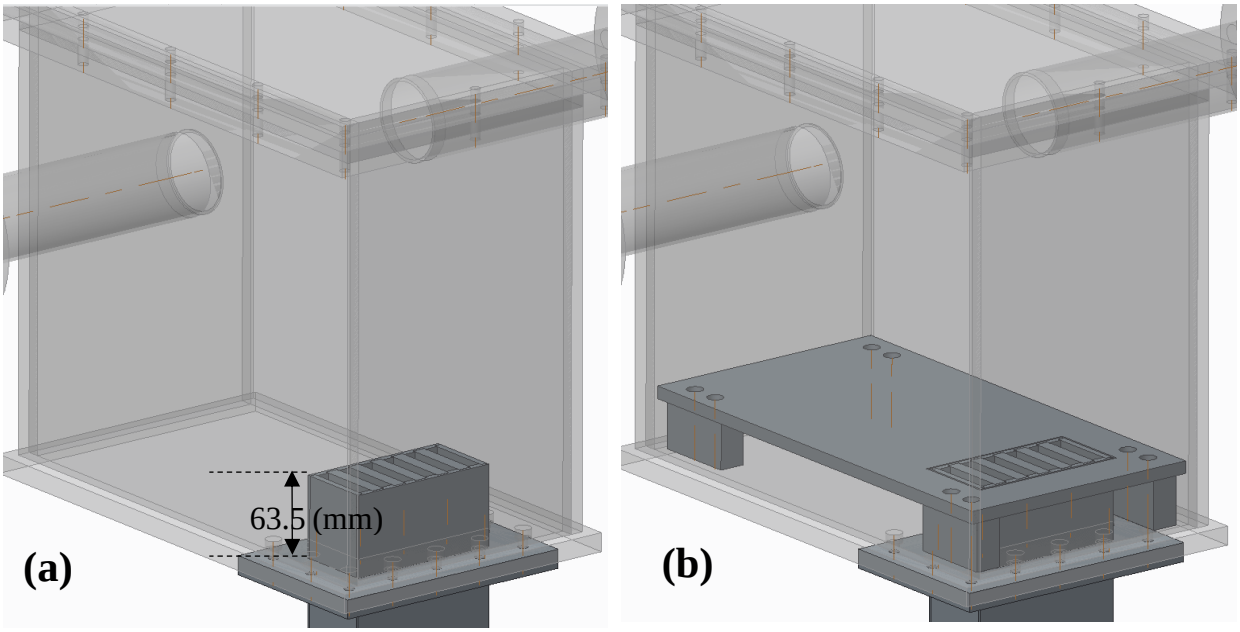


**Figure 9.1: Two experimental configurations considered in the RCCS facility. (a) The risers intruded 63.5 (mm) into the plenum volume, (b) the outlet surfaces of risers were at the same height of the bottom wall.**

Figure 9.2 shows the 2D2C PIV experimental setup. The flow characteristics in the region 1, formed by the middle plane of the risers (an *yz*-parallel plane), and the region 2, formed by the middle plane of a single riser nearest to the exhaust (an *xz*-parallel plane), were investigated by performing PIV measurements. The PIV system consisted of a high repetition rate Nd:YLF, double cavity, dual head laser (Photonics Industries) with an articulated light arm, two digital CMOS Phantom M340 cameras, a high speed controller and a computer. Each laser beam was capable of 35 mJ/pulse at the wavelength of 527 nm. These beams were adjusted by beam combination optics to form a 2-mm-thick laser sheet for the PIV measurements. The high-speed Phantom M340 cameras with a full resolution of 2560 × 1600 pixels, a pixel size of 10 × 10 $\mu m^2$ and 12-bit depth

captured PIV images and instantly stored them to the 12GB high-speed internal RAM. The high speed controller (LaVision model 1108075) controlled the synchronization between the lasers and the cameras. Seeding particles were hollow glass spheres with a mean diameter of 10 µm and were mixed in the storage tank. During the experiments, the water flow was driven from the storage tank, pumped into the plenum via the risers, and returned to the tank. The flow therefore was circulated and that tracers were present in the risers and the plenum.

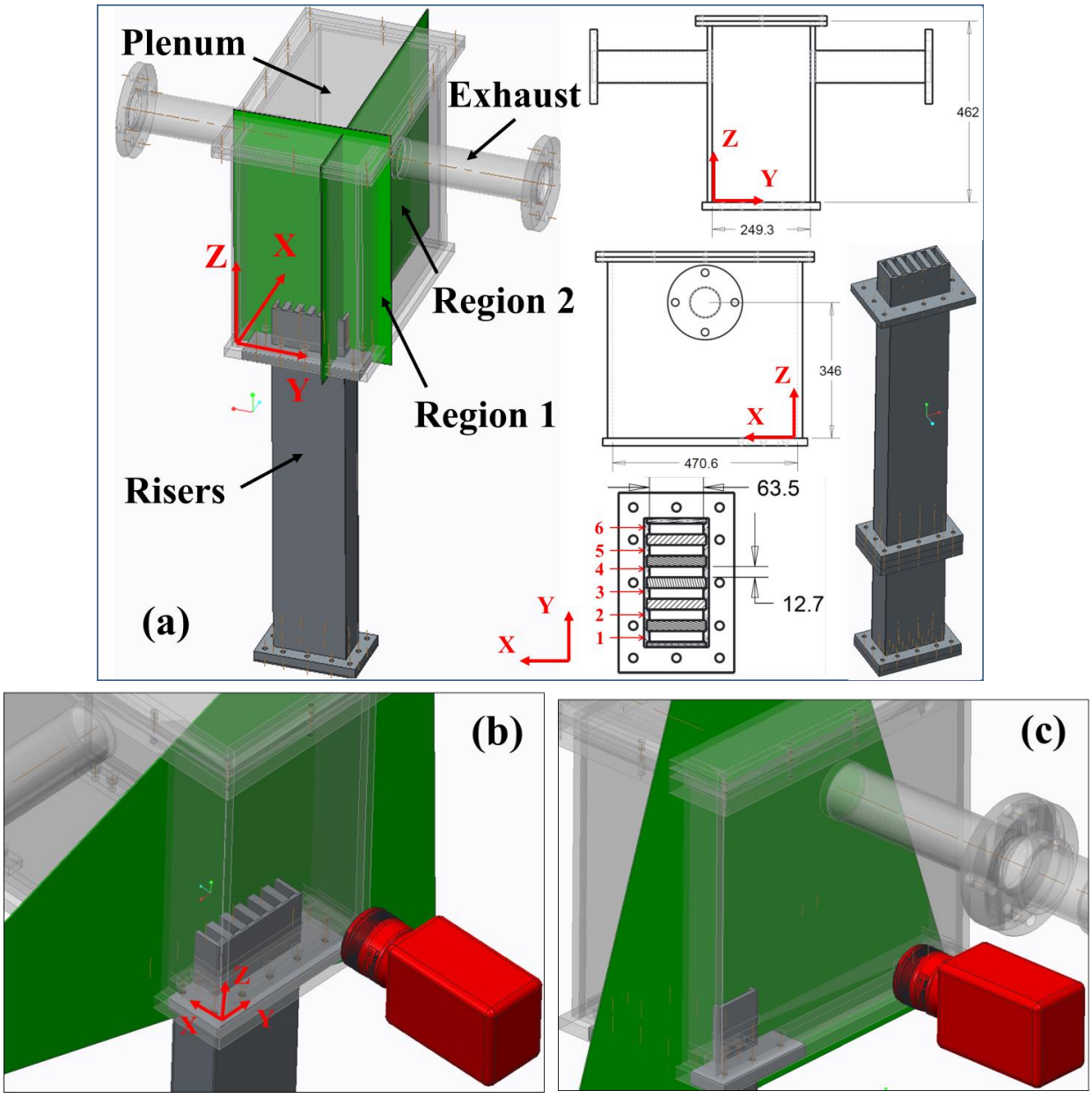


**Figure 9.2: Drawings and dimensions of the plenum and risers in the scaled facility (a), PIV experimental setups for region 1 (b) and region 2 (c).**

In the 2D2C PIV measurements, fluid images in the *yz* plane with $z/D_1$ ranging from 0 to 31 for the region 1, and fluid images in the *xz* plane with $z/D_1$ ranging from 0 to 28 for the region 2, were

taken. At each of the region (1 and 2), two cameras simultaneously recorded the particle images. Fields of views of two cameras were then adjoined to enlarge the measured area (see Figure 9.3).

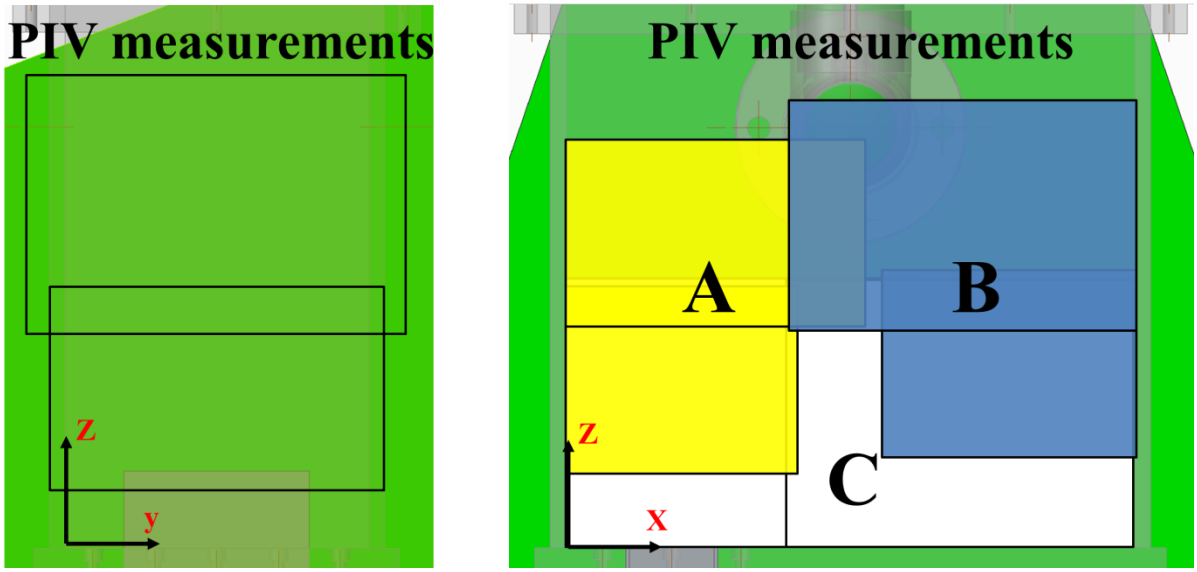


**Figure 9.3: Flow areas covered in the PIV measurements at the region 1 (left) and region 2 (right).**

The PIV system in the Experimental and Computational Multiphase Flow Group (ECMF), UofM can run in a single-frame mode and a double-frame mode. In addition, depending on the purposes of the investigations, image acquisition can operate at a high and low repetition frame rate. Results obtained by the PIV measurements at the high repetition rate can be used to reveal the dynamics flow structures, vortices generated by the risers and evolved in the plenum. On the other hand, results obtained by the PIV measurements at the low repetition rate are useful to characterize the flow characteristics and flow statistics such as mean velocity, turbulent kinetic energy, Reynolds stresses, etc. In the PIV experiments with high repetition rate, a sequence of 2013 images (2560 × 1600 pixels) in a single-frame mode was recorded during each run with a sampling rate ranging from 500 Hz to 700 Hz depending on the riser velocity. Within these frame rates, inter-pulse time delays, denoted by $\Delta t$, varied from 1428 μs to 2000 μs, yielding maximum particle displacements of 10 pixels.

Image acquisition and image processing were done with DaVis 8.2 software by LaVision Gmbh. The PIV experimental images were processed by an advanced image deformation multi-pass multi-grid PIV cross-correlation and a 50% window overlap. For both sets of measurements, the first pass started with an interrogation window of 64 × 64 pixels and the final pass ended with an interrogation of 32×32 pixels. Vectors were calculated from the correlation map with a Gaussian peak fit for sub-pixel accuracy (Raffael et al., 2007). Inside each pass, statistical validations were done to identify and replace erroneous vectors. A median filter (Westerweel, 1994) was applied and standard deviations of the neighboring vectors were used to filter spurious vectors. The grid spacing in the 2D2C PIV velocity vectors varied from 1.84 (mm) to 2.09 (mm) for regions 1 and 2, i.e. 0.14D1 and 0.16D1. The percentage of bad vectors for the PIV measurements approximated from 2% to 5%, respectively.

## 9.1 High-repetition PIV Measurements

This section presents the flow field results obtained from the high repetition PIV measurements on the RCCS facility with the configuration shown in Figure 9.1a. Experimental flow statistics calculated at the central plane of the risers (region 1) and at the central plane of the single riser 1 (region 2) are presented. Results obtained by the PIV measurements at the high repetition rate can be used to reveal the dynamics flow structures, vortices generated by the risers and evolved in the plenum.

### 9.1.1 First configuration: risers intruded 63.5(mm) into the plenum

#### *9.1.1.1 Results from the central yz-plane of the risers*

In this configuration, experimental images were taken at the central plane of risers and the water flow was discharged from different risers with various flow rates. Figure 9.4 shows contours of the time-averaged vertical velocity from the riser 3 and 4 at the riser Reynolds $Re_r = 0.9\times10^4$ and $1.4\times10^4$. Snapshots of instantaneous velocity vectors and vorticity colormaps are displayed to reveal the overall flow dynamics of the risers discharged into the plenum. In this flow configuration, fluid flow discharged from the two risers can be similarly considered as the two parallel plane jets/risers with a jet separation ratio, i.e. ratio of the jet axis distance and $D_1$, of 2, and an aspect ratio of 5. The vertical *z*-axis of the plenum is the plane of symmetry bisecting the distance between two risers. Details on the studies of two parallel jets can be reviewed in the work performed by Miller and Comings (1960), Tanaka (1974), Ko and Lau (1989), Lin and sheu (1990), Nasr and Lai (1990) and Durve et al. (2012). These authors have discussed that for the two parallel risers, three flow regions can be identified. The converging zone is the region from the riser exit to the merging point where the inner shear layers of the risers merge. A low-pressure zone close to the risers' wall and the inner shear layers is created by high entrainment rates in this region. This causes the individual riser flow to curve towards each other. The merging point is defined as the streamwise location where the mean streamwise velocity decays to zero (Nasr and Lai, 1990). Downstream of the merging point, two risers continue to interact with each other up the combined point, defined at the location where streamwise velocity reaches its maximum. Further downstream, the two risers merge to form a single flow pattern. However, compared to the above studies with non-confined parallel jets, flow patterns of the parallel risers in the current experimental configuration were expected to be more complicated because the risers discharged into the plenum with the confined walls and two exhausts.

It is noted that because the riser aspect ratio is 5, the discharged fluid flow from the riser exhibits the three-dimensional structures instead of the quasi-three dimensional patterns commonly found in many previous studies on rectangular jets with the aspect ratio larger than 20.

It can be seen from the Figure 9.4 that after being discharged into the plenum, the risers' flows started to interact with each other along the vertical axis. The riser moved towards the symmetry plane due to a mutual flow entrainment between them (Nasr and Lai, 1990). Time-averaged vertical velocity profiles at several streamwise distance from the riser exits in Figure 9.5 for the cases of two risers (3 and 4) at the Reynolds numbers $Re_r = 0.9\times10^4$ and $1.4\times10^4$ are well overlapped indicating that the Reynolds increase yields insignificant effect to the flow. Vortices were generated by the inner shear layers, rolled upward and appeared to combine or counterbalance each other. On the other hand, vortices created by the outer shear layers were convected by the riser flow further in the vertical direction until they impinged to the plenum top wall, deflect to the plenum corners.

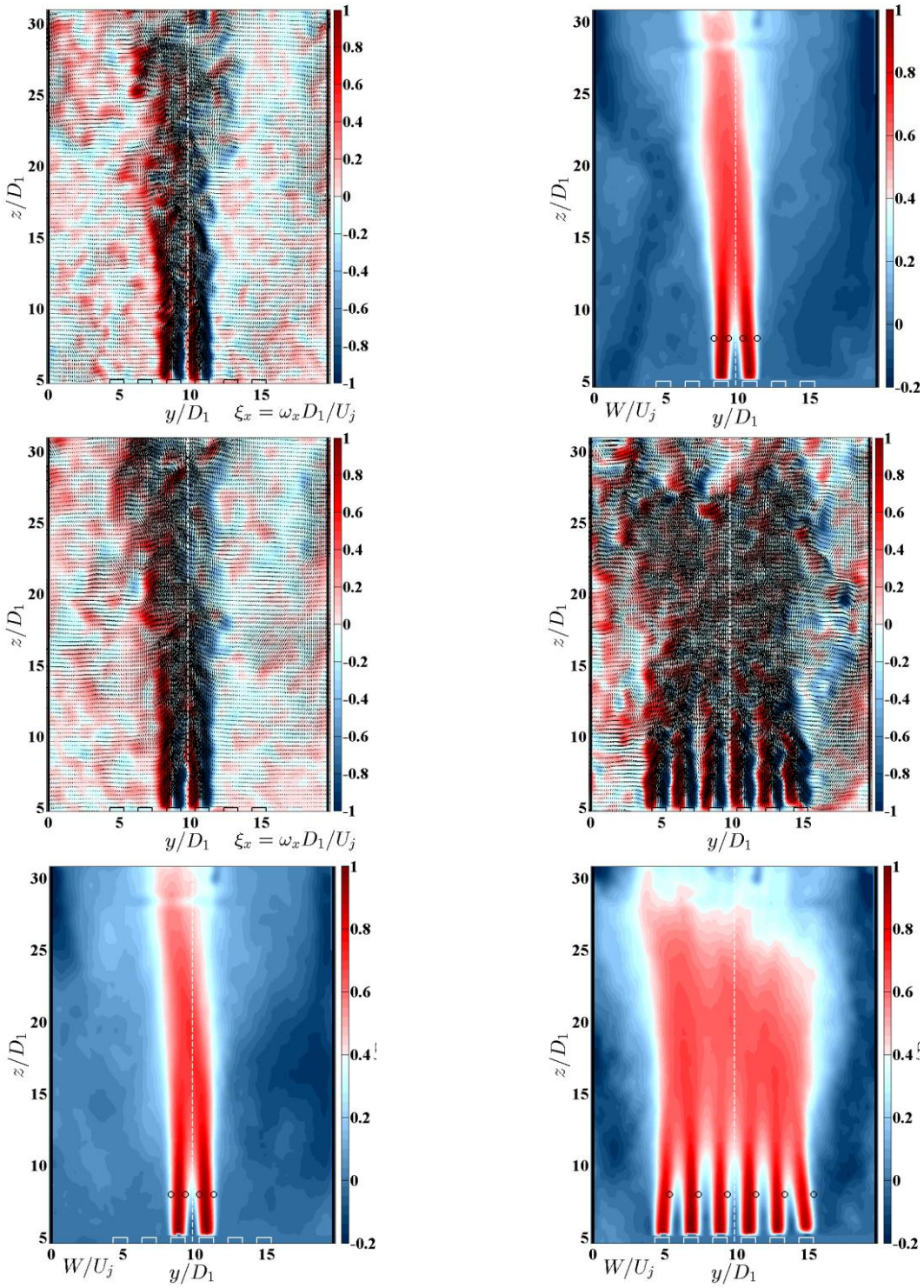


**Figure 9.4: PIV results obtained from the central plane of two risers (3 and 4) for $Re_r$ = $0.9\times10^4$ (top) and $1.4\times10^4$ (middle), and of six risers for $Re_r$ = $1.4\times10^4$ (bottom). Instantaneous velocity and vorticity (left) and time-averaged vertical velocity (right). Velocity and vorticity are normalized by the riser velocity and eddy-turn over time ($D_1/U_j$), respectively.**

It can be seen from the instantaneous velocity vectors and the contours of the mean vertical velocity that there are downward flows on the vertical walls. Such flow patterns were imprints of the secondary recirculation flow appeared at the top corners above the risers while the primary recirculation flow was present in the central volume of the plenum observed in the *xz*-plane PIV measurements. The primary and secondary recirculation flows will be discussed in the next section.

Contours of mean vertical velocity in Figure 9.4 indicate that after merging into the single pattern, the flow started to deviate to the left side of the symmetry plane. The asymmetrical flow of two parallel jets was also found by Ko and Lau (1989), who have reported that the loci of the maximum local mean streamwise velocity and the convecting of the inner and outer vertical structures are nearly parallel to the symmetry plane until $7.5D_j$. In the current configuration, there are several factors that may cause asymmetries in the risers' flow, such as the difference of risers' flow rates, the confinement, the presence of the exhausts, and the pressure difference between two flow exits via the exhausts. Maximum difference among the flow rates of the risers' flows was found to be less than 3% during the PIV experiments. The effects of the plenum confinement (i.e. the top, front and back walls), two exhaust pipes and the pressure difference between the outflows via the exhausts were probably concerned because those have driven the risers flow in the positive x-direction (perpendicular to the PIV measurement plane). The driven force yielded stronger effects to the vortical structures operating in the positive *x*-direction and that caused the combined flow curved toward one side.

The flow patterns and contours of the time-averaged vertical velocity for the case of six risers discharged into the plenum at $Re_r = 0.9\times10^4$ are displayed in Figure 9.4. The instantaneous velocity vectors and vorticity colormap show that the mutual risers' interactions, vortex generation by the shear layers, merging and counterbalancing of vortices, which have been discussed above, were strongly enhanced by the presence of discharged flow from six risers. This figure illustrates a high population of spanwise (*x*-direction) vortices at the size of riser width $D_1$ and a high degree of three-dimensionality of the flow. These vortical structures were also observed near the vertical wall resulting to the downward flows in those flow regions. Moreover, the downward flows increased their penetrations in the negative z-direction and interacted with the two outward risers' flows, i.e. riser 1 and 6. These interactions yielded the two risers' flows curved towards the symmetry plane as can be seen in the contour of mean velocity.

The time-averaged vertical velocity profiles at several vertical distances overplotted in Figure 9.5 have confirmed these interactions. The velocity profiles at $z/D_1 = 6$ and each individual profile of six risers are identical to those from the case of two risers (3 and 4). The overall shapes of the two outward velocity profiles, i.e. locations of the local maximum and minimum peaks, have changed from the location $z/D_1 = 10$ indicating these two risers' flows curvature towards the symmetry plane. The plots of velocity profiles also show that all the risers' flows start to form a single flow pattern from a certain vertical location, around $z/D_1 = 15$ to 16, where all the velocity peaks are nearly flat. It is interesting to find that the merging points, where $W/U_{j\text{-centerline}} = 0$, determined for the cases of two risers and six risers discharged into the plenum were nearly identical, i.e. ranging from $6.5D_1$ to $6.6D_1$. Downstream of the merging point, the risers' flows merged at the combined point of $z/D_1 = 15$ for the case of two risers and $Re_r = 0.9\times10^4$, while the combined point of $z/D_1 = 19.2$ was found for the case of two and six risers and $Re_r = 1.4\times10^4$. The profiles of the r.m.s fluctuating vertical velocity yielded peaks inside the merging region, which was similarly found in Dave et al. (2012), and gradually increased from the combined point. On the other hand, vortices created by the outer shear layers were convected by the riser flow further in the vertical direction

until they impinged to the plenum top wall, deflected to the plenum corners. It can be observed from the instantaneous velocity vectors and the contours of the mean vertical velocity that there are downward flows on the vertical side walls.

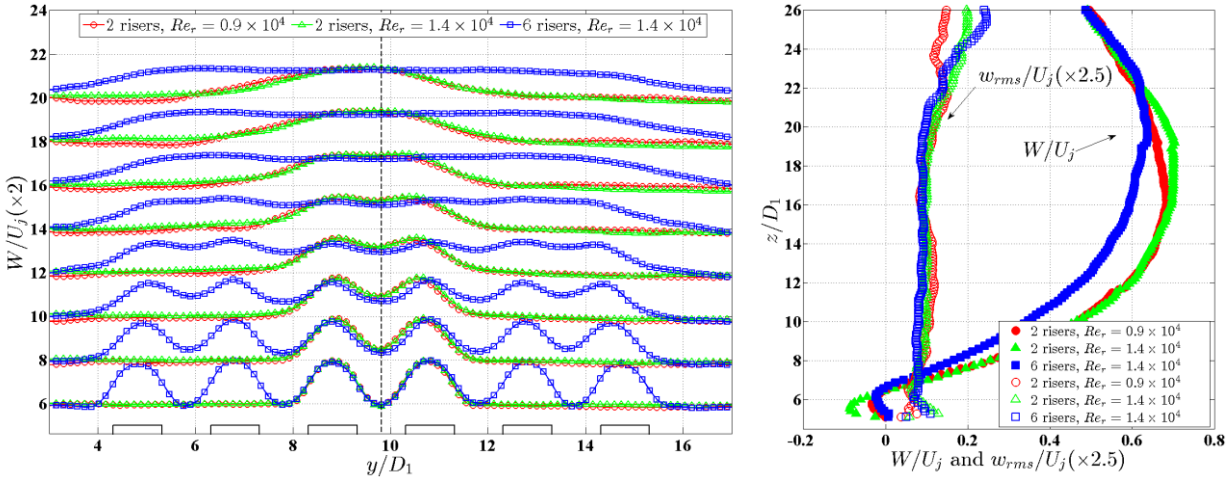


**Figure 9.5: Time-averaged vertical velocity profiles at several vertical (streamwise) distance from the riser exits obtained by the PIV measurements at the yz-plane (left), time-averaged vertical velocity and root-mean-square fluctuating vertical velocity along the riser centerline (right).**

Figure 9.6 shows the power spectra of the fluctuating velocity *v'* (y-direction) versus the Strouhal number, which is defined by $St = fD_1/U_j$, at points 1-4 for the riser Reynolds $Re_r = 0.9\times10^4$ and $1.4\times10^4$. These points were located in the outer and inner shear layers of two risers (see points from left to right in Figure 9.4) and have a distance of $3D_1$ from the riser exit. In the spectral distribution of velocity fluctuations at the inner shear layer, i.e. $y/D_1 = 9.135$ and 10.135, and $z/D_1 = 8$, a dominant Strouhal number St=0.27 was found that is close to the value of $St = 0.273$ obtained by Namer et al. (1998) for the turbulent plane jet at $Re = 6000$. On the other hand, spectral distributions obtained at the points located in the outer shear layer, i.e. $y/D_1 = 8.135$ and 11.135, showed different dominant frequencies at two Reynolds numbers. The wide ranges of frequency detected in the spectral distributions can be explained by the appearance and the penetration of the surrounding vortices into the riser core flows. These vortices returned to the core flows after impinged to the plenum top wall, or those from the downward flows at the plenum vertical walls, and interacted with the vortices that were just generated from the shear layers.

Figure 9.7 displays the spectral distributions of fluctuating velocity *v'* (*y*-direction) versus the Strouhal number at points 1-6 (see points from left to right in Figure 9.5) located in the inner shear layers of six risers for the riser Reynolds numbers $Re_r = 0.9\times10^4$ and $1.4\times10^4$. Similar to the detected dominant frequency of points located in the inner shear layers of two risers, the Strouhal numbers of $St = 0.25$ and 0.27 were seen in the spectral distributions of the points in the inner shear layers of six risers. However, these Strouhal numbers did not always correspond to the most dominant frequency, i.e. points 2 and 5, indicating that the flow fields contained many vortices generated from the six risers and their interactions. Several peaks in the power spectral of point 6, which was located in the outer shear layer, show the similar flow phenomenon of the penetration of surrounding vortices into the riser flow.

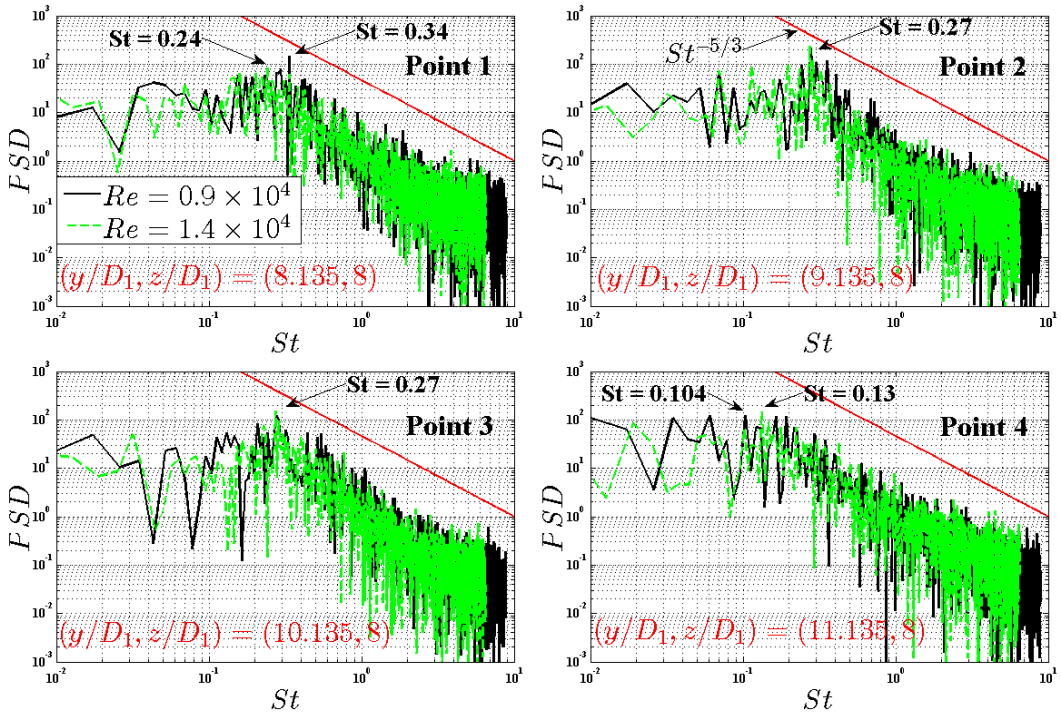


**Figure 9.6: Power spectra of fluctuating velocity v' (y-direction) at points 1-4 (points from left to right in Figure 9.4) located in the shear layers obtained by PIV measurements in the central plane of two risers (3 and 4) for $Re_r = 0.9\times10^4$ (solid black) and $1.4\times10^4$ (dash green).**

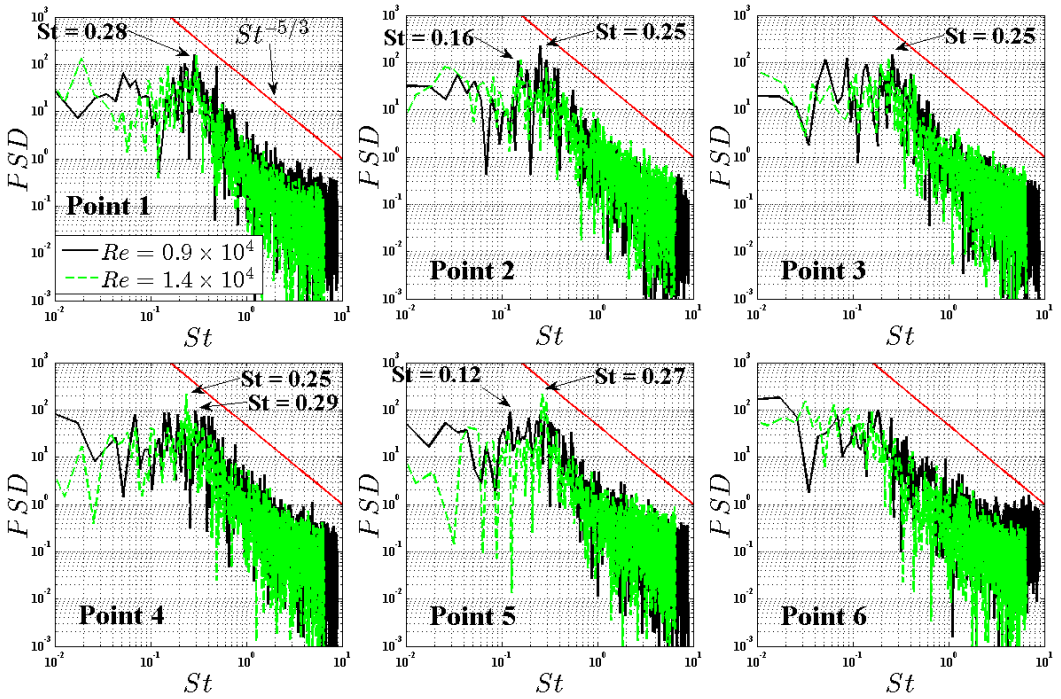


**Figure 9.7: Power spectra of fluctuating velocity v' (y-direction) at points 1-6 (points from left to right in Figure 9.4) located in the shear layers obtained by PIV measurements in the central plane of six risers for $Re_r = 0.9\times10^4$ (solid) and $1.4\times10^4$ (dash).**

### *9.1.1.2 Results obtained from the central xz-plane of the single riser*

In this configuration, images of fluid flow in the central plane of the single riser, i.e. riser 1, were taken while the PIV cameras were arranged and placed at several positions.

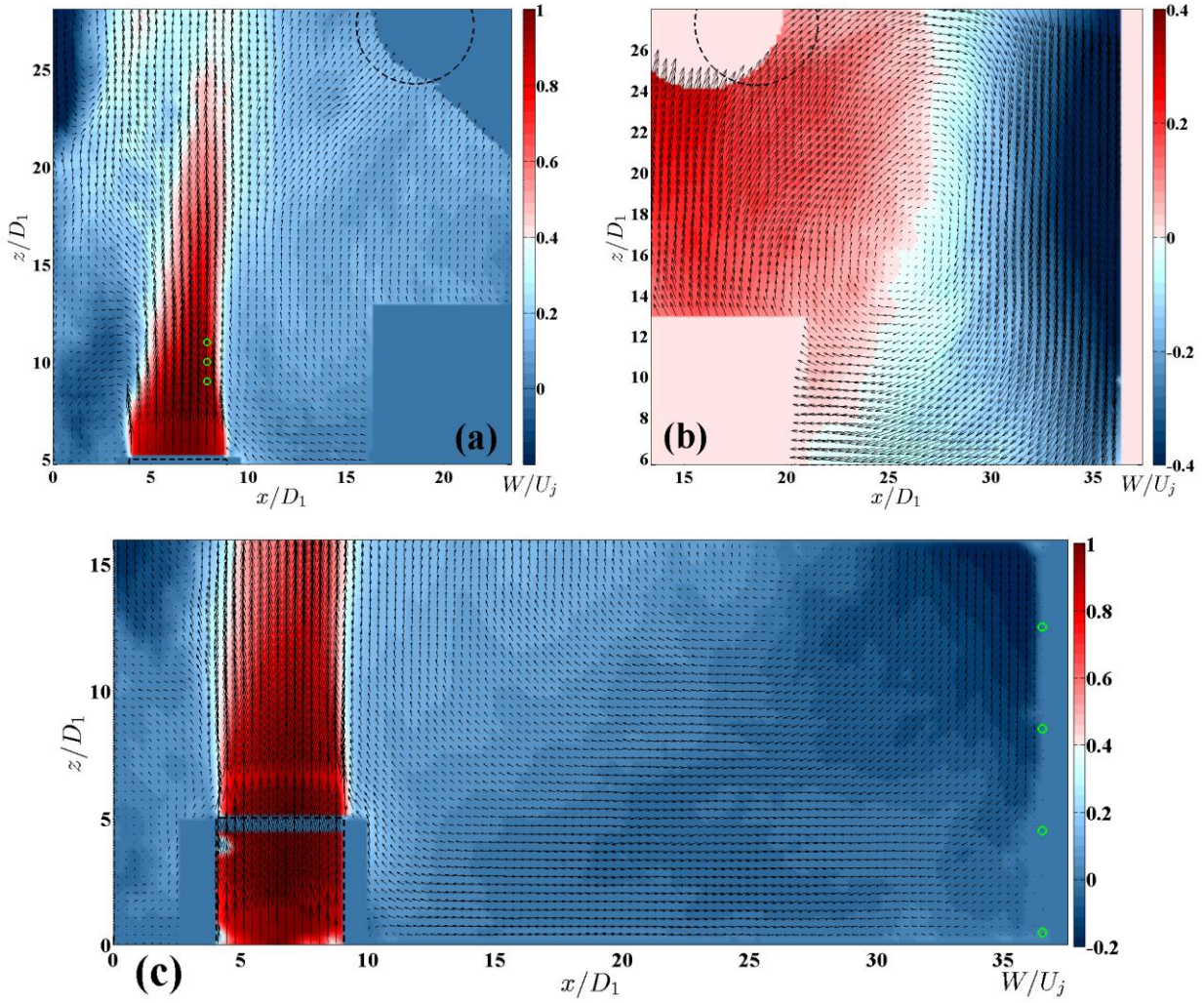


**Figure 9.8: Time-averaged velocity magnitude obtained by PIV measurements in the central plane of the single riser. PIV results and at the area A (a), B (b) and C (c) for $Re_r = 0.9\times10^4$**

Figure 9.3(*right*) shows the areas of the fluid flow in the region 2 measured by the PIV measurements. In these PIV measurements, images of three fluid areas in the *xz*-plane, i.e. A, B and C, were separately captured. For each area, two cameras recorded the experimental images and the obtained velocity vector fields were then merged to provide larger fields of views. Coordinates of the bottom left and top right corners of the measured areas by two cameras were given here. The area A covered ($x/D_1$, $z/D_1$) from (0, 5) to (13.8, 14.9), and from (0, 13.1) to (19.1, 25.2). The area B ranged from (12.2, 13) to (36.2, 28.3), and from (20.9, 5.8) to (36.2, 15). The area C ranged from (0, 0) to (25.6, 16.1), and from (11.8, 0) to (36, 15.5).

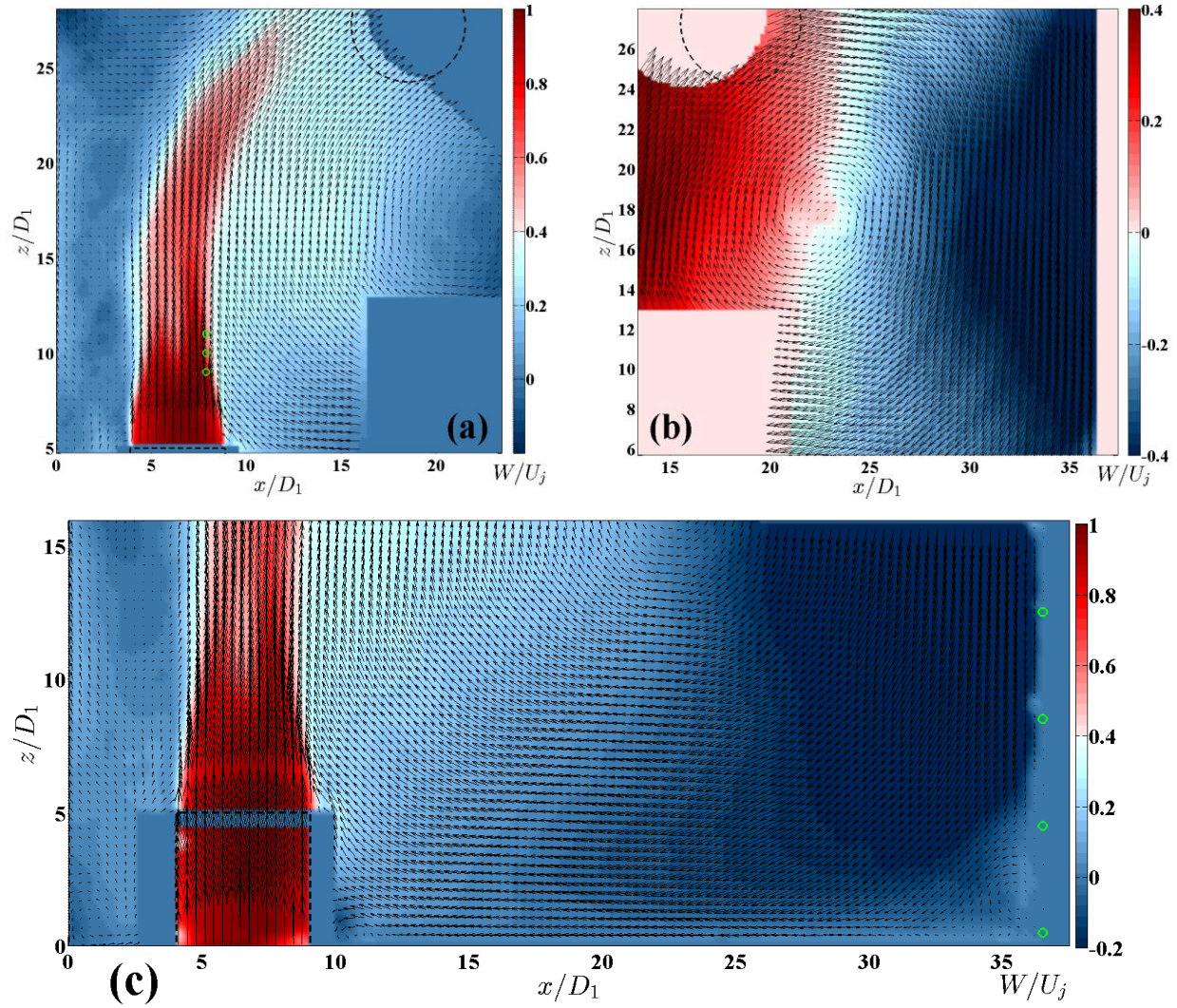


**Figure 9.9: Time-averaged velocity magnitude obtained by PIV measurements in the central plane of the single riser. PIV results and at the area A (a), B (b) and C (c) for $Re_r = 1.4\times10^4$.**

Figure 9.8 and Figure 9.9 show the mean velocity vectors and the contours of the vertical velocity component that were obtained from the PIV measurements in the region 1 and at the area A, B and C for the riser Reynolds numbers for $Re_r = 0.9\times10^4$ and $1.4\times10^4$, respectively. The velocity vectors were normalized by the riser velocity while the horizontal and vertical axes were normalized by the jet width $D_1$.

Effects of an increase in the riser Reynolds number can be seen from the contours of the PIV measurements at the area A where the riser penetrated further into the plenum and its flow curvature was strongly curved towards the exhaust at $Re_r = 1.4\times10^4$. At both Reynolds numbers, the secondary recirculation flows were observed at the top left corner of the plenum. The recirculation region created by the riser flow at $Re_r = 1.4\times10^4$ extended wider in the x-direction because of the riser's greater penetration and its impingement to the plenum top wall. The downward flows found in the PIV experiments at the region 1 (see section 3.1) were caused by the presence of the secondary recirculation flows in the area A. Moreover, the presence of the primary

recirculation can be seen in the central volume of the plenum and its region was separated with the secondary recirculation by the riser's bulk flow. The velocity vectors and colour contours (rescaled to $\pm 0.4W/U_j$ for better visualizations) obtained by the PIV measurements in the area B revealed clearer views of the primary recirculation flows. The increase of riser Reynolds numbers has shifted the center of the primary recirculation region from ($x/D_1$, $z/D_1$) = (25.8, 16.1) for $Re_r$ = $0.9\times10^4$ to ($x/D_1$, $z/D_1$) = (23, 17.5) for $Re_r$ = $1.4\times10^4$. Ratios of the vertical velocity component magnitude to the riser velocity and the width of the return flow region near the vertical right wall also increased in associated with the increase of Reynolds number. The return flow was formed near the vertical wall, directed in the negative *z*-direction and was rather similar to the wall jet flow until it reached the plenum bottom corner. Results obtained from the PIV measurements at the area C partially show the lower regions of the primary recirculation and the bottom corners of the plenum. No recirculation region was visible at the bottom corners at $Re_r$ = $0.9\times10^4$, while two recirculation regions, one with the size $3D_1$ at the bottom right and one with the size of $3D_1$ at the bottom left, were clearly observed at $Re_r$ = 1.4×104. The expansion of the primary recirculation region in size and magnitude probably affected the width of riser flow after the riser exit. At $Re_r$ = 1.4×104, the primary recirculation penetrated deeper into the riser core compared to that effect caused by the secondary recirculation. Both penetrations of the primary and secondary recirculation flows thinned the riser width and yielded two local peaks inside the riser flow.

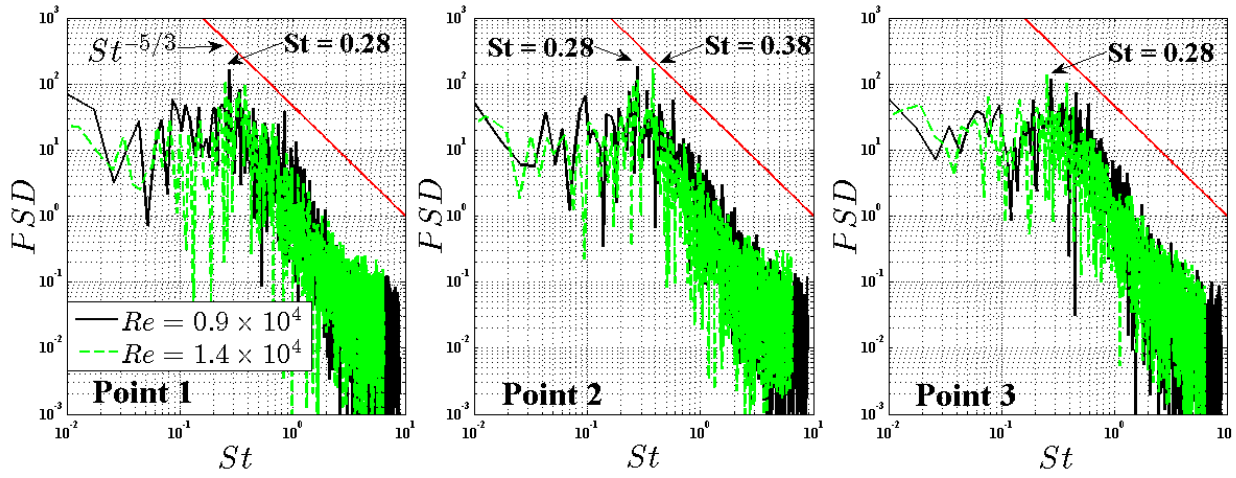


**Figure 9.10: Power spectra of fluctuating velocity u' (x-direction) at points 1-3 (points from bottom to top in Figure 9.8, area A) located in the shear layers obtained by PIV measurements in the central plane of the single riser for $Re_r = 0.9\times10^4$ (solid) and $1.4\times10^4$.**

Figure 9.10, spectral distributions of the fluctuating velocity *u'* (*x*-direction) at three points obtained by the PIV measurements at the area A for the riser Reynolds numbers of $0.9\times10^4$ and $1.4\times10^4$ are shown. These three points (see points from bottom to top in Figure 9.8) were located in the shear layer of the single riser. A dominant Strouhal number *St* = 0.28 is observed that is consistent to the dominant Strouhal number found from the spectral distributions of the other points located in the inner shear layers of the risers' flows. It is mentioned above that due to the riser aspect ratio of 5, the risers' flows generate high populations of vortices from the shear layers formed on both dimensions $D_1$ and $D_2$. The single dominant Strouhal number found on several points located in the shear layers indicated that the vortex generation mechanism is governed by the same dominant frequency. However, in the region characterized by interactions of generated

vortices and those returned after impinging to the confinement wall, the wide range of frequency was observed as in the outer shear layers of the risers.

Figure 9.11 shows spectral distributions of the fluctuating velocity *u'* (x-direction) at four points, which were located near the plenum vertical wall, obtained by the PIV measurements at the area C for $Re_r = 0.9\times10^4$ and $1.4\times10^4$. It is interesting to find that in this region, the dominant Strouhal numbers of $St = 1.89$ and 0.67 were detected for the riser Reynolds number of $0.9\times10^4$ and $1.4\times10^4$, respectively. As shown in the PIV mean velocity vectors, the return flow formed like the wall jet flow near the vertical wall and directed in the negative *z*-direction. However, vortical structures in this region originate from those generated by the risers; their sizes are comparable to the riser width $D_1$. Populations and rolling motions of the large-scale structures strongly depend on the $Re_r$ when more vortices are generated from the riser exits and travelled further into the plenum volume, impinged to the wall. These have yielded the difference in the Strouhal numbers found in this are for the two Reynolds numbers.

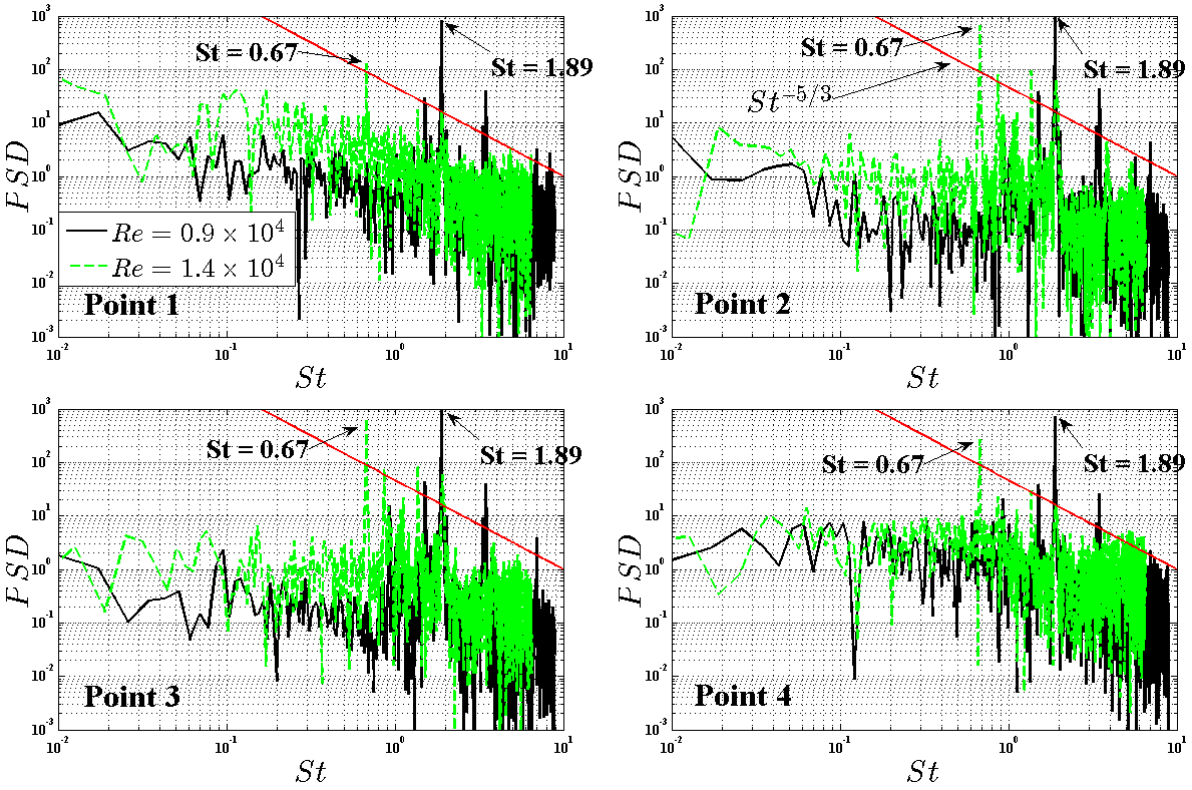


**Figure 9.11: Power spectra of fluctuating velocity u' (x-direction) at points 1-4 (points from bottom to top in Figure 9.8, area C) located near the plenum vertical wall obtained by PIV measurements in the riser central plane for Rer = 0.9×104 (solid) and 1.4×104 (dash).**

## 10 Improvements of the PIV Measurements

PIV systems are used to obtain velocity information by tracking particles between a pair of images. Careful alignment of the calibration targets and monitoring of the PIV's synchronization unit, which synchronizes the cameras and laser, must be monitored. To improve the alignment of the calibration target, an acrylic holder with two legs was made to be able to fix the target at different locations during the calibration process. This holder helped decrease errors created by

misalignment of the calibration target between different measurements. The holder is shown in Figure 10.1, and the acrylic legs can be inserted in any of the 6 risers.

A PIV system consists of three main hardware components: a laser, a camera, and a synchronization unit. Depending on the speed of the laser and the cameras, different flows can be studied with different recording modes. Two common recording modes are: single-frame single-exposure (SFSE) and double-frame double-exposure (DFDE). From these two modes, DFDE is often used to calculate statistical quantities of the flow. SFSE can also be used to obtain statistical quantities, but it requires more images to be recorded because the SFSE images are recorded for shorter time intervals. One of the limitations that is faced when recording images for PIV purposes, is that there is not enough memory to record large areas of interest for a long period of time. The cameras of the LaVision PIV system that were previously used, store the recorded images in the camera's memory, which allowed for continuous recordings for up to 2013 images (at full resolution). However, many more images are necessary for the convergence of statistical quantities such as mean velocity and the Reynolds Stresses. Once the memory is full, the images are transferred from the camera's memory to a computer which takes approximately 20 minutes before being able to start recording again, this not allowing continuous measurements. To address this issue, two other PIV systems with different cameras were tested.

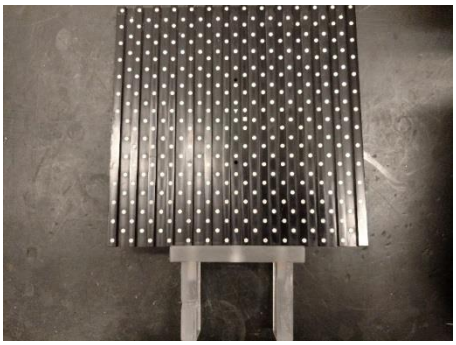

**Figure 10.1: Calibration target with holder.**

**a)** **b)**

**Figure 10.2: a) PIV system assembled in the ECMF laboratory, and b) Calibration target with a small recording area (red).**

The first PIV system that was tested was manufactured by TSI. This system allows only for image recording in DFDE mode and the recorded images are transferred directly to the computer's hard drive – which allows continuous measurement until the computer's hard drive is full. In addition, a second PIV system assembled at the ECMF laboratory at UM was tested as well.

The assembled system, shown in Figure 10.2a, provides some more options than the TSI system. One of the most important options is that this system allows us to record smaller areas by cropping the recording area – this allows for faster recording rates for longer periods of time (continuous recordings). Figure 10.2b shows a small red area which can be selected as a smaller recording region that can be moved on the plane to scan through the whole image. By only recording a smaller region, the images can be recorded at a faster rate to obtain information from different time scales. The improvement of this system allows creating larger continuous data sets for the convergence of the statistical quantities.

## 10.1 Experimental runs and data processing – Configuration without Acrylic Step

The experiments conducted were in constant-density conditions at Re= $0.9\times10^4$ and $1.38\times10^4$ respectively. The configuration and axis is shown in Figure 10.3. To achieve statistical convergence for any of the quantities of interest, the sampling frequency must be low (to ensure independent sampling) and the number of samples must be high. Double-Frame Double-Exposure was chosen to meet these two criteria. Traditionally, most PIV systems had acquisition frequencies up to 30Hz for this reason (Smith and Neal, 2016). By sampling at a lower rate, however, information about the flow happening at higher frequencies may not be captured. Thus, to achieve statistical convergence, and to capture information at higher frequencies, 50Hz was selected as the recording frequency. The information about the six experiments performed are provided in Table 10.1.

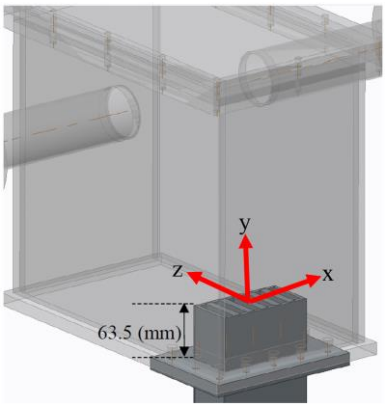


**Figure 10.3: RCCS configuration without acrylic step. Axis is shown in red.**

**Table 10.1: Experiments performed and the corresponding fluid temperature**

| Experiment: | R3-R4 | R2-R5 | R1-R6 | R3-R4 | R2-R5 | R1-R6 |
|---|---|---|---|---|---|---|
| Re | $1.38\times10^4$ | $1.38\times10^4$ | $1.38\times10^4$ | $9\times10^4$ | $9\times10^4$ | $9\times10^4$ |
| Temperature [°C] | 23.06 | 22.95 | 23.19 | 23.31 | 23.06 | 23.5 |

The instantaneous velocity vector fields were obtained using LaVision's DaVis 8.4.0. The vector fields were then used to calculate turbulence statistics along with their corresponding uncertainty estimations. The velocity mean, velocity fluctuations, and the Reynolds stresses were calculated using equations (1), (2), and (3), respectively.

$$\overline{u_i} = \frac{1}{N}\sum_{k=1}^{N} u_i(k) \tag{1}$$

$$u_i'(k) = u_i(k) - \overline{u_i} \tag{2}$$

$$\overline{u_i'u_j'} = \frac{1}{N-1}\sum_{k=1}^{N} u_i'(k)u_j'(k) \tag{3}$$

Here $u_i(k)$ is the instantaneous velocity, $\overline{u_i}$ is the mean velocity, $u_i'(k)$ is the turbulent fluctuation, and $\overline{u_i'u_j'}$ are the Reynolds stresses. In this section, the velocity components u, v, and w have directions x, y, and z, respectively. We note that the subscripts i and j are also sometimes used to represent the x and y directions on the plane of measurement (e.g., $u_1 = u;\ u_2 = v;\ and\ \overline{u_1'u_2'} = \overline{u'v'}$).

Uncertainty analysis plays an important role in experimental and numerical investigations. Often, there are minor variations in the experimental results from measurement to measurement. By providing an uncertainty and its associated confidence level (usually 95%) (Coleman and Steele, 2016), the repeatability of a measurement can be assured. The equation for the propagation of uncertainty is (Mostafa, et al., 2000):

$$\sigma(R) = \left\{\sum_{k=1}^{N}\left(\frac{\partial R}{\partial X_i}\sigma(X_i)\right)^2\right\}^{1/2} \tag{4}$$

where the contribution from the uncertainty of each variable, $\sigma(X_i)$, is taken into account. Here, the relative error due to drag of the seeding particles, and the relative error due to the correlation functions used for vector calculations are taken into account.

Given the variables with sources of uncertainty, the random error component for each of the variables can be calculated (for a confidence interval of 95%):

$$\sigma_{re}(X_i) = \frac{tS(X_i)}{\sqrt{N}} \tag{5}$$

where t is the Student's t-distribution , S is the standard deviation of $X_i$, and N is the number of samples. Furthermore, the statistical uncertainty for the Reynolds stresses can estimated by (Sullivan, 2017):

$$\frac{\sqrt{N-1}}{\chi_L}\overline{u_i'u_j'} \le \overline{u_i'u_j'} \le \frac{\sqrt{N-1}}{\chi_U}\overline{u_i'u_j'} \tag{6}$$

Here, N is the total number of samples and $\chi_L$ and $\chi_U$ are the lower and upper bounds of the square root of the $\chi^2$ values. We note that the uncertainties for the higher order moments are not symmetric.

## 10.2 Low-repetition PIV Measurements

Vortex shedding between parallel plane jets has been reported previously in literature. Since neighboring jets constantly interact due to their proximity, these jets oscillate from side to side under certain conditions. An additional complexity added to these jet interactions in the RCCS facility is that the outlets are offset from the streamwise direction. As a result, the jets curve towards the outlets once a certain height is reached. These three-dimensional effects caused by the geometry of the facility may introduce different phenomena that has not been observed in plane jets. For this reason, a larger number of samples might be needed.

First order moments (i.e., mean velocities) often require a smaller number of samples to achieve convergence than higher order moments (e.g., the Reynolds stresses). For this reason, we checked for statistical convergence of the Reynolds stresses by random sampling velocity vectors from the total set of recorded images and computing their respective Reynolds stresses. The location that was selected was the outer shear layer region because this region is more sensitive to small variations in the flow. The convergence plots are shown in Figure 10.4. From these plots, we determined that using 30k image pairs at a recording frequency of 50Hz would be sufficient to achieve statistical convergence of the Reynolds stresses.

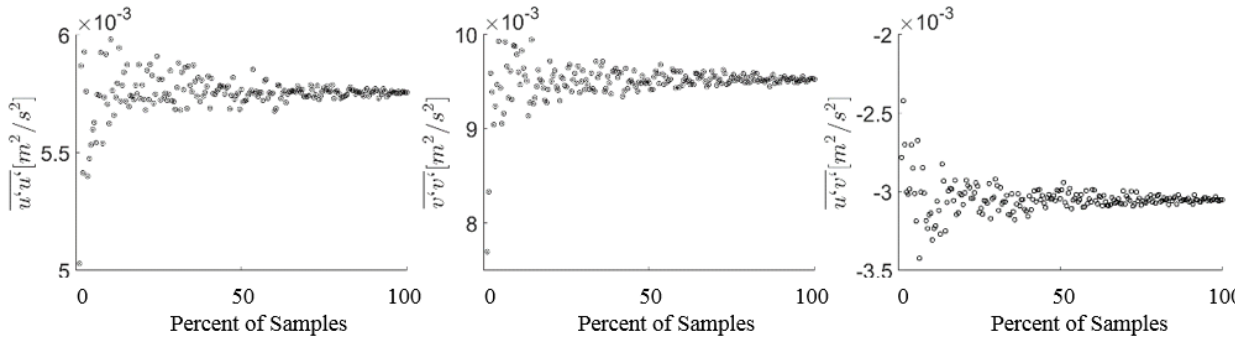


Figure 10.4: Convergence plots of the Reynolds Stresses, $\overline{\boldsymbol{u'u'}}$ (left), $\overline{\boldsymbol{v'v'}}$, (middle), and $\overline{\boldsymbol{u'v'}}$ (right), in the shear layer region at $\boldsymbol{x/L_1 = -1.5}$ ***and*** $\boldsymbol{y/L_1 = 1}$ for the case with two jets for Re=1.38×10$^4$.

## 10.3 Turbulence Statistics

Time-averaged velocity (mean velocity) profiles are first order moments of the instantaneous velocity fields. These mean velocities are often analyzed because of their rather straightforward description of the flow. Further information, however, can be obtained from investigating second order moments of the instantaneous velocity fields (i.e., the Reynolds stresses). In addition to improving our understanding of what is happening physically, the profiles from our field data allow us to investigate the impact of the number of jets on our experiments. With this in mind, these profiles of the time-averaged velocity and the Reynolds Stresses (along with their corresponding uncertainty bands) were plotted to investigate the interaction between the rectangular jets in the RCCS facility. We note that the legends R3-R4, R2-R5, and R1-R6 are for the measurements of risers 3-4 (two jets), 2-5 (four jets), and 1-6 (six jets), respectively.

### 10.3.1 Time-Averaged Streamwise velocity for Re=1.38×10$^4$

Fields and profiles of the streamwise mean velocity, $\overline{v}$, for two, four, and six risers with Re=1.38×10$^4$ are provided in Figure 10.5. From these fields, we observe common characteristics between the three cases. For R3-R4, we observe that the jets merge at approximately $y/L_1 \approx 1$. On the other hand, in R2-R5, jets R2-R3 and R4-R5 converge separately, and, as a result, the streamwise distance at which the converging region occurs between the two inner jets increases. Finally, for the case R1-R6, the jets appear to repel each other. It is interesting to note that the height at which the converging region occurs remains generally the same, with the exception of the converging region of the two middle jets, which is slightly higher.

Next, we compare the velocity profiles at various axial locations for different numbers of jets. At $y/L_1 \approx 1$, we notice that we have fully developed velocity profiles for all of the jets, and that the peaks in the profiles of the two middle jets match quite well for all of the measurements. We notice that $\overline{v}$ is slightly negative closer to the walls for the R3-R4 and R2-R5 measurements, while the velocities near the walls of R1-R6 are positive, indicating the presence of flow entrainment caused by the strong current that the six jets generate. The velocities away from the main flow regions, however, need to be studied separately because the PIV measurements are only optimized for the regions with the largest particle displacements.

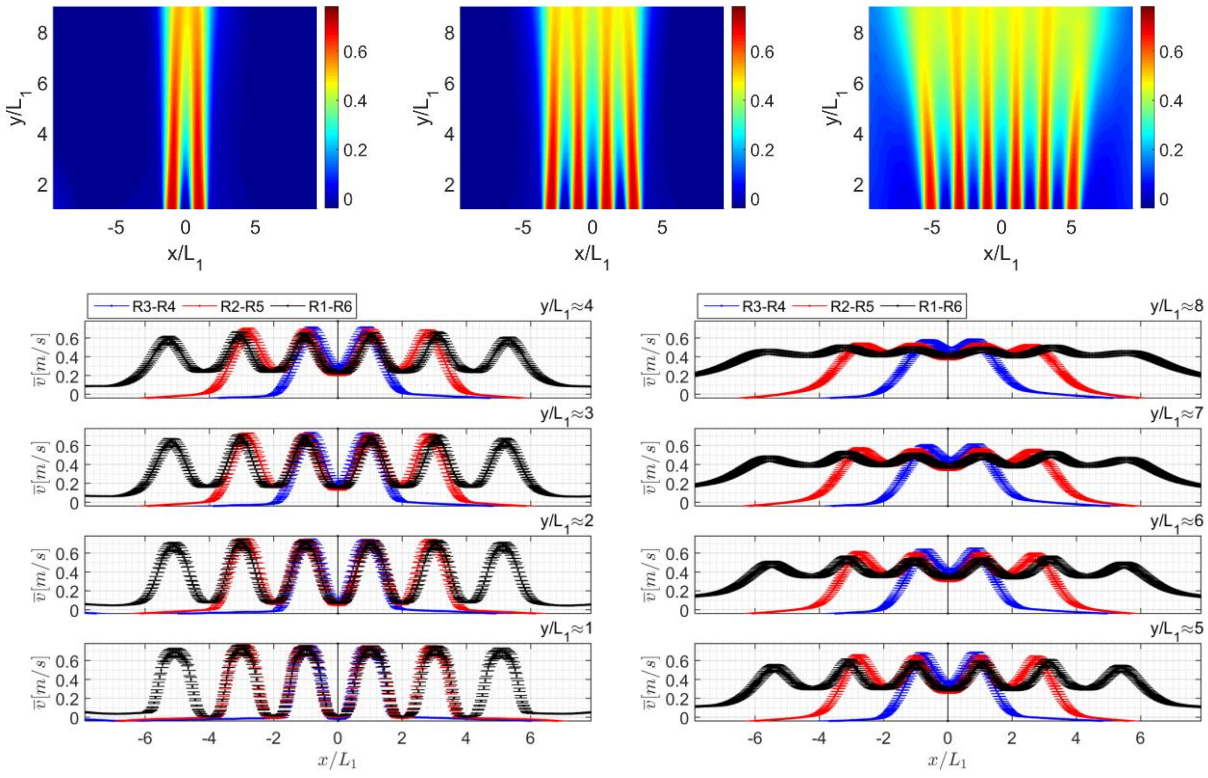


**Figure 10.5: Mean streamwise velocity, $\overline{v}$, fields for R3-R4 (top left), R2-R5 (top middle),and R1-R6 (top right), and the several streamwise locations for Re=1.38×10$^4$.**

Further upstream, other differences arise. At distances between $2 < y/L_1 < 8$, the middle jets in R3-R4 begin merging sooner than in the other two cases. We found that R3-R4 starts merging first, R2-R4 merges second, and R1-R6 merges last. Additionally, R1-R6 has the lowest maximum velocity while R3-R4 has the greatest maximum streamwise velocity at $y/L_1 \sim 8$. This

is caused by the flow path that is taken at the different flow rates. We note that the outlets are offset -- the flow follows its initial direction before curving towards the outlets. It was previously found (Nguyen, et al., 2015) that for higher volumetric flow rates, the flow curved sooner for two measurements with the same number of jets. By the same reasoning, the jets tend to curve towards the outlets faster for R1-R6 since it has a larger overall volumetric flow rate, and the maximum velocity along the streamwise direction is decreased as a result – clearly seen in the outermost jets. Thus, the combination of jet regions may be affected by the curvature of the flow towards the outlets – a three-dimensional effect. At $y/L_1 \sim 8$ we can notice that the jets for all cases have almost merged all together, thus the combined region may not be much higher than that. Moreover, higher flow entrainment is observed outside the core regions in the R1-R6 case -- this behavior is more apparent in the plots of the velocity profiles.

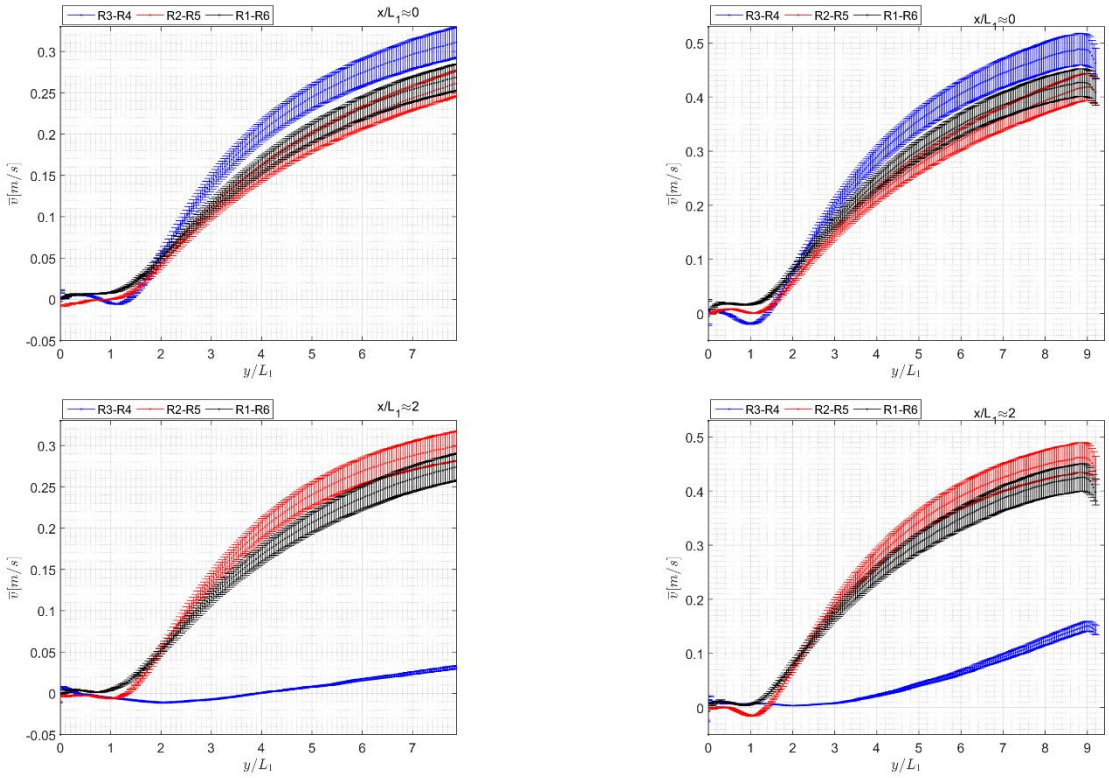


**Figure 10.6: Mean streamwise velocity profiles along the symmetry plane for R3-R4, R2-R5, and R1-R6 for Re=0.9×10$^4$ (top left) and Re=1.38×10$^4$(top right), and in between jets R4-R5 for Re=0.9×10$^4$ (bottom left), and for Re=1.38×10$^4$ (bottom right).**

Plots of the mean streamwise velocity profiles along the symmetry plane of the jets have been previously reported (Anderson and Spall, 2001)that for jet spacing distances ($S/L_1$) greater than 9. The data provided, however, delivers experimental results for $y/L_1 > 20$. In our case, we have $S/L_1$=1 and only range up to $y/L_1 \sim 9$. The plots of the velocity profiles at two Reynolds numbers along the symmetry plane at in between risers 4 and 5 ($x/L_1$=2) is shown in Figure 10.6. The results from our experiments show negative velocities near the jet inlets and the velocities appear to approach a maximum at higher $y/L_1$ for both Reynolds numbers. In the experimental cases provided by Anderson and Spall, this maximum is reached near the "combined region" of the jets; this also occurs in our results, but at a different $y/L_1$ location. It is possible that this merging region occurs sooner because the location of the outlets plays an

important role on this region. The plots at $x/L_1$=2 also show the same behavior as the plot along the symmetry plane even though the jets are not converging in all regions.

### 10.3.2 Reynolds Stresses for Re=1.38×10$^4$

In this section, we discuss the results obtained for the profiles of the shear and normal Reynolds stresses. The normal shear stresses give information about turbulent intensity along each direction of the flow. Additionally, the shear stresses provide additional information about the formation and expansion of the shear regions.

Fields and profiles of the normal shear stress, $\overline{u'u'}$, at several streamwise locations are reported in Figure 10.7. We observe that at $y/L_1 \approx 1$, the $\overline{u'u'}$ profiles for all the cases have high turbulent intensity in the shear regions (outside the core flow). This behavior is also seen in the profiles for $\overline{v'v'}$, but with higher intensities. This occurs because, near the regions where the jets begin, most of the flow is in the streamwise direction, and higher fluctuations appear in that direction as a result.

Furthermore, from the fields in Figure 10.7, we can see that the peaks of $\overline{u'u'}$ merge at downstream distances between $4 < y/L_1 < 8$; here $\overline{u'u'}$ increases and the peaks merge. In these regions, we observe an increase in the Reynolds stresses and a redistribution of energy between the jets. For cases R3-R4 and R2-R5, $\overline{u'u'}$ starts increasing in the locations between the jets and decreasing in the regions of the outermost shear layers.

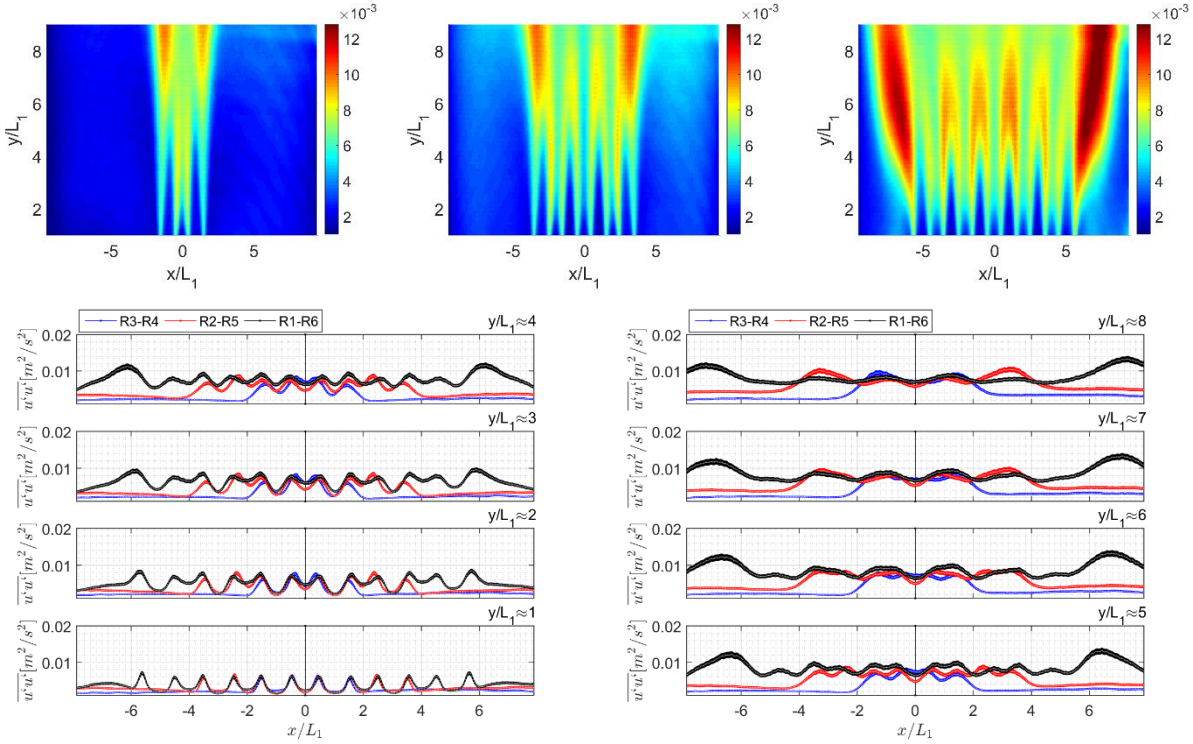


**Figure 10.7: Normal Reynolds Stress $\overline{u'u'}$, fields for R3-R4 (top left), R2-R5 (top middle), and R1-R6 (top right), and the several streamwise locations for Re=1.38×10$^4$.**

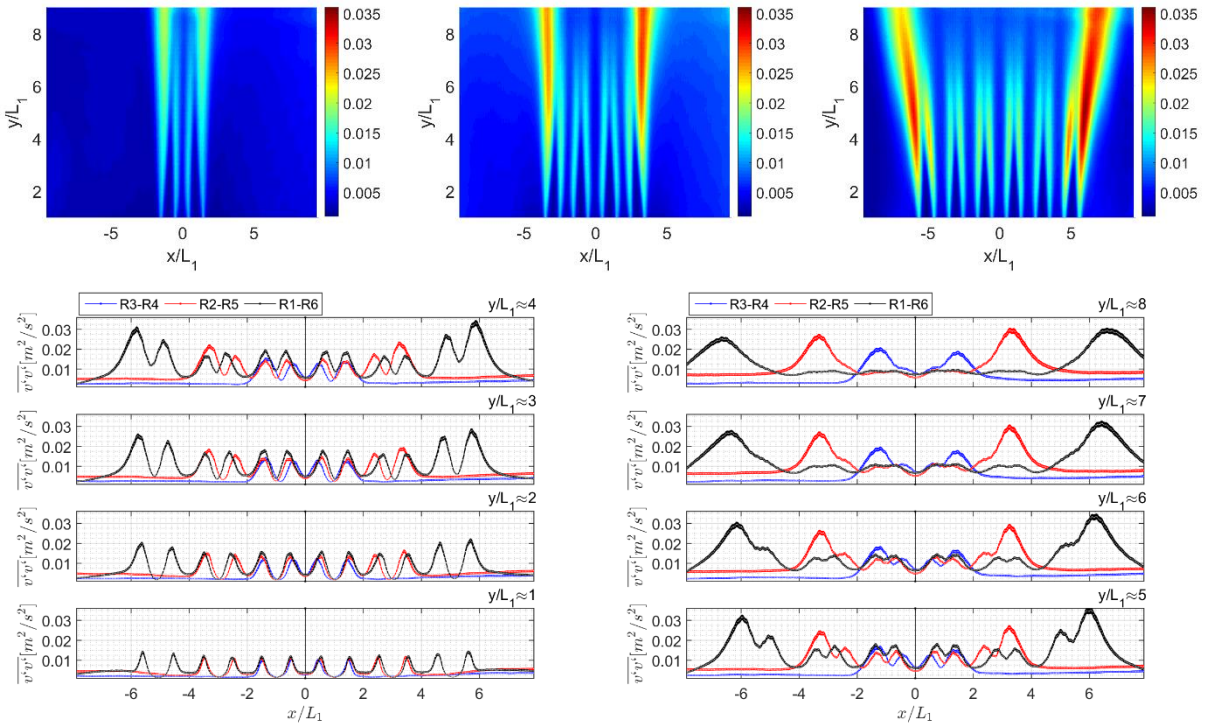


**Figure 10.8 Normal Reynolds Stress, $\overline{v'v'}$, fields for R3-R4 (top left), R2-R5 (top middle), and R1-R6 (top right), and the several streamwise locations for Re=1.38×10$^4$.**

The shear stresses, $\overline{u'v'}$, provide information about the behavior of the shear layer regions. Figure 10.9 shows both positive and negative regions – indicating the rolling direction of the flow along those regions. A negative shear stress indicates that the eddies around those locations are rolling counterclockwise, while the positive regions indicate that the eddies are rotating clockwise. From this, we observe the alternation between positive and negative shear stresses as we move across the jet. Initially, $\overline{u'v'}$ is small but, as the jets travel further downstream, $\overline{u'v'}$ increases until it reaches a maximum and then decreases. This occurs for all of the shear layers inside the outermost shear layers.

For example, at $y/L_1 \approx 1$, the shear stresses are small, but increase as $y/L_1$ increases. The shear layer regions between the jets, however, expand until about $y/L_1 \approx 4$ and start decaying from then on. The decay of the amplitude of the shear stress occurs approximately at the merging region between the jets. This merging region is more apparent in Figure 10.8, where the shear layers attach. Noteworthy is that the shear stress keeps increasing for the outermost shear regions because there is no attachment with other jets.

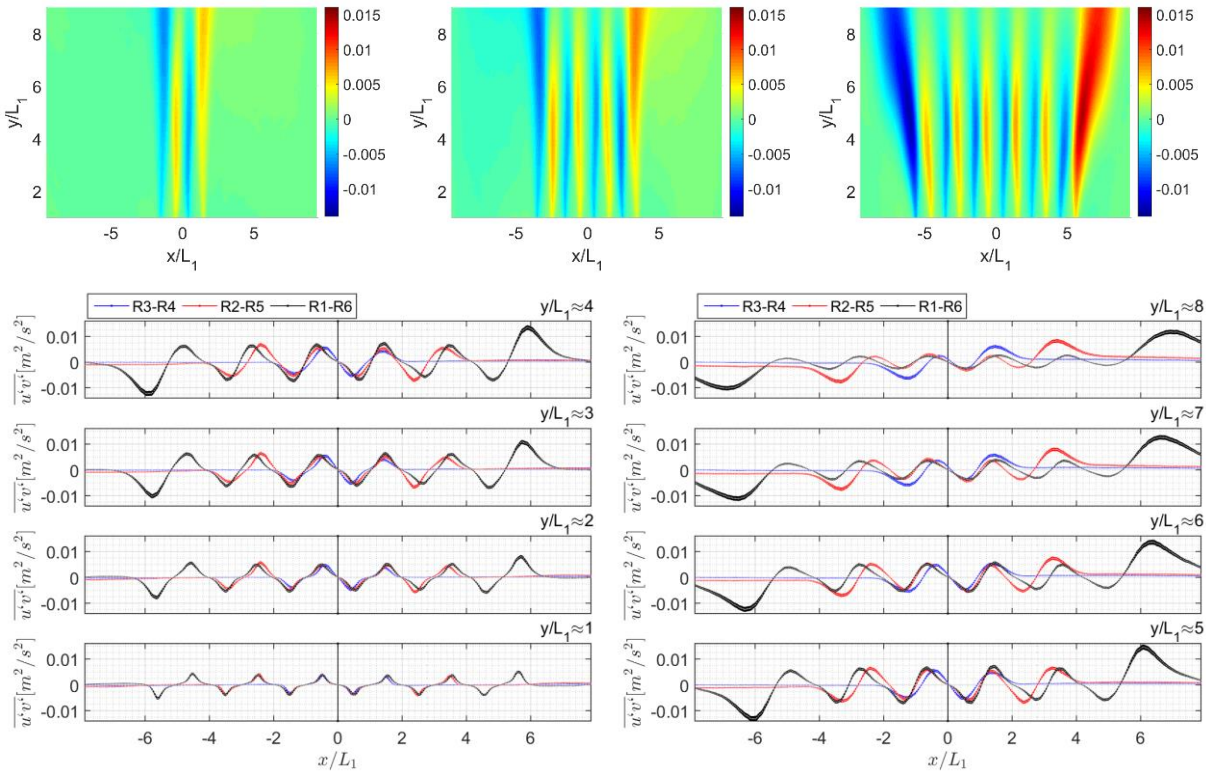


**Figure 10.9: Shear Stress $\overline{u'v'}$, fields for R3-R4 (top left), R2-R5 (top middle), and R1-R6 (top right), and the several streamwise locations for Re=1.38×10$^4$.**

### 10.3.3 Time-Averaged streamwise velocity and Reynolds Stresses for Re=0.9×10$^4$

The mean velocity profiles of the streamwise velocity, $\overline{v}$, and the Reynolds stresses are shown in Figure 10.10 and Figure 10.11, respectively.

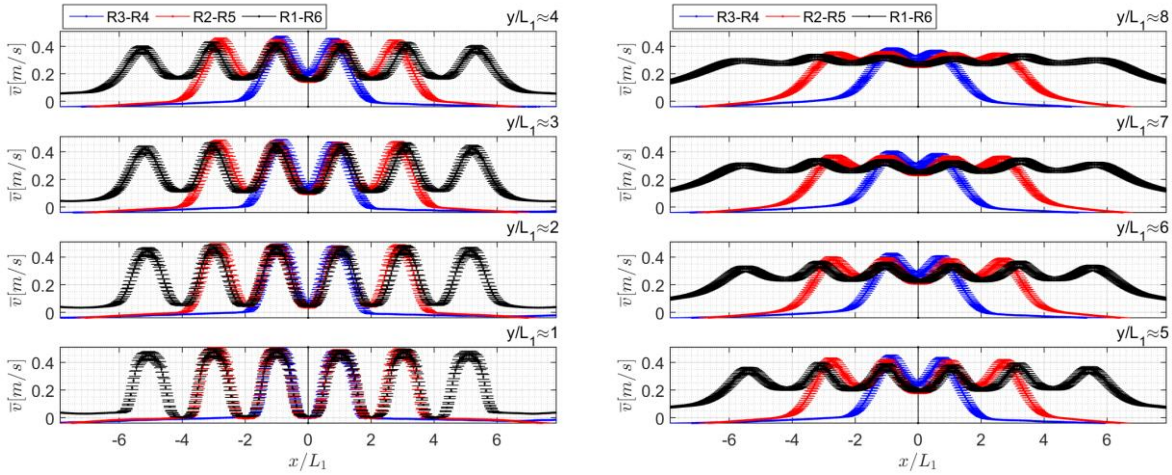


**Figure 10.10: Mean streamwise velocity, $\overline{v}$, profiles for R3-R4, R2-R5 and R1-R6 at several streamwise locations for Re=0.9×10$^4$.**

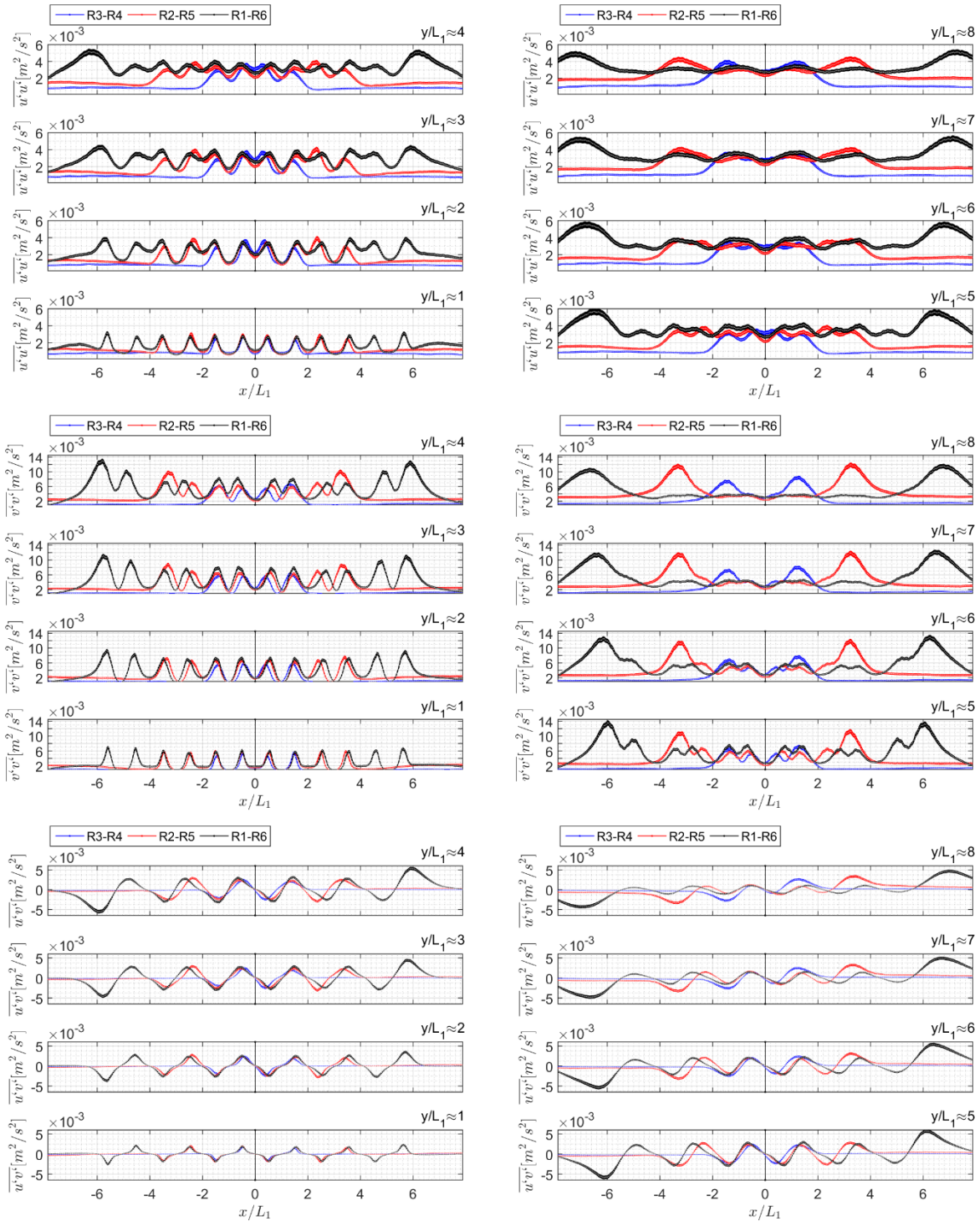


**Figure 10.11: Reynolds stress profiles for R3-R4, R2-R5 and R1-R6 at several streamwise locations for Re=0.9×10$^4$.**

All of the profiles for Re=0.9×104 are remarkably similar to those for Re=1.38×104, except with lower magnitudes. The Reynolds stresses show the same patterns, indicating that the flow characteristics do not change for these two different Reynolds numbers.

# 11 Experimental Results – Configuration with Acrylic Step

## 11.1 Results for 2, 4, and 6 Jets at Re $= 1.38 \times 10^4$.

All of the experiments were repeated with the acrylic step in place (shown in Figure 9.1b), and the axis orientation is the same as that in Figure 10.3. The fluid temperatures for each experiment are shown in Table 11.1. The mean streamwise velocity profiles at several locations are shown in Figure 11.1. These profiles exhibit the same general shape as the profiles without the steps; however, some differences are present. In the case of six jets, the regions near the walls are more spread out. For better comparison, the profiles for six jets for the two cases were plotted in the same graph as shown in Figure 11.2.

At $y/L_1$, the profiles are very similar with the exception of the regions closer to the wall. The level of symmetry is affected and higher velocities are present in these regions. This increase in velocity indicates that entrainment is induced when the step is in place. Additionally, the jets start merging sooner and the magnitudes of the velocities tend to be slightly larger for $y/L_1 > 5$, which indicates that the jets tend to curve towards the outlet farther away when the step is in place.

**Table 11.1: Experiments performed and the corresponding fluid temperature – Configuration with step in place.**

| Experiment: | R3-R4 | R2-R5 | R1-R6 | R3-R4 | R2-R5 | R1-R6 |
|---|---|---|---|---|---|---|
| Re | $1.38\times10^4$ | $1.38\times10^4$ | $1.38\times10^4$ | $9\times10^4$ | $9\times10^4$ | $9\times10^4$ |
| Temperature [°C] | 27.31 | 27.06 | 26.44 | 27.37 | 27.00 | 26.62 |

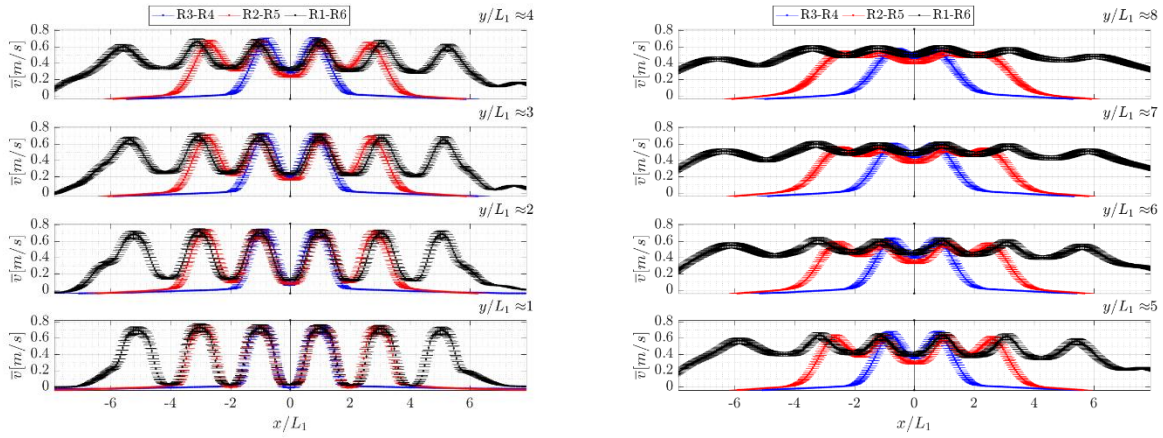


**Figure 11.1: Mean streamwise velocity, $\overline{v}$, fields for R3-R4 (top left), R2-R5 (top middle),and R1-R6 (top right), and the several streamwise locations for Re=1.38×104 – With step in place.**

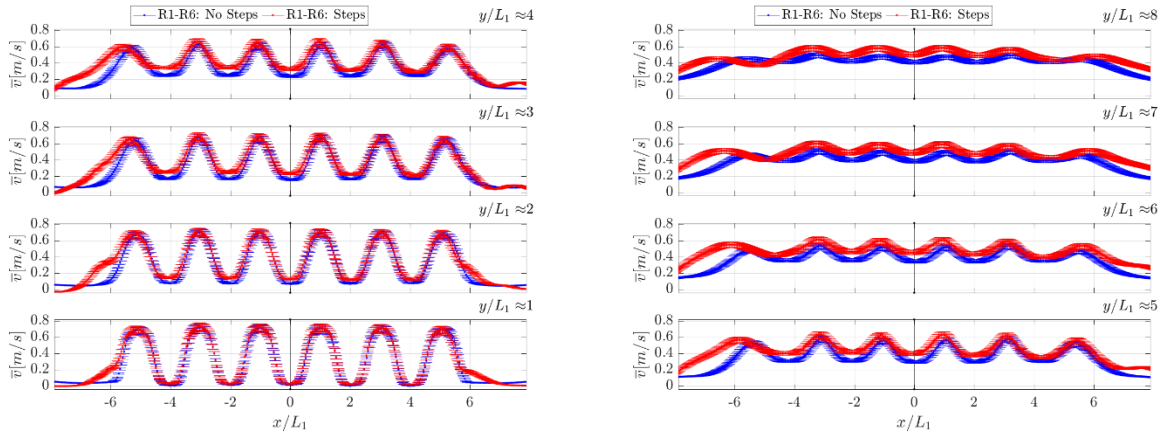


**Figure 11.2: Comparison of the mean streamwise velocity, $\overline{v}$, profiles for R1-R6 at several streamwise locations for Re=1.38×10$^4$ – With and without the step in place.**

The Reynolds stress $\overline{u'u'}$ profiles, shown in Figure 11.3, provide some additional insight about the differences in the flow. Again, the profiles for the six jets exhibited the largest changes. Instead of having local minima in the middle of adjacent jets as seen in Figure 10.7, local maxima appear in between adjacent jets for $y/L_1 > 1$. This indicates that there are larger velocity fluctuations in the cross-stream direction with this configuration. Furthermore, the magnitudes also increased in the regions between the leftmost and rightmost jets and the walls.

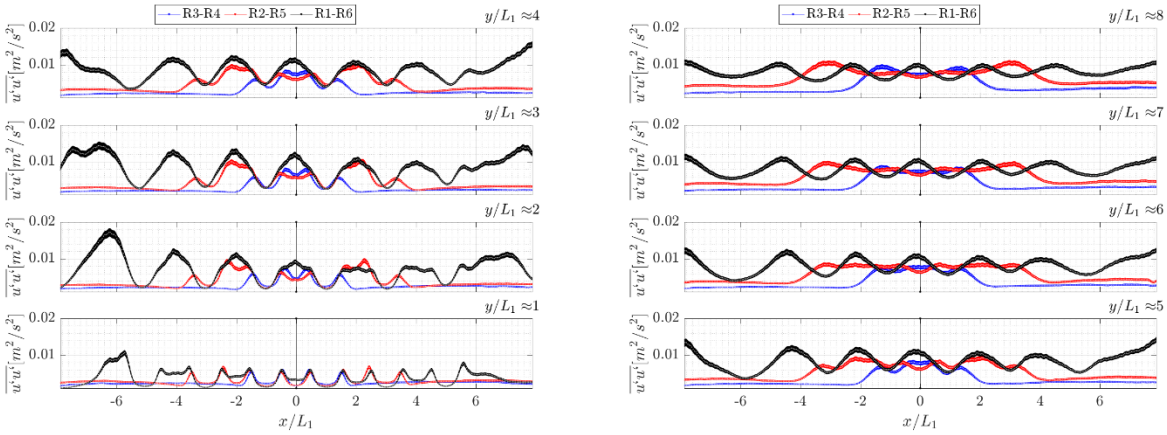


**Figure 11.3: Reynolds normal stress $\overline{u'u'}$ profiles at the several streamwise locations for R3-R4 (two), R2-R5 (four), and R1-R6 (six) jets. Re=1.38×10$^4$ with step in place.**

The Reynolds stress $\overline{v'v'}$ profiles, shown in Figure 11.4, also show the largest changes in the regions closest to the walls. Compared to the plots of the experiments without the step (Figure 10.8), the regions near the walls show intensities of smaller amplitude. This implies that, while higher entrainment occurs, the strength of the fluctuations in that region is smaller on average. Similarly, the shear stresses shown in Figure 11.5, also varied. The peaks near the walls, previously observed in Figure 10.9, decreased in magnitude, which indicates that the shear in that region is less dominant because of the entrainment.

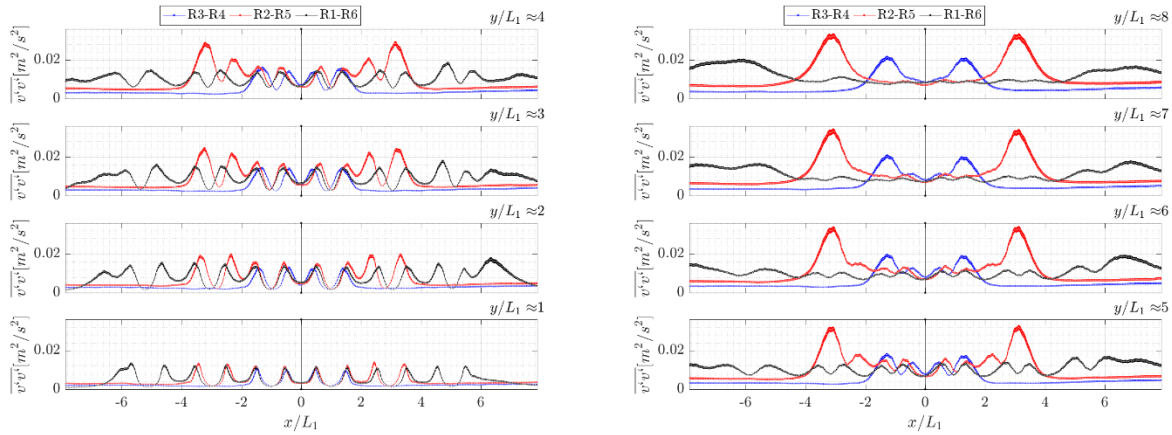


**Figure 11.4: Reynolds normal stress $\overline{v'v'}$ profiles at the several streamwise locations for R3-R4 (two), R2-R5 (four), and R1-R6 (six) jets. Re=1.38×10⁴ with step in place.**

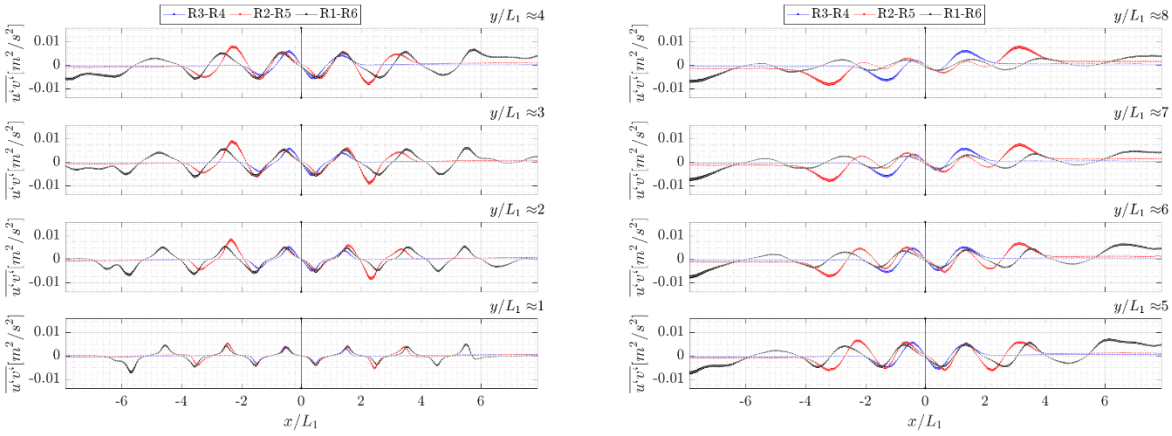


**Figure 11.5: Reynolds shear stress $\overline{u'v'}$ profiles at the several streamwise locations for R3-R4 (two), R2-R5 (four), and R1-R6 (six) jets. Re=1.38×10⁴ with step in place.**

## 11.2 Experimental Results for 2, 4, and 6 Jets at Re $= 0.9 \times 10^4$.

For completeness, the velocity and Reynolds stress profiles at Re $= 0.9 \times 10^4$ are shown in Figure 11.6. As previously observed, all of the profiles resemble the same features as the case with the higher Reynolds number, just with lower amplitudes.

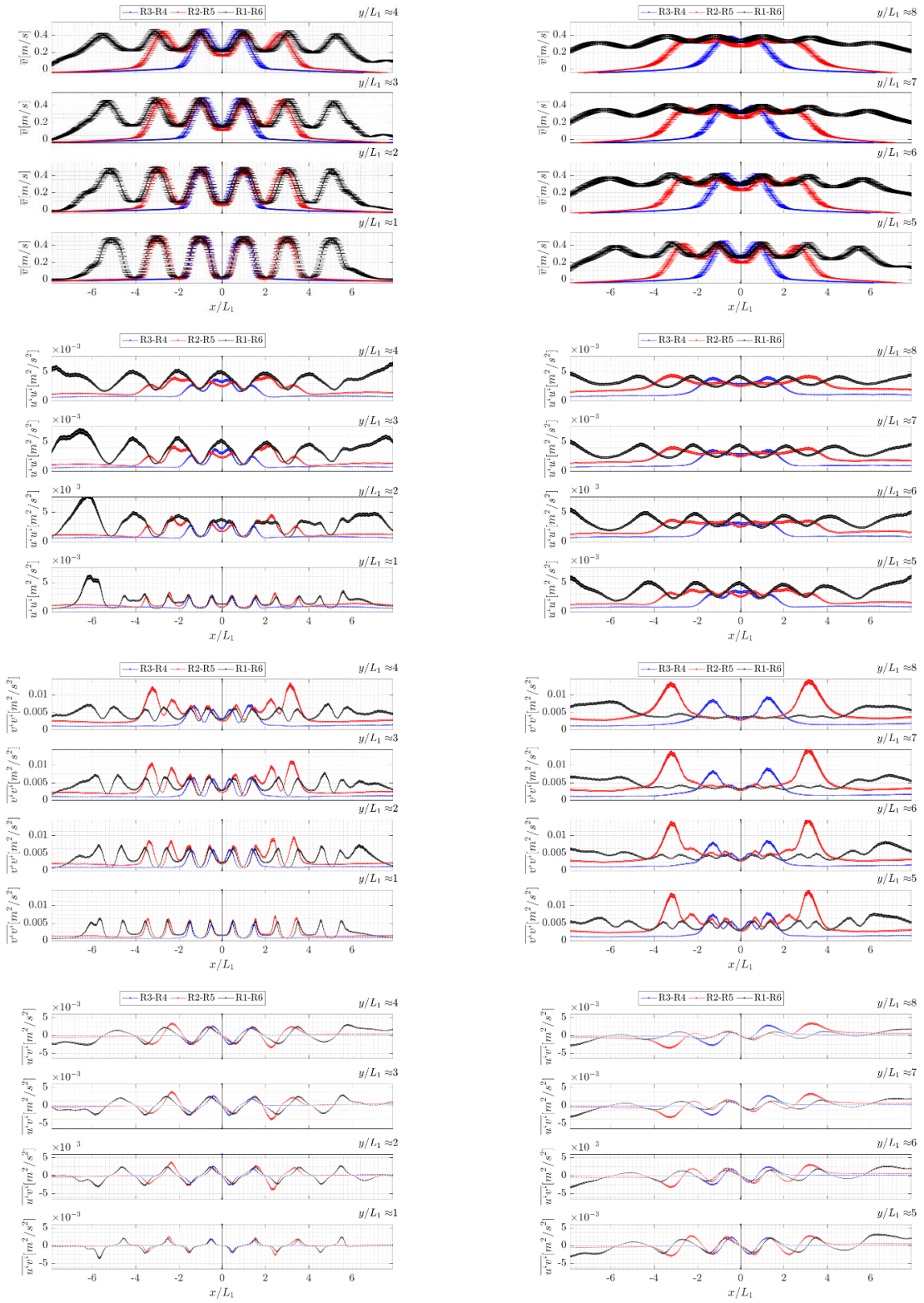


**Figure 11.6: Mean streamwise velocity, $\overline{v}$, and Reynolds stress profiles at the several streamwise locations for R3-R4 (two), R2-R5 (four), and R1-R6 (six) jets. Re=0.9×10$^4$ with step in place.**

# 12 CFD SIMULATIONS – ASSESSMENT OF RANS-BASED TURBULENCE MODELS

The Experimental data was compared to CFD results to assess the predictive capabilities of RANS-based turbulence models. CFD simulations of the RCCS facility were run using STAR-CCM+ 11.06.011. The turbulence model that was utilized for these tests is the Standard k– ϵ Two-Layer model with the quadratic constitutive relations. Due to the rectangular geometry of the RCCS facility, the trimmer volume mesh was utilized to prevent irregular mesh volumes which could introduce mesh biased velocity fluxes across the cells. To fully resolve the velocity profiles in the CFD simulations, a fine mesh size of 0.7mm was used in the region right after the risers as shown in Figure 12.1 (a-c). With this mesh size, a total of 18 grids are generated across and in between each one of the risers. Since the tank is large (relative to the risers), the fine mesh was only generated in the region after the risers. To reduce the amount of computational cells, every other region had a mesh size of 2.8mm. With the fine and coarse regions, approximately 12.1 million cells were generated. The interaction between six jets was studied for Reynolds numbers $Re_{Riser} = 0.9 \times 10^4 \; and \; 1.38 \times 10^4$. At the inlets, a fully developed profile was set as the boundary conditions for the risers, and at the outlets, pressure boundary conditions were chosen. To avoid disturbances in the flow due to the outlet boundary conditions, and to not significantly increase the number of cells in the domain, the outlets were extruded as shown in Figure 12.1(a-b). The velocity profiles from the centerline of the rectangular ducts were compared at several axial locations as shown in Figure 12.1 (c). The CFD results shown in the following sections are those of steady state simulations, unless stated otherwise.

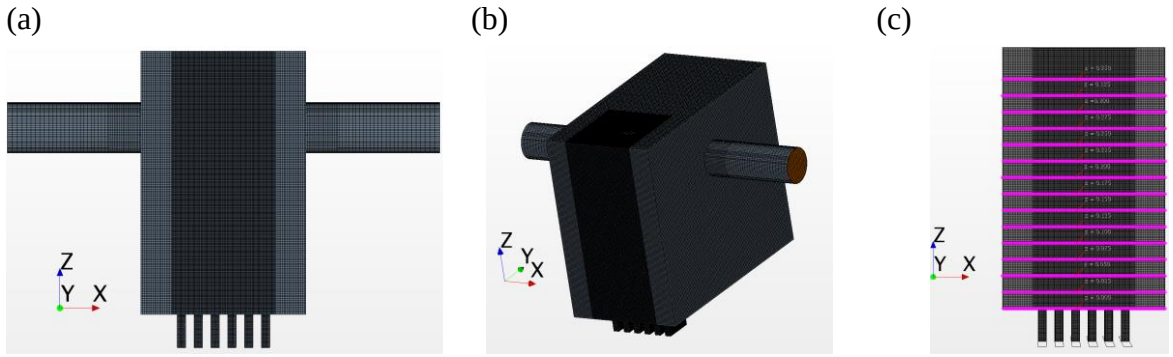


**Figure 12.1: Mesh of the test facility – (a) Front view, (b) size view, and (c) front view with multiple line probes.**

The computational domain with the streamlines starting from all six risers is shown in Figure 12.2a. From the image of the streamlines, one can clearly see the recirculation areas that can be investigated a multiple locations. In addition, the vector fields at multiple locations of the tank were generated to further investigate other regions that might be of interest. Figure 12.2b is the vector field on the midplane of riser 6. From this vector field, additional smaller recirculation regions can be distinguished.

a) b)


**Figure 12.2: Steady state simulation: a) Streamlines in the upper plenum, and b) Vector field on the midplane of the riser 6.**

Similarly, other recirculation regions appear one the midplane of all six risers and on the plane parallel to the outlets as shown in Figure 12.3a and Figure 12.3b, respectively. By observing the streamlines and the vector fields obtained from CFD simulations, the PIV measurements can be focused on the regions where certain structures are found. The steady state simulations showed oscillatory behavior in between iterations, and for this reason, transient simulations were executed. Several screenshots at different time steps of the transient simulation are shown in Figure 12.4(a-h). As shown in Figure 12.4, the jets tend to oscillate towards the directions of the outlets. The most noticeable features of these oscillations were that the jets closest to the walls oscillated a lot more than the jets in between, and that the region close to the top of the tank was constantly changing in time.

As observed in the experiments and simulations, the jets converge and diverge from time to time; however, by time averaging the instantaneous fields, we can observe the overall behavior of the jets. The simulation's mean streamwise velocity field (averaged over a total simulation time of 600 seconds) is shown in Figure 12.5. The time averaged result shows a symmetric mean velocity field very similar to that of the experiments as shown in Figure 12.6. To understand where the major differences appear between the experiments and CFD results, several profiles were compared.

a) b)

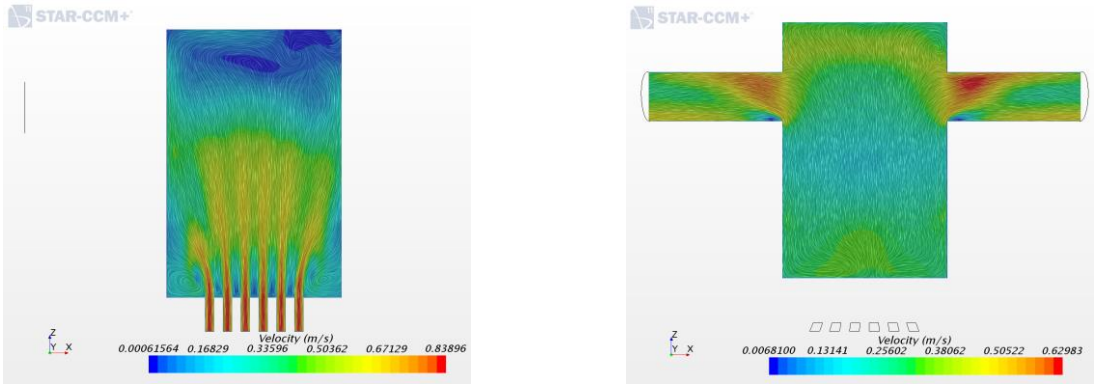


**Figure 12.3: Steady state simulation: a) Velocity vector field on the midplane of all six risers and b) Vector field on the outlet plane.**

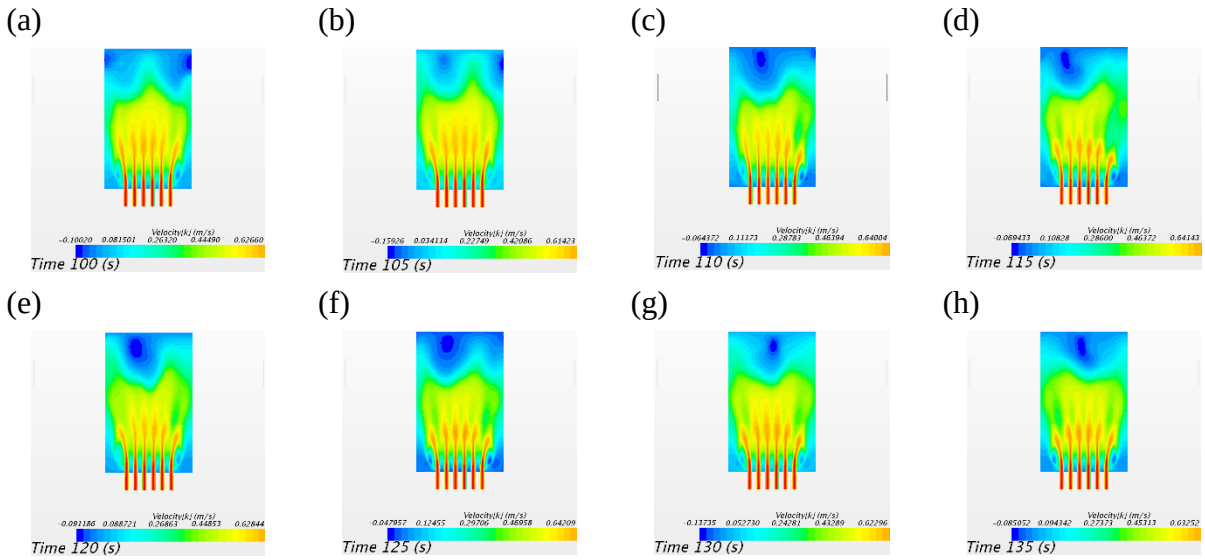


**Figure 12.4(a-h): Transient simulation: Streamwise velocity fields at different time steps – Six jets at Re $= 1.38 \times 10^4$.**

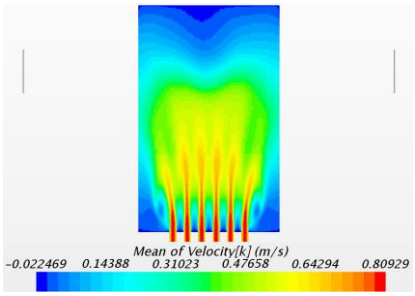


**Figure 12.5: Transient simulation: Mean streamwise velocity, $\overline{v}$, for six jets at Re $= 1.38 \times 10^4$.**

The comparison between the CFD and experimental mean streamwise velocity profiles is shown in Figure 12.6. We note that the y-axis is not normalized to show the actual differences in the magnitudes between the results. The profiles show relative good agreement for $y/L_1 < 3$; however, larger differences appear further away from the inlets. The largest differences occur in between the leftmost jet and the wall. Both, the experiment and simulation results show some asymmetry, which may be caused by bifurcations effects. Additionally, some smaller differences occur around the jet cores. The jets merge sooner in the experiment, which indicates that the kinetic energy is dissipated (or redistributed) earlier as the jets travels away from the inlets. These differences could be further understood by investigating the in-and-out of plane jet motion caused by the interactions with the neighboring jets and outlets. Furthermore, the Reynolds stresses can provide us additional information about what's occurring in the regions with the largest discrepancies.

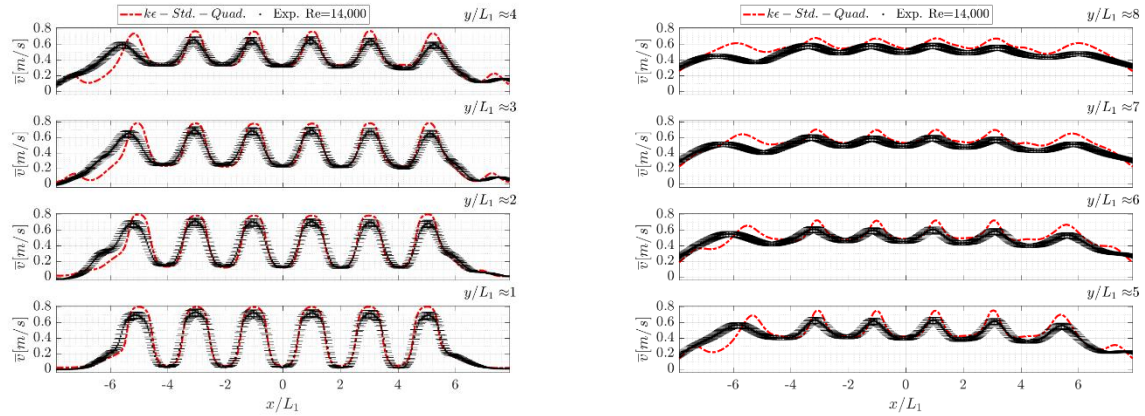


**Figure 12.6: Simulation versus experimental results: Mean streamwise velocity, $\overline{v}$, for six jets at Re $= 1.38 \times 10^4$.**

The plot of the normal stress $\overline{u'u'}$ (cross-stream direction) profiles is shown in Figure 12.7. For several streamwise distances, the magnitude of $\overline{u'u'}$ is higher in the CFD results. At $y/L_1 = 1$, the experimental and CFD results show the same general shape, but differ in magnitude. For $6 > y/L_1 > 1$, the two dominant peaks remain in the vicinity of the jets for the CFD results but disappear in the experiments. In the middle between the jets, the magnitude of $\overline{u'u'}$ is largest in the experimental results indicating that these is a lot more left to right motion in these locations. On the other hand the CFD results indicate a lot more motion in the vicinity of the jets (double peaks). For $y/L_1 > 6$, the differences are a lot smaller which could be caused the redistribution of kinetic energy.

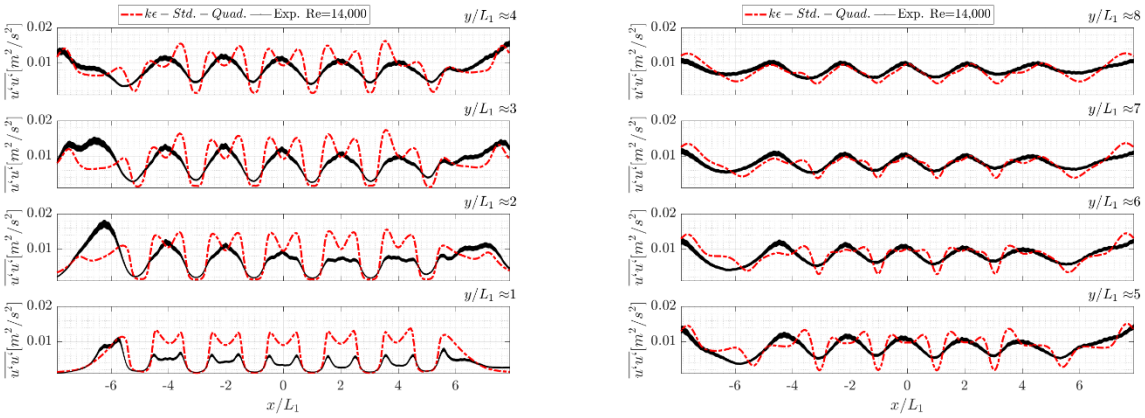


**Figure 12.7: Simulation versus experimental results: Mean streamwise Reynolds normal stress, $\overline{u'u'}$, for six jets at Re $= 1.38 \times 10^4$.**

The Reynolds normal stress $\overline{v'v'}$ (streamwise direction) profiles are shown in Figure 12.8. Here, there is much better agreement between the CFD and experimental results. The largest differences occur in the regions closer to the walls and in the vicinity of the jets (peaks). As in the $\overline{u'u'}$ profiles, the peaks in the simulation results are slightly higher around the shear layer of the jets. On the other hand, for $y/L_1 > 5$, the experimental results are higher near the walls, which indicate stronger turbulence intensities due to the recirculation of the flow in these regions. Furthermore, the shear stresses $\overline{u'v'}$ profiles are shown in Figure 12.9. The agreement between the two results

is very good, with the exception of the regions close to the walls. From these comparisons, we can infer that while there is a relative good agreement between the experimental and CFD velocity profiles, several discrepancies might appear in the Reynolds stresses. The differences between the CFD and experimental results could be accounted for by considering the geometrical uncertainties in the experiments and the uncertainty from the CFD results. These sources of uncertainty were not accounted for in these results, and will have to be explored in future work.

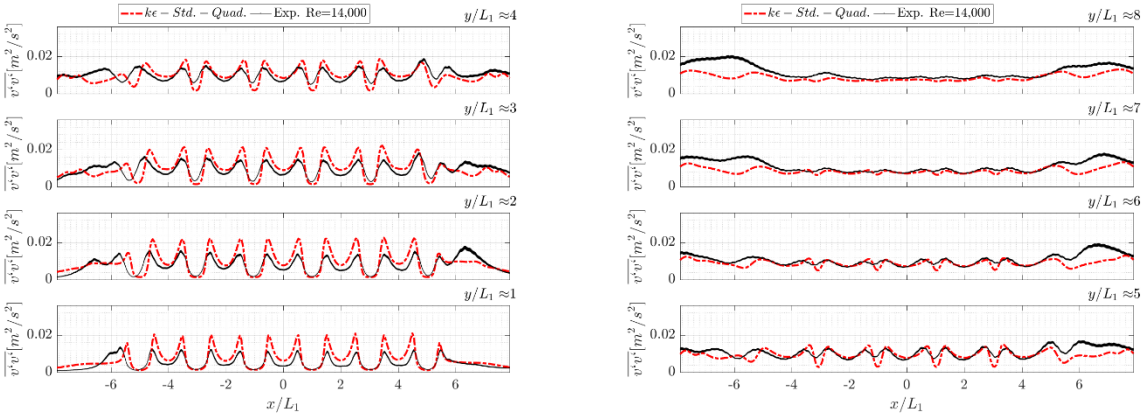


**Figure 12.8: Simulation versus experimental results: Mean streamwise Reynolds normal stress, $\overline{v'v'}$, for six jets at Re $= 1.38 \times 10^4$.**

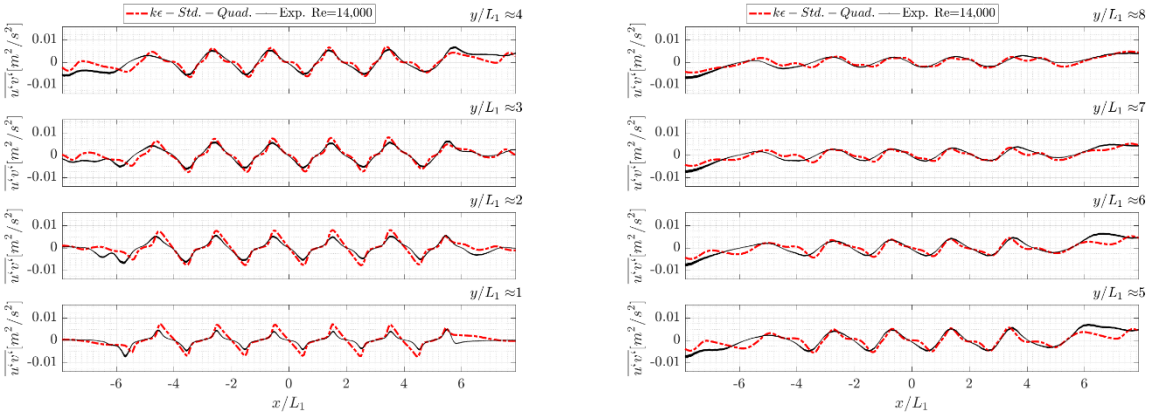


**Figure 12.9: Simulation versus experimental results: Mean streamwise Reynolds shear stress, $\overline{u'v'}$, for six jets at Re $= 1.38 \times 10^4$.**

# 13 PART II – CONCLUSIONS

A separate effect test facility has been designed and built at the University of Michigan to investigate jet interactions in the upper plenum of the air-cooled RCCS design. The facility has been scaled based on the ANL full scale air RCCS facility. Water has been selected as working fluid to facilitate the use of advanced measurement techniques, such as PIV. CFD simulations have been performed to verify the scaling before the facility was built. A PIV setup has been designed

and install on the facility to allow for long measurement times and therefore achieve good measurement statistics.

Two experimental configurations have been considered, to investigate the effect of the risers penetration into the upper plenum. A rich, high-resolution experimental database has been built for the two configurations, including different Re numbers and different numbers of active jets (2, 4 and 6 respectively). Primary and secondary recirculation flows have been identified and characterized in detail.

The high-resolution data were then used to assess current CFD RANS models. Overall good qualitative agreement is observed between simulations and experimental results. The jet velocity profiles show good agreement for $y/L_1 < 3$; however, larger discrepancies are observed further away from the jets inlet. The largest discrepancies are observed in the region between the leftmost jet and the wall.

Future work should be focus on further assessing the discrepancies between CFD RANS and experiments and in using Large Eddy Simulations to gain more insight into modeling improvements needed for current CFD RANS models.

# 14 REFERENCES PART I

Abro, E., and G.A. Johansen. 1999. Void fraction and flow regime determination by low-energy multi-beam gamma-ray densitometry. In 1st world congress on industrial process tomography. Buxton, Greater Manchester.

Achard, Jean-Luc, Donald A. Drew, and Richard T. Lahey. 1985. The analysis of nonlinear density-wave oscillations in boiling channels. Journal of Fluid Mechanics 155:213–232.

Adineh, Mahtab, Mohammadreza Nematollahi, and Ali Erfaninia. 2015. Experimental and numerical void fraction measurement for modeled two-phase flow inside a vertical pipe. Annals of Nuclear Energy 83:188 – 192.

Ambrosini, W., P. Di Marco, and J. C. Ferreri. 2000. Linear and nonlinear analysis of density wave instability phenomena. International Journal of Heat and Technology 18(1).

Ardron, K.H., and R.B. Duffey. 1978. Acoustic wave propagation in a flowing liquid-vapour mixture. International Journal of Multiphase Flow 4(3):303 – 322.

Aspen Aerogels. 2015. Pyrogel xt. Aspen Aerogels.

Bae, Y. Y., B. H. Cho, J. H. Kim, M. H. Kim, and Y. W. Kim. 2014a. Design of 1/4 scale performance test facility for the pmr200 rccs. In Proceedings of the 2014 22nd international conference on nuclear engineering. Prague, Czech Republic.

Bae, Yoon-Yeong, Sung-Deok Hong, and Yong-Wan Kim. 2014b. Scaling analysis of pmr200 reactor cavity cooling system. Nuclear Engineering and Design 271:523 – 529. SI : HTR 2012.

Baker, O. 1954. Simultaneous flow of oil and gas. Oil and Gas Journal 54:185–195.

Bakhmet'ev, A. M., M. A. Bol'shukhin, V. V. Vakhrushev, A. M. Khizbullin, O. V. Makarov, V. V. Bezlepkin, S. E. Semashko, and I. M. Ivkov. 2009. Experimental validation of the cooling loop for a passive system for removing heat from the aes-2006 protective envelope design for the leningradskaya nuclear power plant site. Atomic Energy 106(3):185–190.

Banowski, Manuel, Matthias Beyer, Lutz Szalinski, Dirk Lucas, and Uwe Hampel. 2017. Comparative study of ultrafast x-ray tomography and wire-mesh sensors for vertical gas-liquid pipe flows. Flow Measurement and Instrumentation 53(A):95–106.

Barron, John, and Colin Ashton. 2007. The effect of temperature on conductivity measurement. Tech. Rep., Reagecon Diagnostics.

Bergles, A. E., P. Goldberg, and J.S. Maulbetsch. 1967. Acoustic oscillations in a high pressure single channel boiling system. Tech. Rep., EURATOM Report.

de Bertodano, Martin Lopez, William Fillmer, Alejandro Clausse, and Victor H. Ransom. 2017. Two-fluid model stability, simulation and chaos. Switzerland: Springer.

Blasius, P.R.G. 1913. Das aehnlichkeitsgesetz bei reibungsvorgangen in flüs sigk eiten. Forschungsheft 131: 1–41.

Boure, J.A., A.E. Bergles, and L.S. Tong. 1973. Review of two-phase flow instability. *Nuclear Engineering and Design* 25(2):165 – 192.

Boyer, Christophe, Anne-Marie Duquenne, and Gabriel Wild. 2002. Measuring techniques in gas-liquid and gas-liquid-solid reactors. *Chemical Engineering Science* 57(16):3185 – 3215. Jean-Claude Charpentier Festschrift Issue.

Bruggeman, D. A. G. 1935. Berechning verschiedener physikalischer konstanten von hererogenen substanzen dielektrizitaetskonstanten und leitfaehigkeiten der mischkoerper aus isotropen substanzen. Annalen der Physik 5(24).

CGAL. 2015. Computational geometry algorithms library v. 5.4. http://www.cgal.org.

Chabot, J., H. Farag, and H. de Lasa. 1998. Fluid dynamics of bubble columns at elevated temperature modelling and investigation with refractive fiber optic sensors. Chemical Engineering Journal 70(2):105 – 113.

Cheng, Lixen. 2014. Frountiers and progress in multiphase flows I. Springer International Publishing.

Cheng, Nian-Sheng. 2008. Formulas for friction factor in transitional regions. J. Hydraulic Eng. 134:1357–1362.

Chexal, B., J. Horowitz, and G.S. Lellouche. 1991. An assessment of eight void fraction models. Nuclear Engineering and Design 126(1):71 – 88.

Chexal, V.K., and A. E. Bergles. 1972. Two-phase flow instabilities in a low pressure natural circulation loop. In Proceedings of the 13th national heat transfer conference, vol. 69, 37–45. Denver, Colorado: AlChE.

Choi, Keun Ho, and Won Kook Lee. 1990. Comparison of probe methods for measurement of bubble properties. Chemical Engineering Communications 91(1):35–47. http://dx.doi.org/10.1080/00986449008940700.

Churchill, Stuart W. 1973. Empirical expressions for the shear stress in turbulent flow in commercial pipe. AIChE Journal 19(2):375–376.

Churchill, Stuart W., and Humbert H.S. Chu. 1975. Correlating equations for laminar and turbulent free convection from a vertical plate. International Journal of Heat and Mass Transfer 18(11):1323 – 1329.

Colebrook, C. F. 1939. Turbulent flow in pipes, with particular reference to the transition region between the smooth and rough pipe laws. Journal of the Institution of Civil Engineers 11(4):133–156. http://www. icevirtuallibrary.com/doi/pdf/10.1680/ijoti.1939.13150.

C.P. Tzanos, M.T. Farmer. 2006. Feasibility study for use of the natural convection shutdown heat removal test facility (nstf) for initial vhtr water-cooled rccs shutdown. Tech. Rep., Argonne National Labratory.

Czuber, E. 1884. Zur theorie der geometrischen wahrscheinlichkeiten. In Sitzungsberichte der mathematisch-naturwissenschaftliche klasse der kaiserlichen akademie der wissenschaften, vol. 90, 719 – 742. Wein.

Dave, A.J., A. Manera, M. Beyer, D. Lucas, and H.-M. Prasser. 2016. Uncertainty analysis of an interfacial area reconstruction algorithm and its application to two group interfacial area transport equation validation. Nuclear Engineering and Design 310:620 – 637.

Dirac, P.A.M. 1943. Approximate rate of neutron multiplication for a solid of arbitrary shape and uniform density part 1. Tech. Rep. MS-D-5, British Reports: Second World War Atomic Energy Research.

Dix, G.E. 1971. Vapor void fraction for forced convection with subcooled boiling at low flow rates. Ph.D. thesis, University of California - Berkley.

EPRI. 2014. Advanced nuclear technology: Advanced light water reactor utility requirements document. Tech. Rep. 3002003129, EPRI.

Faghihi, Reza, Mohammadreza Nematollahi, Ali Erfaninia, and Mahtab Adineh. 2015. Void fraction measurement in modeled two-phase flow inside a vertical pipe by using polyethylene phantoms. International Journal of Hydrogen Energy 40(44):15206 – 15212. The 4th International Conference on Nuclear and Renewable Energy Resources (NURER2014), 26-29 October 2014, Antalya, Turkey.

Fair, J. R. 1960. What you need to design thermosyphon reboilers. Petr. Refiner 39(2):102–123.

Friedel, L. 1979. Improved friction pressure drop correlations for horizontal and vertical two-phase flow. 3R Int. J. Piping Eng. Prac. 87(7):485 – 491.

Fukuda, Kenji, and Tetsuo Kobori. 1979. Classification of two-phase flow instability by density wave oscillation model. Journal of Nuclear Science and Technology 16(2):95–108. http://www.tandfonline.com/ doi/pdf/10.1080/18811248.1979.9730878.

Furuya, M., F. Inada, and T.H.J.J. van der Hagen. 2005a. Flashing-induced density wave oscillations in a natural circulation bwr-mechanism of instability and stability map. Nuclear Engineering and Design 235(15): 1557 – 1569.

Furuya, M., T. Kanai, T. Arai, H. Takiguchi, H.-M. Prasser, U. Hapel, and E. Schleicher. 2016. Three-dimensional velocity vector determination algorithm for individual bubble identified with wire-mesh sensors. In Specialist workshop on advanced instrumentation and measurement techniques for nuclear reactor thermal hydraulics. Liverno, Italy.

Furuya, Masahiro, Fumio Inada, and Tim H. J. J. Van Der Hagen. 2005b. Characteristics of type-i density wave oscillations in a natural circulation bwr at relatively high pressure. Journal of Nuclear Science and Technology 42(2):191–200. http://www.tandfonline.com/doi/pdf/10.1080/18811248.2005.9726379.

Goudarzi, N., and S. Talebi. 2013. Linear stability analysis of a double-channel two-phase natural circulation loop. Progress in Nuclear Energy 67:114 – 123.

Griffith, P. 1962. Geysering in liquid-filled lines. In Asme, Paper No. 62–HT–39.

Guanghui, Su, Jia Dounan, Kenji Fukuda, and Guo Yujun. 2002. Theoretical and experimental study on density wave oscillation of two-phase natural circulation of low equilibrium quality. Nuclear Engineering and Design 215(3):187 – 198.

Haaland, S.E. 1983. Simple and explicit formulas for the friction factor in turbulent pipe flow. J. Fluids Eng. 105(1):89 – 90.

van der Hagen, T.H.J.J., A.J.C. Stekelenburg, and D.D.B. van Bragt. 2000. Reactor experiments on type-i and type-ii {BWR} stability. Nuclear Engineering and Design 200(1-2):177 – 185.

Harms, A. A., and C. F. Forrest. 1971. Dynamic effects in radiation diagnosis of fluctuating voids. Nuclear Science and Engineering 46(3):408 – 413.

Harms, A.A., and F.A.R. Laratta. 1973. The dynamic-bias in radiation interrogation of two-phase flow. International Journal of Heat and Mass Transfer 16(7):1459 – 1465.

Haskin, Troy C. 2016. On the stability of natural circulation loops with phase change. Master's thesis, University of Wisconsin - Madison.

Hewitt, G.F., and D.N. Roberts. 1969. Studies of two-phase flow patterns by simultaneous x-ray and flash photography. United Kingdom Atomic Energy Authority.

Hibiki, Takashi, and Mamoru Ishii. 2003. One-dimensional drift-flux model and constitutive equations for relative motion between phases in various two-phase flow regimes. International Journal of Heat and Mass Transfer 46(25):4935 – 4948.

HTGR-86-024. 1986. Preliminary safety information document for the standard mhtgr. volume 1, (includes latest amendments). Stone and Webster Engineering Corp.

IAEA. 2001a. Current status and future development of modular high temperature gas cooled reactor technology. Tech. Rep. 1198, International Atomic Energy Agency.

IAEA 2001b. Thermohydraulic relationships for advanced water cooled reactors. Vienna: INTERNATIONAL ATOMIC ENERGY AGENCY. IAEA-TECDOC-1203.

Ishii, M. 1971. Thermally induced flow instabilities in two-phase mixtures in thermal equilibrium. Ph.D. thesis, Georgia Institute of Technology.

Ishii, M., and I. Kataoka. 1984. Scaling laws for thermal-hydraulic system under single phase and two-phase natural circulation. Nuclear Engineering and Design 81(3):411 – 425.

Ishii, Mamoru, and Takashi Hibiki. 2011. Thermo-fluid dynamics of two-phase flow. Verlag, New York: Springer.

Ito, D., H.-M. Prasser, H. Kikura, and M. Aritomi. 2011. Uncertainty and intrusiveness of three-layer wire-mesh sensor. Flow Measurement and Instrumentation 22(4):249 – 256.

Jiang, S.Y., M.S. Yao, J.H. Bo, and S.R. Wu. 1995. Experimental simulation study on start-up of the 5 {MW} nuclear heating reactor. Nuclear Engineering and Design 158(1):111 – 123.

Joseph, Daniel D., and Bobby H. Yang. 2009. Friction factor correlations for laminar, transition, and turbulent flow in smooth pipes. Physica D: Nonlinear Phenomena 239:1318–1328.

Kelly, J.E., and M.S. Kazimi. 1982. Interfacial exchange relations for two-fluid vapor-liquid flow: a simplified regime-map approach. Nuc. Sci. and Eng. 81(3):305–318.

Kim, Jong Moon, and Sang Yong Lee. 2000. Experimental observation of flow instability in a semi-closed two-phase natural circulation loop. Nuclear Engineering and Design 196(3):359 – 367.

Kumar, Sailesh B., Davood Moslemian, and Milorad P. Dudukovic´. 1995. A γ-ray tomographic scanner for imaging voidage distribution in two-phase flow systems. Flow Measurement and Instrumentation 6(1):61 – 73.

Ledinegg, M. 1938. Instability of flow during natural and forced circulation. Die Warme.

Lee, Y.-G, W.-Y Won, B.-A Lee, and S. Kim. 2017. A dual conductance sensor for simultaneous measurement of void fraction and structure velocity of downward two-phase flow in a slightly inclined pipe. Sensors 17(5): 1063.

Light, Truman S. 1984. Temperature dependence and measurement of resistivity of pure water. Anal. Chem. 56:1138 – 1142.

Lisowski, D., Chan Soo Kim, G.C. Park, and M .L. Corradini. 2016. Comparative study on scaling analysis between two reduced scale tests for reactor cavity cooling system. Tech. Rep. 2014-006-K, ANL, KAERI, and UW.

Lisowski, D. D., S. M. Albiston, R. M. Scherrer, T. C. Haskin, M. H. Anderson, A. Tokuhiro, and M. L. Corradini. 2011. Experimental studies of ngnp reactor cavity cooling system with water. In Icapp. Nice, France.

Lisowski, Darius. 2013. Thermal hydraulic analysis of an experimental reactor cavity cooling system with water: Performance and stability. Ph.D. thesis, University of Wisconsin - Madison.

Lisowski, Darius D., Taeseung Lee, Dennis J. Kilsdonk, Nathan C. Bremer, Craig D. Gerardi, Stephen W.

Lomperski, and Mitchell T. Farmer. 2015. Status report on the water-based nstf rccs capability. Tech. Rep. ART-23, Argonne National Laboratories.

Lisowski, D.D., O. Omotowa, M.A. Muci, A. Tokuhiro, M.H. Anderson, and M.L. Corradini. 2014. Influences of boil-off on the behavior of a two-phase natural circulation loop. International Journal of Multiphase Flow 60: 135 – 148.

Mandhane, J.M., G.A. Gregory, and K. Aziz. 1974. A flow pattern map for gas-liquid flow in horizontal pipes. International Journal of Multiphase Flow 1(4):537 – 553.

Manera, A., H.-M Prasser, T.H.J.J. van der Hagen, R. F. Mudde, and W.J.M. de Kruijf. 2001. A comparison of void-fraction measurements during flashing-induced instabilities obtained with a wire-mesh sensor and a gamma-transmission set-up. In Proc. 4th international conferance on multiphase flow. New Orleans, LA.

Manera, A., H.-M. Prasser, D. Lucas, and T.H.J.J. van der Hagen. 2006. Three-dimensional flow pattern visualization and bubble size distributions in stationary and transient upward flashing flow. International Journal of Multiphase Flow 32(8):996 – 1016.

Manera, A., U. Rohde, H.-M. Prasser, and T.H.J.J. van der Hagen. 2005a. Modeling of flashing-induced instabilities in the start-up phase of natural-circulation {BWRs} using the two-phase flow code {FLOCAL}. Nuclear Engineering and Design 235(14):1517 – 1535.

Manera, Annalisa, and Tim H. J. J. van der Hagen. 2003. Stability of natural-circulation-cooled boiling water reactors during startup: Experimental results. Nuclear Technology 143(1):77–88.

Manera, Annalisa, Horst Michael Prasser, and Tim H J J Van Der Hagen. 2005b. Suitability of drift-flux models, void-fraction evolution, and 3-d flow pattern visualization during stationary and transient flashing flow in a vertical pipe. Nuclear Technology 152(1):38–53.

Marcel, Christian P., M. Rohde, and T.H.J.J. Van Der Hagen. 2010. Experimental investigations on flashing-induced instabilities in one and two-parallel channels: A comparative study. Experimental Thermal and Fluid Science 34(7):879 – 892.

MatWeb. 2017. Steel, general properties. MatWeb material property data.

Maxwell, J. 1881. A treatise on electricity and magnitism, vol. 1. 2nd ed. Oxford University Press Warehouse.

Miller, Richard W. 1996. Flow measurement engineering handbook. McGraw-Hill.

Muci, Moses A. 2014. Thermal hydraulic analysis of an experimental reactor cavity cooling system with air.

Master's thesis, University of Wisconsin - Madison.

Munson, B.R., D.F. Young, T.H. Okiishi, and W.W. Huebsch. 2009. fundamentals of fluid mechanics. 6th ed. Wiley and Sons.

Nayak, A. K., P. K. Vijayan, D. Saha, V. Venkat Raj, and Masanori Aritomi. 1998. Adequacy of power-to-volume scaling philosophy to simulate natural circulation in integral test facilities. Journal of Nuclear Science and Technology 35(10):712–722. http://dx.doi.org/10.1080/18811248.1998.9733932.

Nayak, A. K., and P.K. Vijayan. 2008. Flow instabilities in boiling two-phase natural circulation system: A review. Science and Technology of Nuclear Installations 2008.

Nayak, A.K., P. Dubey, D.N. Chavan, and P.K. Vijayan. 2007. Study on the stability behaviour of two-phase natural circulation systems using a four-equation drift flux model. Nuclear Engineering and Design 237(4):386 – 398.

Nayak, A.K., M.R. Gartia, and P.K. Vijayan. 2008. An experimental investigation of single-phase natural circulation behavior in a rectangular loop with al2o3 nanofluids. Experimental Thermal and Fluid Science 33(1):184 – 189.

Nayak, A.K., P.K. Vijayan, V. Jain, D. Saha, and R.K. Sinha. 2003. Study on the flow-pattern-transition instability in a natural circulation heavy water moderated boiling light water cooled reactor. Nuclear Engineering and Design 225(2âŁ“3):159 – 172.

Nuryadin, S., M. Ignaczak, D. Lucas, and Deendarlianto. 2015. On the accuracy of wire-mesh sensors in dependence of bubble sizes and liquid flow rates. Experimental Thermal and Fluid Science 65:73 – 81.

Oh, Chang H., Cliff Davis, Larry Siefken, Richard Moore, Hee C. NO, Jong Kim, Goon C. Park amd John C. Lee, and William R. Martin. 2006. Development of safety analysis codes and experimental validation for a very high temperature gas-cooled reactor. Tech. Rep., Idaho National Labratories.

Oh, Jae Jong. 2015. Melcor model and analysis of uw water-cooled reactor cavity cooling system. Master's thesis, University of Wisconsin - Madison.

Pietruske, Heiko, and Horst-Michael Prasser. 2007. Wire-mesh sensors for high-resolving two-phase flow studies at high pressures and temperatures. Flow Measurement and Instrumentation 18(2):87 – 94.

Pike, R. W., Bert Wilkins, and H. C. Ward. 1965. Measurement of the void fraction in two-phase flow by x-ray attenuation. AIChE Journal 11(5):794–800.

Porter, B. 1968. Stability criteria for linear dynamical systems. New York/London: Academic Press.

Prasad, Gonella V. Durga, Manmohan Pandey, and Manjeet S. Kalra. 2007. Review of research on flow instabilities in natural circulation boiling systems. Progress in Nuclear Energy 49(6):429 – 451.

Prasser, H.-M. 2013. Generalized cross-correlation technique for the measurement of time-dependent velocities. In Proc. 16th international meeting on nuclear reactor thermal hydraulics. Pisa,Italy.

Prasser, H.-M., M. Beyer, A. Böttger, H. Carl, D. Lucas, A. Schaffrath, P. SchÃ¼tz, F.-P. Weiss, and J. Zschau. 2005a. Influence of the pipe diameter on the structure of the gas-liquid interface in a vertical two-phase pipe flow. Nuclear Technology 152(1):3–22.

Prasser, H.-M, A Böttger, and J Zschau. 1998. A new electrode-mesh tomograph for gas-liquid flows. Flow Measurement and Instrumentation 9(2):111 – 119.

Prasser, H.-M., M. Misawa, and I. Tiseanu. 2005b. Comparison between wire-mesh sensor and ultra-fast x-ray tomograph for an airâŁ“water flow in a vertical pipe. Flow Measurement and Instrumentation 16(2âŁ“3): 73 – 83. Tomographic Techniques for Multiphase Flow Measurements4th International Symposium on Measurement Techniques for Multiphase Flows.

Prasser, H.-M., D. Scholz, and C. Zippe. 2001. Bubble size measurement using wire-mesh sensors. Flow Measurement and Instrumentation 12(4):299 – 312.

Prasser, H. M, S. Stucki, T. Betschart, and J. Eisenberg. 2015. Interfacial area density measurement using a three-layer wire-mesh sensor. In 16th international topical meeting on nuclear reactor thermal hydraulics. Chicago, IL.

Prasser, Horst-Michael. 2007. Evolution of interfacial area concentration in a vertical airâŁ“water flow measured by wireâŁ“mesh sensors. Nuclear Engineering and Design 237(15):1608 – 1617. NURETH-11.

Prasser, Horst-Michael, and Matthais Beyer. 2007. Bubble recognition algorithms for the processing of wire-mesh sensor data. In 6th international conferance on multiphase flow. Leipzig, Germany.

Prasser, Horst-Michael, and Richard Häfeli. 2016. Signal response of wire-mesh sensors to an idealized bubbly flow. In Specialist workshop on advanced instrumentation and measurement techniques for nuclear reactor thermal hydraulics. Livorno, Italy.

Rahim, R. Abdul, M.H. Fazalul Rahiman, K.S. Chan, and S.W. Nawawi. 2007. Non-invasive imaging of liquid/gas flow using ultrasonic transmission-mode tomography. Sensors and Actuators A: Physical 135(2): 337 – 345.

Richter, S., M. Aritomi, H.-M. Prasser, and R. Hampel. 2002. Approach towards spatial phase reconstruction in transient bubbly flow using a wire-mesh sensor. International Journal of Heat and Mass Transfer 45(5):1063 – 1075.

Rue, Robert E. De La, and Charles W. Tobias. 1959. On the conductivity of dispersions. Journal of The Electrochemical Society 106(9):827–833. http://jes.ecsdl.org/content/106/9/827.full.pdf+html.

Russ, John C. 2011. Image processing handbook 6th edition. 6th ed. Boca Raton, FL: CRCPress.

Schlegel, J.P., and T. Hibiki. 2015. A correlation for interfacial area concentration in high void fraction flows in large diameter channels. Chemical Engineering Science 131:172 – 186.

Shaban, H., and S. Tavoularis. 2016. On the accuracy of gas flow rate measurements in gas-liquid pipe flows by cross-correlating dual wire-mesh sensor signals. International Journal of Multiphase Flow 78:70 – 74.

Sharaf, S, M Da Silva, U Hampel, C Zippe, M Beyer, and B Azzopardi. 2011. Comparison between wire mesh sensor and gamma densitometry void measurements in two-phase flows. Measurement Science and Technology 22(10):104019.

Sigrist, L., O. Dossenbach, and N. Ibl. 1980. On the conductivity and void fraction of gas dispersions in electrolyte solutions. Journal of Applied Electrochemistry 10(2):223–228.

Simiano, M., and H.-M Prasser. 2007. Estimation of individual bubble velocities in a gas-liquid flow using wire-mesh sensors. In Proc. 6th international conferance on multiphase flow. Leipzig, Germany.

Simoneau, Jan-Patrice, Julien Champigny, Brian Mays, and Lewis Lommers. 2007. Three-dimensional simulation of the coupled convective, conductive, and radiative heat transfer during decay heat removal in an {HTR}. Nuclear Engineering and Design 237(15-17):1923 – 1937. NURETH-11th International Topical Meeting on Nuclear Reactor Thermal Hydraulics.

SNL. 2010. Melcor computer code manuals. Sandia National Laboratory.

Taitel, Yemada, and A. E. Dukler. 1976. A model for predicting flow regime transitions in horizontal and near horizontal gas-liquid flow. AlChE Journal 22(1).

Tebug, T. 2009. Experimental study of the influence of the axial distance between the electrode grids on the void fraction measured by wire-mesh sensors. Tech. Rep., ETH Zurich: Laboratory on Nuclear Energy Systems.

teletronic. 2012. Wire mesh system wms200 specification. Tech. Rep. 1.06, Teletronic Rossendorf GmbH.

Thome, J. R. 2007. Engineering data book iii. Lausanne, Switzerland: Wolverine Tube inc.

Todreas, Neil E., and Mujid S. Kazimi. 2012. Nuclear systems volume i thermal hydraulic fundamentals. 2nd ed. CRC Press.

Tompkins, Casey. 2017. Experimental investigations in a reactor cavity cooling system with advanced instrumentation for the study of instabilities, oscillations, and transients. Ph.D. thesis, University of Wisconsin - Madison.

Wu, Zongxin, Dengcai Lin, and Daxin Zhong. 2002. The design features of the htr-10. Nuclear Engineering and Design 218(1-3):25 – 32.

Zhang, Zhiqiang, Martina Bieberle, Frank Barthel, Lutz Szalinski, and Uwe Hampel. 2013. Investigation of upward cocurrent gasâŁ“liquid pipe flow using ultrafast x-ray tomography and wire-mesh sensor. Flow Measurement and Instrumentation 32:111 – 118.

Zircar. 2005. Refractory board types zircal-18, zircal-45 and zircal-95. Tech. Rep. ZRCI-301, ZRCI Refractory Composites.

Zuber, N. 1980. Problems in modeling of small break loca. Tech. Rep. NUREG-0724, U.S. Nuclear Regulatory Commission, Washington, D.C.

Zuber, N., F.W. Staub, G. Bijwaard, and P.G. Kroeger. 1967. Steady state and transient void fraction in two-phase flow systems. final report for the program of two-phase flow investigation. volume 1. Tech. Rep. GEAP–5417, General Electric Co.

Zuber, N.N., and J.A. Findlay. 1965. Average volumetric concentration in two-phase flow systems. J. Heat Transfer 87(4):453 – 468.

Tsumaki, Koji, Takahiro Kanamori, Fuminobu Takashi, and Takashi Ikeda. 1984. Measurement of void fraction distribution by gamma-ray computed tomography. Journal of Nuclear Science and Technology 21(4): 315–317. http://www.tandfonline.com/doi/pdf/10.1080/18811248.1984.9731049.

Vijayan, P.K, and H Austregesilo. 1994. Scaling laws for single-phase natural circulation loops. Nuclear Engineering and Design 152(1):331 – 347.

Wallis, G. B., and J. H. Heasley. 1961. Oscillations in two-phase flow systems. J. Heat Transfer 83(3):363 – 369.

Wangjiraniran, Weerin, Yuichi Motegi, Steffen Richter, Hiroshige Kikura, Masanori Aritomi, and Kazuhiko

Yamamoto. 2003. Intrusive effect of wire mesh tomography on gas-liquid flow measurement. Journal of Nuclear Science and Technology 40(11):932–940. http://www.tandfonline.com/doi/pdf/10.1080/18811248. 2003.9715436.

Winterton, R.H.S. 1998. Where did the dittus and boelter equation come from? International Journal of Heat and Mass Transfer 41(4):809 – 810.

# REFERENCES PART II

Albertson, M. L., Dai, Y. B., Jensen, R. A. and Rouse, H. (1950), Diffusion of Submerged Jets, Transactions of ASCE, Vol. 115, pp. 639-664.

E. A. Anderson and R. E. Spall, "Experimental and numerical investigation of two-dimensional parallel jets", *Journal of Fluids Engineering,* **123,** pp. 401-406 (2001).

Chen, C. J. and Chen, C. H., On Prediction and Unified Correlation for Decay of Vertical Buoyant Jets, Journal of Heat Transfer (ASME), 101(3), 1979, pp: 532-537.

H. Coleman, W. G. Steele, 'Handbook of Fluid Dynamics', Ch. 51, Taylor & Francis Group (2016)

ECMFL, http://www.umich.edu/~nuclear/labs/ecmf/

Durve, A and Patwardhan, A. W and Banarjee, I and Padmakumar, G and Vaidyanathan, G, "Numerical investigation of mixing in parallel jets", *Nuclear Engineering and Design*, **242**, 2012.

Ko, NWM and Lau, KK, "Flow structures in initial region of two interacting parallel plane jets", *Experimental Thermal and Fluid Science*, **2**(4), 1989.

M. T. Farmer, et. al., "Natural Convection Shutdown Heat Removal Test Facility (NSTF) Evaluation for Generating Additional Reactor Cavity Cooling System (RCCS) Data", ANL-GenIV-058, 2005.

FreePCB User Guide Version 1.4 (http://www.freepcb.com/)

Gerber File Format Specification Rev. J2". Ucamco. June 2014. Retrieved 6 July 2014

Lin, YF and Sheu, MJ, "Investigation of two plane paralleltiinven ilated jets", *Experiments in Fluids*, **10**(1), 1990.

D. Lisowski, Thermal Hydraulic Analysis of an Experimental Reactor Cavity Cooling System with Water: Performance and Stability, PhD Thesis, University of Wisconsin, 2013.

D. Lisowski et al, "Influences of boil-off on the behavior of a two-phase natural circulation loop", International Journal of Multiphase Flow, V60, pp135–148, 2014.

Lisowski, D. D., Moses, M. A., Anderson, M. H., Corradini, M. L., Design Considerations for a Scaled Reactor Cavity Cooling System with Air for the VHTR, 15th International Topical Mtg on Nuclear Reactor Thermal-hydraulics, NURETH-15, Pisa, Italy, May 12-15, 2013.

Mi Jianchun, Nathan, G. J. and Luxton, R. E., Centerline mixing characteristics of jets from nine differently shaped nozzles, Experiments in Fluids, 28(1), 2000, pp: 93-94.

Miller, D.R., Comings, E.W., "Force momentum fields in a dual-jet flow", *Journal of Fluid Mechanics* **7**, pp. 237–256, 1960.

A. A. Mostafa, M.M. Khalifa, and E.A. Shabana, "Experimental and numerical investigation of multiple rectangular jets", *Experimental Thermal and Fluid Science,* **21,** pp. 171-178(2000).

Namer, I and Ötügen, MV, "Velocity measurements in a plane turbulent air jet at moderate Reynolds numbers", *Experiments in Fluids*, **6**(6), 1998.

Nasr, A and Lai, JCS, "Comparison of flow characteristics in the near field of two parallel plane jets and an offset plane jet", *Physics of Fluids*, **9**(10), 1997.

T. Nguyen, V. Petrov, A. Manera, "A separate-effect test facility for CFD-grade measurements of the RCCS upper plenum", *Proc. of the 16th Int. Topical Meeting on Nuclear Reactor Thermal Hydraulics (NURETH-16)*, Chicago, IL, USA, 2015.

T. Nguyen, V. Petrov, A. Manera, "Design of a scaled experimental facility for the NGNP Reactor Cavity Cooling System", *American Nuclear Society 2014 Winter Meeting and Technology Expo*, Anaheim, California, 2014.

Prasser, H.-M.; Böttger, A.; Zschau, J., A New Electrode-Mesh Tomograph for Gas-Liquid Flows,Flow Measurement and Instrumentation 9 (1998) 111-119.

Raffel M., Willert C., Wereley S., Kompenhans J., *Particle image velocimetry: a practical guide*. Springer-Verlag, 2007.

Rouse, H., Yih, C. S., and Humphreys, H. W. (1952), Gravitational Convection from a Boundary Source, Tellus, Vol. 4, pp. 201-210.

B. Smith, D. Neal, "Re-thinking of data acquisition rates in the era of expensive data", 2016 ASME Fluids Engineering Division Summer Meeting, Washington, D.C., July 10-14, 2016, pp. 1-8 (2016).

M. Sullivan, Statistics: Informed Decision Using Data. Pearson, third edition. (2017)

Tanaka, E., "The interference of two-dimensional parallel jets (1st report, experiments on dual jet)". *Bulletin JSME* **13**, pp. 272–280, (1970).

Tanaka, E., "The interference of two-dimensional parallel jets (2nd report, experiments on the combined flow of dual jet)". *Bulletin JSME* **17**, pp. 920–927, 1974.

Tollmien, W. (1926), Berechnung Turbulenter Ausbreitungsvorgange, ZAMM, 6, pp. 468-478.

Turner J. S., Jets and Plumes with Negative or Reversing Buoyancy, Journal of Fluid Mech. 26, 1996, pp: 779-792.

C. Tzanos, "CFD Analysis for the Applicability of the Natural Convection Shutdown Heat Removal test Facility (NSTF) for the simulation of the VHTR RCCS", ANL-GenIV-055, 2005.

R. V. Vilim and E. E. Feldman, "Scalability of the Natural Convection Shutdown Heat Removal Test Facility (NSTF) Data to VHTR/NGNP RCCS Designs", ANL-GenIV-049, 2005

Yannopoulos, P. and Noutsopoulos, G., The plane vertical turbulent buoyant jet, Journal of Hydraulic Research, 28(5), 1990, pp: 565-580.

Yannopoulos, P. and Noutsopoulos, G., Interaction of vertical round turbulent buoyant jets - Part I: Entrainment restriction approach, Journal of Hydraulic Research, 44(2), 2006, pp: 218-232.

Westerweel J., "Efficient detection of spurious vectors in particle image velocimetry data", *Experiments in Fluids*, **16**(3), 1994.

# APPENDIX A: Technical drawings of UWRCCS test facility and experimental test matrix

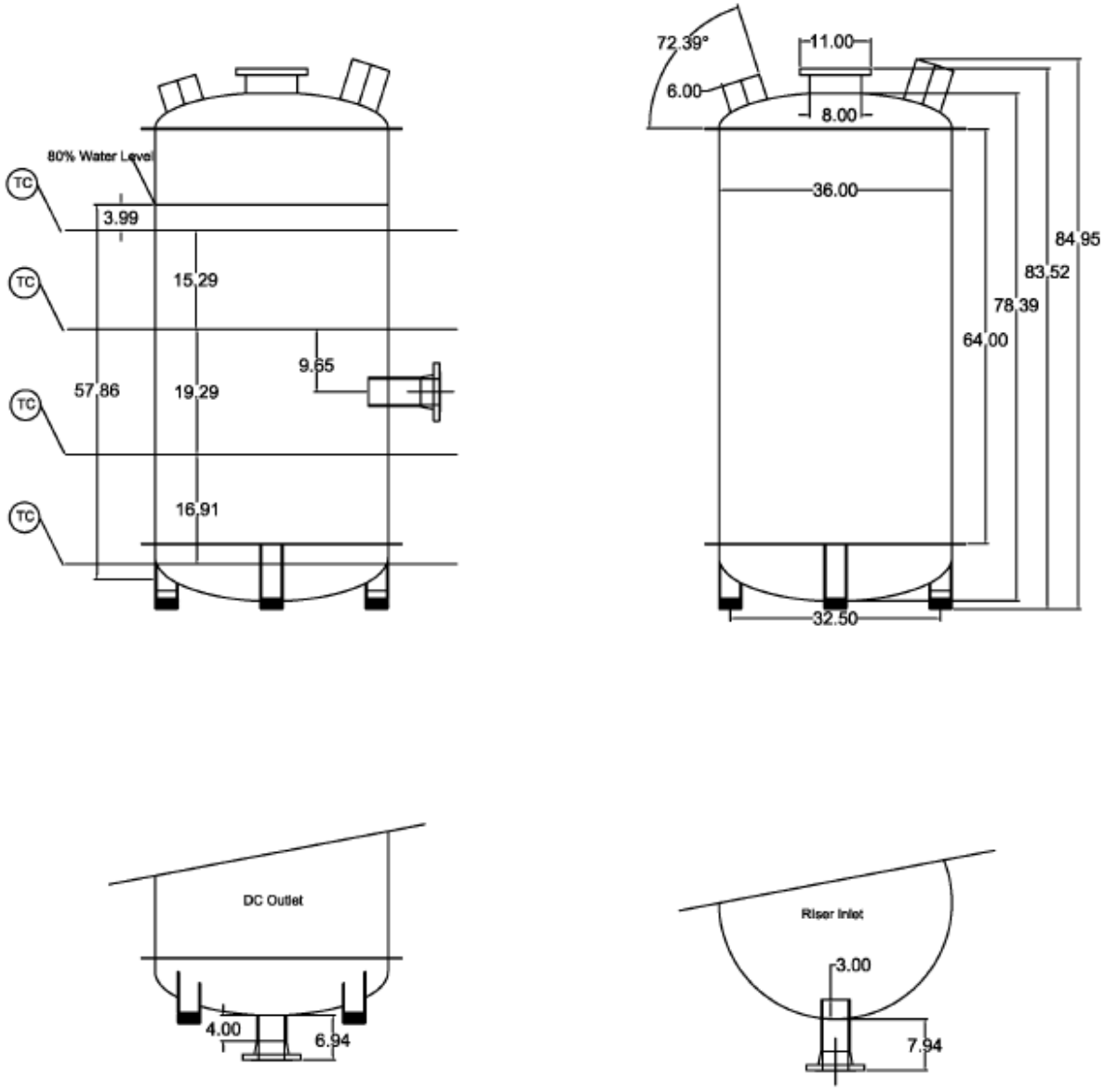


Water storage tank

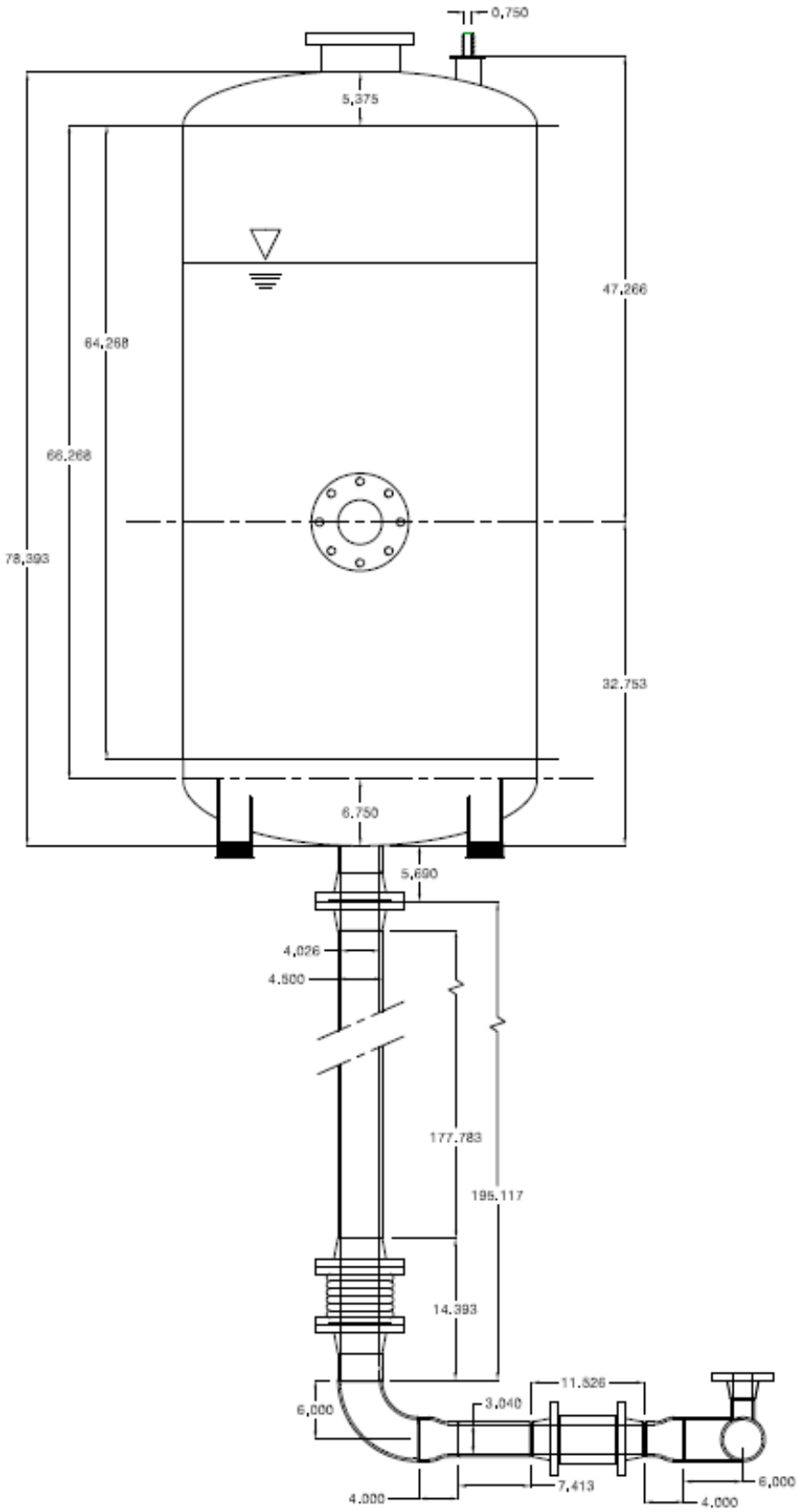


Front view of water storage tank, downcomer and lower network

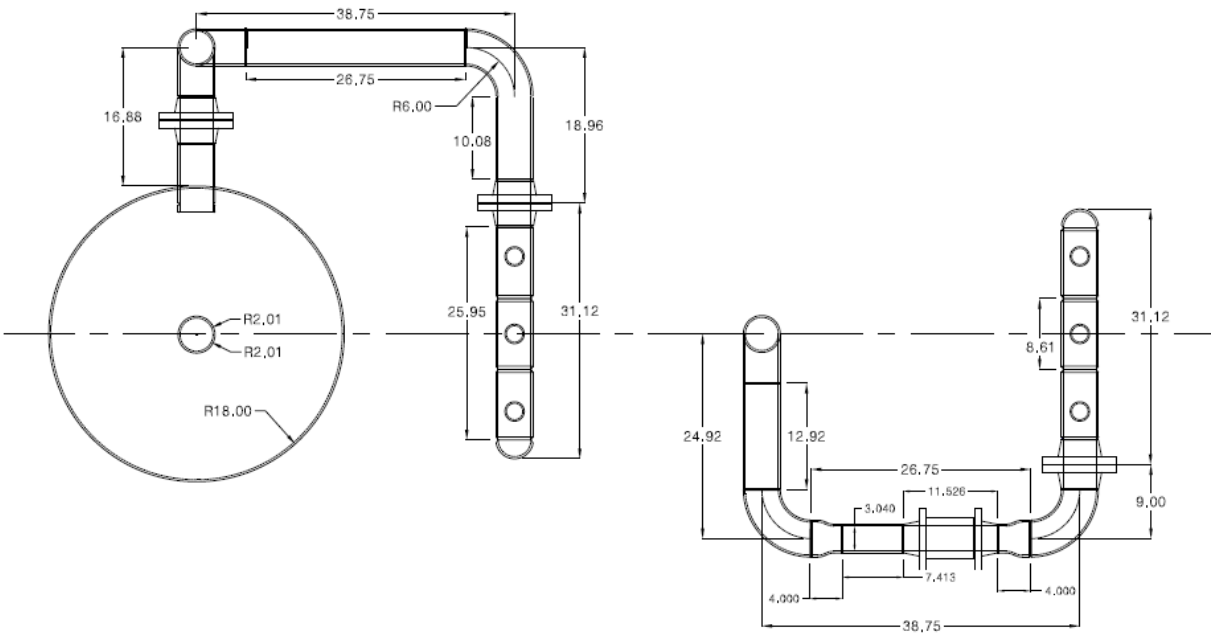


Plan view of upper and lower networks

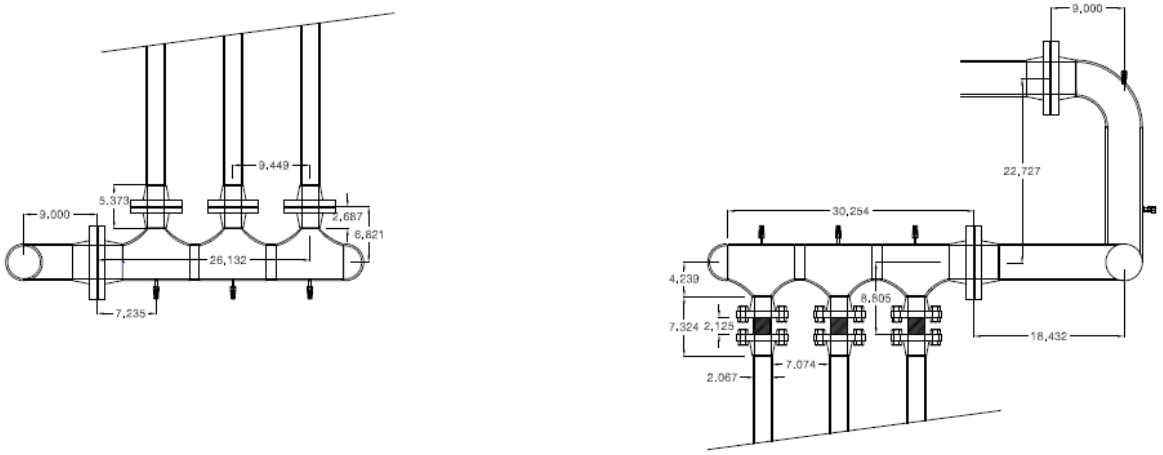


Front view of upper and lower networks

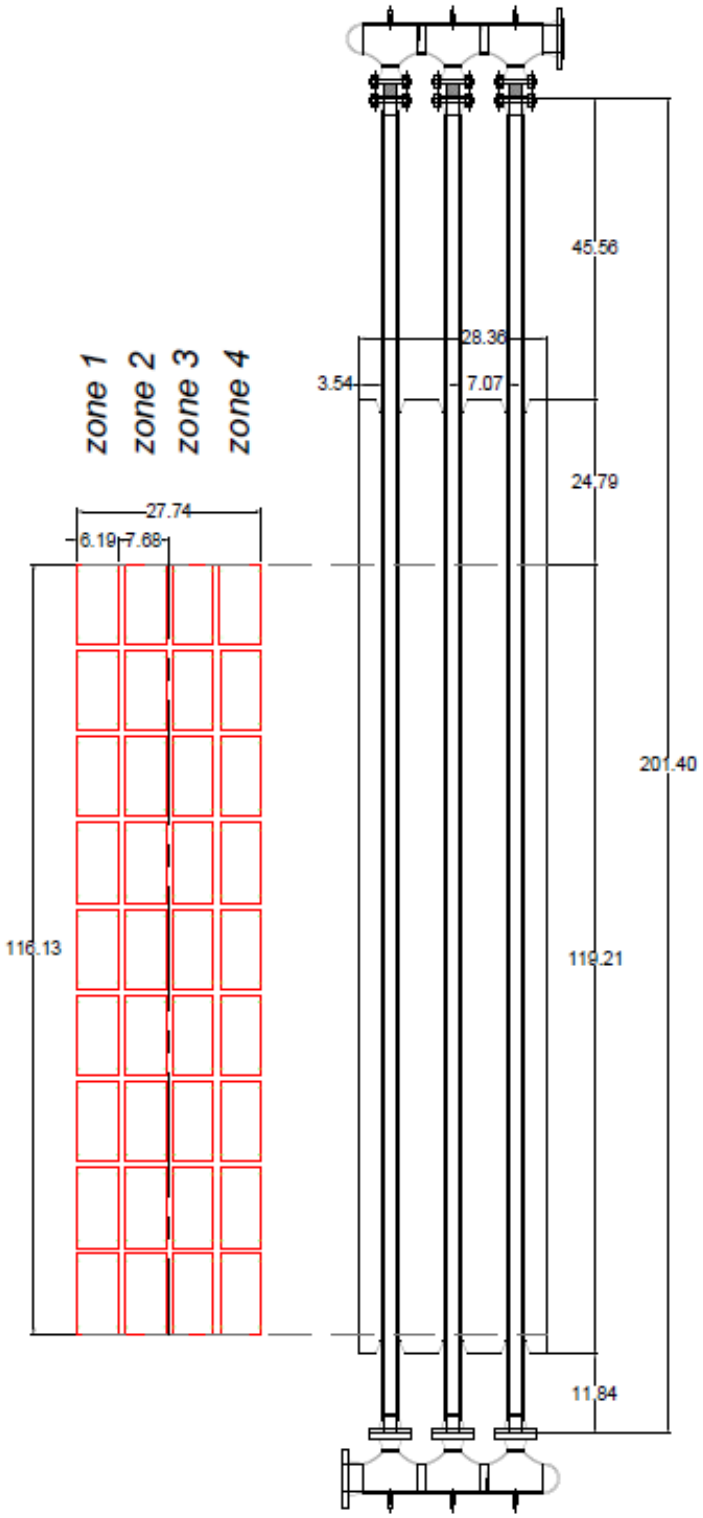


Alignment of radiant heaters and riser tubes section

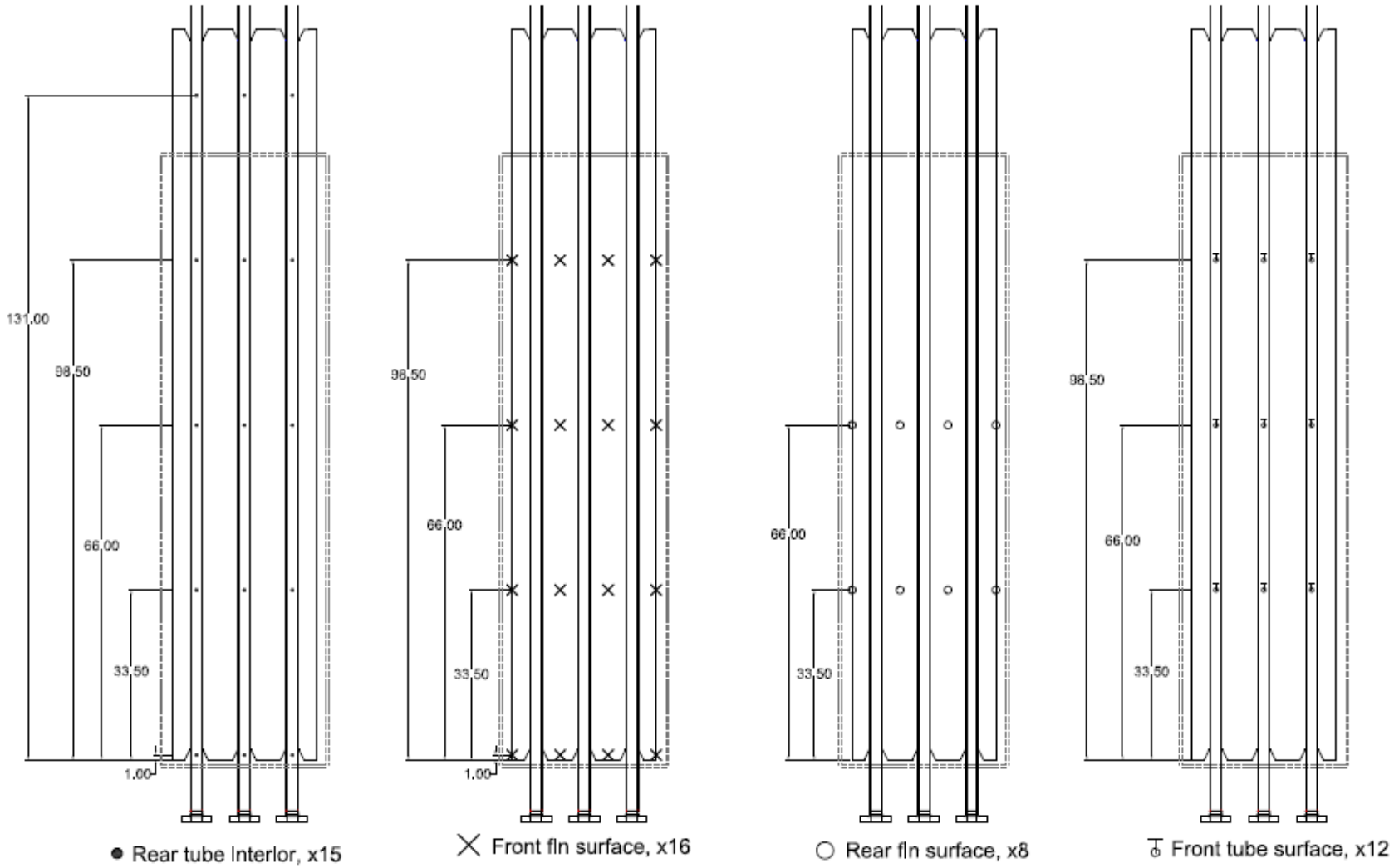


Placement of fluid and surface thermocouples on test section

| Num. | Power [kW] | Purpose | Tank Level [in.] | Presented |
|---|---|---|---|---|
| 103 | 15.19 | 60% Volume | 38.25" | No |
| 105 | 15.19 | 60% Volume, WMS | 38.25" | No |
| 106 | 15.19 | 55% Volume, WMS | 33.50" | No |
| 107 | 15.19 | 70% Volume, WMS | 46.75" | No |
| 108 | 15.19 | 60% Volume, WMS | 38.25" | Yes |
| 110 | 15.19 | 60% Volume, pressurized, WMS | 38.25" | No |
| 111 | 15.19 | 60% Volume, pressurized, WMS | 38.25" | Yes |
| 112 | 15.19 | 60% Volume, pressurized, WMS | 38.25" | No |
| 113 | 15.19 | 60% Volume, pressurized, WMS | 38.25" | No |
| 116 | 15.19 | 60% Volume, isothermal, WMS | 38.25" | Yes |
| 117 | 15.19 | 60% Volume, pressurized, WMS | 38.25" | Yes |
| 118 | 15.19 | 60% Volume, pressurized, WMS | 38.25" | Yes |
| 119 | 15.19 | 60% Volume, variable pressure, WMS | 38.25" | Yes |
| 120 | 15.19 | Pressurized Forced Drain | 52.00" | Yes |
| 121 | 15.19 | 80% Volume, orifice | 52.50" | No |
| 122 | 15.19 | 80% Volume, orifice | 51.625" | No |
| 123 | 15.19 | 70% Volume, orifice | 46.75" | No |
| 124 | 15.19 | 60% Volume, 1/2 orifice | 38.25" | No |
| 125 | 15.19 | 60% Volume, 1/2 orifice, WMS | 39.00" | Yes |
| 126 | 15.19 | 80% Volume, 1/2 orifice, WMS | 53.25" | Yes |
| 127 | 15.19 | 70% Volume, 1/2 orifice, WMS | 46.50" | Yes |
| 128 | 15.19 | 60% Volume, 1/8 orifice, WMS | 38.50" | Yes |
| 129 | 12.19 | 70% Volume, 1/8 orifice, WMS | 46.8125" | Yes |
| 130 | 15.19 | 80% Volume, 1/8 orifice, WMS | 52.75" | Yes |
| 131 | 15.19 | 60% Volume, 1/8 orifice, WMS | 38.50" | Yes |
| 133 | 15.19 | 60% Volume, 1/4 orifice, WMS | 38.50" | Yes |
| 134 | 15.19 | 70% Volume, 1/4 orifice, WMS | 47.00" | Yes |
| 135 | 15.19 | 80% Volume, 1/4 orifice, WMS | 53.00" | Yes |
| 137 | 15.19 | 60% Volume, mixed orifice, WMS | 39.1875" | Yes |
| 138 | 15.19 | 70% Volume, mixed orifice, WMS | 46.75" | Yes |
| 139 | 15.19 | 80% Volume, mixed orifice, WMS | 53.25" | Yes |
| 140 | 15.19 | 60% Volume, mixed orifice, WMS | 38.375" | Yes |
| 141 | 8.5 | 60% Volume, asymmetric heating, WMS | 38.75" | No |
| 142 | 15.19 | 60% Volume, refill, WMS | 38.375" | Yes |

Two-phase testing overview

# APPENDIX B: Technical drawings of UM separate-effect test facility

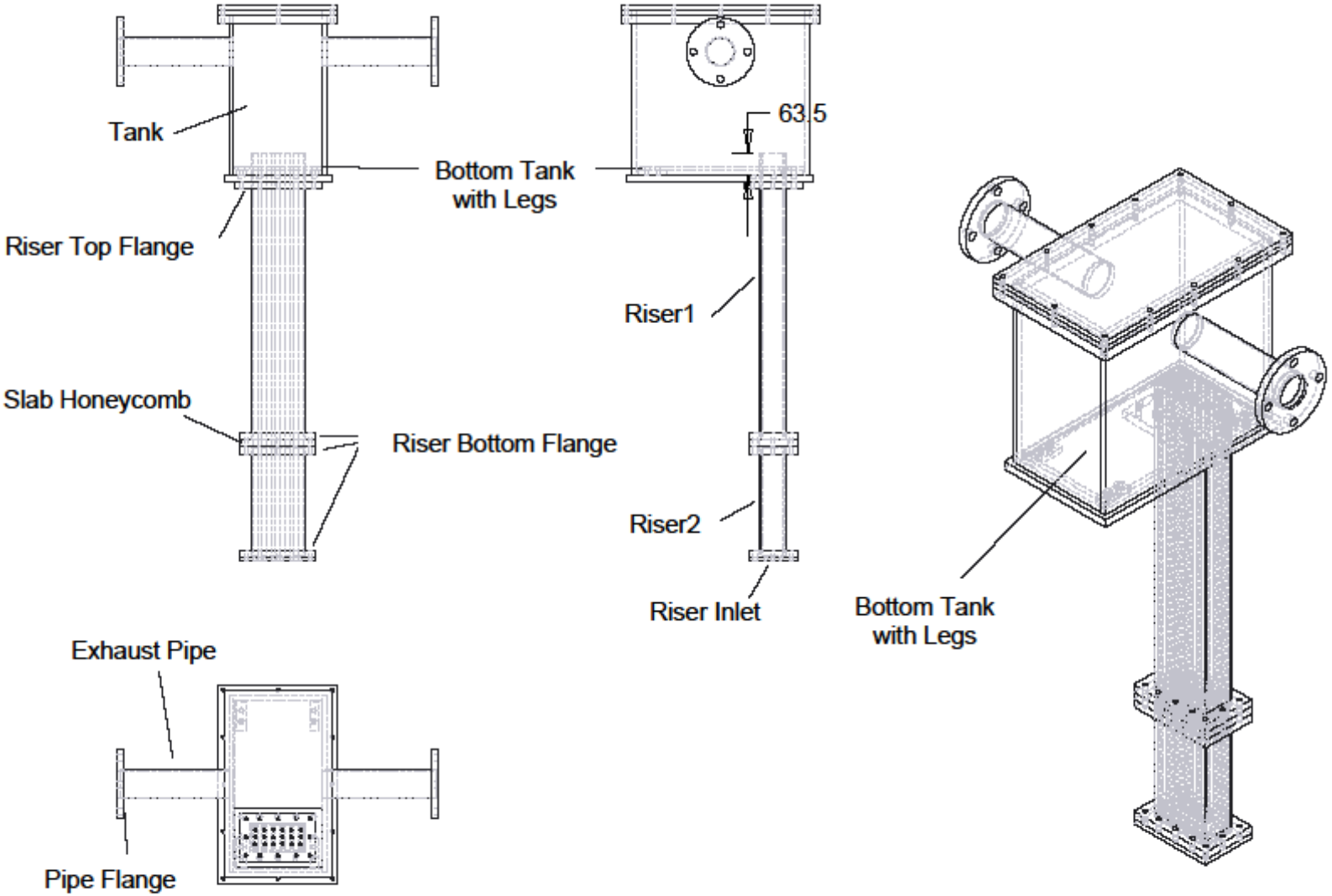

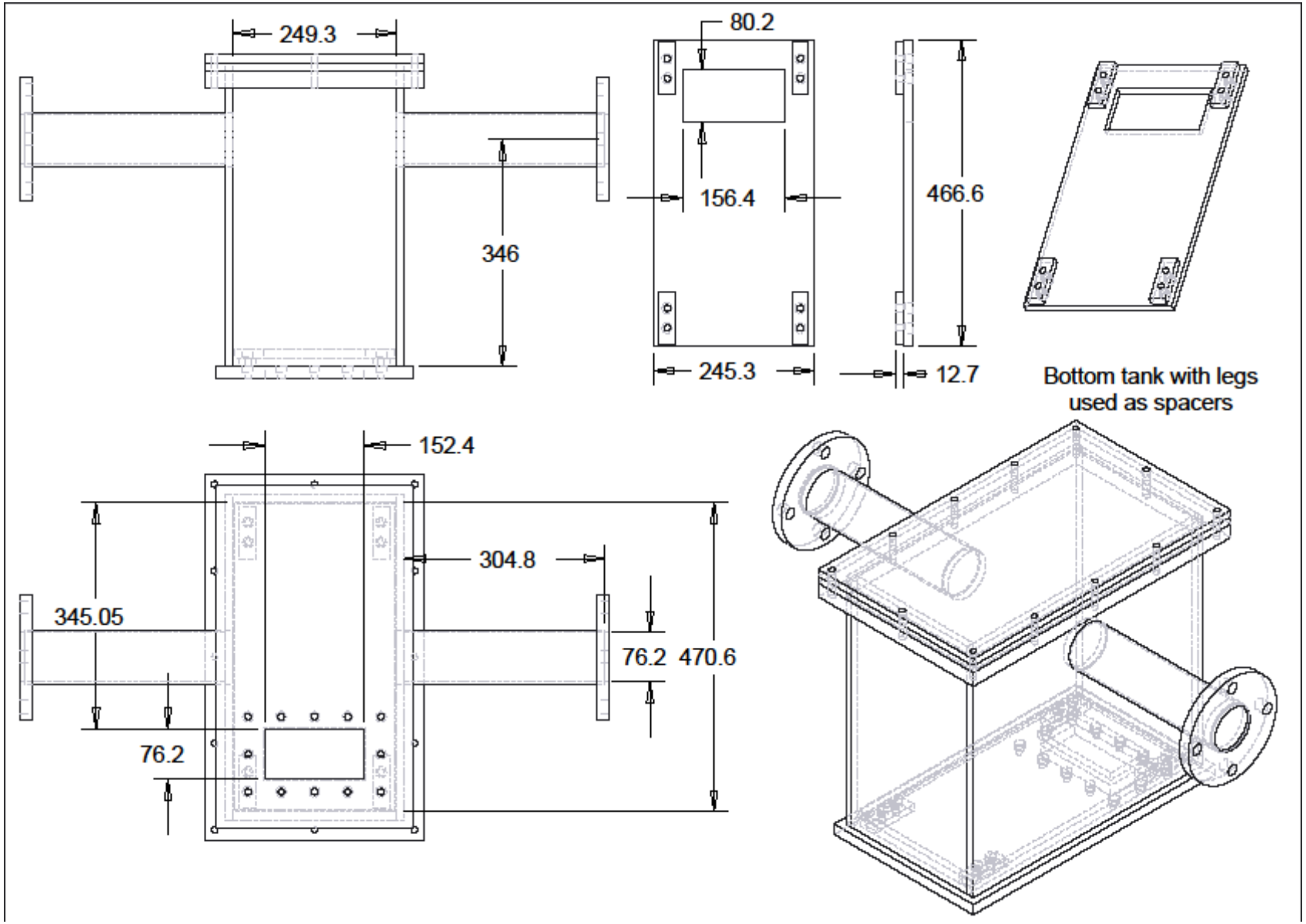
249.3
346
80.2
156.4
245.3
466.6
12.7
Bottom tank with legs
used as spacers
152.4
304.8
345.05
76.2
76.2
470.6

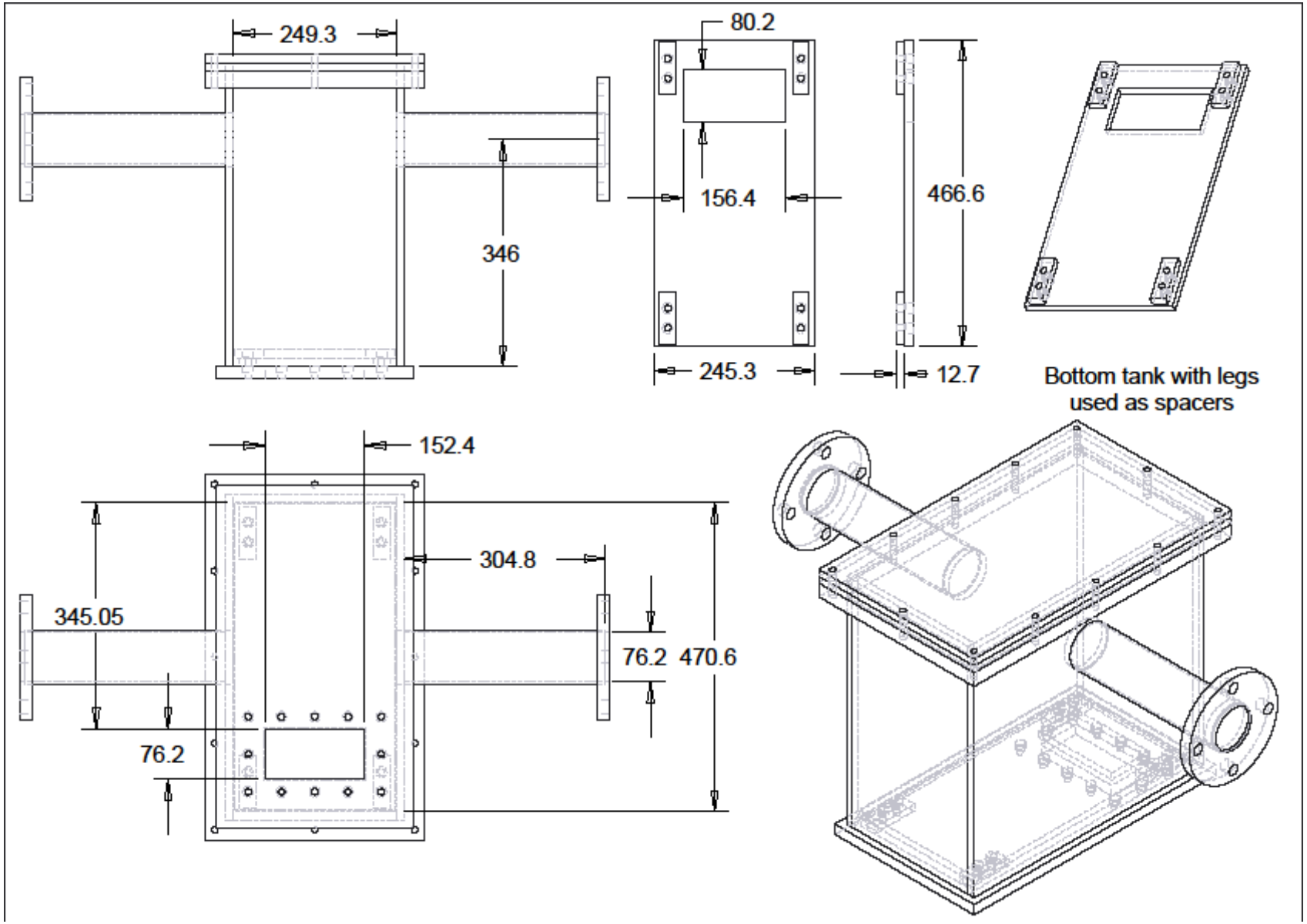
249.3
346
80.2
156.4
245.3
466.6
12.7
Bottom tank with legs
used as spacers
152.4
304.8
345.05
76.2
76.2
470.6

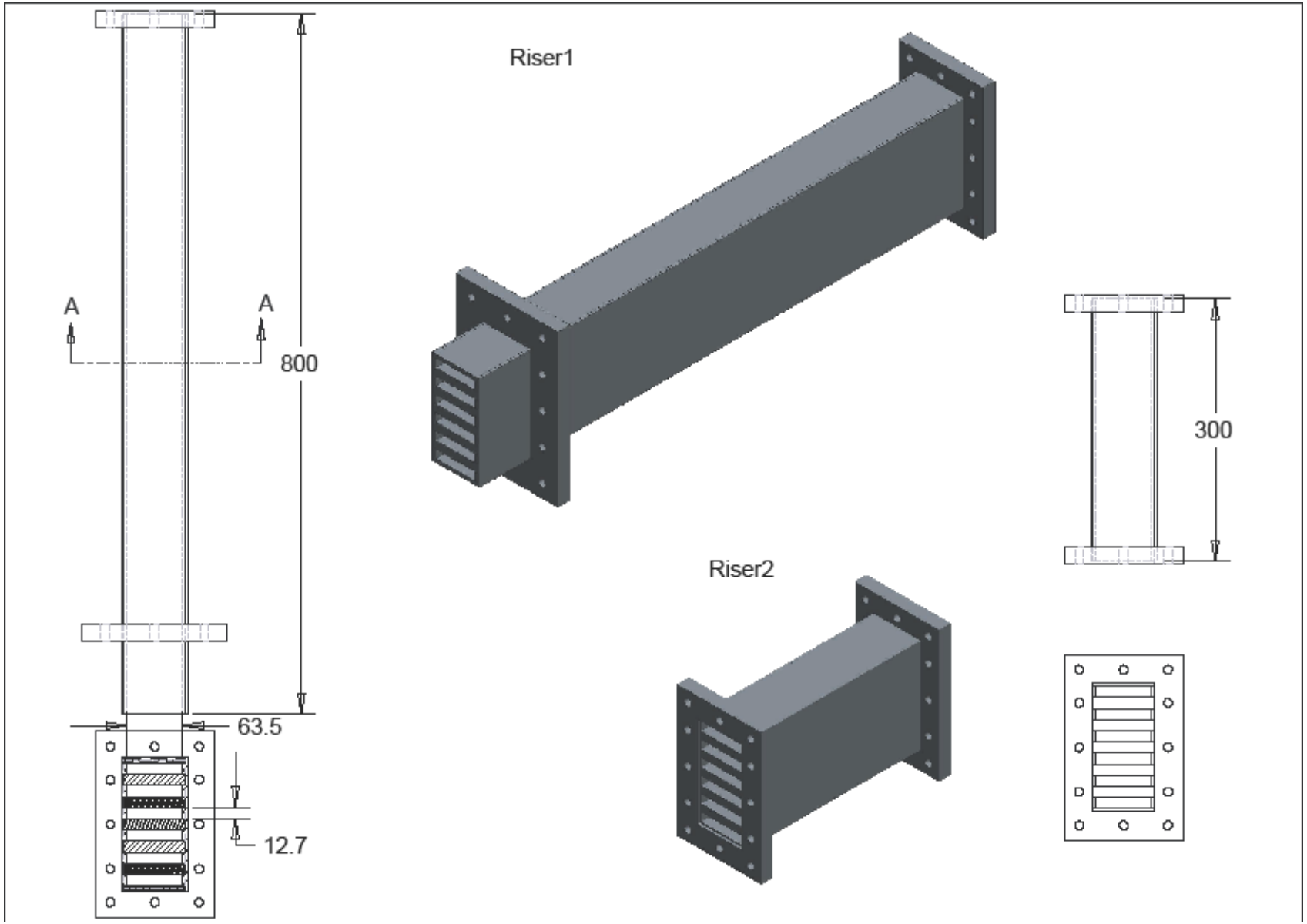
A
A
800
63.5
12.7
Riser1
300
Riser2